Errata

p12	line 5	masses (amsses)
p35	line 27	mono- (mon-)
p37	line 11	50 A^{o} in height
p82	line 18	boundaries (bounaries)
p109	Eqn (5.5) and (5.6) $- q/2\epsilon$ instead of $- q/2$.	
p110	Eqn (5.9) should read $q_o/2\epsilon = q/2\epsilon - NeV/q$.	
p121	line 3	tunnelling (tunneling)
p123	Footnote	by convention (be convention)
p133	Fig 5.6	L_c in A^{o}
p134	last line	and (an)
p137	line 8	and (are)
p140	line 6	will (well)
p159	line 14	barrier width (barrier depth)
p161	Fig 6.6	$\mathcal{E}_{crit}$ in V/cm
p168	line 4	of (lf)
p168	line 30	resistivity (rsisitivity)
p178	Eqn (7.7) should read $\frac{dv}{dz} = \pm \frac{F(v)}{L}$	
p201	line 15	changes (change)
p205	line 13	ratio (ration)
p246	Ref. (W14)	Cambridge (cambrideg)

CONDUCTION IN THIN INSB FILMS

by

Ling Chung Ho, B.Sc.

A Thesis submitted to the
University of London, for
the degree of Doctor of
Philosophy.

Electrical Engineering Department,
Imperial College of Science and Technology,
London SW7.

April 1972.

To

my Father and my Mother,

in gratitude and affection.

Acknowledgments

I would like to acknowledge my gratitude to my supervisor, J.C. Anderson, Ph.D., D.Sc., F.Inst.P, Professor of Electrical Materials, at Imperial College, for his continual help, guidance, and encouragement over the past three and a half years.

I would like to thank Dr C. Juhasz of Imperial College, Dr R. Egerton of Zenith Radio, and Dr J. Harris (now at Waterloo University, Canada) for their critical suggestions.

I am also deeply indebted to my colleagues, in particular, to Mr J. Fisher and Mr E. Weidmann, with whom I had many fruitful discussions.

To the section secretary, Miss S. Flint, and to our techician, Mr Percy Robinson, I record my sincere thanks.

Finally, I must thank the University of London for financial support and also to Professor Anderson for a bursary.

Abstract

InSb thin films in the thickness range, 1000 - 3000 A°, were prepared by the flash-evaporation technique, on to heated substrates, held at about 300 °C. A post-evaporation heat treatment at about 400 °C, for 2 - 3 hours, gave the films the desired electrical properties.

The films were highly polycrystalline, having an average crystallite size approximately equal to the film thickness. A linear relation between the electron mobility and the mean crystallite size was obtained.

Electron concentrations and electron (Hall) mobilities were typically $5 - 20\times10^{16}$ cm^{-3} and 1000 - 4000 cm^2/V sec, respectively. A gate field, applied orthogonally through the substrate, was observed to alter the carrier mobility. An increase in the mobility with a positive gate field, by a factor of 30, was recorded at liquid nitrogen temperature. It was proposed that the grain boundaries are associated with a potential barrier, which effectively scatters the carriers. This model could also explain the temperature dependence of the electron mobility. Typical potential barriers in good-mobility films were found to be about 0.04 eV.

High-field measurements were made using 10 nsec voltage pulses. The results were interpreted in the light of the barrier model. Electrical breakdown occurred when the applied field was of the order of $1 - 2\times10^4$ V/cm, and the phenomenon was attributed to avalanche multiplication of carriers. The breakdown field was found to be related to a voltage drop of approximately 0.4 V across each crystallite boundary.

Surface conductance studies were made by means of the ac field effect. Surface trapped charge density and the sample resistivity were both found to be functions of the applied electric field. The former was interpreted using a slow surface-state trapping model, whilst the latter was believed to be another manifestation of the barrier effect.

CONTENTS

CHAPTER 3 Experimental Techniques and Metal Contacts

CHAPTER ONE: INTRODUCTION

The oringinal aim of this project was to study the high-field effects in thin InSb films, with the view to developing a high-voltage thin-film transistor (TFT). InSb was the material chosen for two reasons:

(1) It was by far the best understood of all the compound semiconductors, and

(2) In the thin-film form, though considerable amount of work had already been done, here[+] and elsewhere, to the best of the author's knowledge, no information was then available on the high-field effects.

In the course of this investigation, a number of papers (L1, L2, C1, C2) related to this work, appeared and these will be discussed in the subsequent chapters.

Initial measurements of InSb thin films, showed that the electrical breakdown field was about two orders of magnitude up on the bulk figure, for which a wealth of (high-field) data already existed. In addition, many of the interesting phenomena associated with high fields in the bulk, were not observed in thin films. It was therefore necessary to study the conduction process, in general, in greater detail, with the purpose of gaining a deeper insight into the carrier transport, and without, at the same time, deviating too much from the original idea.

A résumé of the physical properties of bulk InSb, followed by a discussion of the relevant published work, in particular, the scattering mechanism, is given in

---

[+] Thin-film Group, Electrical Engineering Department, (Materials Section), at Imperial College.

Chapter Two. This forms the background understanding required for the interpretation and the comparison of thin-film data.

Thin films have properties that are very different from those of the bulk. The finite thickness leads to the following effects:

(1) The classical size effect (L3, S1, S2, F1, G1, Z1, A1). When the film thickness is comparable to the carrier mean free path, carrier scattering at the surfaces, both as a result of this geometrical limitation as well as the presence of a surface potential, becomes important. This produces a mobility reduction in the film.

(2) The quantum size effect (B1, I1, T1). Because of the finite thickness, quantisation of the transverse component of the carrier momentum results, giving rise to a quasi-discrete energy levels of the form

$$E = \frac{\hbar^2}{2m_t^*}\left(\frac{\pi}{t}\right)^2 N^2 + \frac{\hbar^2}{2m_l^*}\left(k_x^2 + k_y^2\right) \qquad (1.1)$$

where

$2\pi\hbar$ is the Planck's constant,

m_t^* , m_l^* are the transverse and longitudinal effective masses,

k_x , k_y are the longitudinal components of the carrier momentum,

N is the quantum number replacing the transverse component of the momentum, k_z, and

t is the film thickness.

The first two levels are separated by

$$\Delta E_{21} = \frac{3}{2}\frac{\hbar^2}{m_t^*}\left(\frac{\pi}{t}\right)^2, \qquad \text{taking } N = 1,\ 2 \qquad (1.2)$$

The effect occurs only when $\Delta E_{21} \gg kT$[4], and also when $\Delta E_{21} \gg \hbar/\tau$, where τ is the carrier relaxation time. The first condition implies that carriers obey the non-degenerate statistics, whilst the second implies a long relaxation time, i.e. a high-mobility film. These requirements are met at room temperature for film thickness, $t \sim 100$ A^{o}, and at low temperatures or for small $m_t^* \sim 0.01 m_o$ (m_o being the electronic mass), for $t \sim 1000$ A^{o}.

The quantisation effect gives rise to specific physical phenomena in thin films. Oscillations in the conductivity and Hall coefficient in Bi thin films, have been observed by Ogrin et al and were attributed to this effect (T1). Incorporating this effect in the solution of the Boltzmann transport equation, Tavger (T1) shows that the carrier relaxation time and hence the mobility vary linearly with film thickness. In Chapter Three, a correlation between film thickness, crystallite size and carrier mobility will be made.

Chapter Four is devoted to Hall and magnetoresistance studies. As for bulk, data from these measurements are used to characterise the films. Measurements of p-type films enable the electron to hole mobility ratio to be estimated. This ratio is needed in the surface conductivity studies.

The polycrystalline nature of thin films have many important consequences. Grain boundaries reduce rotational symmetry and increase degeneracy of the energy band edge in such semiconductor films as p-type Ge and

---

[4] The Boltzmann constant, k, will always be associated with the temperature, T, so that confusion with the carrier wave vector does not arise.

p-type Si (T1). They are regions of lattice mismatch and are therefore expected to affect carrier transport. In Chapter Five, a potential barrier model is proposed to explain the very low electron mobility observed, and also the temperature dependence of the mobility. The presence of a potential associated with the grain boundaries, will be demonstrated by dc field-effect experiments.

High-field measurements are described in Chapter Six. Grain boundaries will be seen to play a vital part in determining the breakdown field strength. Both positive and negative differential conductivity have been observed, and they will be interpreted purely as thin-film phenomena.

Finally, Chapter Seven is a supplement to the high-field effects. Direct evidence of trapping of excess carriers, generated by the high fields, is reported. Interpretation of this result will be based on a slow surface-state trapping model.

CHAPTER TWO: Semiconductor Properties of InSb

2.1 Crystal structure

InSb crystallizes in the zinc-blende or sphalerite structure. This could be visualized as being composed of two interpenetrating f.c.c. lattices of In and Sb, displaced relative to each other by one quarter of the body diagonal and along the diagonal. The space group is $F\bar{4}3m$ and the point group is $\bar{4}3m$. Unlike the diamond structure, InSb crystal does not possess a centre of symmetry, an important consequence of which is the presence of a piezo-electric effect. x-ray measurements indicate a lattice constant of 6.4789 A^{o} (M1).

2.2 Crystal bonding

In the diamond lattice, the four outer electrons in the s^2p^2 configuration combine into sp^3-hybrids, each of which then forms tetrahedral bonds (paired electrons of opposite spins). The zinc-blende structure has an average of four valence electrons per atom, the III and V atoms having s^2p^1 and s^2p^2 configurations respectively. Three types of bonding could be described for such a structure:

(1) Covalent bonding - Each V atom donates one electron to a III atom, forming sp^3-hybrids. The bonding is then as in diamond.

(2) Ionic bonding - The III atoms donate all 3 electrons to the V atoms, forming III^{3+} and V^{3-} ions, each with spherically symmetrical closed-shell configuration. The bonding between the ions is then purely electrostatic.

(3) Neutral bonding - Each atom retains its number of electrons and there is no charge difference between the atoms.

The above bonding is highly idealised and the actual bonding does not correspond to any one of them. Though bonding in InSb is predominatly covalent (H1), there is nevertheless some degree of ionicity as evidenced from the study of cleavage planes (P1) and dielectric constant measurements (M1).

Coulson et al (C3) have considered this problem theoretically and obtained an effective ionic charge, $e^* = 0.46\ e$ (e being the electronic charge), using the LCAO method. For an ionic crystal with simple cubic structure, Szigeti (S3) has derived the relation,

$$\epsilon_0 - \epsilon_\infty = \frac{4\pi n_o e_s^{*2}}{M\omega_t^2}\left[\frac{\epsilon_\infty + 2}{3}\right]^2 \tag{2.1}$$

where

ϵ_0 , ϵ_∞	is the dielectric constant at low and high frequencies, respectively,
M	is the reduced mass of the ions,
n_o	is the number of ion pairs per unit volume,
ω_t	is the transverse optical phonon frequency, and
e_s^*	is the effective ionic charge (due to Szigeti).

Using Eqn (2.1), Spitzer and Fan (S4) obtained from infra-red reflectivity measurements an effective ionic charge, $e_s^* = 0.34\ e$.

2.3 Dielectric constant

Because of the essentially covalent bonding, the static and optical dielectric constants, ϵ_0 and ϵ_∞, respectively at low and high frequencies are not expected to be high. ϵ_∞ may be obtained from infra-red lattice absorption (S4), and ϵ_0 deduced from it using the Lyddane-Sachs-Teller relationship (L4),

$$\frac{\epsilon_0}{\epsilon_\infty} = \left[\frac{\omega_l}{\omega_t}\right]^2 \qquad (2.2)$$

where ω_t and ω_l are the transverse and longitudinal optical phonon frequencies. Table 2.1 gives the dielectric constants of some III-V and some (more ionic) II-VI compounds.

Table 2.1

Dielectric constant	InSb	InAs	GaAs	GaSb	PbTe	PbSe
Static	18.70	14.55	12.90	15.00	400	280
Optical	16.76	11.78	10.92	13.80	33	23
References	(R1)				(E1)	

2.4 Phonon dispersion

Fray et al (F2) made a detailed study of the absorption spectrum of high quality single crystals of n-type InSb $(n \sim 2.5 - 50 \times 10^{13}\ cm^{-3})$ in the wavelength range, 15 - 130 μm and over the temperature range 4.2 - 90 ^{o}K. They found absorption bands, previously not reported, and interpreted all the principle absorption peaks in terms of multiple phonon interactions. Fig 2.1 depicts the relation between energy and wave vector of the phonon, $\underline{q}$. The acoustic curves (A) consist of two branches, the transverse (T) and the longitudinal (L). The optical branches (O) have higher energy.

2.5 Band structure

Becuase of the f.c.c. translational symmetry in

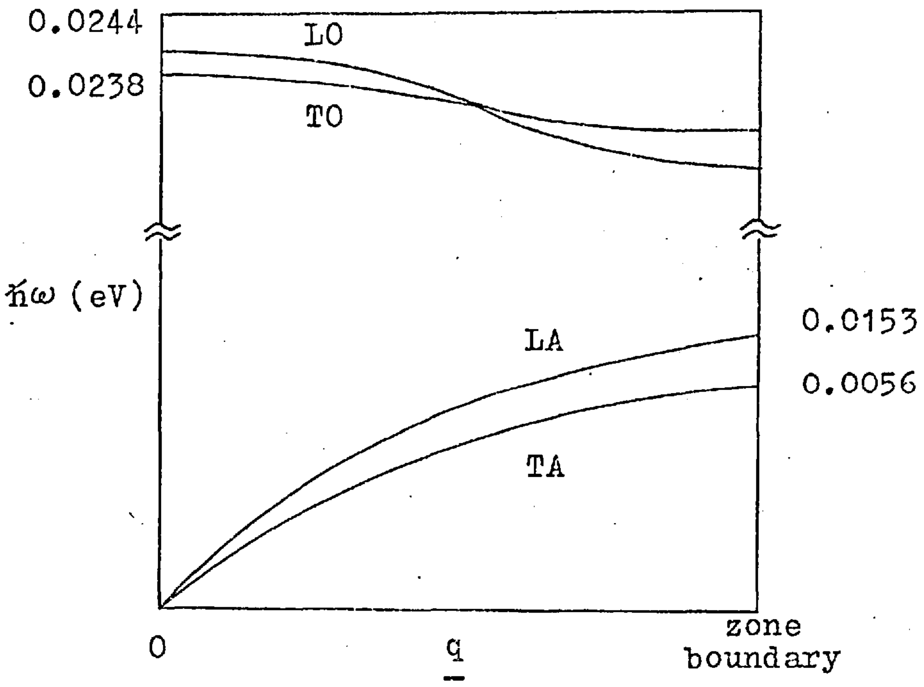

Fig 2.1: Phonon dispersion curves

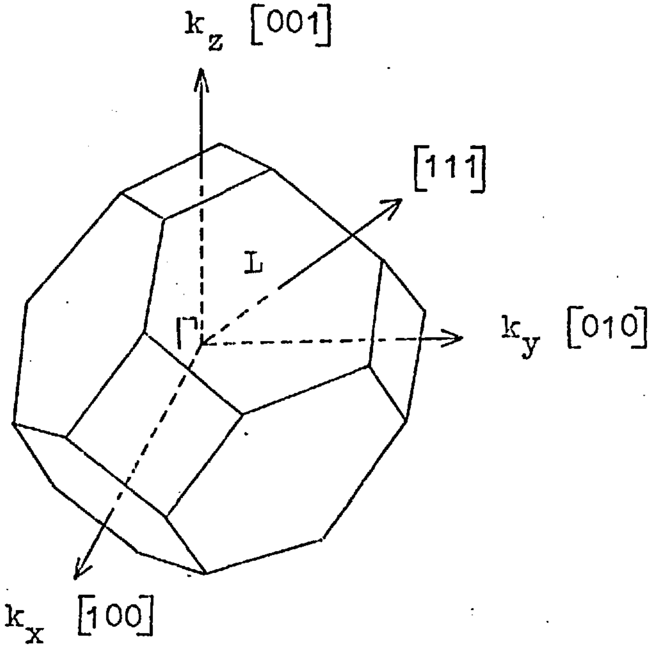

Fig 2.2: First Brillouin zone of a zinc-blende lattice

InSb, the first Brillouin zone is a truncated octahedron in k-space, in common with all diamond and zinc-blende lattices. Important symmetry points and lines of interest are shown in Fig 2.2. Cyclotron resonance (D1) and magnetoresistance (T2, F3) measurements indicate that the conduction band minimum is located at $\underline{k} = 0$, i.e. at the zone centre, point Γ. From pure symmetry arguments, Dresselhaus (D2) made quantitative calculations of the conduction and valence bands in the vicinity of important symmetry points. Kane (K1), however, has refined the theoretical treatment. He takes into account the exact interaction of the conduction and valence bands via the $\underline{k}.\underline{p}$ interaction and the $\underline{k}$-independent spin-orbit interaction. The results with reference to Fig 2.3 are presented here.

2.5.1 The conduction band

Near $\underline{k} = 0$, the conduction band is parabolic and spherical, with an effective mass, $m_n^* = 0.013\ m_o$, m_o being the free electron mass. As $\underline{k}$ increases, the conduction band becomes highly non-parabolic (but still spherical) and the effective mass, defined more generally by the tensor, ${m_{i,j}^*}^{-1} = \hbar^{-2}(\partial^2 E/\partial k_i \partial k_j)$, is therefore energy-dependent. Kane obtains the energy-wave vector $E(k) - k$ relationship, which is hyperbolic rather than parabolic, of the form normally quoted:

$$E + \frac{E^2}{E_g} = \frac{\hbar^2 k^2}{2m_n^*} = \gamma(E) \qquad (2.3)$$

where

E is the electron energy with reference to the bottom of the conduction band,

E_g is the density-of-states band gap, given by $E_g = 0.25 - 9.5\times10^{-5}\ T$ eV (E2), and

m_n^* is the effective mass at the bottom of the conduction band.

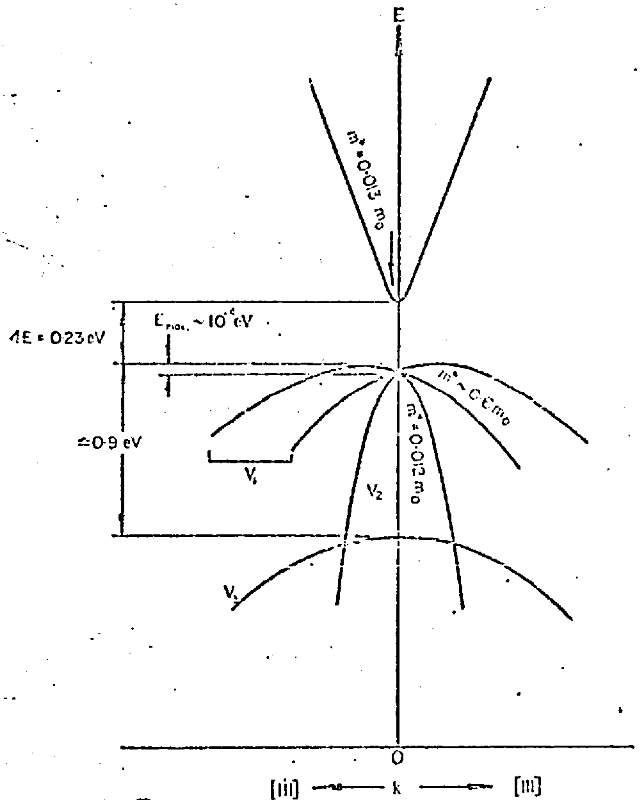

Fig 2.3

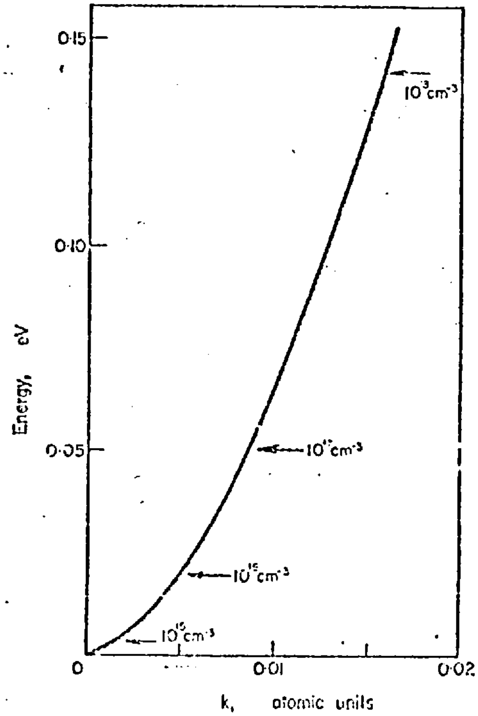

Fig 2.4

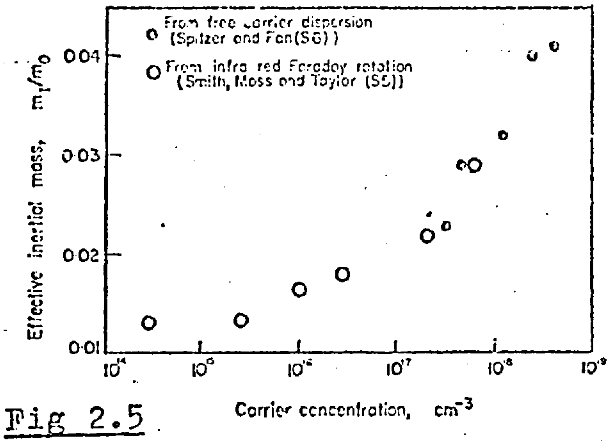

Fig 2.5

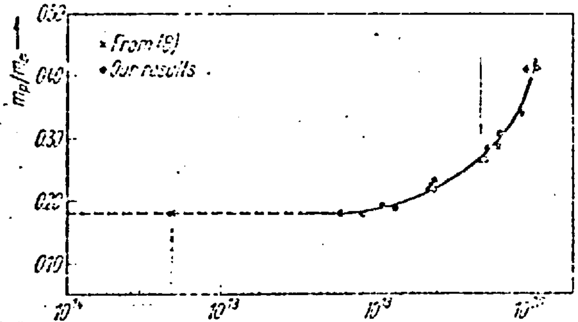

Fig 2.6

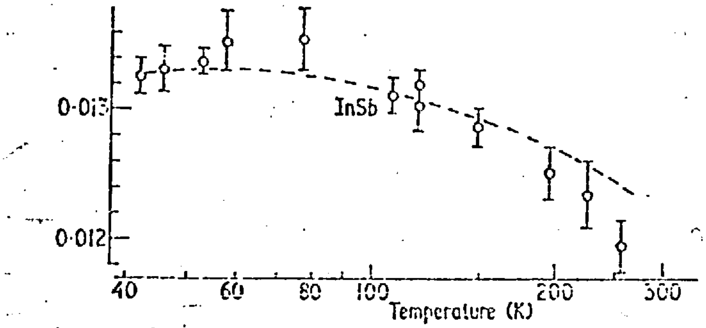

Fig 2.7

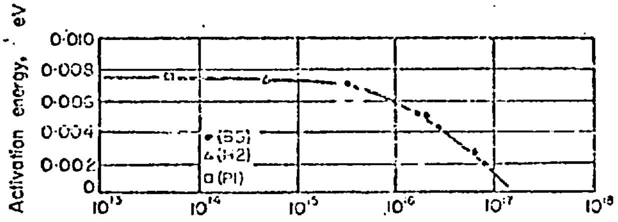

Fig 2.8

Fig 2.3, 2.4, 2.5, 2.8 from Ref. H2
Fig 2.6 from Ref. B3
Fig 2.7 from Ref. S7

Eqn (2.3) is valid for $E \sim 0.45$ eV (M2).

The most direct evidence of the spherical symmetry of the conduction band has come from the microwave cyclotron resonance experiments of Dresselhasus et al (D1), who found that the resonance was independent of the direction of the magnetic field in a (110) plane. For a band with spherical symmetry, the longitudinal magnetoresistance should be zero (S5), and it has been found in n-type InSb that it is indeed an order of magnitude smaller than the transverse magnetoresistance (H2). Measurements of the change of resistivity produced by elastically straining n-type InSb are also consistent with a spherical conduction band having its minimum at $\underline{k} = 0$ (P2).

The next conduction band minimum lies approximately 0.45 eV up and only becomes important in high-field transport (S6).

2.5.2 The valence band

Theoretical work suggests the existence of three valence bands, the general features being quite similar to that of Ge and Si.

(1) A 'heavy-hole' band, V_1, which is nearly parabolic but non-spherical. The energy maximum is about 10^{-3} eV higher than its zero $\underline{k}$ value, being displaced from the zone centre (due to spin splitting) by approximately 0.3 per cent of the distance to zone edge (K1) and along the $\langle 111 \rangle$ directions. The constant energy surfaces are eight equivalent ellipsoids.

(2) A 'light-hole' band, V_2, degenerate with V_1 at $\underline{k} = 0$, which is non-parabolic but spherical and is therefore similar to the conduction band. The hole effective mass at the bottom of the band is $m_{p2} = 0.012\ m_o$ (C4, F4).

(3) A third band, split off by spin orbit coupling, lies too low to be of importance in the present consideration.

The non-sphericity (or anisotropy) in band V_1 introduces two principal effective masses, the longitudinal and the transverse effective amsses, m_l^* and m_t^*, defined thus (S5):

$$m_l^{*-1} = \hbar^{-2} \frac{\partial^2 E}{\partial k_l^2} \qquad (2.4)$$

and

$$m_t^{*-1} = \hbar^{-2} \frac{\partial^2 E}{\partial k_t^2} \qquad (2.5)$$

where $\underline{k}_l$ and $\underline{k}_t$ are wave vectors parallel and perpendicular to the [111] direction.

The earliest attempt (D1) to measure the heavy-hole mass in p-type InSb yielded a value of 0.18 m_o. This figure was believed to be inaccurate because the cyclotron resonance was thought to have been obscured by plasma effects. Bagguley et al (B2) obtained the following measurements:

$$\begin{aligned} m_{p1} = \; & 0.45 \pm 0.03\, m_o \text{ in the } [111] \text{ direction,} \\ & 0.42 \pm 0.03\, m_o \text{ in the } [110] \text{ direction,} \\ & 0.34 \pm 0.03\, m_o \text{ in the } [100] \text{ direction.} \end{aligned}$$

An average value of 0.41 m_o is usually taken (M1). However, a recent paper by Boishakov et al (B3) favours 0.18 m_o. The discrepancy arises appar-ently due to different interpretation of results.

The effective mass that occurs in transport equations is the inertial effective mass, m_i, defined through the relation,

$$\mu = e\tau/m_i \tag{2.6}$$

where μ is the mobility and τ is the relaxation time. The inertial mass is simply related to the longitudinal and transverse masses by the equation:

$$m_i^{-1} = \tfrac{1}{3}\left[m_l^{-1} + 2m_t^{-1}\right] \tag{2.7}$$

As distinct from the inertial effective mass, a density-of-states mass, m_d, which occurs in carrier statistics, is defined thus

$$g(E) = \frac{4}{h^3}(2m_d)^{3/2} E^{\frac{1}{2}} \tag{2.8}$$

where $g(E)$ is the density-of-states function.

2.5.3 Effects of non-parabolicity

The small effective mass at the bottom of the conduction band means a very low density of states, giving rise to the following consequences:

(1) A small number of carriers fills up the band rapidly to high energy, Fig 2.4. However, because of the rapid deviation from parabolicity, carriers cannot attain very high energy, resulting in the 'cooling of electrons' (M2, M3, L5) and negative differential mobility (S6, P3), in high-field transport.

(2) For $T > 200\ ^{\circ}K$, even intrinsic material has a degenerate electron distribution (M1).

(3) For $n \sim 5\times10^{15}\ cm^{-3}$, non-parabolicity has to be taken into account if large errors are to be avoided.

Non-parabolicity in the 'light-hole' band V_2, is not important because the hole effective mass is mainly determined by the 'heavy-hole' band V_1, in view of the latter's much higher density of states.

2.5.4 Carrier concentration-dependence of effective mass

The dependence of effective mass on carrier concentration has been studied by many workers (H2). Fig 2.5 and 2.6 show the dependence for electrons and holes. The electron effective mass starts to increase from its value of $0.013\ m_o$ at a rather low concentration of 10^{15} cm^{-3}. For holes, quoting the work of Boishadov et al (B3), it can be seen that the hole effective mass remains practically constant up to a concentration of $\sim 10^{18}\ cm^{-3}$.

2.5.5 T-dependence of electron effective mass

Stradling and Wood (S7) have investigated the magnetophonon effect in the longitudinal and transverse magnetoresistance of high-purity samples of n-type InSb and deduced from it the temperature dependence of the band edge effective mass. Fig 2.7 shows the experimental results which agree well with theoretical predictions from the dilational component of the change in band gap with temperature.

2.5.6 Band gap

InSb has a direct gap, the conduction and valence band extrema being very nearly at $\underline{k} = 0$. The most direct method of measurement is via optical absorption of infra-red radiation, using the relation: $h\nu = E_g^*$, where ν is the cut-off frequency. Fan and Gobeli (F4) obtained a room temperature 'optical gap' for direct transition of 0.175 eV. This was shown to be strongly temperature-dependent by Roberts and Quarrington (R2), who obtained a $0\ ^oK$ value of $E_g^*(0) = 0.23$ eV.

Another common method for obtaining the energy gap has come from the study of intrinsic Hall data (P4). The concentration of holes and electrons for intrinsic conduction (non-degenerate) is given by (M1):

$$n_i = (n_o p_o)^{\frac{1}{2}} \exp(-E_g/2kT) \tag{2.9}$$

where

$$n_o = 2\left[\frac{2\pi m_n^* kT}{h^2}\right]^{3/2}$$

$$p_o = 2\left[\frac{2\pi m_p^* kT}{h^2}\right]^{3/2}$$

Because intrinsic InSb is degenerate for $T > 200$ °K, only the purest crystals ($N_d - N_a \sim 10^{13}$ cm^{-3}) are used. Intrinsic conduction is indeed found over a wide range of temperature (M1). A plot of $\log(n_i^2 T^{-3})$ as a function of T^{-1} yields the 'thermal' gap. In the interpretation, the following assumptions are made:

(1) That the effective masses, m_n^* and m_p^*, are independenct of temperature. It was shown earlier that m_n^* varies but little from 0 °K to about 100 °K, but for higher temperatures at which intrinsic measurements are made, the variation is expected to be quite significant.

(2) That the energy gap, E_g', is assumed to vary linearly with temperature, thus

$$E_g' = E_g'(0) + \alpha T \tag{2.10}$$

Madelung and Weiss (M14) obtained $E_g' = 0.27 - 3\times10^{-4}\ T$ eV. Ehrenreich (E2) suggested that the discrepancy between the two 0 °K values of the band gap obtained optically and thermally, could be due to the fact that for thermal transitions between bands, the phonon distribution has time to achieve equilibrium, but not so for optical transitions.

The thermal coefficient, α , is actually the sum of two terms: the actual dependence of energy gap on temperature (R2), and a smaller pressure term arising as a result of thermal expansion of the crystal lattice (E2).

2.6 Transport properties

There is now considerable information published on the transport properties of InSb. Investigations over wide ranges of doping level and temperature, electric and magnetic fields have resulted in a good understanding of this material. Much theoretical work has been done to explain the experimental observations. However, there are some discrepancies between the results of various workers. This difficulty arises mainly because of a lack of precise knowledge in the scattering mechanisms governing the transport process, which depends very much on the temperature and the purity of the crystals.

The purest crystal reported contained less than 10^{13} donors/cm^3, so that the material is intrinsic even down to 150 °K. Impurities arise as a result of a slight deviation from stoichiometry, i.e. an excess of In or Sb atoms. But because of the high mobility ratio, $b = \mu_n/\mu_p \sim 100$, the material is always n-type even if there is an excess of holes. p-type InSb may be prepared by doping with acceptor impurities, such as Zn, Hg, Cu, Si, Ge.

2.6.1 Impurity levels

The presence of impurity atoms in an otherwise regular lattice introduces energy levels within the band gap. Depending on the position relative to the band edges, they can donate or accept electrons. The activation energy is usually obtained from the variation of $\log R_H$ with temperature, where R_H is the Hall coefficient. Considering a hydrogen-like model, the ionization energy ΔE of an impurity is given by

$$\Delta E = \frac{13.6}{\epsilon^2} \frac{m^*}{m_o} \quad \text{eV} \tag{2.11}$$

In view of the low electron mass, Eqn (2.11) gives a very low value for the ionization energy for donors, ~ 0.0007 eV. Interaction between donors would readily lead to a broadening of the impurity levels and a subsequent merging with the conduction band. Hall measurements on n-type InSb containing 5×10^{13} cm^{-3} donors down to 1.7 ^{o}K by Putley failed to detect a donor ionization energy (P5). It was therefore concluded that the donor levels lie in the bottom of the conduction band.

The simple model gives an acceptor ionization energy of 0.02 eV, if the effective mass is taken to be 0.41 m_o. Putley (P6) found an ionization energy of ~ 0.0075 eV for Zn and Cd. Crystals rendered p-type by heat-treatment have activation energy of 0.018 eV, while Broom and Rose-Innes (B4) found an empirical law of the form:
$E_a = 0.01 - 2\times10^{-8}\, n_a^{\frac{1}{3}}$ eV, n_a being the impurity concentration. The variation of activation energy as a function of acceptor concentration is shown in Fig 2.8.

2.6.2 Scattering process

Three major scattering mechanisms limiting mobility in single crystals will now be considered.

(1) Deformation-potential scattering, via longitudinal acoustic modes: Lattice vibrations produce local variations in the energies of the conduction and valence bands, giving rise to an effective scattering mechanism for charge carriers. In Group IV semiconductors, this is the most important mechanism limiting mobility. For pure acoustic scattering, Bardeen and Shockley (B5) have obtained an expression for the mobility,

$$\mu_{ac} = \frac{\sqrt{8\pi}\, e\hbar^4 c_1}{3E_1^2 m^{*5/2}(kT)^{3/2}} \qquad (2.12)$$

where

c_1 is the average longitudinal elastic constant which is often expressed in terms of the density, ρ , of the material and the speed of sound wave, c_s, through the crystal, thus $c_s^2 = c_1/\rho$, and

E_1 is the deformation potential, i.e. the displacement of band edge per dilatation of lattice.

It can be seen that $\mu \sim m^{*-5/2}\, T^{-3/2}$. The $T^{-3/2}$ temperature dependence is not usually exactly obeyed, suggesting that this is not the only mechanism operating. Since this is an elastic process, a relaxation time characterising such a process can be defined, its dependence on carrier energy being $\tau \sim E^{-\frac{1}{2}}$.

(2) Polar optical scattering: When the two atoms in the unit cell are not alike, their relative motion results in a polarisation of the crystal. This may lead to a strong interaction with the carriers. The optical phonon energy (only the longitudinal mode is of importance here) is 0.0244 eV for small phonon vector and is comparable to the electron energy, kT being 0.026 eV at room temperature. The

scattering is inelastic and since, in the formulation of the Boltzmann transport equation, the perturbed distribution is assumed to deviate only slightly from the equilibrium distribution, no relaxation time can be defined in this case. An analysis was first given by Howarth and Sondheimer (H3) for a simple parabolic band and spherical constant energy surfaces. The Boltzmann equation was solved approximately using the variational principle introduced by Kohler (K2). Ehrenreich (E2) has modified the treatment to allow for non-parabolicity in InSb. He showed that polar optical scattering limits mobility (in cm^2/V sec) to

$$\mu_{po} = 1.7\times10^{30}\left(\frac{e}{e_c^*}\right)^2 \left(\frac{m_o}{m^*}\right)^{3/2} T^{\frac{1}{2}} MV\frac{\omega_l}{2\pi}F\left(\frac{\Theta_D}{T}\right)\left[\exp\left(\frac{\Theta_D}{T}\right) - 1\right] \tag{2.13}$$

where

M	is the reduced mass of the atoms,
V	is the volume of the unit cell,
$\omega_l/2\pi$	is the longitudinal optical frequency,
$\Theta_D = h\nu/k$	is the Debye temperature, and
e_c^*	is the effective charge defined by Callan[4].

The function $F(\Theta_D/T)$ takes on a value of 1 at high temperatures, falls to a minimum of 0.6 when $\Theta/T \sim 1$, and then increases steadily with Θ/T, being equal to $\frac{3}{8}(\pi\Theta_D/T)^{\frac{1}{2}}$ (H2).

(3) <u>Impurity scattering</u>: Scattering by the Coulomb field associated with a charged impurity centre (ionised donor or acceptor) results in a relaxation time, which is

---

[4] A distinction is to be made between e_c^* and the effective ionic charge, e_s^*, mentioned earlier. They are related by the equation (M1):

$$e_s^* = e_c^*\left[3\epsilon_\infty/(\epsilon_\infty + 2)\right]$$

proportional to $E^{3/2}$ approximately. Such a process is therefore expected to be effective at low temperatures when the average carrier energy is low. Brooks (B6) has obtained an expression for the mobility in nondegenerate semiconductors:

$$\mu_i = \frac{2^{7/2} \epsilon^2 (kT)^{3/2}}{N_i^{3/2} e^3 m^{*\frac{1}{2}} B} \tag{2.14}$$

where

$$B = \log (1 + b) - \frac{b}{1 + b} ,$$

$$b = \frac{6m^*(kT)^2 \epsilon\epsilon_0}{\pi n\hbar^2 e^2}$$

N_i is the concentration of ionised impurities, $N_a^- + N_d^+$

Apart from the 3 major scattering mechanisms, there are others to be considered: neutral impurity, electron-electron, electron-hole, piezoelectric scattering via transverse and longitudinal acoustic modes; structural defects and grain boundaries in polycrystals and thin films, and surface scattering.

The dependence of μ on effective mass and temperature is summarised in Table 2.2. Also included in the table are the energy-dependence of the relaxation time $\tau(E)$ and the Hall factor, r_H. The mobility discussed above is the conductivity mobility, defined for an n-type semiconductor, as $\mu = \sigma/ne$, where σ is the conductivity. However, it is the Hall mobility, μ_H, that is usually measured. This quantity is the product of Hall coefficient R_H and conductivity, given by $\mu_H = R_H\sigma = r_H\sigma/ne$. (The mass anisotropy factor has been ignored here because of the

Table 2.2

Scattering mechanism	$\mu \sim (m^*)^x (T)^y$		E^z	$\mu_H = r_H \mu$
	x	y	z	r_H
Deformation-potential	-5/2	-3/2	-1/2	3/8
Polar ($T \geqslant \Theta_D$)	-3/2	expon.	independ.	1.00 - 1.14
Ionized impurity	-1/2	3/2	3/2	$315\pi/512$
Neutral impurity	1	independ.	independ.	1
Electron-hole	-1/2	3/2	3/2	$315\pi/512$

spherical conduction band in InSb). The Hall factor depends on the scattering mechanisms and is given by $r_H = \langle\tau^2\rangle / \langle\tau\rangle^2$ (S5). $\langle\tau\rangle$ is the mean relaxation time, averaged with the weighting function EN(E), where N(E) is the electron density-of-states function.

2.6.3 Electron mobility in InSb

The first extensive measurements of the conductivity and Hall coefficient were carried out by Weiss (W1) in 1953. Since then, many workers have reproduced and confirmed his results. An electron mobility, $\mu_n \sim 78\,000$ cm^2/V sec, at room temperature is now very well established and this rises to about 1.2×10^6 cm^2/V sec at liquid nitrogen temperature for pure crystals with net donor impurity $N_d - N_a \sim 10^{13}$ cm^{-3}. The room temperature value is rather insensitive to impurity concentration below about 10^{16} cm^{-3}. Hall coefficient increases with decreasing temperature, remaining practically constant below $\sim 200\ ^{o}K$. For samples with impurity concentration $N_d - N_a \sim 10^{18}\ cm^{-3}$, an anomalous decrease of R_H with decreasing temperature has been observed by Galavanov et al (G2).

Mobility results of various workers are plotted in Fig 2.9, 2.10, 2.11 to show (1) the temperature dependence, and (2) the impurity concentration dependence for the two temperatures mentioned.

It can be seen from Fig 2.9 that the Hall mobility for the purest sample increases up to about $60\ ^{o}K$ and then decreases. For $T > 200\ ^{o}K$, in the intrinsic regime, all samples follow a T^{α} law, where $\alpha \sim -1.6$. Earlier workers attributed this temperature behaviour to a dominant acoustic mode scattering as α is near to -1.5. (A $T^{-1.5}$ law is not expected to be strictly obeyed in InSb even for pure acoustic scattering because of degeneracy.) However, Ehrenreich (E3) showed that a combination of polar scattering and electron-hole scattering would yield a $T^{-1.7}$ temperature dependence.

Table 2.3 shows the electron mobility calculated on the bases of various scattering mechanisms. The apparent discrepancies can be reconciled if the following points are considered:

(1) Many parameters available to early workers were not precisely known, and consequently much of the work was speculative. The effective charge took on various values. In their experiment on infra-red absorption by conduction electrons in degenerate InSb, Haga and Kimura (H4) deduced an acoustic deformation potential, E_1, of 30 eV, in contradistinction to Ehrenreich's figure of 7.2 eV (E2).

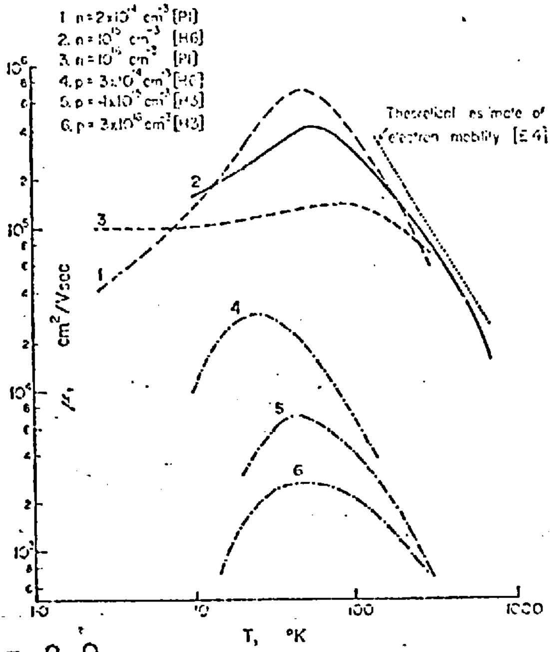

Fig 2.9

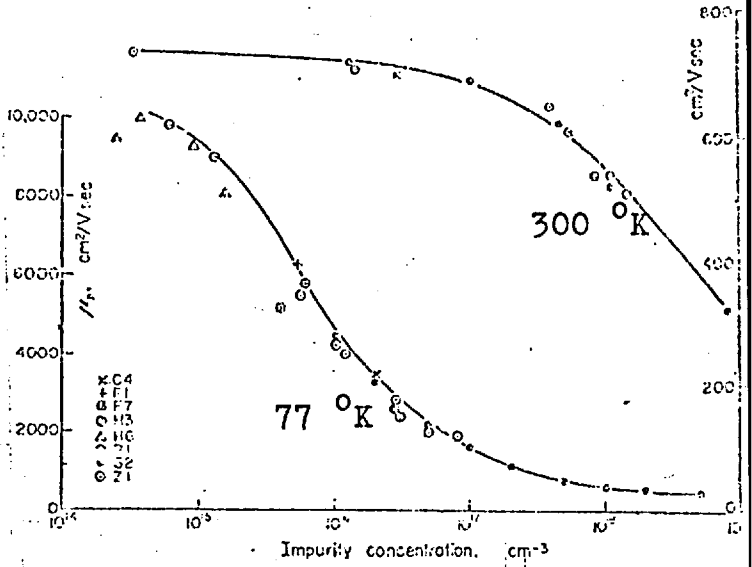

Fig 2.12

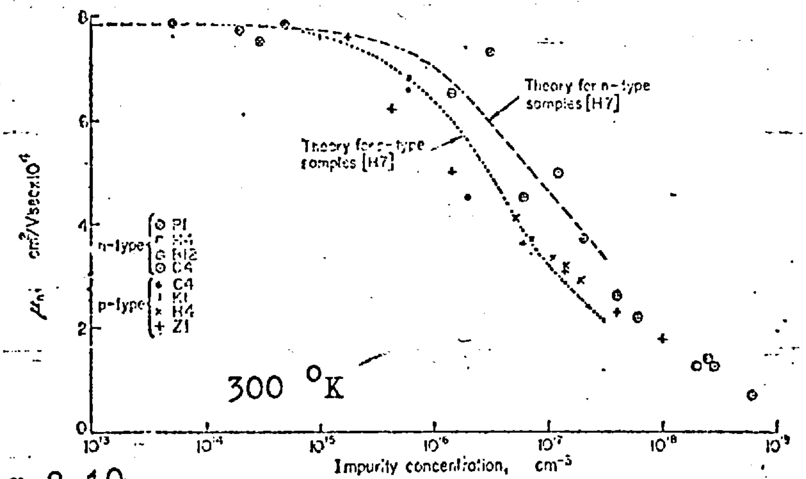

Fig 2.10

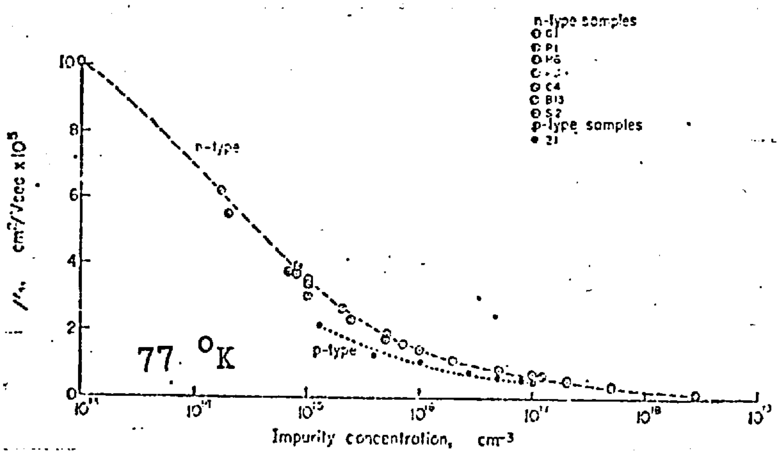

Fig 2.11

All figures from Ref. H2

Table 2.3 Calculated electron mobility in cm^2/V sec

Scattering mechanism	77 ^oK	300 ^oK	500 ^oK	Refs.
Deformation-potential	-	3×10^6	5×10^5	E2
Electron-hole	-	4×10^5	5×10^4	E2
Polar optical	-	8×10^4	3×10^4	E2
Polar optical + Electron-hole	-	6×10^4	3×10^4	E3
Polar optical + Deformation-potential + piezoelectric	3×10^6	1.3×10^5	-	R1
Polar optical + Ionized impurity[‡]	8×10^3	7×10^3	6.5×10^3	G2

[‡] This sample has an exceptionally high impurity content, $N_d - N_a \sim 7\times10^{18}$ cm^{-3}.

There was uncertainty too in the dielectric constant and the Debye temperature.

(2) The non-parabolicity was often not or insufficiently allowed for, the consequences of which are now realised to be considerable.

(3) In many cases, investigations were carried out over a rather limited range of temperature or concentration. Conclusions were then drawn, based on an effect sensitive to a particular scattering mechanism.

A systematic approach towards resolving this problem would reasonably necessitate the use of (1) a correct conduction band, for which as remarked earlier, Kane has given a theory, and (2) a correct conduction electron wave function. At $\underline{k} = 0$, the conduction minimum has an s-like symmetry around each atom, whereas, the valence-band functions have p-symmetry. Remote from $\underline{k} = 0$, the non-parabolicity of the conduction band prevails, resulting in a deviation from the pure s-symmetry due to an increasing admixture of the p-function. The electron wave function is then constructed from a linear combination of the s- and the p-functions. The transition probability between two electron states as a result of interaction with a scattering centre is then calculated from the absolute square of the overlap integrals of the respective wave functions. Exploiting the above concepts, the electron mobility has been calculated for various scattering mechanisms, leading to a picture now in reasonable agreement with experimental data. Results from three sources will now be discussed.

In the temperature range 200 - 500 °K, Ehrenreich (E2) found that scattering by polar optical phonons dominates. His theoretical calculations of mobility and thermoelectric power were in good agreement withthe experiments of Hrostowski et al (H5). For $T > 500$ °K, electron-hole scattering becomes comparable to optical polar scattering; the former in view of the large hole to electron effective mass ratio ($m_n^*/m_p^* \sim 30$), could be satisfactorily regarded as ionized impurity scattering. Deformation potential scattering was found to be negligible, consistent with the $m^{*-5/2}$ dependence of μ, as indicated by Eqn (2.12). Also a pure s-symmetry of the conduction band prohibits coupling of the electron to non-polar phonons (W2). In a later paper, Ehrenreich (E3) considered screening effects due to intrinsic carriers. A combination of optical polar scattering and electron-hole scattering gave a much improved agreement with experiment up to 700 °K.

Galavanov et al (G2) investigated samples with impurity concentration from $10^{15} - 10^{19}$ cm^{-3} over the temperature range 77 - 773 ^{o}K. Measured mobility was compared with calculated values, taking into account scattering due to ionised impurity, optical polar phonons and electron-hole interaction. Assuming reciprocal mobilities to add, i.e. employing Mathiessens rule, a mixed mobility was calculated. Results showed that at 77 ^{o}K, the main scattering is due to ionised impurities and optical phonons. From measurements of thermoelectric power, Filipchenko and Nasledov (F5) arrived at the same conclusion. Further calculations gave evidence to the contribution of acoustic phonons, particularly at higher temperatures, $T \sim 700$ ^{o}K, in addition to polar optical and ionised impurity scattering. This does not contradict the earlier results of Ehrenreich. At high temperatures or high electron concentrations, electrons populate states remote from $\underline{k} = 0$; the wave functions begin to have significant p-contributions, which now allow coupling of electrons to acoustic phonons.

Finally, a recent work by Rode (R1), considers a proper combination of various scattering mechanisms before the perturbed electron distribution function is calculated so that Matthiessens rule is not invoked. His work agrees generally with that of Ehrenreich and Filipchenko and Nasledov. He pointed out that below ~ 100 ^{o}K, piezoelectric scattering (acoustic mode) could well be important. His results also suggest the probability of intervalley scattering at $T > 750$ ^{o}K, since at such high temperatures, $n > 6 \times 10^{18}$ cm^{-3} and the Fermi level is about 0.35 eV above the conduction band edge (R3).

2.6.4 Hole mobility in InSb

In III-V compounds, holes generally have a much lower mobility than electrons. The mobility ratio in InSb is a temperature-dependent quantity, the dependence being $\sim 6.3\ T^{\frac{1}{2}}$ for $T > 250\ ^{o}K$, and the ratio has the value of just over 100 at room temperature. For $T < 100\ ^{o}K$ p-samples exhibit hole conduction; the hole mobility can be directly measured. In the temperature range 30 - 100 ^{o}K, a hole mobility of $\mu_p \sim 5.4 \times 10^{6}\ T^{-1.45}\ cm^2/V\ sec$ has been observed (H2), while for $T > 100\ ^{o}K$, Cunningham et al (C5) give $\mu_p \sim 2.55 \times 10^{7}\ T^{-1.81}\ cm^2/V\ sec$. At the higher temperature, an indirect hole mobility measurement has to be employed, making use of the magnetic field dependence of resistivity or Hall coefficient, or the photo-electric effect. The highest reliable room temperature hole mobility is found to be $\sim 750\ cm^2/Vsec$ for samples with about 5×10^{14} acceptors/cm^3, rising to about 10 000 cm^2/V sec at liquid nitrogen temperature. Fig 2.12 shows the dependence of mobility on acceptor concentration.

There is, up to date, not much information available on the scattering in p-type InSb. A theoretical treatment of the hole mobility must take into account the degenerate p-like valence bands and a possible interband scattering. Previous workers (M1, H2) considered polar optical scattering to dominate as in n-type material. This view has now to be abandoned because of the predominantly p-like wave functions. Recent work by Wiley and DiDomenico (W2) shows that the temperature dependence in p-type III-V compounds can be satisfactorily explained by a combination of acoustic and non-polar optical scattering. Their approach is similar to the treatment given by Brown and Bray (B7) for p-type Ge. Free carrier absorption measurement in p-type GaP at 300 °K (W2), indicates a combination of acoustic and non-polar optical scattering and shows polar optical scattering to be much weaker. Their theoretical treatment is in good agreement with the published data of a number of direct-gap III-V compounds and is also expected to hold for p-type InSb.

CHAPTER THREE: Experimental Techniques and Metal Contacts

This chapter is devoted to a description of the evaporation system, and a study of the film structure and the metal-semiconductor contacts.

3.1 The vacuum system

The thin film samples were all prepared in the vacuum system shown in Fig 3.1, which consisted of a working chamber, evacuated by an Edwards F403 diffusion pump containing silicone 705 oil, and backed by a 1SC150B rotary pump. A liquid nitrogen cold trap, situated between the chamber and the diffusion pump, prevented the backstreaming of oil vapour and reduced the partial pressure of any gas present. The system was capable of an ultimate pressure of $\sim 1\times10^{-6}$ torr, as measured by an ionisation gauge.

The interior of the chamber together with the top plate containing the substrate assembly is shown in Fig 3.2. The chamber was partitioned to provide three different sources for evaporating the semiconductor, the metal contacts and the insulator. The evaporation sources were made from 2 thou molybdenum sheet, in the form of a boat of dimension approximatley 1cm×0.5cm; in the case of InSb evaporation, a molybdenum strip, shaped in the form of a V, was used. A current of up to 100 A was provided through external electrodes built into the base plate.

The substrate assembly was about 15 cm away from the sources. This consisted of a substrate holder which could be manually rotated over the different sources from the outside. The substrates used were 2"x1" Corning

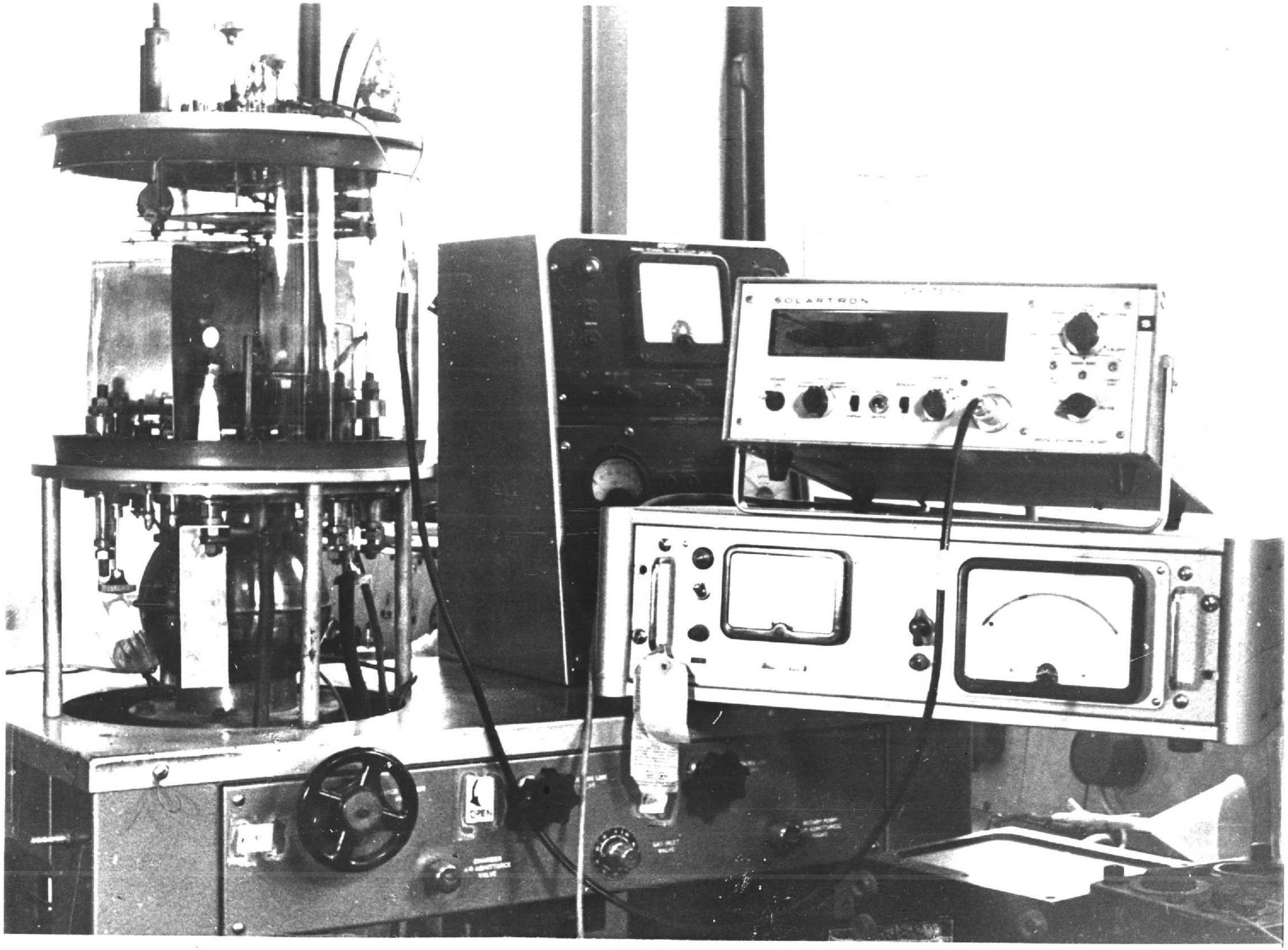

Fig 3.1: Evaporating Plant with Monitoring Equipment

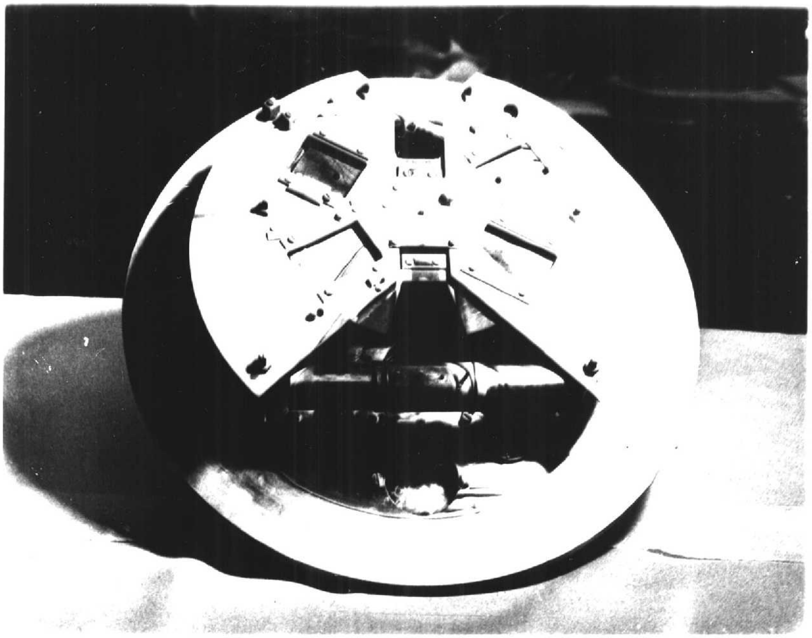

(1) Substrate Assembly

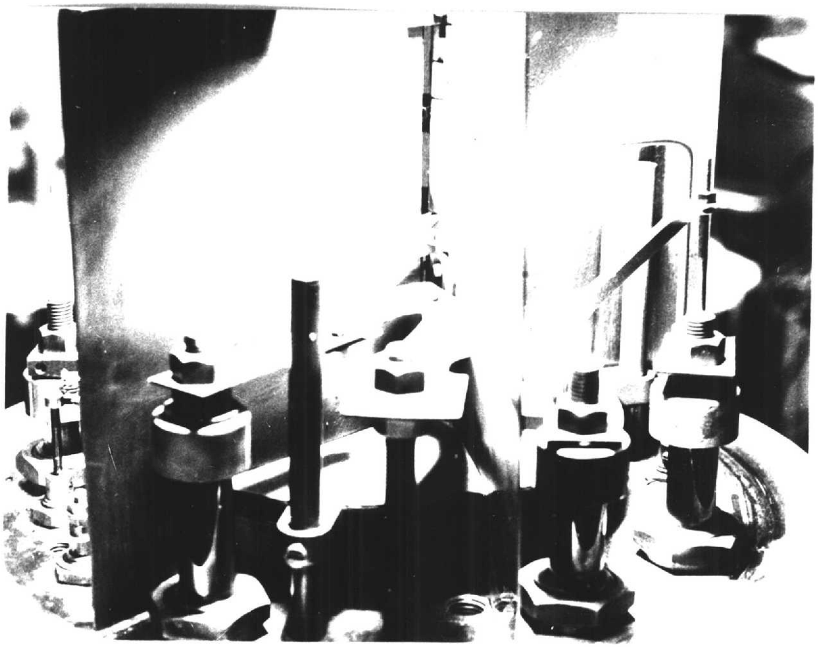

(2) Sources for Metal Contacts and Semiconductor

Fig 3.2

7059 glass or mica, coated on one side with a thick layer of graphite to facilitate absorption of radiant heat from the substrate heater, this being a coil made from a 40 thou tantalum wire. An iron-constantan thermocouple, pressing against the 'back' face of the substrate[4], measured the substrate temperature. A quartz crystal was located near the substrate. This was connected to an Edwards film thickness monitor, which enabled evaporation rate and film thickness to be measured during film growth.

A shutter was placed between the source and the substrate, and could be rotated away to permit film deposition.

The 'bridge-shaped' outline of the samples was defined by a molybdenum mask, prepared by a photo-etching technique.

3.2 Film preparation

3.2.1 Survey of evaporation techiques

Vacuum deposition of III-V compounds on to substrates can be achieved in a number of ways (W3). In order to preserve stoichiometry in the resulting films, certain thermodynamic conditions must be met, chiefly through the source and substrate temperatures, the deposition rate and the vacuum pressure. Because the evaporation process does not provide as much control of the growth conditions as crystallization from the melt, the films consist of small crystallites, randomly orientated and contain a high density of defects. Evaporation of III-V compounds presents an additional difficulty since the vapour pressures of the two constituent elements could

---

[4] Mica substrates gave somewhat better films and were used subsequently.

differ by some orders of magnitude (W3), so that precise stoichiometry would be difficult to maintain. Up to date, the following methods have been employed, for InSb.

(1) Direct evaporation - The starting material is stoichiometric and the charge is evaporated to completion to ensure that the film as a whole has the stoichiometric ratio. A post-deposition heat treatment renders the film homogeneous. But usually the adherence coefficients are different for the two vapours so that it is necessary to start off with a charge containing an excess of one element, usually the more volatile V element. Mobilities in the region of 500 cm^2/V sec have been reported (D6, R7).

(2) Flash evaporation - The charge is in the form of a finely ground powder, continuously dispensed on to the source, which is held at a temperature much above the melting point of the material. As each grain hits the hot source, it vaporises almost instantaneously, the more volatile component getting deposited first. Consequently, the film consists of alternate layers of III and V elements. A thermal treatment would bring about homogeneity. For films in the 10 000 A^o range, the mobility could be as high as 10^4 cm^2/V sec (J1).

A modified form, useful in the preparation of thicker films in the μm region, is to dispense the entire charge on to the cold source and to evaporate it almost instantaneously by passing a large current, 200 - 300 A. The resulting films usually have large crystallites in the region of μm, or are often dendritic, having room temperature mobilities in excess of 10^4 cm^2/V sec, after annealing in argon, at the melting point, for about 5 minutes (G4).

(3) The three-temperature method - This involves evaporating the two elements from different sources, using different temperatures and deposition rates, the Sb rate being the higher of the two. The substrate is maintained above the condensation temperature of Sb, but below the melting point of InSb. Precise control of the three temperatures is somewhat difficult, but the method yields good mobilities, around 10^4 cm^2/V sec (J1, G3, S8).

Other methods employed include plasmatic spluttering (C6), growth from a non-stoichiometric melt containing an excess of Sb (W4), and microzone synthesis and crystallization of composite vacuum-deposited In and Sb layers (W5, L1). A recent paper (O1) reports a 'source-temperature-programmed' evaporation method, which consists of a very slow initial evaporation rate of InSb powder containing an excess of Sb. This is to ensure a low density of nuclei, with correspondingly large crystallite size. The evaporation rate is subsequently increased, according to a 'pre-programmed pattern', which is experimentally determined. The resulting films, with thickness in the μm region, have a maximum electron mobility of 61 000 cm^2/V sec at room temperature, and about 3.5×10^{15} cm^{-3} donors.

3.2.2 Preparation of InSb films

Flash evaporation was employed exclusively in the present study. The starting material was zone-refined, polycrystalline n-type InSb[4], having a net donor impurity, $N_d - N_a \sim 1 \times 10^{14}$ cm^{-3} and a mobility, $\mu \sim 1 \times 10^5$ cm^2/V sec at 77 °K. The finely crushed powder was loaded onto a V-shaped chute, which could be mechanically agitated from outside the vacuum chamber. The source temperature was kept at about 1500 °C, as determined by an optical pyrometer.

---

[4] From R.R.E., Malvern.

Prior to evaporation, the source was baked for a few minutes to expel any absorbed gases. The deposition rate was difficult to control. However, previous work showed that this was of no consequence (J1, L6), since the 'goodness' of the films depends, to a large extent, on the post-deposition thermal treatment. An evaporation time of about 1 min would be needed to produce a 3000 A^{o} film. The substrate temperature was kept around 250 – 300 ^{o}C. If the temperature was lower, the arriving atoms would not have the energy to diffuse across the surface, so that the crystallites would be small. A temperature higher than 300 ^{o}C would cause excessive re-evaporation of Sb, leading to a metallic film, low in mobility. A vacuum pressure of $\sim 2\times10^{6}$ torr was used. This was found not to be a critical parameter. Films prepared in a pressure of $\sim 1\times10^{-5}$ torr were not found to be inferior in their electrical properties.

A post-deposition annealing was essential. This could be done by coating the film with an insulating layer, such as SiO, MgF_2, etc, and then baking it to a temperature just below its melting point for a few hours. The insulating layer prevented re-evaporation of either component at the higher temperature. In view of the subsequent need to make well-defined contacts to the semiconductor, the insulator was quite undesirable in the present work. Annealing was achieved, in this case, by first letting the system up to air, while the substrate was still hot, so that a few mon-layers of protective oxide was formed[+], and then baking it to as high a temperature as possible. In this case, 400 ^{o}C was about the limit, if appreciable loss of Sb was to be prevented. The lower temperature

---

[+] Possibly In_2O_3 (W3).

could be compensated by a longer annealing time. For annealing beyond about three hours, only marginal improvement in the mobility was obtained.

p-type films were prepared in essentially the same manner by flash evaporation on to a substrate at about 380 °C, from a mixture of $In+3Sb+7\times10^{-4}Cu$ (F6). The excess Sb was to compensate for the increased re-evaporation of Sb at this higher substrate temperature. Often it was found necessary to evaporate a very thin 'seeding' layer first, at a lower temperature of ~250 °C. No annealing was found necessary.

Film thickness was determined by measuring the height of the step produced by the film on the substrate, on an interferometer. It was necessary to deposit a layer of highly reflecting material, such as Ag or Al, across the step. By measuring the fractional shift in the multiple-beam interference fringes and knowing the wavelength of the monochromatic light (sodium), the thickness was obtained.

3.3 Electron microscopy

Film surface features and film structure were studied on the JEM-7 electron microscope.

3.3.1 Surface replica

To study the surface features of these films, a carbon replica was made. A thin amorphous layer of carbon about 200 - 300 A° thick was deposited on top of the semiconductor film. The carbon film was then removed from the substrate by immersion in a dilute HF solution and examined in the microscope. A faint outline of the surface was obtained. The contrast could be improved by shadowing the specimen. This involved an additional evaporation of a mixture of carbon and platinum from an oblique angle. After stripping the C/Pt film, platinum remains with the carbon and this reduces the electron-transparency of the film. Shadowing has the added advantage that the roughness of the surface could be estimated. The replica method is particularly useful in the study of film nucleation.

Fig 3.3 shows a shadowed carbon replica. The lack of surface topography is evident, the 'mountains' and 'valleys' being typically 50 A^{o} height.

3.3.2 Film structure

Samples for film structure study were similarly removed from the substrates. They were usually too thick for transmission microscopy, and it was therefore necessary to thin them down to less than about 1000 A^{o}, by prolonged etching.

Fig 3.4 is a micrograph of an unannealed film, the average crystallite size is not more than 100 A^{o}. The ring diffraction pattern is typical.

Fig 3.5 is a micrograph of a well-annealed film, clearly demonstrating the polycrystalline nature. Selected area diffraction shows that the individual crystallites are single crystals; the hexagonal symmetry suggests that they grow with the $\{111\}$ planes parallel to the substrates. The corresponding diffration pattern over the entire area of the film, shown in the figure, is indicative of the fact that these crystallites are well oriented about the $\langle 111 \rangle$ axis, and not, however, of a single-crystal film. Evidence of a certain amount of twinning is suggested by

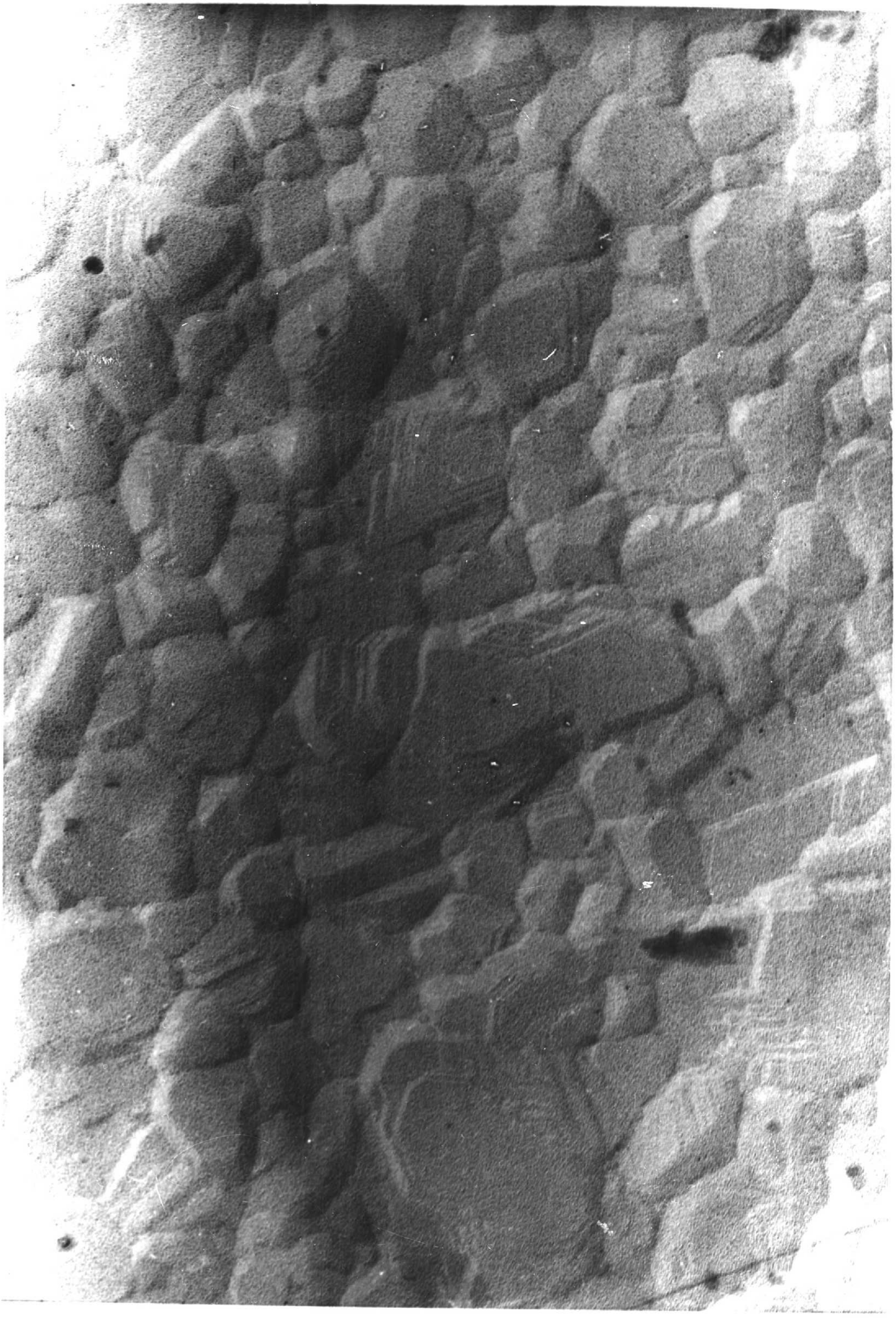

Fig. [illegible]: Carbon Replica, shadowed at an angle of 10°
(x30 000)

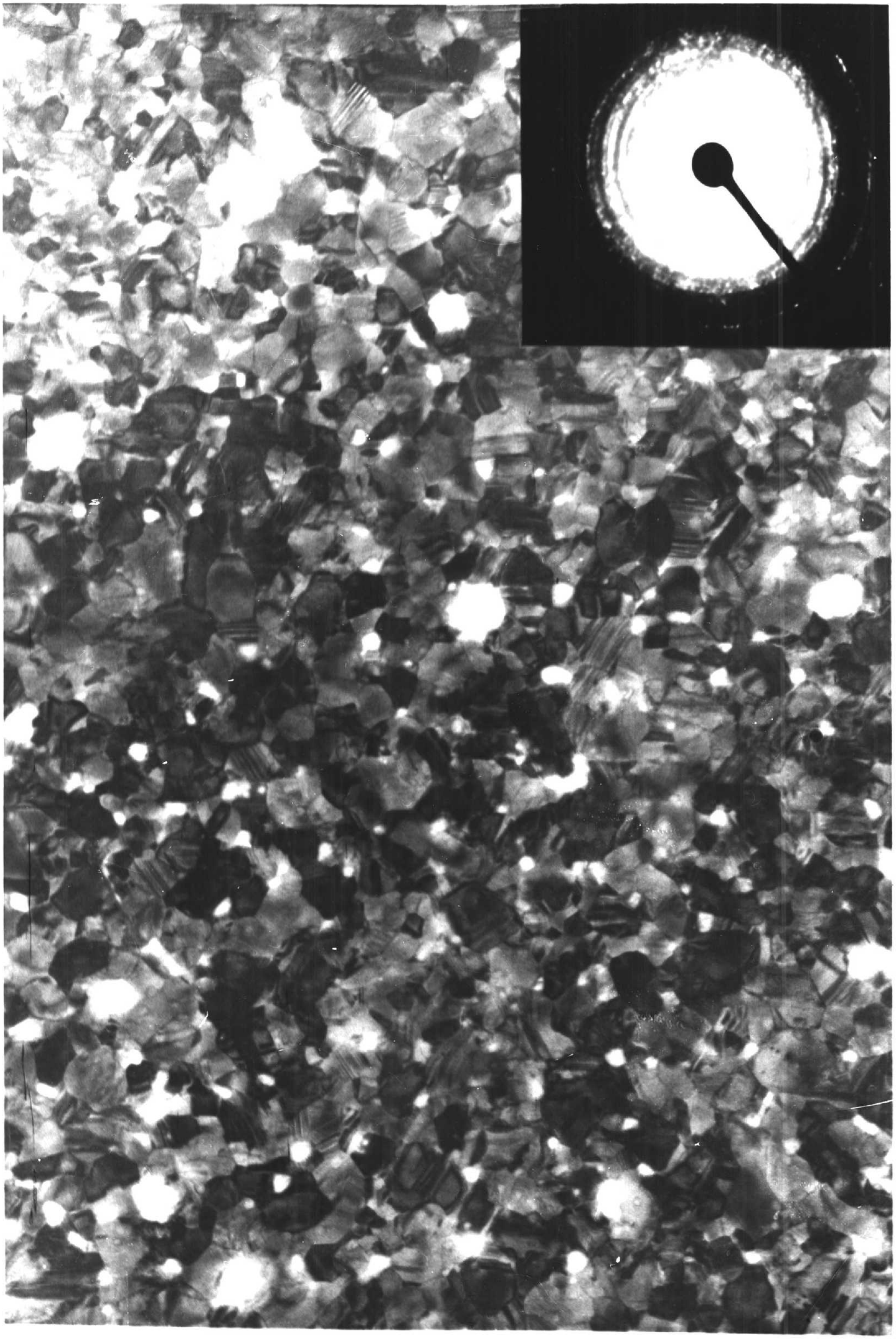

Fig 3.4: Micrograph of an unannealed film (x 140 000)

Fig 3.5: Micrograph of a well annealed film (×70 000)

the presence of satellite spots around the main (bright) spots. From the size of the spots, an upper limit of the angle of misorientation between crystallites can be estimated. This is found to be about 10°.

It is fairly obvious from the micrographs, that these films contain a high density of defects. Dislocation lines and stacking faults are clearly discernible within individual crystallites. Films grown on mica substrates, particularly at higher substrate temperatures and after prolonged annealing, reveal a certain amount of epitaxial growth. The crystallites tend to have triangular or hexagonal grain boundaries, having straight edges. This is absent on amorphous glass substrates, which lack the hexagonal symmetry of mica.

3.3.3 Crystallite size

The crystallite size is an important parameter, being a good indication of the film mobility. Because of the distribution in the size, the average must be taken. Roike and Ueda (R4) obtained the mean crystallite size from the profile of the (111) reflection peak, obtained from x-ray diffraction. Using the Scherrer equation, the mean size, d_{111} (of the crystallites oriented in the $[111]$ direction) is given by

$$d_{111} = k_s \lambda / \beta^{\frac{1}{2}} \cos \Theta \qquad (3.1)$$

where $\beta^{\frac{1}{2}}$ is the pure x-ray diffraction broadening deduced from the half-maximum linewidth of the (111) diffraction profile, λ is the x-ray wavelength, and Θ the reflection angle. The parameter, k_s, depends on the shape and size distribution of the crystallites.

A less elegant method is due to Williamson (W6). A series of random lines are drawn on the micrograph. From the intersections with the grain boundaries, the crystallite size is obtained from the relation, $d = \Sigma L / \Sigma N$, where ΣL is the total length of the lines and ΣN, the total number of intersections. To eliminate any bias, inevitable in this method, perpendicular lines were drawn, 1 cm apart, across the entire micrograph and a distribution graph was obtained. The total length taken on an 8"×10" micrograph was about 1 metre. The mean of the distribution curve was taken to be the average crystallite size.

Fig 3.6 shows such a distribution for a film whose thickness is ~1000 A^{o}. The curve peaks around 700 A^{o}, whereas the mean size is about 850 A^{o}. It can be seen that the distribution has a considerable 'tail' and there are few crystallites with dimensions less than about 200 A^{o}. The significance of this behaviour will be considered later.

A second curve, obtained in a similar manner but taking into account all visible defects (as indicated by changes in intensity on the micrograph), is also shown in Fig 3.6. This curve shows a greater assymetry and peaks at a lower size, about 300 A^{o}. This parameter is a rough measure of the density of defects present in these films, and should be an important consideration, when comparison, based on average crystallite size, is made of the electrical properties of different films.

As remarked earler, the 'goodness' of the films is a function of the post-deposition thermal treatment. Hence, in the thickness range (1000 - 3000 A^{o}) studied, the film thickness is not always indicative of its mobility. Fig 3.7 (1) shows the variation of the room temperature

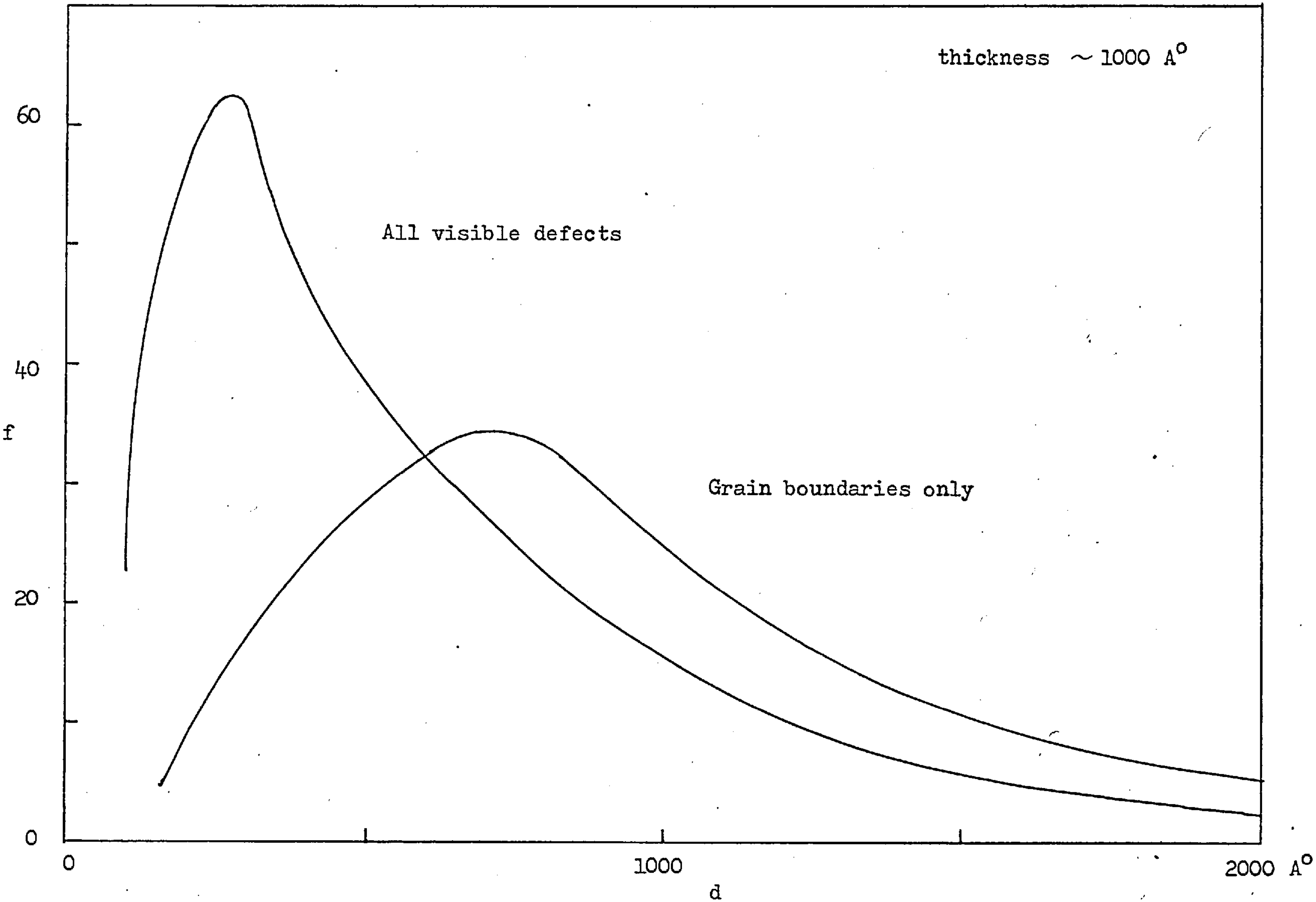

Fig 3.6: Crystallite size distribution

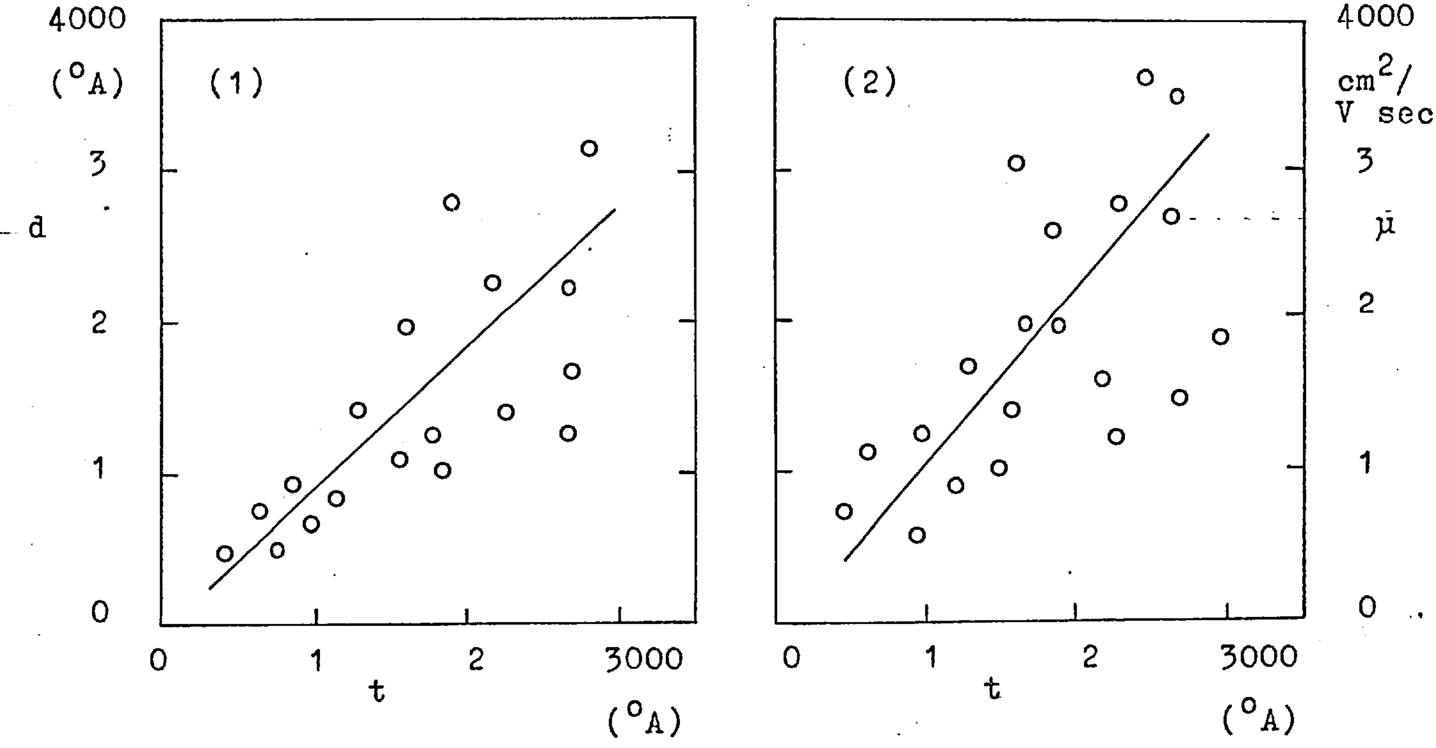

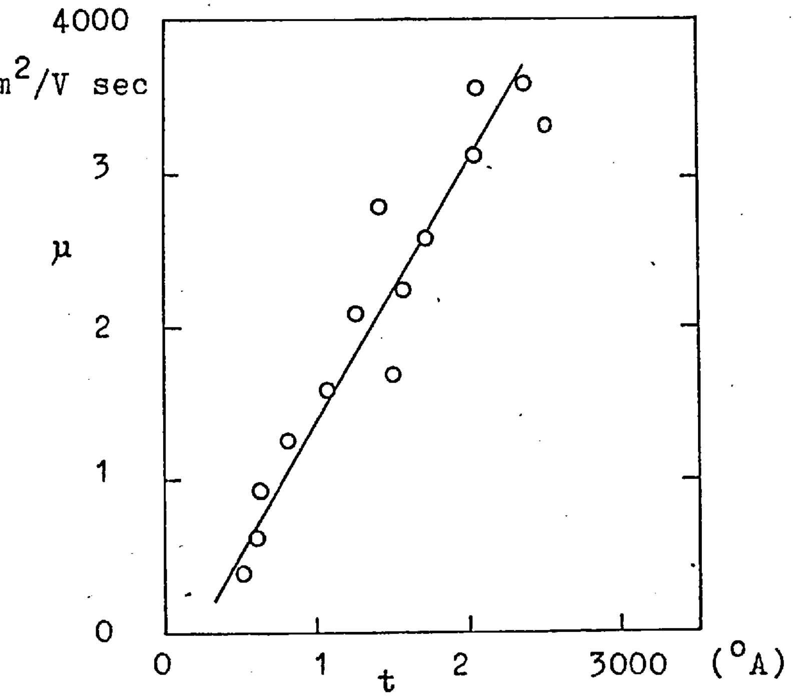

(1) d-t mean island size/ thickness

(2) μ-t mobility/thickness

(3) μ-d mobility/mean island size

<u>Fig 3.7</u>: Correlation between mobility, thickness, and mean island size

mobility with thickness for a number of films. The large scatter, due mainly to non-stoichiometry and inadequate annealing, clearly illustrates this point. Fig 3.7 (2) is a plot of the mean crystallite size as a function of film thickness. There is, again, considerable scatter, but generally, the mean crystallite size of a well-annealed film is approximately equal to its thickness. A more meaningful way to display mobility-thickness correlation is to plot mobility as a function of mean crystallite size, as shown in Fig 3.7 (3). The scatter, in this case, is greatly reduced.

3.3.4 Film growth

Atoms arriving at the substrate surface get into a high energy vibrational state, from which they relax into the 'ground' state of the substrate atoms in a time of $\sim 10^{-11}$ sec. They take up 'preferred sites', i.e. sites with lowest energy. Depending on the substrate temperature, the atoms on the surface ('adatoms') can re-evaporate, after an average time, τ_a, given by

$$\tau_a = \nu_o^{-1} \exp (E_a/kT) \tag{3.2}$$

where ν_o is a lattice phonon frequency, of the order of $10^{12} - 10^{13}$ sec^{-1}. E_a is the binding energy of the atom with the substrate, which is of the order of 0.1 eV/atom for van der Waals type bond, and of the order of 1 eV/atom for ionic or covalent bonds. The thermal energy of the substrate can also cause the adatoms to change sites, the number of 'hops', v per second, being given by

$$v = \nu_1 \exp (- E_d/kT) \tag{3.3}$$

where ν_1 is another vibrational frequency, often taken to be equal to ν_o. E_d is the activation energy for surface diffusion.

During diffusion, adatoms collide and adhere to form clusters of atoms. When a critical size is reached, a cluster becomes stable. Growth from such a stable, nucleating site proceeds further by the addition of more atoms, until the nuclei coalease to form a continuous film. In the process of coalescence, defects such as dislocations, stacking faults, grain boundaries and inclusions of foreign atoms are formed.

During annealing, considerable redistribution of crystallites (grains) occurs, driven by the thermodynamic requirement of the system to diminish the large overall interfacial energy. Thus large crystallites grow larger at the expense of smaller ones, thereby reducing the total grain boundaries as well as decreasing the number of crystallites. Annealing brings, in addition, homogeneity within individual crystallites, without which, the film would not exhibit semiconducting properties.

Crystallite size distribution is therefore highly dependent on annealing process. The distribution function has often been assumed to be Gaussian, without a priori physical justification. Chakraverty (C7) has studied the problem theoretically in well-annealed discontinuous thin films. For grain growth to be predominantly controlled by a surface diffusion mechanism, the distribution function is in the form of an approximate δ-function; the grain size variation cannot exceed about 1.33 times the mean grain size. If, however, the interface transfer of adatoms is the dominant mechanism, then the grain size cannot be expected to exceed roughly twice the mean grain size (the distribution, still remaining approximately δ-function). Experimental data of Ni and Au deposited on NaCl substrates, appear to support this theory for films in the thickness range of 200 A° (C7).

The distribution function for InSb films of thickness 1000 - 3000 A° does not correspond to a δ-function. It would appear that Chakraverty's theory for thicker films, is not applicable here. Nor is the distribution Gaussian and it has not proved possible, in the present work, to provide an explanation of the actual distribution observed.

3.3.5 Discussion

Consider the film to be composed of crystallites of resistivity, ρ_i (depending on the crystallite size, x_i), in series with crystallite boundaries of constant resistivity, ρ_B. If ρ_T is the total resistivity of this composite structure, then

$$\rho_T \sum_{0}^{N} f_i x_i = \sum_{0}^{N} f_i \left[\rho_i (x_i - \Delta x) + \rho_B \Delta x \right] \qquad (3.4)$$

where Δx is the width of the boundary, which is assumed to be constant, and f_i is the crystallite size distribution. Now,

$$\rho_T = 1/ne\mu_T \quad ;$$

$$\rho_i = 1/ne\mu_i = 2m^* \langle c \rangle / ne^2 x_i \qquad (3.5)$$

where

n is the free carrier density in the crystallite,
μ_T is the total (observed) mobility,
m^* is the effective mass of the carrier, and
$\langle c \rangle$ is the mean thermal velocity.

In Eqn (3.5), use has been made of the relation, $\mu = e\tau/m^*$, where the relaxation time, τ, is taken to equal $x_i/2\langle c\rangle$ ($x_i/2$ being the mean free path). From Eqns (3.4) and (3.5),

$$\rho_T \sum f_i x_i = \sum \rho_i f_i x_i + \Delta x\, \rho_B \sum f_i (1 - \rho_i/\rho_B)$$

i.e.

$$\frac{1}{ne\mu_T} = \frac{2m^*\langle c\rangle}{ne^2}\,\frac{1}{\bar{x}} + \rho_B \Delta x\, \frac{\sum f_i(1 - \rho_i/\rho_B)}{\sum f_i x_i} \qquad (3.6)$$

Assume $\rho_i/\rho_B \ll 1$, then

$$\frac{1}{\mu_T} = \left[\frac{2m^*\langle c\rangle}{e} + ne\,\Delta x\, \rho_B\right] \frac{1}{\bar{x}} \qquad (3.7)$$

where $\bar{x} := \sum f_i x_i / \sum f_i$, is just the mean crystallite size (= d). Eqn (3.7) shows that the overall carrier mobility is linearly dependent on the mean crystallite size, and independent of the size distribution. Since the mean crystallite size is proportional to the film thickness (Fig 3.7 (3)), the result is also consistent with Tavger's prediction (T1), based on a quantum size effect consideration.

It can be shown from Chapter Five, that the boundary resistivity, $\rho_B \sim \exp(e\phi_0/kT)$; ϕ_0 is the barrier potential and is significant in InSb films, so that the assumption $\rho_i/\rho_B \ll 1$, is probably good. In Pb salt films (E1), where ϕ_0 is low, the assumption becomes questionable. In this case, Eqn (3.6) must be used, and it is expected that the mobility would now depend on the crystallite size distribution.

3.4 Ohmic contacts

In the study of semiconductor thin films, it is vital that the metal contacts have low resistance and are strictly ohmic, i.e. having a linear current-voltage relation. The criterion of a symmetrical current-voltage characteristic is not valid here, since, by the very nature of the metal-semiconductor-metal structure, even rectifying contacts would produce symmetry. A rectifying contact would give rise to effects that might significantly overshadow the semiconducting properties. The presence of contact resistance, for example, severely degrades thin film transistor characteristics (L6).

The nature of a metal-semiconductor contact depends, in the first place, on the respective work functions. Successful ohmic contacts have been produced in bulk semiconductors, by thermal diffusion or high-energy bombardment of metal atoms having the correct work function, eg Sb-doped Au for n-type Ge and Ga-doped Au for p-type Ge (P5). But, in thin films, where contacts are vacuum-deposited, the presence of surface states, is an even more important consideration (M4, F7, H6). At this stage of surface technology, it appears that there is no universal rule in governing the choice of the contact metal (A2).

Six pairs of contacts of Ag, Al, Au, In, Sn, and Sb on both n-type and p-type InSb films were studied on the Tektronix curve tracer (type 575). The metal contacts, of approximate dimensions 0.1cm×0.1cm, were vacuum-deposited side by side on a single InSb film, through wire masks. The semiconductor gaps were 0.005 thou wide. Initial measurements showed wide variation in the sample resistance, as shown in Table 3.1. This can only be

Table 3.1 Contact resistance at 77 ^{o}K (measuring voltage = 1.5 V)

Contact metal	Resistance (n-type)	Resistance (p-type)
Ag	13 KΩ	48 KΩ
Al	150	46
Au	210	24
In	10	38
Sn	11	25
Sb	250	24

attributed to the different contact metals, since the resistivity does not vary over the film by more than about 10%.

Fig 3.8 (1) shows a set of I-V characteristics for an n-type film, at 77 ^{o}K. Only In, Sn and Ag exhibit ohmic behaviour, Sb being the most non-ohmic in this case. The behaviour at higher temperatures is essentially similar, though the increase in conductivity might lead to serious joule heating. The maximum electric field across the gap used, was about 200 V/cm. Though this is well below the breakdown field for InSb films (Chapter Six), heating would probably have occured, in view of the fairly low sweeping rate of the curve tracer (50 Hz).

For p-type films, none of the metals studied prove to be satisfactory. The I-V characteristics are shown in Fig 3.8 (2). Sb which forms the most non-ohmic contact in n-type films, now appears to make the 'best' contact.

3.4.1 Contact resistance and capacitance measurements

The charge redistribution that occurs at the

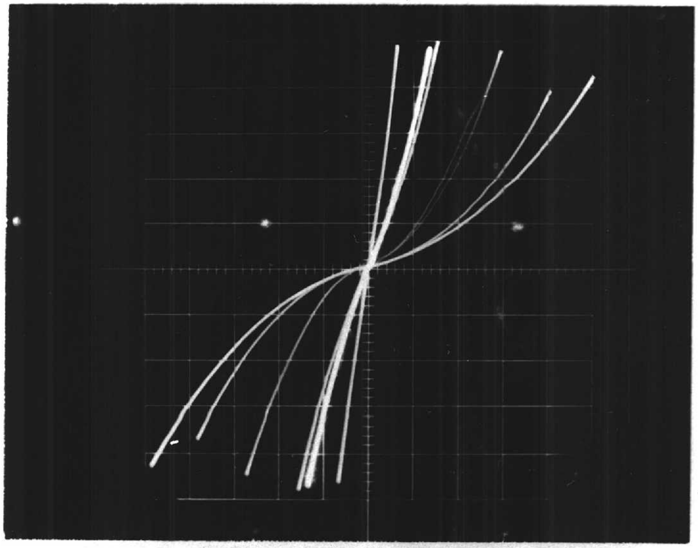

(1) n-type sample, nC41
Curves (Top left to right):
In, Sn, Ag, Al, Au, Sb

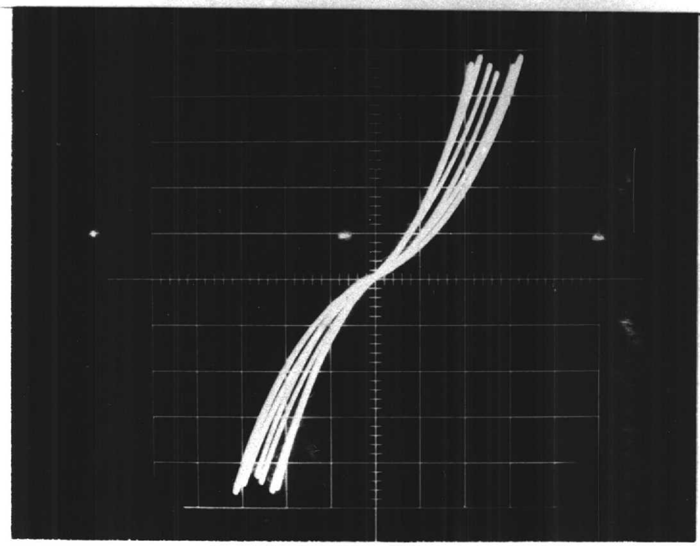

(2) p-type sample, pF15
Curves (Top left to right):
Sb, Au, Sn, In, Al, Ag

Fig 3.8: I-V characteristics of metal-InSb-metal contacts of
(1) an n-type sample, at 77 °K;
(2) a p-type sample, at 77 °K.
Horizontal axis - 5 V/cm Vertical axis - 0.2 mA/cm

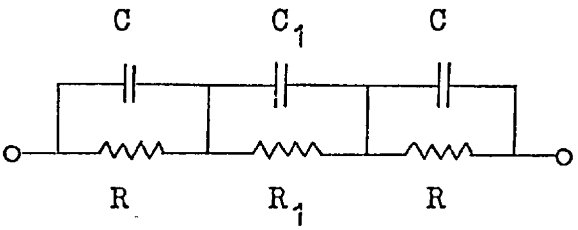

Fig 3.9

metal-semiconductor interface results in a contact resistance, R, and a capacitance, C, both of which are voltage, temperature and frequency dependent (H6). This can be represented by an equivalent circuit, shown in Fig 3.9, where R and C are associated with the metal contact, and R_1 and C_1, the corresponding elements for the grain boundaries. Contribution due to the body of the crystallites is neglected here.

As discussed in Appendix A, for the purpose of measurement, the circuit can be regarded either as a series equivalent with a resistance, R_s, in series with a capacitance, C_s, or as a parallel equivalent with a resistance, R_p, in parallel with a capacitance, C_p. Considering low and high frequencies, the limiting values for the resistance and capacitance, in both cases, are given in Table 3.2.

Table 3.2

	$\omega \to 0$	$\omega \to \infty$
R_s	$2R + R_1$	0
C_s	∞	$CC_1/(C + 2C_1)$
R_p	$2R + R_1$	$RR_1(C + 2C_1)^2/(RC^2 + 2R_1C_1^2)$
C_p	$(2CR^2 + C_1R_1^2)/(2R + R_1)^2$	$CC_1/(C + 2C_1)$

Measurements of the series and parallel elements of the equivalents were made on a Wayne-Kerr Bridge, over a frequency range from about 200 Hz - 2 MHz, the signal voltage being a few tenths of mV's. Fig 3.10, 3.11, 3.12 and 3.13 show the frequency dependence of the measured resistance and capacitance for Au and Al contacts, for $T = 77\ ^{\circ}K$ and $296\ ^{\circ}K$.

3.4.2 Results

The experimental data are in good agreement with the asymptotic behaviour predicted for $\omega \rightarrow 0$. For the Au contact at $296\ ^{\circ}K$, $2R + R_1 \sim 2.7\times10^3\Omega$. The resistivity of InSb at this temperature was measured and found to be $\sim 0.064\Omega$-cm, giving $R_1 \sim 650\Omega$. Hence, $R \sim 10^3\Omega$. At $77^{\circ}K$, $2R + R_1 \sim 3.4\times10^5\Omega$; R_1 increased to $\sim 0.44\times10^5\Omega$. Hence, $R \sim 1.5\times10^5\Omega$. (The figure, $2R \sim 3\times10^5\Omega$, is higher than that given in Table 5.1 for Au, since for the latter, a higher measuring voltage of 1.5 V was used.)

The absence of an asymptotic behaviour at 10^6 Hz, would suggest that for frequencies lower than this, C_1 could be neglected (small compared to C)[4]. Under this assumption, $C_p \rightarrow 2CR^2/(2R + R_1)^2$, from which C was found to be 580 pF at $296\ ^{\circ}K$ and 2300 pF at $77\ ^{\circ}K$. No attempt is made to express R and C in the usual units of Ωcm^{-2} and $pFcm^{-2}$, since the current is non-uniform over the area of the metal contact. This could be achieved by having a three-layer sandwich structure, in which case, $R_1 = C_1 = 0$.

Gulaeyev (G4) has made resistance and capacitance measurements on InSb films in the 10^9 Hz range, and failed

---

[4] This, however, does not imply that the capacitance across a grain boundary, C_o, can be neglected, since $C_o = N_1C_1$ (see Appendix) and N_1 is of the order of 10^3.

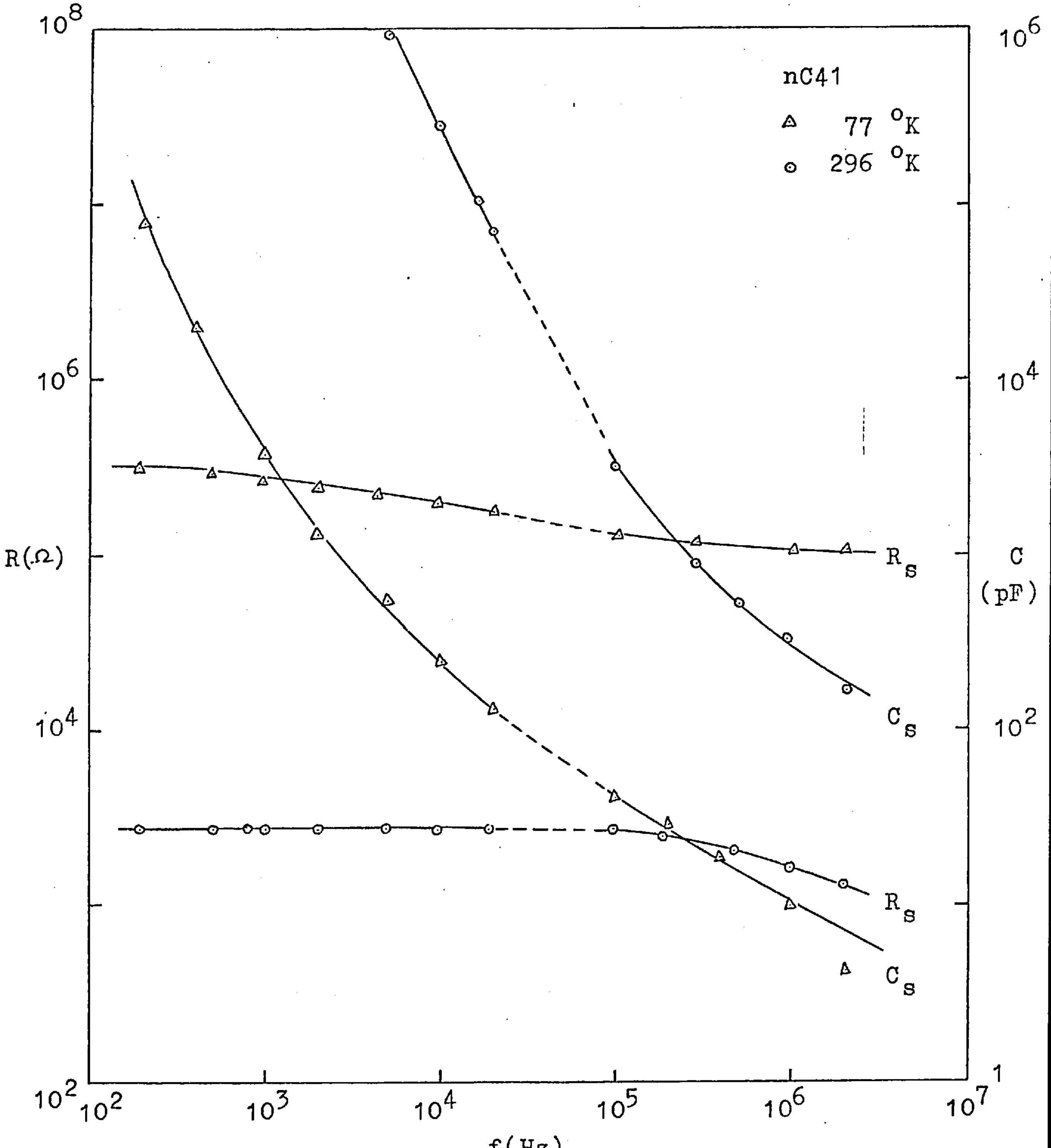

Fig 3.10: Au-InSb-Au Structure

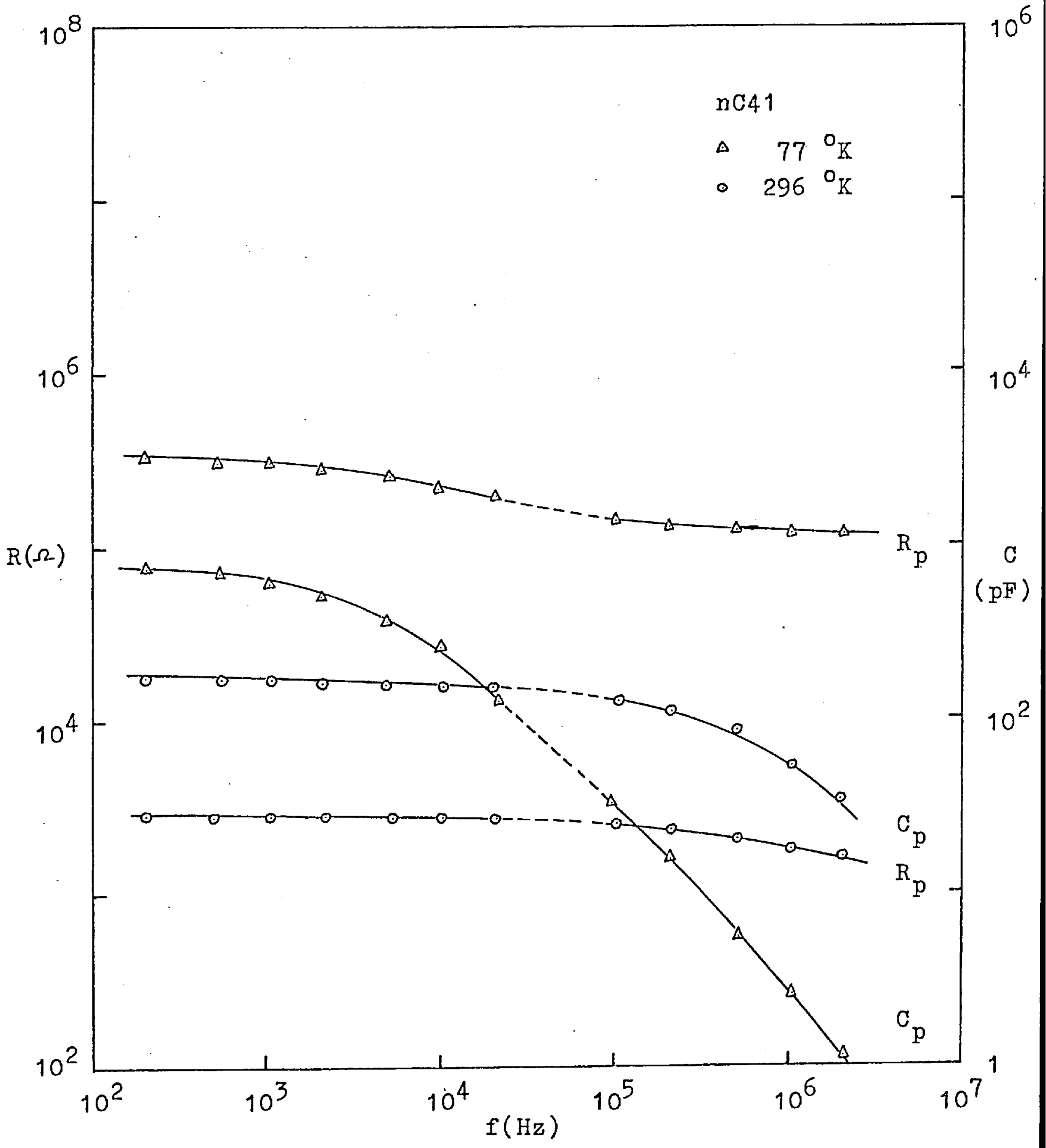

Fig 3.11: Au-InSb-Au Structure

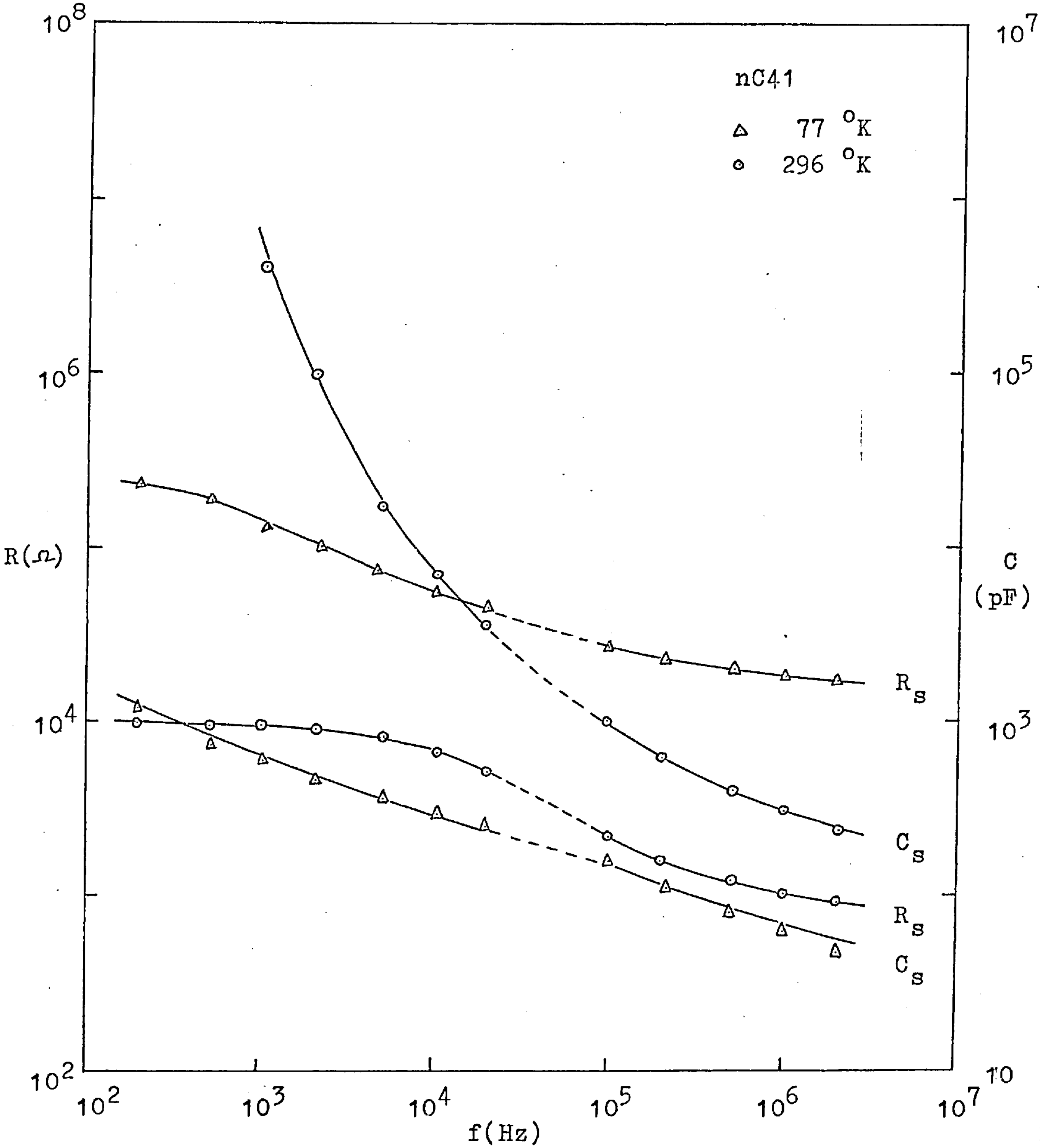

Fig 3.12: Al-InSb-Al Structure

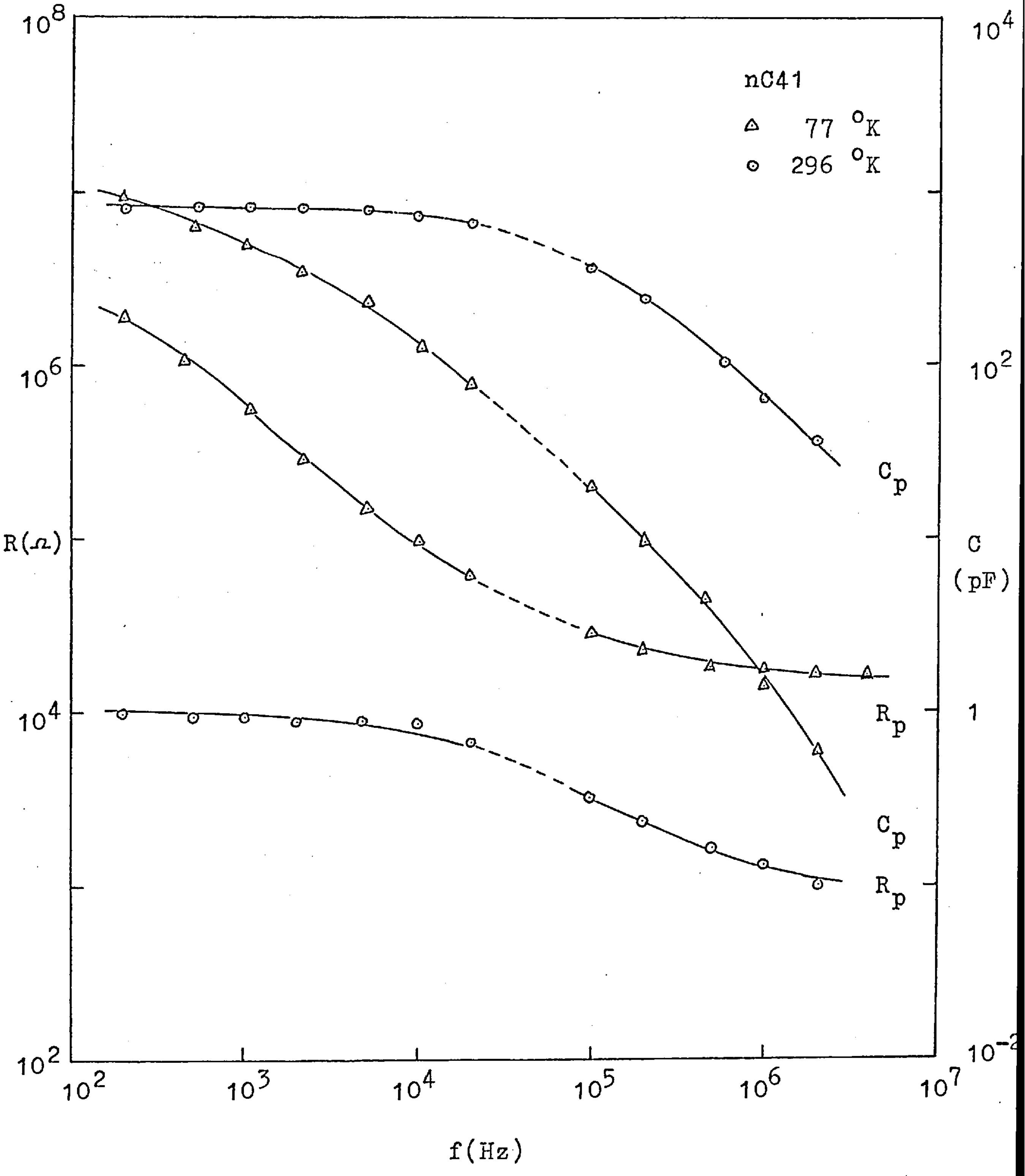

Fig 3.13: Al-InSb-Al Structure

to detect any appreciable value for C_1. This justifies the previous assumption that C_1 is small.

For the Al contact, the following values were obtained:

T = 296 °K $R \sim 4.2\times10^{3}\Omega$; $C \sim 1800$ pF

T = 77 °K $R \sim 9.8\times10^{5}\Omega$; $C \sim 2100$ pF

The capacitance and resistance associated with ohmic contacts are small and difficult to measure, in the present set-up. At 77 °K, In contact, for example, has a capacitance of less than 1 pF.

3.4.3 Discussion

Metal-semiconductor behaviour has often been interpreted in terms of charge transfer between the metal and the semiconductor, due to the thermodynamic requirement to equalise the Fermi levels on either side of the interface (H6). Depending on the respective work functions and the initial relative positions of the Fermi levels, the resulting surface energy band bending (almost entirely in the semiconductor) would determine the I-V characteristics. This ideal situation, however, is seldom realized, owing to the presence of surface states (Chapter Seven).

Filling up of these states, by charges from the semiconductor, produces an initial energy band bending. Equilibrium, after the deposition of a metal contact, is now achieved by a charge transfer between the metal, the semiconductor bulk, and the charged surface states. In particular, if the surface state density is high, which is the case in many semiconductors (M4, F7), the charge involved, comes almost entirely from the surface states, so that very little change in the surface band bending results. Surface states may thus have a overriding influence on the current-voltage behaviour of such a contact.

Lack of precise information on the surface states, at the present, prevents a clear understanding of the contacts. And it is not intended, here, to go into the physics in any detail, other than to establish a good ohmic contact.

CHAPTER FOUR: Hall-effect and Magnetoresistance Measurements

4.1 Theory

4.1.1 Hall effect

Smith (S5) shows that in a mixed conduction of electrons and holes, the Hall coefficient is given by

$$R_H = -\frac{1}{e}\frac{(nb^2 - p)}{(nb + p)^2} \tag{4.1}$$

and the conductivity by

$$\sigma = e\mu_n(n + p/b) \tag{4.2}$$

where n and p are the electron and hole concentrations, and b is the electron to hole mobility ratio, μ_n/μ_p. A Hall factor, r_H (see Table 2.2), different for electrons and for holes, which has a value between 1 and 2 (S5), has been neglected here. As discussed in Sec 2.6.2, r_H depends on the scattering mechanisms. A precise model for the scattering process is not possible in thin films; consequently, r_H is taken to be 1. This, of course, implies taking the relaxation time to be constant.

In intrinsic samples, when conduction of one carrier dominates that of the other, Eqns (4.1) and (4.2) can be approximated to the following:

For $n \gg p$,

$$R_H \sim -1/ne; \qquad \sigma \sim ne\mu_n \tag{4.3}$$

And for $p \gg n$,

$$R_H \sim +1/pe; \qquad \sigma \sim pe\mu_p \tag{4.4}$$

Hence, in extrinsic semiconductors, measurements of Hall coefficient not only give the semiconductor type, but the carrier density as well. The Hall mobility, μ_H, as distinct from the conductivity mobility (as expressed in the conductivity equations), is defined by $\mu_H = |R_H \sigma|$, being related to the conductivity mobility through the Hall factor. Hereafter, the mobility refered to would be the measurable Hall mobility.

If, however, the mobility ratio is known, then it should be possible to determine both carrier densities and mobilities, in the case of mixed conduction, from Eqns (4.1) and (4.2).

To allow for the effect of the magnetic field, the following expressions for the Hall coefficient and conductivity, in a two-carrier system are used (C12):

$$R_H = \frac{R_1 \sigma_1^2 (1 + \sigma_2^2 R_2^2 B^2) + \sigma_2^2 R_2 (1 + \sigma_1^2 R_1^2 B^2)}{(\sigma_1 + \sigma_2) + \sigma_1^2 \sigma_2^2 B^2 (R_1 + R_2)^2} \quad ; \qquad (4.5)$$

$$\sigma = \frac{(\sigma_1 + \sigma_2)^2 + \sigma_1^2 \sigma_2^2 B^2 (R_1 + R_2)^2}{(\sigma_1 + \sigma_2) + \sigma_1 \sigma_2 B^2 (\sigma_1 R_1^2 + \sigma_2 R_2^2)} \qquad (4.6)$$

where 1, 2 refer to the two species of carriers, electrons and holes. B is the magnetic field. Eqns (4.5) and (4.6) are generally true even if the carrier relaxation time, τ, is not constant.

The Hall factor, r_H, is given by $\langle \tau^2 \rangle / \langle \tau \rangle^2$, where the average is taken over the carrier distribution function. In InSb, optical phonon scattering dominates at $T \sim \theta_D$, the Debye temperature being $\sim 280\ ^{o}K$ (R1), and is important even in the vicinity of 200 °K. Because of the large energy change (compared to the initial electron energy) associated with this type of scattering, a scattering time cannot be defined (E2). However, Smith (S5) has shown that for degenerate semiconductors, applicable to InSb in the temperature range 77 - 300 °K and for $N_d - N_a \sim 2\times10^{16}\ \mathrm{cm}^{-3}$, only carriers with energy $E \sim E_f$ (the Fermi energy), contribute to conduction. Hence, only the relaxation time of these carriers is important, i.e. $\tau \sim \tau(E_f)$, which can therefore be assumed to be constant.

In highly polycrystalline films, as far as scattering is concerned, the bulk contribution is probably negligible compared to the effects due to grain boundaries and other defects. In view of this, the scattering time is governed almost entirely by the crystallite size, being the time taken for the carrier to traverse a distance equal to half the mean crystallite size. The mean free path of the carriers, λ, is therefore $d/2$, where d is the mean crystallite size. If d exceeds a certain critical size, d_{crit}, so that $\lambda < d_{crit}$, then the grain boundaries are not expected to limit the mobility. Hence, μ/d curves (see Fig 3.7) should saturate; the ultimate mobility would approach bulk value, depending on the degree of perfection of the crystallites and the extent to which surface and other defects contribute to scattering.

Under the above assumption of a constant relaxation time, Eqns (4.5) and (4.6) become, after substitution from Eqns (4.3) and (4.4) for the separate species of carriers,

$$R_H = -\frac{1}{e}\,\frac{(nb^2 - p) + \mu_n^2B^2(n - p)}{(nb + p)^2 + \mu_n^2B^2(n - p)^2} \qquad (4.7)$$

$$\sigma = e\mu_n \frac{(nb + p)^2 + \mu_n^2 B^2 (n - p)^2}{(nb + p)b + \mu_n^2 B^2 (n + bp)} \tag{4.8}$$

The Hall mobility is now

$$\mu_H = \mu_n \frac{(nb^2 - p) + \mu_n^2 B^2 (n - p)}{(nb + p)b + \mu_n^2 B^2 (n + bp)} \tag{4.9}$$

4.1.2 Magnetoresistance

The application of a magnetic field causes a curvature in the mean free path of the carriers (due to the Lorentz force). This increases carrier scattering in general, resulting in an increase in the sample resistivity. If, however, the constant energy surfaces are spheres, and a constant relaxation timecould be assumed, then in a one-carrier system, the presence of a transverse magnetic field would not produce a resistivity change (S5). This no longer holds when two species of carriers contribute to conduction. Considering spherical constant-energy surfaces, again a constant relaxation time, and only effects quadratic in the magnetic field, the fractional change in resistivity, from Eqn (4.8), is given by

$$\frac{\Delta\rho}{\rho_o} = -\frac{\Delta\sigma}{\sigma_o} = \chi R_o^2 \sigma_o^2 B^2 \tag{4.10}$$

where ρ_o, σ_o, R_o are the low-field resistivity, conductivity and Hall coefficient, respectively. χ is the transverse magneto-resistance coefficient, defined by,

$$\chi = \frac{npb(1 + b)^2}{(nb^2 - p)^2} \tag{4.11}$$

The maximum magnetoresistance is realized in a semiconductor disk with one electrode in the centre and the other (co-axial) along the periphery: the Corbino disk. The electric field has only the radial component, and the current paths are logarithmic spirals making an angle, θ, the Hall angle, with the radial direction. The current-field relation is given by the Hall-Ohm equations:

$$\underline{\mathcal{E}} = \rho\underline{J} - R_H\underline{J}\wedge\underline{B} \quad ; \tag{4.12}$$

$$\underline{J} = \sigma\underline{\mathcal{E}} + \sigma R_H\underline{J}\wedge\underline{B} \tag{4.13}$$

where

$\underline{J}$ is the current density vector,

$\underline{\mathcal{E}}$, $\underline{B}$ are the electric and magnetic field vectors, and

σ, ρ are the scalar conductivity and resistivity.

The components of $\underline{\mathcal{E}}$ in cylindrical coordinates are

$$\mathcal{E}_r = \rho J_r - R_H J_\phi B \quad ; \tag{4.14}$$

$$\mathcal{E}_\phi = \rho J_\phi + R_H J_r B = 0 \tag{4.15}$$

Hence, the magnetic-field dependent resistivity, $\rho(B)$, is given by

$$\rho(B) = \mathcal{E}_r/J_r = \rho(1 + \tan^2\theta) \tag{4.16}$$

where

$$\tan\theta = R_H B/\rho$$

The Corbino magnetoresistance is therefore

$$\frac{\Delta\rho}{\rho_o} = \left[\rho(B)/\rho_o - 1\right] = \tan^2\theta \tag{4.17}$$

In a one-carrier system, $\tan\theta$ is just μB; the magnetoresistance bears a quadratic relationship with B, in agreement with Eqn (4.10).

Wieder (W7) obtains an expression, when conduction is due to two species of carriers, of the form

$$\frac{\Delta\rho}{\rho_o} = \frac{\left[\mu_1^2\sigma_1/\sigma_o + \mu_2^2\sigma_2/\sigma_o\right]B^2 + (\mu_1\mu_2B^2)^2}{1 + \left[\mu_1^2\sigma_2/\sigma_o + \mu_2^2\sigma_1/\sigma_o\right]B^2} \qquad (4.18)$$

where $\sigma_o = \sigma_1 + \sigma_2$, the zero-field (magnetic) conductivity. Making the appropriate substitutions for σ_o and μ, in Eqn (4.18), gives

$$\frac{\Delta\rho}{\rho_o} = \left[\frac{\mu_n}{b}\right]^2 \frac{(1 + cb^3) + (1 + cb)(\mu_nB)^2}{(1 + cb) + (1 + c/b)(\mu_nB)^2} B^2 \qquad (4.19)$$

where

$b = \mu_n/\mu_p$, is the mobility ratio, and
$c = n/p$, is the carrier density ratio.

4.2 Experimental details

Fig 4.1 shows the physical shape of the Hall sample used, having a width, w = 0.1 cm and a length between contacts 2 and 3, l = 0.3 cm. The length to width ratio, l/w, must be greater than about 2.5 if the shorting effect (of the Hall voltage) is to be negligible (P5).

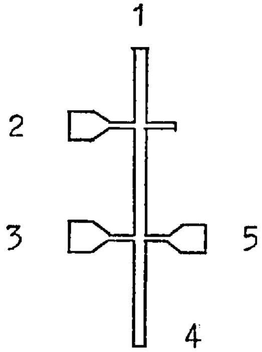

Fig 4.1

In or In/Bi alloy (the latter having a melting point of 75 °C for a 33% Bi content) was soldered on to the five contacts. A dc current, typically 100 µA, was passed between contacts 1 and 4 of the sample; its value was accurately determined by measuring the voltage drop across a standard 100 Ω resistance, in series with the sample. The conductivity voltage, V_{23}, measured between contacts 2 and 3, was made on a Solartron digital voltmeter which had an input impedance varying between 10 MΩ to greater than 5000 MΩ, depending on the voltage range. Such high input impedance is necessary, since the resistance measured at 2 and 3 was usually a few hundred KΩ. The resistance could easily increase to a few MΩ at 77 °K, particularly for thinner samples, when correction to the voltmeter reading became necessary for measurements made on the lower input impedance range. This is achieved by considering the meter input impedance to be in parallel with the resistance of the sample. From the observed voltmeter reading and the current, the true voltage drop can be found.

The sample was mounted inside a brass tube provided with external leads and placed inside a 'Thermos' flask, between the pole-pieces (6-cm gap) of a permanent magnet. The magnetic field was 2 kG. To measure the Hall voltage, V_H, between contacts 3 and 5, the sample was rotated in the magnetic field and the maximum and minimum meter readings were noted. This was done to eliminate the standing voltage (due to electrodes 3 and 5 not aligned directly opposite one another), which could be 10 times as high as the actual Hall voltage. The difference between the two readings is twice the Hall voltage. No correction was necessary as the measurements were made on the highest impedance range.

The conductivity and Hall coefficient were obtained from the following formulae:

$$\sigma = \frac{1}{w}\frac{1}{t}\frac{I}{V_{23}} \; ; \qquad (4.20)$$

$$R_H = \frac{V_{23}t}{IB} \tag{4.21}$$

where

V_{23}, V_H are the conductivity and Hall voltages,
I is the current,
B is the magnetic field (which is normal to the plane of the sample), and
t is the sample thickness.

The 'Thermos' flask could be filled with liquid nitrogen, thus enabling the temperature variation to be made continuously down to 77 °K. A brass heating tube was also available for measurements up to 150 °C (just below the melting point of In solder). The magnetic field-dependence experiments were carried out on a variable gap electro-magnet, capable of a maximum field of 20 kG.

The Hall geometry is not suitable for magneto-resistance study, since the effect is small in thin films, in view of their low mobility ($\mu B \ll 1$). The Corbino disk, in which $l/w = 0$ and the Hall field is completely shorted out, was employed. Samples were prepared by evaporating In or Sn on to the semiconductor films, through circular wire masks of known diameter. The physical size of these samples could be made as small as 0.1 cm in diameter. In this case, contacts could not be made by soldering. Silver dag provided the alternative and proved to be highly satisfactory.

4.3 Results

A large number of Hall samples were prepared, under various evaporating conditions, the results of some of them being shown in Table 4.1. It can be seen that μ_H

Table 4.1

Sample	t(A^{o})	μ_H(296, 77^{o}K) (cm^2/V sec)	n(296, 77^{o}K) (×10^{16} cm^{-3})	T$_s$(^{o}C)	T$_a$(^{o}C)	Press. (torr)
nA5	2000	300	31	200	300	1×10^{-6}
nA12	3000	960	4.5	220	360	2
nA19	500	440	15	200	360	3
nA20	1000	600	18	230	360	2
nA26	700	600	20	230	350	2
nA33	3000	1170 (200)	7 (3.0)	230	370	2
nA74	3000	1400 (1100)		230	360	2
nA78	2500	1600 (1400)		230	360	2
nB4	1800	1600	5.2	260	380	3
nB5	2250	3200 (80)	3.3 (2.3)	250	400	2
nB34	1150	1200	5.6	260	400	3
nC24[1]	3000	2860 (2100)	21 (18)	360	400	10
nF8	1100	1200 (120)	6.8 (2.0)	300	420	8
nF9	1600	1700	5.2	310	410	15
nF11	1380	1160	4.9	320	420	6
nF15	1500	1580 (80)	4.9 (1.1)	290	430	6
nF16	2000	1300 (160)	8.9 (5.3)	290	430	12
nF18[2]	1880	4600 (90)	4.0 (3.5)	310	390	2
nF20	2100	2560 (360)	5.2 (3.8)	300	430	4
nF27[3]	1500	3010 (830)	9.7 (7.0)	290	500	6
J1[4]	3-5000	6-15000 (1-4000)	(10^{16}- 10^{17})			
	bulk[5]	(10^{5})	(~2×10^{14})			

---

[1] Evaporated from a 1:3 In/Sb mixture, at a higher substrate temperature of about 380 ^{o}C.

[2] Annealed for 14 hours, followed by slow cooling.

[3] Coated with SiO.

[4] From Ref. (J1).

[5] Polycrystalline InSb, from R.R.E.

Note: Figures in brackets are for liquid nitrogen temperature.

and n do not depend critically on the pressure (for pressure $< 2\times10^{-5}$ torr) and the substrate temperature, T_s. Rather, these parameters are critically dependent on the post-evaporation annealing temperature, T_a. Samples annealed below 360 °C are generally poor in mobility and have high carrier concentration $\sim2\times10^{17}$ cm^{-3} at 296 °K. Annealing at about 420 °C and using a somewhat elevated T_s (in the nF- series) produce much better films, with correspondingly larger crystallites. In this case, the carrier concentrations are generally lower $\sim5\times10^{16}$ cm^{-3} at 296 °K. The highest mobility obtained was 4600 cm^2/V sec in a sample of thickness 1880 A° (nF18). This sample was annealed for 14 hours at 390 °C and followed by slow cooling.

In polycrystalline films, Hall effect measurements give the carrier concentration in the crystallites (V1). For films of the thickness range investigated (1000 - 3000 A°), the space charge region at either surface represents a significant portion of the film's total thickness. As will be seen in Chapter Seven, the space charge is always in depletion, the surface band bending being roughly two-thirds up the band-gap. Hence, the Hall effect does not give a true value of the carrier density within the crystallites. A correction, based on the simple Schottky solution of the Poisson equation, is used. He assumes a depletion region completely devoid of carriers and having a uniform distribution of ionised impurities, N_d. Under this assumption, the depletion depth, z_s, is given by

$$z_s = \left[\frac{2\epsilon\epsilon_0 v_s}{eN_d}\right]^{\frac{1}{2}} \tag{4.22}$$

where v_s is the surface band bending, which will be seen to be approximately -25 kT or about 0.16 eV at 77 ^{o}K. Lile (L6) finds this to be relatively independent of temperature. Using this value, the depletion depth becomes

$$z_s = 1.6 \times 10^{11} N_d^{-\frac{1}{2}} \ (A^o) \quad (4.23)$$

where N_d is in cm^{-3}.

Assuming the film to be depleted to the same extent at both the mica/InSb and the free surface, the corrected carrier density becomes

$$n_{cor} = n_{mea} t/(t - 2z_s) \quad (4.24)$$

where n_{mea} is the measured Hall concentration and t is the film thickness. For $N_d \sim 2 \times 10^{17}$ cm^{-3}, $2z_s \sim 800$ A^o. Hence, this correction becomes of doubtful validity when the thickness is less than about 1000 A^o. A correlation between n_{cor} and n_{mea} is shown for different thicknesses in Fig 4.2.

For films less than about 800 A^o, the space charge regions from either surface overlap, thus depressing the Fermi level further into the band-gap. In the absence of overlapping, the Fermi level in the 'bulk' crystallite is determined solely by the impurity concentration. This no longer holds for thinner films, which are therefore expected to exhibit lower carrier density. Moreover, it is not possible to extract any 'bulk' properties from measurements on such a film.

The temperature dependences of μ of some typical n-type films are shown in Fig 4.3, the general behaviour of these curves being in agreement with previous reports

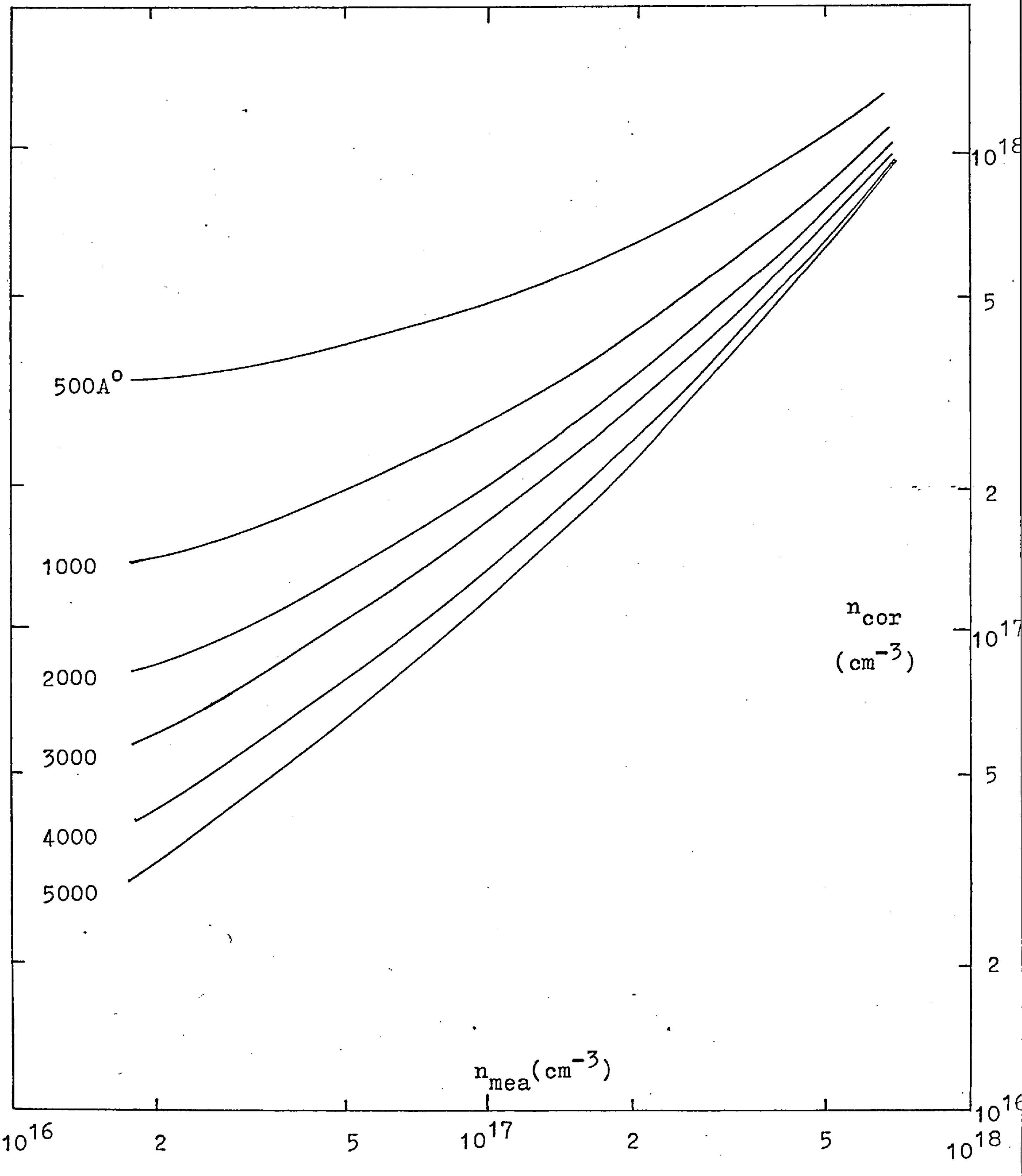
500A°
1000
2000
3000
4000
5000
n_{cor}
(cm^{-3})
$n_{mea}(cm^{-3})$
10^{16}
2
5
10^{17}
2
5
10^{18}
10^{18}
5
2
10^{17}
5
2
10^{16}

Fig 4.2

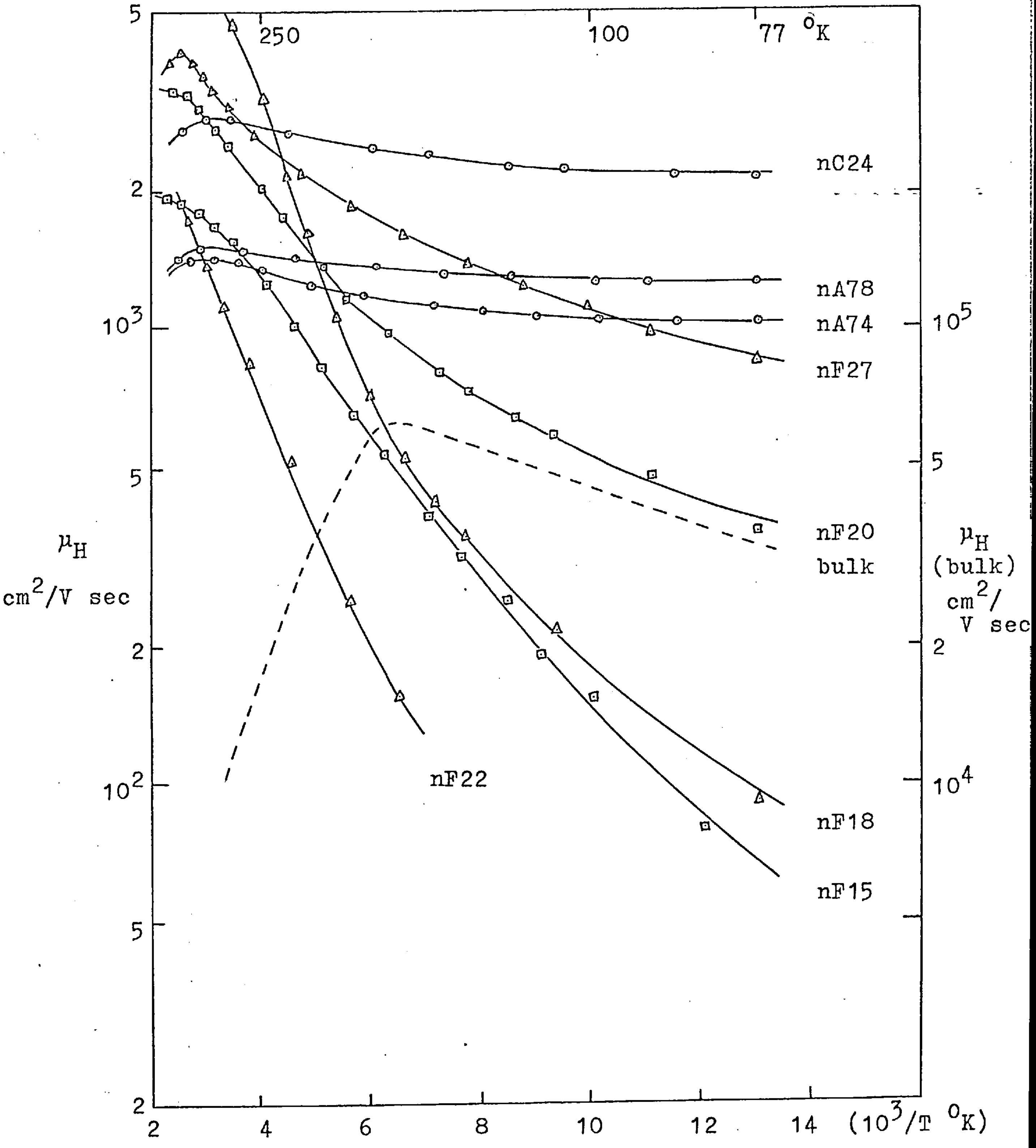

<u>Fig 4.3</u>: Temperature variation of Hall mobility

(J1, P7, W3). The bulk behaviour is also included in the figure for the purpose of comparison. The measurement of the bulk sample having dimensions $0.5 \times 0.5 \times 5$ mm^3 and with 5 grain boundaries (as revealed by CP4 etch) traversing the entire cross-section of the rectangular slab, was carried out using ameasuring field of 0.1 V/cm[4]. The apparent discrepancy between the observed mobility of $\sim 3 \times 10^4$ cm^2/V sec at 77 °K and the quoted figure of $\sim 10^5$ cm^2/V sec, could be explained by the fact that the magnetic field of 2 kG used was sufficiently high to produce a reduction in mobility of about a factor of 3 (G5).

4.3.1 Impurity concentration

The variation of electron concentration $(1/R_H e)$ after correcting for the space charge layers at the surfaces, with temperature is shown in Fig 4.4. After correction, most of the films have carrier concentration in the 10^{17} cm^{-3} range. It is seen that below about 200 °K, the electron concentration is relatively insensitive to temperature, being equal to the excess donor impurities (i.e. $N_d - N_a$), which do not have any detectable ionization energy in this temperature range (M1). Above 300 °K, all samples show intrinsic carrier concentrations.

Evaporated thin films invariably show a much higher impurity concentration than the starting materials. In InSb films, $N_d - N_a \sim 10^{17}$ cm^{-3}, whereas the starting material has an impurity content of $\sim 10^{14}$ cm^{-3}. This increase could be due to foreign atoms included in the film lattice during preparation. But, as has been seen

---

[4] For impurity-dominated scattering, which is probably the case here at 77 °K, mobility increases with electric field as (S9)

$$\mu = \mu_o (1 + \beta \mathcal{E}^2).$$

Hence, the necessity to use low measuring fields.

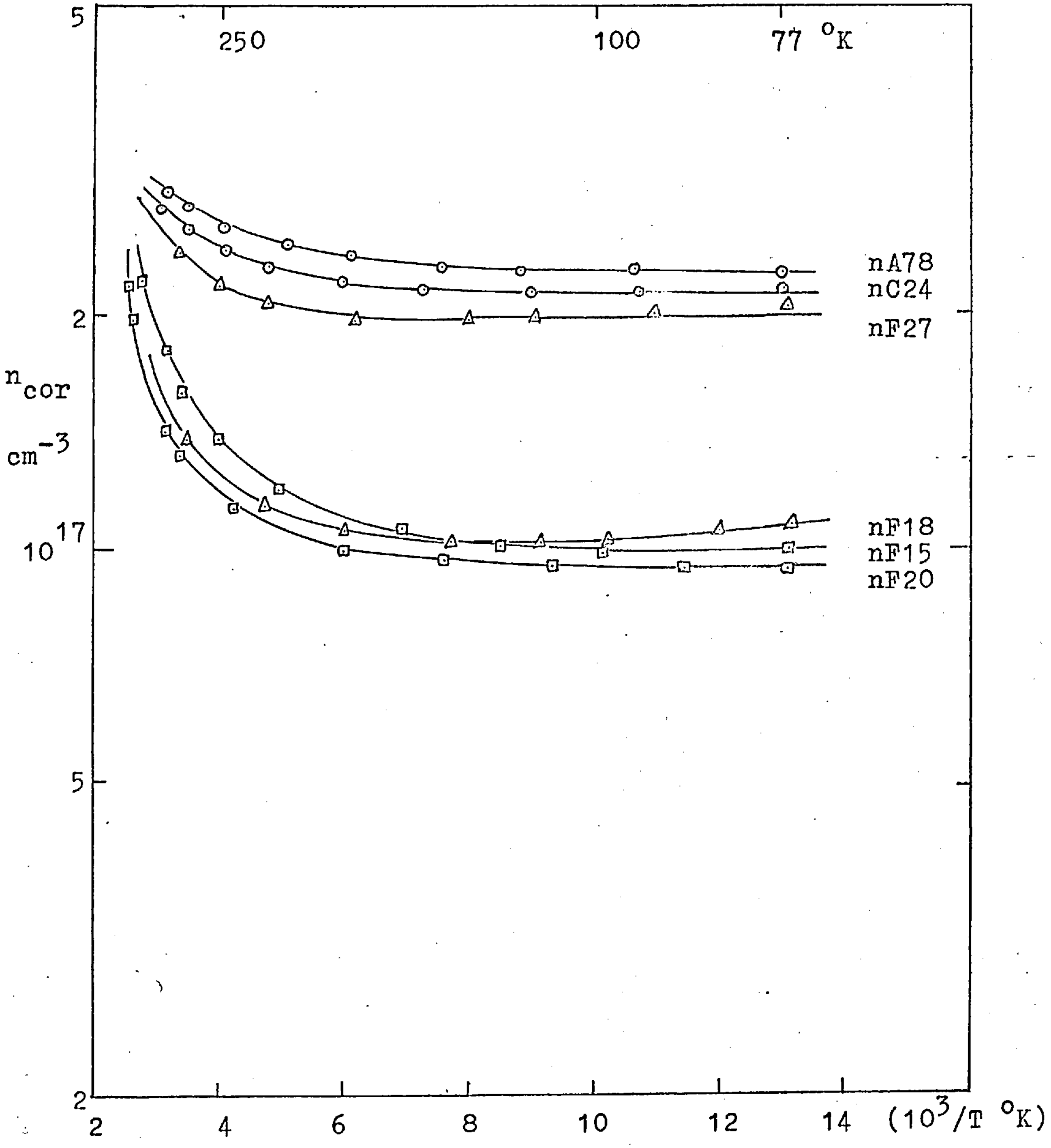

Fig 4.4: Temperature variation of electron concentration

earlier, the evaporation pressure is not a critical condition and as pointed out by Juhasz (J1), the importance of a good vacuum has perhaps been over-emphasized by many early workers. Foreign atoms (inclusions) would definitely affect the electrical properties, since they distort the regular lattice periodicity. So far, there is no evidence of their importance, and it may be inferred from this, that their effect is small compared to other defects.

The presence of a thin layer of oxide at the surface (deliberately introduced), might actually lead to a reduction in the carrier concentration. Such a reduction has been observed in n-type lead salt films, due to the compensation effect of the p-type oxide layer on the Hall voltage (E1). Surface states would trap or release carriers depending on the temperature. These processes therefore affect the carrier concentration. However, Juhasz points out that compensation occurs between acceptor- and donor-like states, resulting in a negligible contribution to the impurity concentration.

The conditions of thin film preparation are no where near the thermodynamic steady state conditions encountered in single-crystal growth. Film structures are therefore expected to contain more crystallographic defects. Moreover, the comparatively rapid cooling after annealing enhances the population of the defects, since at higher temperatures, a larger number of defects in thermal equilibrium in the crystallites is possible, and on rapid cooling they become 'locked' in the lattice. (For this reason, a slow cooling is desirable and accounts for the relatively higher mobility in sample nF18.)

The presence of crystallographic defects is evident from electron microscopy study. Edge dislocations in InSb are known to introduce acceptor levels because of the presence of unsatisfied dangling bonds, and cannot therefore contribute to an increase in the donor concentration (W8, M5). However, large-angle crystal boundaries behave differently to dislocations and could introduce donor levels (M6). Juhasz suggests that thin films might contain large-angle crystallite boundaries, and their cumulative effect could account for the high impurity concentration. This does not seem to be a very satisfactory explanation. Electron diffraction shows the crystallites to grow in the (111) plane and well oriented about the $[111]$ axis. Consequently, the region of mismatch between crystallites should be expected to be small; in fact, measurements of the diffraction spots gave a maximum angle of misorientation of about 10° (Chapter Three). From this point of view, crystallite boundaries would behave like low-angle dislocations; their presence, if at all, serves only to reduce the donor concentration. The presence of satellite spots about the 'main' hexagonal pattern (spots), indicates twins and twin boundaries. No dangling bonds are associated with twin boundaries (M7), which are therefore not expected to produce any effect on the impurity concentration.

The crystalline structure of $\{111\}$ surfaces are different from the interior of the crystal due to lattice distortion (W3). x-ray studies show that the lattice constant in III-V compounds could be twice as large at the $\{111\}$ surface as in the bulk. The tensile stress associated with such lattice distortion leads to an increase in the band gap and consequent decrease in the intrinsic carrier population.

The increase in the impurity concentration could perhaps be easily accounted for if a slight non-stoichiometry is assumed, i.e. an excess of In or Sb. This is plausible since the vapour pressures of In and Sb differ by orders of magnitude; the resulting film stoichiometry would be expected to deviate slightly from the original material. An excess of 1 in 10^5 Sb atoms would be sufficient to produce a donor concentration of 10^{17} cm^{-3}.

4.3.2 Hall mobility

Mobilities observed in the films are all in the range of 1000 - 4000 cm^2/V sec at room temperature. Compared to the bulk figure of 3×10^4 cm^2/V sec at 300 ^oK and for the same impurity concentration, this represents a reduction of some 10 - 30 times. At 77 ^oK, the reduction is even higher, by as much as a factor of 10^3, since in this case, mobility increases with decreasing T for bulk and decreases with T for thin films. A temperature dependence of the form, $\mu \sim T^m$ is applicable, m being approximately -1.6 for bulk (for $T > 200$ ^oK) and 0.4 - 0.7 for thin films (for $T \sim 100 - 300$ ^oK). A mobility peak has been observed in the vicinity of 350 ^oK for the higher carrier density films and around 450 ^oK for lower carrier density films. The decrease at temperatures higher than these, marks the onset of bulk behaviour and might suggest at these temperatures, films behave in much the same way as bulk. This perhaps is the case, since optical phonon scattering and to a lesser extent, inter-carrier scattering dictate carrier transport in bulk InSb at high temperatures, and are also expected to be the most significant mobility-limiting mechanisms in films. At lower temperatures, the mobility reduction must be interpreted in the light of thin film defects. This section is devoted to examining those scattering processes peculiar to thin films, bearing in mind that the background scattering (due to bulk) is always present.

(1) Surface scattering

In Chapter Three, a correlation between mobility, mean crystallite size and thickness was made. Generally, mobility decreases with decreasing thickness. This is compatible with the surface scattering theory of Fuchs and Sondheimer (F1, S1) and of Schrieffer (S2): the largest surface effect (geometry and surface potential) is observed in crystals with dimensions comparable to the carrier mean free path. The effects of surface on carrier transport are summarised in Appendix B.

Consider the simplified case. Many et al (M4) show that the reduced average mobility, $\bar{\mu}$, is approximately given by

$$\bar{\mu} = \mu_b/(1 + 2\lambda/t) \tag{4.25}$$

where μ_b is bulk mobility. For a film with thickness, $t = 1000$ A°, the typical observed mobility is 1000 cm^2/V sec at room temperature. Taking an appropriate value of $\mu_b \sim 3\times10^4$ cm^2/V sec, the mean free path, λ, is found to be approximately 2200 A° (see Appendix C). This gives a reduced mobility of ~6000 cm^2/V sec for the film, which is 6 times as high. Clearly surface scattering cannot be the dominant mobility-limiting mechanism. Indeed, Schrieffer's theory predicts significant reduction only for surfaces that are in strong accumulation, as , for example, in the case of CdS films on SiO (W9). The depleted surface in InSb films tend to repel electrons and prevent them from reaching the surface.

(2) Dislocation scattering

The sphalerite structure of InSb can be visualised as consisting of a series of (111) planes of In and Sb atoms, with alternate large and small spacings between them. Slip dislocations occur most readily between the widely spaced pairs of (111) planes, since fewer bonds are broken in this case. When such a dislocation occurs, an extra half-plane of atoms (In or Sb) is introduced into the lattice. The atoms at the edge of this half-plane would consequently have free or dangling bonds (H7, H8). Screw dislocations, however, do not lead to dangling bonds and are unimportant here (W3).

From the electrical point of view, such dangling bonds existing in dislocations are important, as they can give rise to energy levels within the band gap, thereby acting as traps to conduction carriers. The theory of dislocations has been treated in great detail by Read (R5), who considers the dangling bonds to be acceptors capable of capturing electrons from the conduction band. Thus the dislocation acts as a negatively charged line, with a cylindrical space charge of positively charged ions around it. If the dislocation lines are perpendicular to the current flow, then since the conduction electrons have to follow curved paths that wind around them, a reduction in electron mobility is to be expected. This, however, is not the case if the charged cylinders are parallel to the current flow, which follows from Read's assumption that scattering at the surface of the cylinders is specular.

The mobility of minority carriers, however, can actually increase in the presence of dislocations (M7). If the space charge cylinders are parallel to the current flow, then the minority carriers are constrained to move in the vicinity of the dislocation line with an enhanced mobility.

The above concepts have been applied to bulk InSb (W8, B8, B9, B10). In view of the many unknown parameters, which are possible to estimate in bulk but not in films, a quantitative model is not attempted here. A rough estimate of the effects of dislocations will now be considered. Dexter and Seitz (D5) treat the scattering of carriers at randomly-arranged edge-type dislocations by the method of the deformation potential and obtain an expression for the dislocation mobility, μ_D, given by

$$\mu_D = (\alpha_d T)^{-1}; \quad \alpha_d = \frac{3\pi}{32} \frac{E_i^2 b^2 m_i}{k\hbar e} \frac{1 - 2\nu^2}{1 - \nu} N \qquad (4.26)$$

where

E_1	is the deformation potential, of the order of several eV's (see Sec 2.6.3),
b	is the Burger's vector, ~ 5 A^{o},
ν	is the Poisson ratio, ~ 0.4, and
N	is the density of dislocation in units of cm^{-2}.

The T^{-1} relation gives very approximately the right form of temperature dependence for bulk material but not for thin films. The dislocation density, N, in bulk InSb is of the order of 10^6 cm^{-2} (W8); no data is available for thin films. However, in PbS films, N was observed to be as high as 2×10^{10} cm^{-2} (E1). Using this assumed value of N and other appropriate values for the various parameters in Eqn (4.26), μ_D is found to be of the order of a few tenths of cm^2/V sec, such a low value being in agreement with that obtained by Egerton (E1) for lead salt films.

That the actual observed mobility is higher than the calculated dislocation mobility by some 2 - 3 orders of magnitude would imply perhaps a gross over-estimation of the dislocation density. In the derivation of Eqn (4.26), Dexter and Seitz assume the dislocations to be uniformly distributed in a continuous medium. This is not justifiable in InSb films, since edge dislocations are preferentially oriented in the $\{111\}$ planes. The space charge cylinders lie in a plane parallel to current flow, and as remarked earlier, mobility reduction is not expected to be considerable.

Prolonged annealing of films followed by slow cooling usually improves the mobility. This is interpreted to mean a reduction in dislocation density (and also an increase in crystallize size), and is sufficient, if only qualitative, evidence for dislocation scattering.

(3) Grain boundary scattering

Grain (crystallite) boundaries are regions of lattice mismatch and affect carrier transport in two ways: (1) they scatter carriers, limiting the mean free paths to approximately half the mean crystallite size, and (2) the presence of dangling bonds trap carriers, giving rise to a potential barrier. The second effect will be discussed in the next section.

Grain boundary scattering leads to a mobility, given by

$$\mu_B = \frac{e l_B}{m_i \langle c \rangle} \qquad (4.27)$$

where l_B is the mean free path, taken to equal half the mean crystallite size, and $\langle c \rangle$ is the mean thermal velocity. Consider a 2000 A^o film. The average thermal velocity can be calculated as in Appendix C, using the appropriate

Fermi-Dirac statistics and taking into account the non-parabolicity of the conduction band of InSb. In Fig 4.5 is plotted the grain boundary mobility as a function of temperature and for different Fermi energies.

Again it is seen that the temperature variation of μ_B does not explain the observed temperature dependence in the measured films. Comparison of mobility would be meaningful only at the temperature corresponding to the mobility peak, when the films start to exhibit 'bulk' behaviour. The highest mobility sample (nF18) of similar thickness (1880 A^o) has a peak mobility of ~ 6000 cm^2/V sec at 400 ^{o}K. The grain boundary mobility corresponding to this temperature and for $(E_c - E_f)/kT = -2$, is ~ 12500 cm^2/V sec, i.e. twice the peak value. Since the film mobility can be further improved by protective annealing (J1), i.e. reducing other scattering centres, thereby bringing the value nearer to the estimated grain boundary mobility, it would appear that grain bounaries do indeed play an important part in limiting carrier mobility.

(4) <u>Potential barrier scattering</u>

As pointed out earlier, InSb films probably contain low-angle grain boundaries, which have been considered to be vertical arrays of edge dislocations with dangling bonds (M7). The distance, D, between two dislocation lines is given by

$$D = \frac{b}{2 \sin \Theta/2} \qquad (4.28)$$

where

b is the Burger's vector, and

Θ is the angle of misorientation.

Mataré (M7) defines low-angle boundary to be in

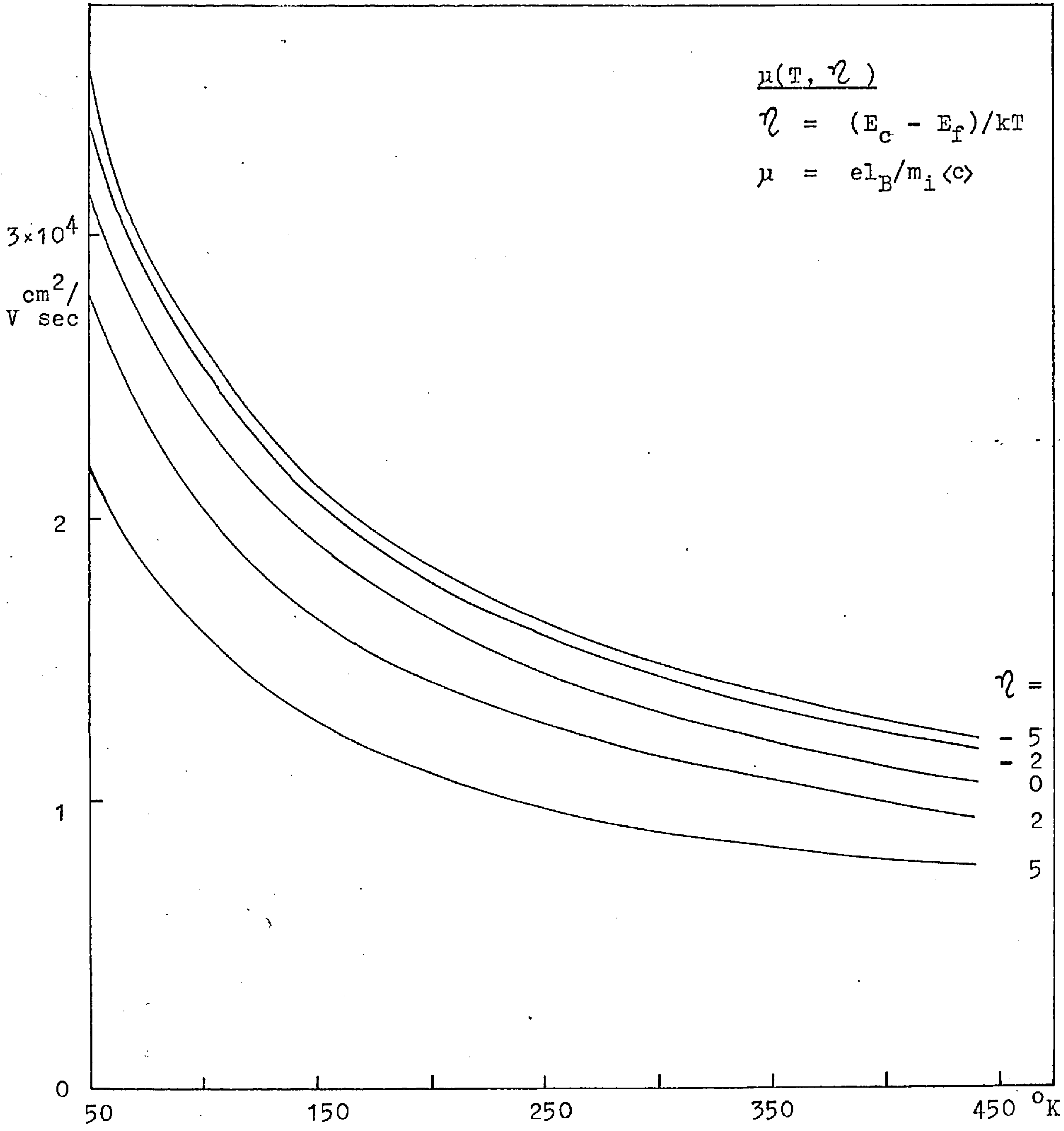

Fig 4.5: Calculated mobility as a function of temperature for various Fermi levels

the range $0.1 < \Theta < 5^{\circ}$. Taking the lower limit, $\Theta = 0.1^{\circ}$, $D = 2900$ A$^{\circ}$; taking the upper limit, $\Theta = 5^{\circ}$ (i.e. half the maximum angle of misorientation), $D = 76$ A$^{\circ}$. The lower limit is obviously unrealistic.

The spacing, c, between dangling bonds in a dislocation line for pure edge dislocation is

$$c = 0.866\ b \tag{4.29}$$

A 5° grain boundary therefore contains $N_t = (D \times c)^{-1}$ $\sim 3 \times 10^{13}$ dangling bonds/cm^2 of grain boundary surface. Consider the space charge cylinder around a dislocation line. The radius, R, is given by

$$e \pi R^2 (N_d - N_a) = ef/c$$

i.e.

$$R = \left[f/c \pi (N_d - N_a) \right]^{\frac{1}{2}} \tag{4.30}$$

where the 'filling factor', f, is given by[4]

$$f = \left[1 + \exp (E_{td} - E_f)/kT \right]^{-1} \tag{4.31}$$

E_{td} being the trap energy of the dislocation acceptor. Using an impurity concentration, $(N_d - N_a) \sim 10^{17}$ cm^{-3}, and taking $f = 1$, i.e. complete filling of dangling bonds, the space charge radius is found to be ~ 750 A$^{\circ}$, which is not credible, in view of the fact that the mean crystallite size is only of this order of magnitude. This therefore leads to the assumption that $f \ll 1$. In InSb, the filling factor is typically of the order of 0.01 (W8).

Trapping of carriers at dangling bonds leads to a difference in carrier concentration in the crystallites and in the grain boundaries. If n_1 and n_2 are the

---

[4] The Fermi statistics is not strictly valid here (M7).

concentration in the respective regions, then the difference causes a diffusion potential to set up, given by (H6):

$$e\phi_o = kT \log (n_1 / n_2) \tag{4.32}$$

In the derivation of Eqn (4.32), the non-degenerate Maxwell-Boltzmann statistics has been assumed.

In Chapter Five, the presence of a grain boundary potential barrier, ϕ_o, will be demonstrated, and it will be shown that, under this condition, mobility, $\mu \sim \exp(-e\phi_o/kT$ which is capable of explaining the observed temperature variation.

4.3.3 p-type films - Hall coefficient

Over 10 p-type samples were prepared from a 1:3 In/Sb mixture doped with Cu. Fig 4.6 shows the temperature variation of Hall coefficient with temperature. At high temperatures, the conduction process is n-type because of the higher mobility of electrons, though the hole population exceeds the electron population. But at lower temperatures, the conduction is p-type, i.e. hole-dominated, since now $p \gg n$.

R_H goes through zero when the contribution due to the two species of carriers cancel out, i.e. when

$$p = n \frac{(b^2 + \mu_n^2 B^2)}{(1 + \mu_n^2 B^2)} \quad \text{from Eqn (4.7)}$$

$$\rightarrow b^2 n \quad \text{for low B}$$

Below about 150 ^oK, R_H does not vary with T. This is the 'exhaustion' region, the excess acceptor density being given by

$$N_a - N_d = 1/eR_{H,ex} \tag{4.33}$$

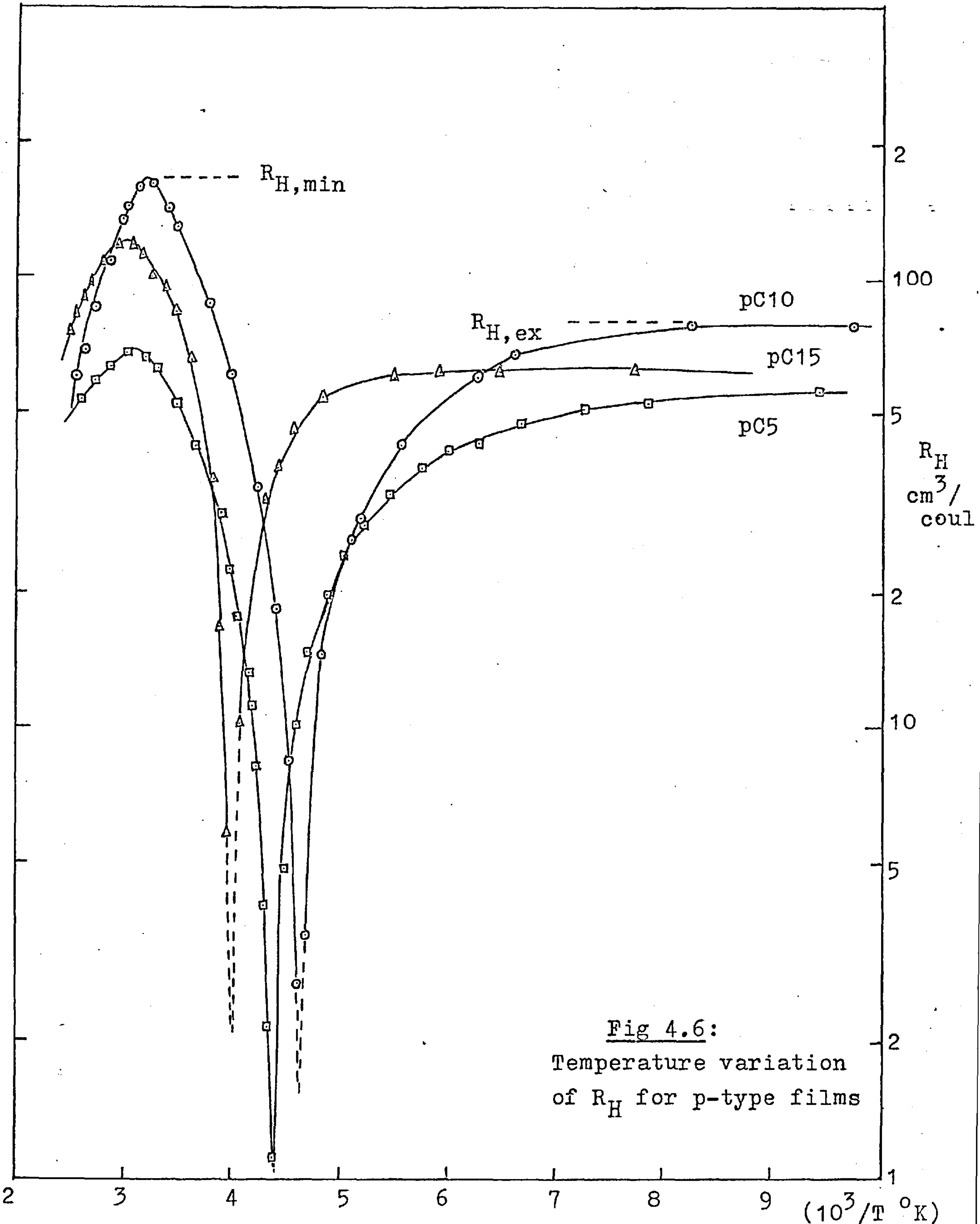

Fig 4.6: Temperature variation of R_H for p-type films

Around room temperature, R_H goes through a minimum, i.e. at $dR_H/dT = 0$.

Now

$$\frac{dR_H}{dT} = \frac{dR_H}{dn}\frac{dn}{dT}$$

But

$$\frac{dn}{dT} \neq 0$$

Therefore differentiating Eqn (4.1), (ignoring for the present the magnetic field dependence) and setting dR_H/dn to zero, the Hall minimum occurs when $p = nb$. Using this value of p in Eqn (4.1) leads to

$$R_{H,min} = -\frac{1}{e}\frac{b-1}{4nb} \qquad (4.34)$$

Charge neutrality requires (assuming complete ionisation of impurities)

$$p + N_d - n - N_a = 0$$

whence,

$$n = nb - (N_a - N_d)$$

$$= (N_a - N_d)/(b - 1) \qquad (4.35)$$

Using Eqns (4.34), (4.35) and (4.33),

$$\frac{|R_{H,min}|}{R_{H,ex}} = \frac{(b-1)^2}{4b} \qquad (4.36)$$

The above derivations can only be considered to be approximate, since a number of hidden assumptions, applicable only in the presence of non-degenerate statistics and parabolic bands, have been included. Eqn (4.36) can be solved for b. However, it is strictly valid only when $R_{H,min}$ is measured in the presence of vanishingly small magnetic field. $R_{H,ex}$ is not expected to depend on B since it is measured for $p \gg n$ (see Eqn (4.7)). To correct for the effect of magnetic field (2 kG being used), $R_{H,min}$ was measured as a function of B, from 50 G to 20 kG, and extrapolated to zero B. This is shown in Fig 4.7 for sample pC15. Care was taken to maintain a constant temperature, 42 ^{o}C in this case, as $R_{H,min}$ was found to be a sensitive function of T. From the curve, it was deduced that $R_{H,min}$ decreases by about a factor of 1.5 from 0 to 2 kG.

Knowing the mobility ratio, the electron and hole mobilities at the 'Hall minimum' temperature can be estimated. At Hall minimum, the conductivity is given by

$$\begin{aligned} \sigma_{min} &= ne\mu_n + pe\mu_p \\ &= 2ne\mu_n \qquad (4.37) \end{aligned}$$

where use of the relation $p = nb$ has been made. Combining Eqns (4.34) and (4.37), gives

$$R_{H,min}\sigma_{min} = (b - 1)\mu_n/2b \qquad (4.38)$$

The results of Hall measurements are shown in Table 4.2 for some p-type films.

The mobility ratio of films in the thickness range 1000 - 2000 A^{o} is therefore around 10. For thicker films in the μm region, Potter and Wieder (P8) obtain a higher mobility ratio of approximately 32. The bulk mobility ratio for similar impurity concentration is about 60 at room temperature.

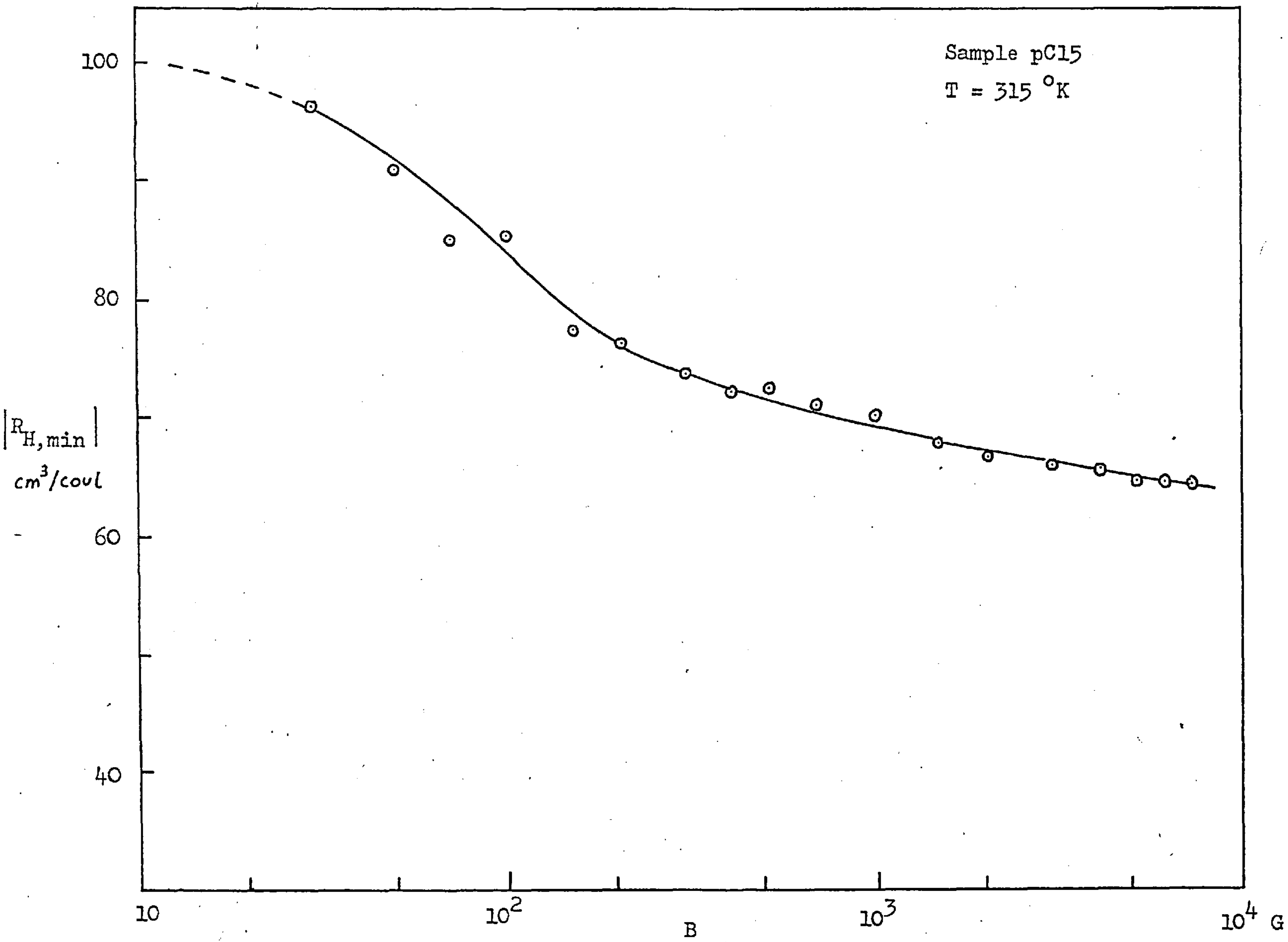

<u>Fig 4.7</u>: Variation of $|R_{H,min}|$ with magnetic field

Table 4.2[4]

Sample	thickness (A^o)	μ_n	μ_p (cm^2/V sec)	b	$N_a - N_d$ ($\times 10^{16} cm^{-3}$)
pC5	1000	570	40	13	10
pC9.3	1500	2500	250	10	8
pC10	1200	2640	180	14	8
pC11	1500	4500	510	8.8	6
pC15	1700	1450	170	8	15
pC39.1	1500	3000	300	15	9

[4] The mobility values were measured at temperatures corresponding to the Hall minima.

p-type films, measured nine months after preparation, were found to show n-type characteristics. It is believed that the copper atoms diffused out of the body of the crystallites and deposited themselves along the grain boundaries (which are not regions of lowest energy). Since Hall measurements give the carrier density within the crystallites (V1), the presence of acceptors, segregated at the grain boundaries, can not thus be detected. The fast diffusion of copper atoms even at room temperature has been demonstrated by Edmond (E4).

4.3.4 Magnetic-field dependence

(1) Hall coefficient

Quantum effects would start to be important when $\mu B \sim 1$. Ortenberg and Landwehr (O2) studied the effect of strong magnetic field in the range 0 - 200 kG in pure n-type InSb at liquid helium temperatures and found that the Hall coefficient actually increases substantially. The reduction in free electron concentration is called 'magnetic freeze-out', the effect being caused by the lowering of the binding energy of shallow donor states by the magnetic field. However, at 77 °K, the work of Fujisada et al (F8) on n-type InSb (20 μm thick) with $\mu \sim 7 \times 10^5$ cm^2/V sec and $N_d - N_a \sim 10^{14}$ cm^{-3}, shows a gradual decrease of Hall coefficient with magnetic field. The decrease was found to be significantly less (in high B) after a lapse of some three months. (The time-dependent characteristic is attributed to the formation of a surface layer.)

With a film mobility of 3000 cm^2/V sec, quantum effects would be noticeable in a magnetic field in excess of 30 kG. Hence, for a magnetic field within the 20 kG range, such effects need not be considered. If conduction is due to one species of carriers, then the Hall coefficient is independent of the magnetic field, i.e. Eqn (4.7) becomes Eqn (4.3) and (4.4). This has been found to be true at least for B up to about 10 kG at 77 °K, when $n \gg p$ for n-type films, and $p \gg n$ for p-type films. But at room temperature, when $n \sim p$, Eqn (4.7) predicts a dependence of R_H on B, although B is still not sufficiently high enough to affect μ. In Fig 4.8, the Hall coefficient is plotted as a function of B at 296 °K for both types of films. It can be seen that R_H remains practically constant with magnetic field for n-type films, while in p-type films, R_H decreases slightly with B.

Fig 4.9 is a theoretical plot of Eqn (4.7), using a mobility value, $\mu_n = 3000$ cm^2/V sec, for 4 different values of the mobility ratio. n-type samples (for $c = n/p \gg 1$) show no significant variation with B. But for p-type samples, R_H decreases with B, the decrease being greater for lower b. Thus the observed behaviour is in qualitative agreement with Eqn (4.7).

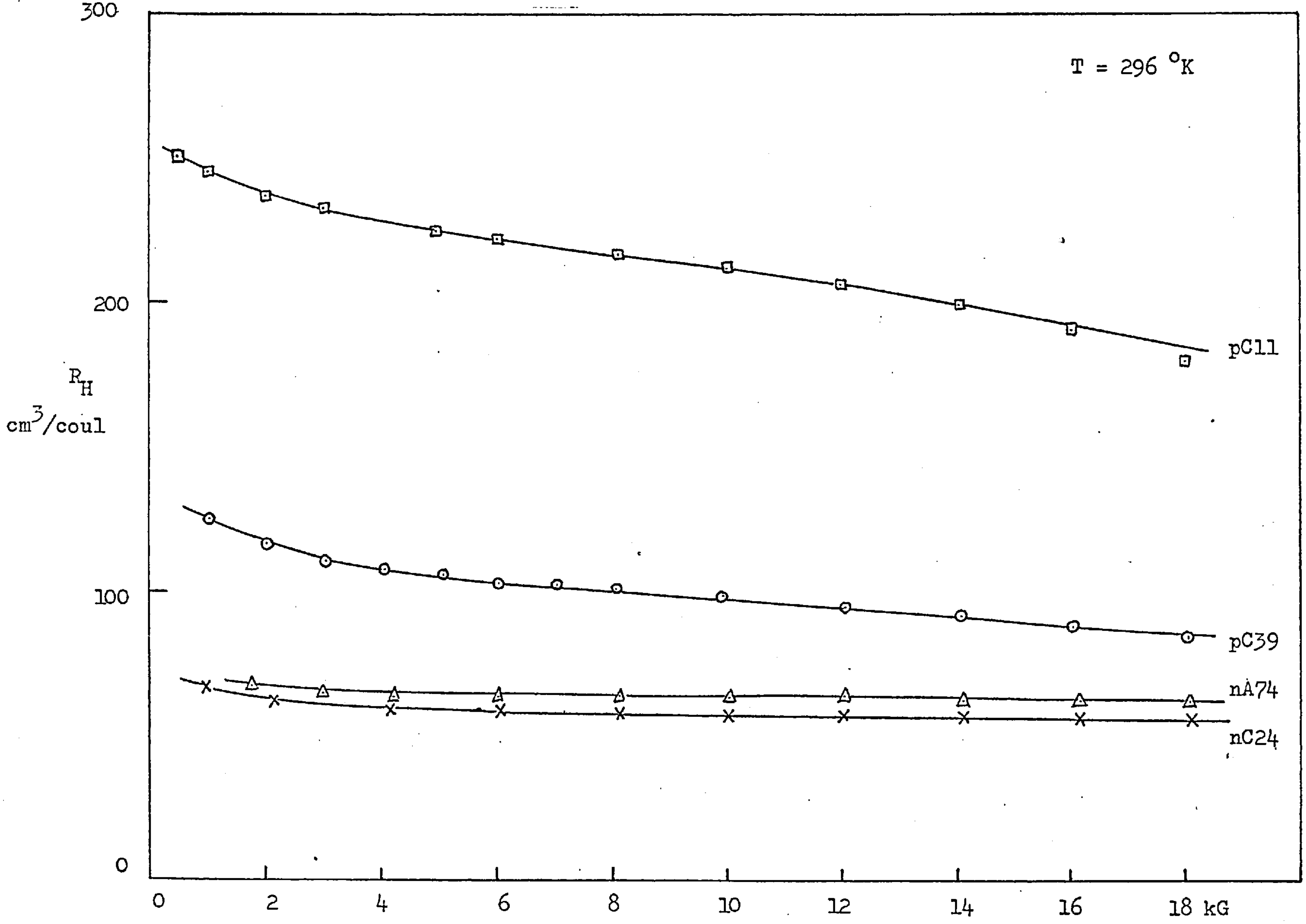

Fig 4.8: Variation of Hall coefficient with magnetic field

$$\frac{R_H(B)}{R_H(0)} = \frac{1 + \mu_n^2 B^2 (c - 1)/(cb^2 - 1)}{1 + \mu_n^2 B^2 (c - 1)^2/(cb + 1)^2}$$

$c = n/p$

$b = \mu_n/\mu_p$

$\mu_n = 3000 \text{ cm}^2/\text{V sec}$

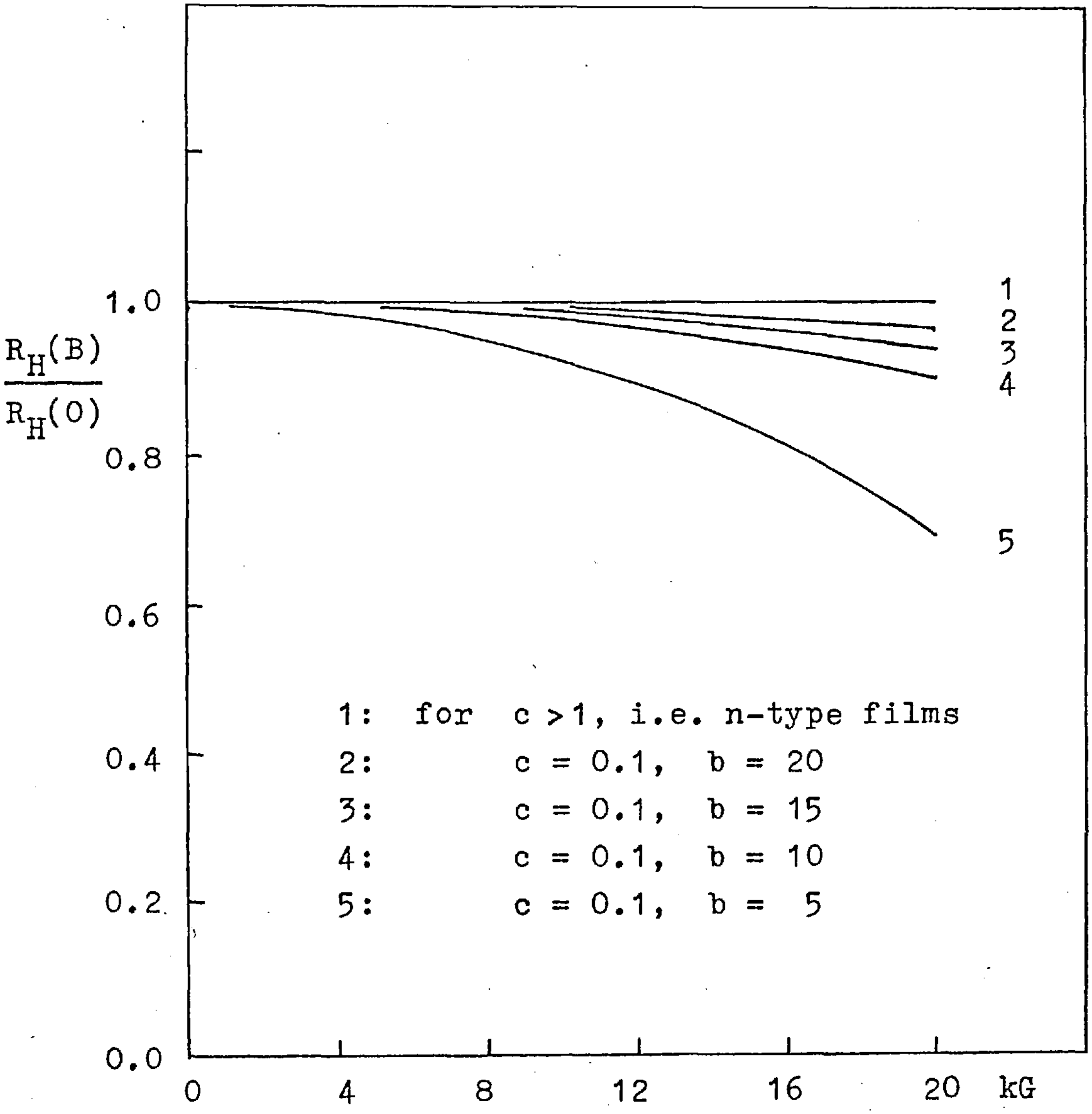

Fig 4.9: Theoretical variation of R_H with magnetic field

The presence of both holes and electrons has been shown to be responsible for the magnetic field dependence of R_H in n-type samples. Another explanation is also possible. This is due to the formation of a high-resistivity 'surface' layer, superposed on to a lower-resistivity 'bulk' layer. Wieder (W7) has considered the galvano-magnetic coefficients of such a two-layer structure, based on a theory by Hlasnik (H9) and obtained an expression for the Hall coefficient in a one-carrier system as follows:

$$R_H(\text{effective}) = R_{Hb} \frac{g^2 t/t_b}{(1 + g)^2 + (\mu_b B)^2} \qquad (4.39)$$

where

$R_{Hb} = \mu_b/\sigma_b$, is the 'bulk' Hall coefficient,
$g = \sigma_b t_b/\sigma_s t_s$, is the ratio of the 'bulk-like' sheet conductivity to the 'surface-like' sheet conductivity.
t_b, t_s are the thickness of the bulk and the surface layers, and
t is the total thickness of the film.

A similar expression can be obtained in the case of a two-carrier system. The effective Hall coefficient would thus be expected to fall with B. Experimental data of Wieder (W7) and Lile (L1) strongly support the two-layer model.

(2) <u>Hall mobility</u>

The product $R_H\sigma$ gives the Hall mobility where conduction is due to one species of carriers. This is true for $T < 200\ ^oK$ in n-type, and $T < 150\ ^oK$ in p-type films, as is evident from Fig 4.4 and 4.6. At 77 ^oK, when minority carriers are negligible, measurements show that the Hall mobility is practically independent of magnetic field, at least for B up to 10 kG[4].

At room temperature, electrons and holes for both n-type and p-type samples exist in comparable numbers. From Eqn (4.9), $R_H\sigma$ is expected to vary with B, in much the same manner as R_H, discussed previously. Fig 4.10 shows the variation for two n-type and two p-type samples. All p-type films exhibit a decrease of $R_H\sigma$ with B, the reduction being as high as 40% for sample pC11 over a field range of 20 kG. n-type samples, however, appear to show an anomalous behaviour. $R_H\sigma$ decreases first from $B = 0$, and starts to increase for $B > 2$ kG.

Eqn (4.9) is plotted graphically in Fig 4.11, using an electron mobility, $\mu_n = 3000$ cm^2/V sec. The decrease in $R_H\sigma$ (for $b = 10$) is seen to be less than that observed. This discrepancy could be removed if a higher electron mobility is used, which probably is justifiable, since the mobility within individual crystallites is probably higher than the measured mobility.

For the anomaly exhibited by the n-type films, no explanation will be offered here.

4.3.5 Magnetoresistance

(1) Magnetic-field dependence

Fig 4.12 shows the magnetoresistance, made on Corbino disks, as a function of B^2. The quadratic dependence is clearly well obeyed for B up to 20 kG.

---

[4] Measurements of p-type films was somewhat difficult because of the low hole mobility and consequently a high sample impedance. Correction for voltmeter loading was found to be necessary.

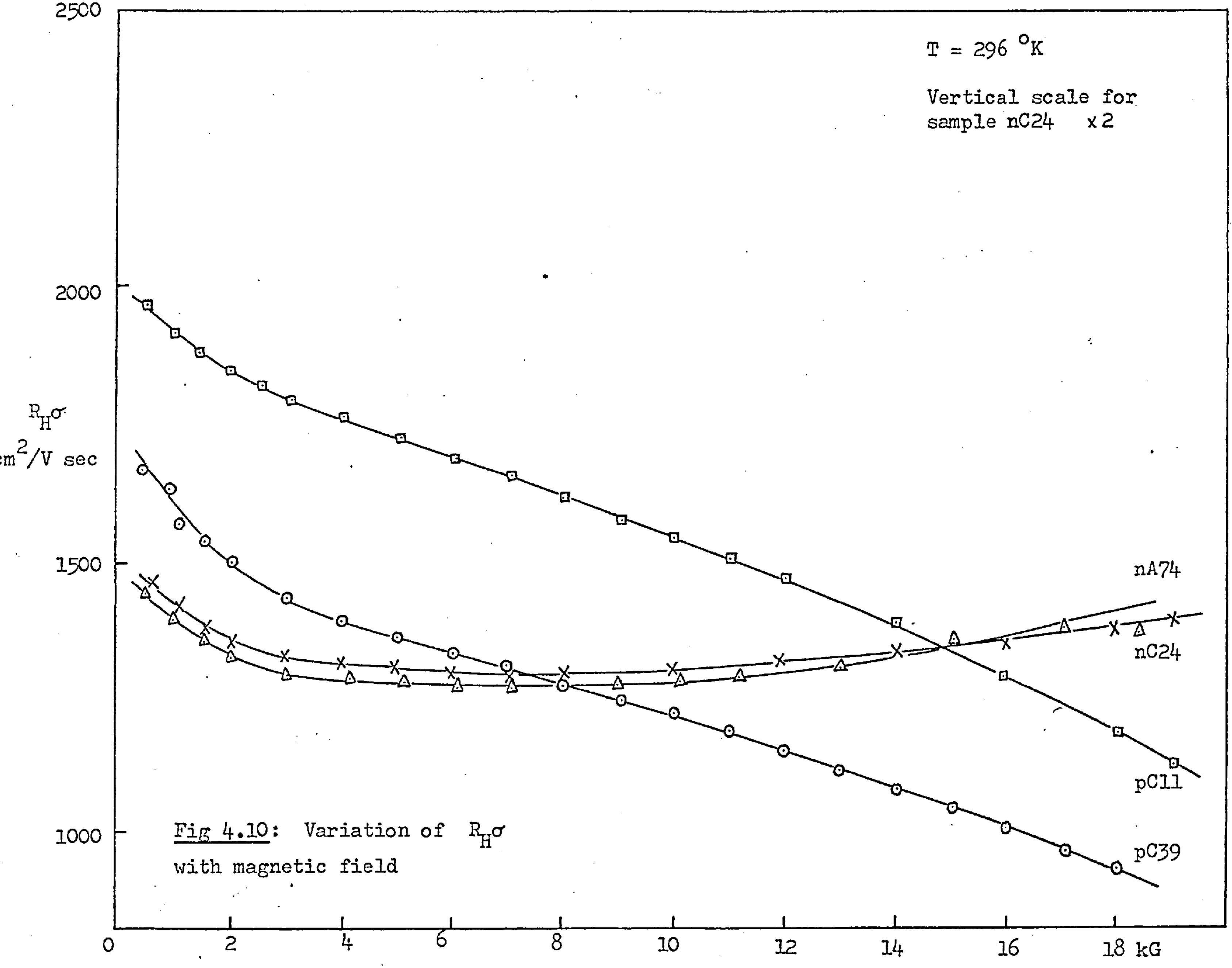

Fig 4.10: Variation of $R_H\sigma$ with magnetic field

$$'\mu' = R_H\sigma = \frac{(cb^2 - 1) + \mu_n^2B^2(c - 1)}{(cb + 1)b + \mu_n^2B^2(c + b)}\ \mu_n$$

$b = \mu_n/\mu_p$

$c = n/p$

$\mu_n = 3000\ \mathrm{cm}^2/\mathrm{V\ sec}$

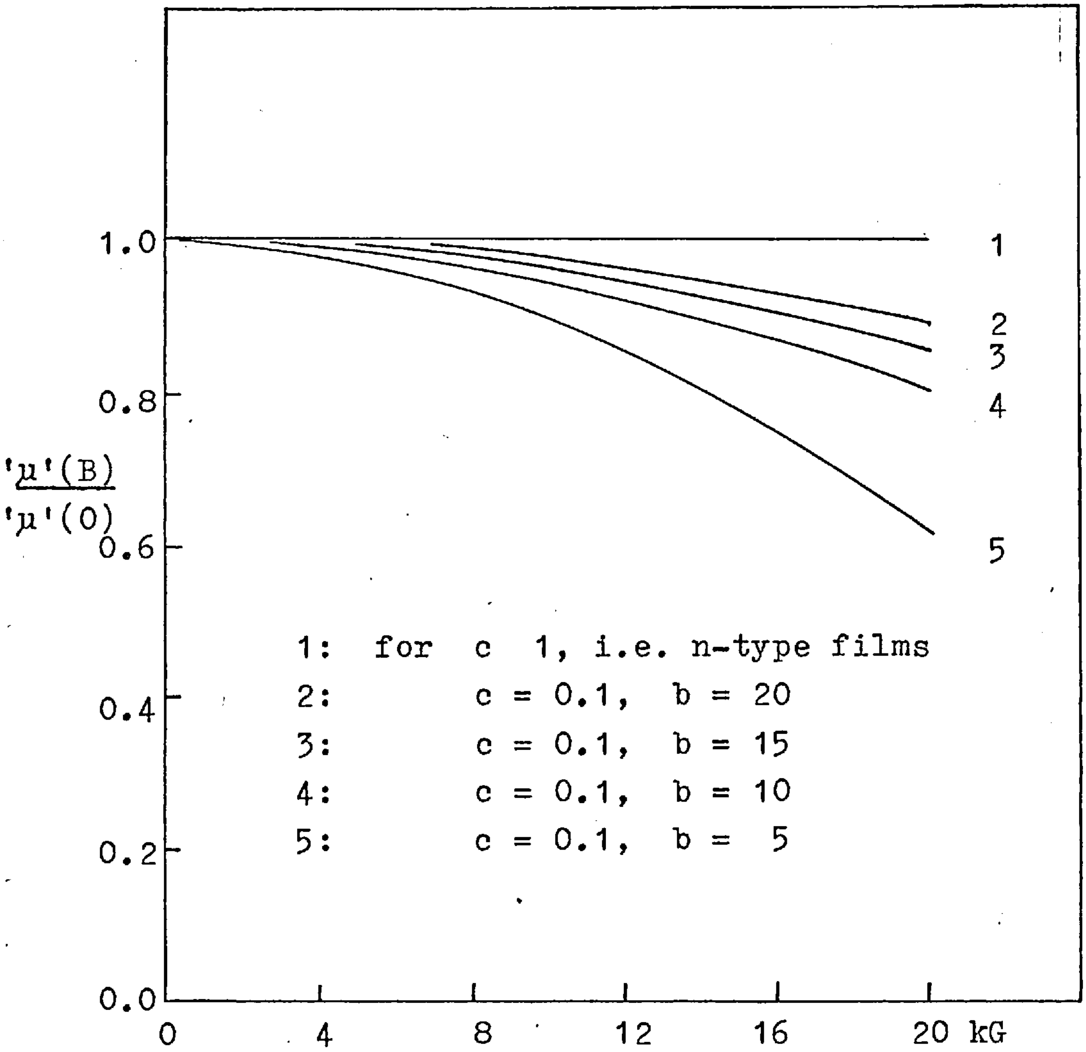

Fig 4.11: Theoretical variation of 'u' with magnetic field

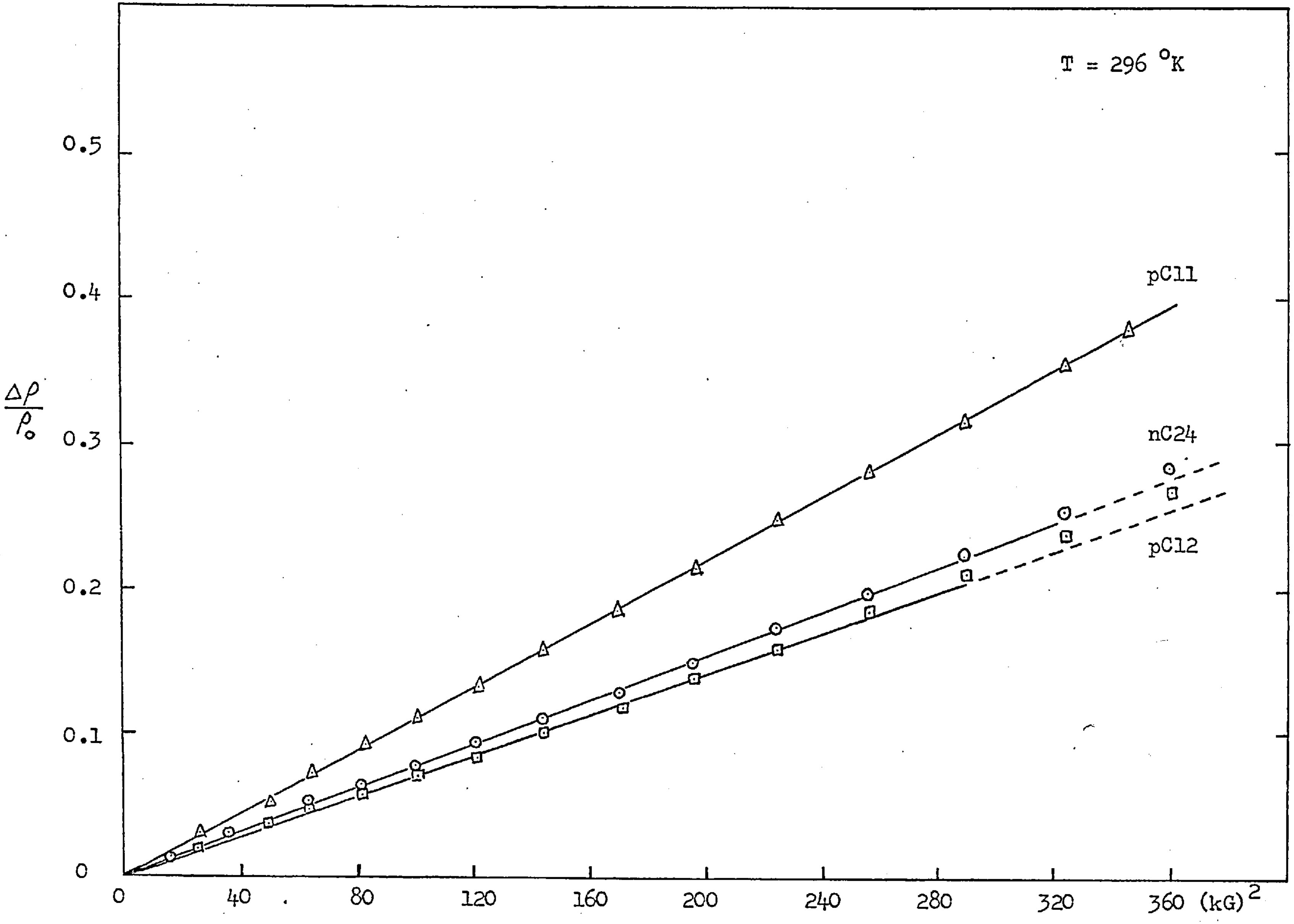

Fig 4.12: Variation of magnetoresistance with B^2

The theoretical treatment of the magnetoresistance effect is usually based on the assumption that the carrier densities deviate little from their thermal equilibrium values. Welker et al (W10) studied the contribution to magnetoresistance due to a deviation of carrier density from thermal equilibrium. In thin films, surface band bending causes carrier densities to vary across the thickness of the film. Lile (L1) considered the existence of diffusion forces due to carrier gradients and obtained an expression for the magnetoresistance of the form

$$A_o B + A_1 B^2$$

where A_o and A_1 are constants, which depend among other parameters, on the thickness of the film, carrier scattering time, diffusion length, and surface recombination velocities. He showed that the linear term in B has a maximum when

$$n(\mu_n)^{\frac{1}{2}} \sim p(\mu_p)^{\frac{1}{2}}$$

Taking $\mu_n/\mu_p = b \sim 10$, this occurs when $p \sim 3n$, a condition not encountered at room temperature in the present films. This might explain why the linear effect is not observed.

Lile found that the coefficients, A_o and A_1 could be made positive or negative by changing the magnetic field direction. This is due to the different recombination velocities at the two surfaces, the lower rate being associated with the substrate surface, since some of the dangling bonds are taken up by the substrate lattice, leading to a reduction in recombination sites. The theory of Wieder and Pikus (see L1) predicts a maximum surface contribution when the film thickness is comparable to the bulk diffusion length, $(D\tau)^{\frac{1}{2}}$, where the diffusion coefficient, $D = (2kT/e)\left[\mu_n\mu_p/(\mu_n + \mu_p)\right]$ and τ is the relaxation time. An estimate of the bulk diffusion length, using τ from Appendix C, shows that this parameter is much smaller than the present film thickness. This could account for the fact that no difference is observed for the magnetoresistance when B is applied in opposite directions; also, negative mangetoresistance is not present.

In n-type films, $n \gg p$ and Eqn (4.17) holds, i.e.

$$\Delta\rho/\rho_o B^2 = \mu_n^2$$

From Fig 4.11, the slope of $\Delta\rho/\rho_o B^2$ is $0.27/400$ $(\mathrm{kG})^{-2}$ for sample nC24. This gives

$$\mu_n = (0.27/400)^{\frac{1}{2}} \times 10^5 = 2600\ \mathrm{cm}^2/\mathrm{V\ sec},$$

which compares favourably with the value of $2860\ \mathrm{cm}^2/\mathrm{Vsec}$, obtained from Hall measurement (see Table 4.1).

For sample pC11, $\Delta\rho/\rho_o B^2 = 9.75\times10^6$ at $B = 20$ kG. Substituting this result into Eqn (4.19), and assuming $b = 8.8$ (see Table 4.2) and $c = n/p \sim 1.5\times10^{16}/6\times10^{16} \sim 0.25$, electron mobility was found to be $4000\ \mathrm{cm}^2/\mathrm{V\ sec}$, at room temperature. Hall measurements give $\mu_n \sim 4500\ \mathrm{cm}^2/\mathrm{V\ sec}$, but at the 'Hall minimum' temperature, which is some 20 - 30 ^{o}K higher. The agreement is again reasonable.

(2) <u>Temperature dependence</u>

Fig 4.13 shows the temperature dependence of the magnetoresistance of two samples for a constant magnetic field, $B = 8$ kG. $\Delta\rho/\rho_o$ is a function of μ and c ($= n/p$), whose total temperature variation is consequently reflected in the observed magnetoresistance.

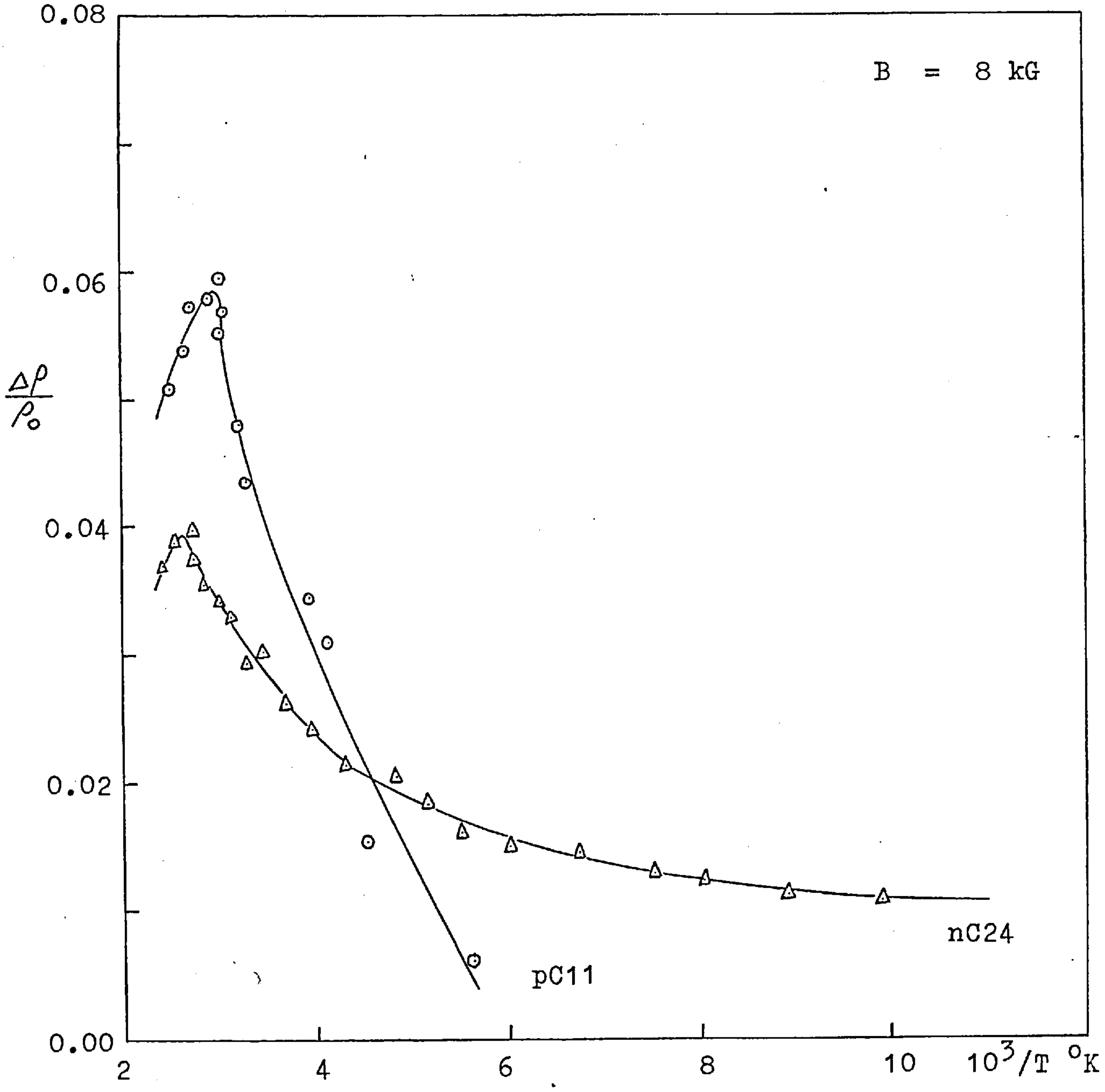

Fig 4.13: Temperature variation of magnetoresistance

In Eqn (4.19), the second term, involving $(\mu_n B)^2$ is much smaller compared to the first, both in the numerator and in the denominator. It can therefore be approximated to

$$\Delta\rho/\rho_o \sim \left[\frac{\mu_n}{b}\right]^2 \frac{1 + cb^3}{1 + cb}$$

Considering $c = n/p \gg 1$, i.e. n-type films,

$$\Delta\rho/\rho_o \sim \mu_n^2 \left[1 - 1/bc + (1 - 1/b^2)/(bc)^2 - \ldots\right]$$

$$\sim \mu_n^2 \left[1 - 0.1/c + 0.01/c^2 - 0.001/c^3 + \ldots\right] \tag{4.40}$$

And for $c = n/p \ll 1$, i.e. p-type films at low temperature,

$$\Delta\rho/\rho_o \sim \mu_p^2 \left[1 + 10^3 c - 10^4 c^2 + \ldots\right] \tag{4.41}$$

where $b = 10$ has been assumed.

The T-dependence of c can be found from the following equations[4]:

$$n = p + N_d - N_a \quad ;$$

$$np = n_i^2 = AT^3 \exp(-E_g/kT)$$

where A is a constant. The above equations give

$$c = 1 + 2\left[1 + \left\{1 + 4(n_i/N_d - N_a)^2\right\}^{\frac{1}{2}}\right]^{-1}$$

Since $n_i/N_d - N_a$ is of the order of 0.1 at room temperature and decreases rapidly with diminishing T, c consequently

---

[4] Again, to be considered only approximate, since they are valid for non-degenerate statistics and parabolic bands.

is not very temperature sensitive; so that $\Delta\rho/\rho_0$ would vary as μ_n^2, i.e. $\exp(-2e\phi_0/kT)$ approximately. p-type films are also expected to behave in the same manner near room temperature, since the conduction is electron-dominated, though at lower T, the exponential fall of $\Delta\rho/\rho_0$ with $1/T$ is clearly absent. This is because the origin of the exponential dependence is associated with the grain boundary potential, which is a barrier to electron conduction but not to hole conduction. The magnetoresistance 'peak' is a further indication of the temperature dependence of $\Delta\rho/\rho_0$ through μ_n.

(3) The electric-field dependence

In n-type films, $\Delta\rho/\rho_0$ gives a measure of the electron mobility through Eqn (4.17). By making the spacing between the two electrodes of the Corbino disk small, it is possible to make measurements of $\Delta\rho/\rho_0$ and therefore μ_n up to high electric fields. This is a useful method of measuring the electric field dependence of the electron mobility. In thin films, high field measurements on the usual 'bridge-shaped' sample proves difficult because of problems of impedance matching.

Fig 4.14 shows $\Delta\rho/\rho_0$ as a function of electric field, $\mathcal{E}$. Both dc field and short voltage pulses of 10 nsec duration were employed. The details of the pulse measurement are given in Chapter Six. For the dc field, $\Delta\rho/\rho_0$ increases rapidly when $\mathcal{E} \sim 10^2$ V/cm. This is due to Joule heating and the resulting generation of comparable numbers of electrons and holes. In the pulse case, the increase is observed in the vicinity of $\mathcal{E} \sim 10^4$ V/cm. This corresponds to the breakdown field of InSb thin films, when avalanche generation of carriers sets in. Heating can be eliminated here, since the pulses are short. It

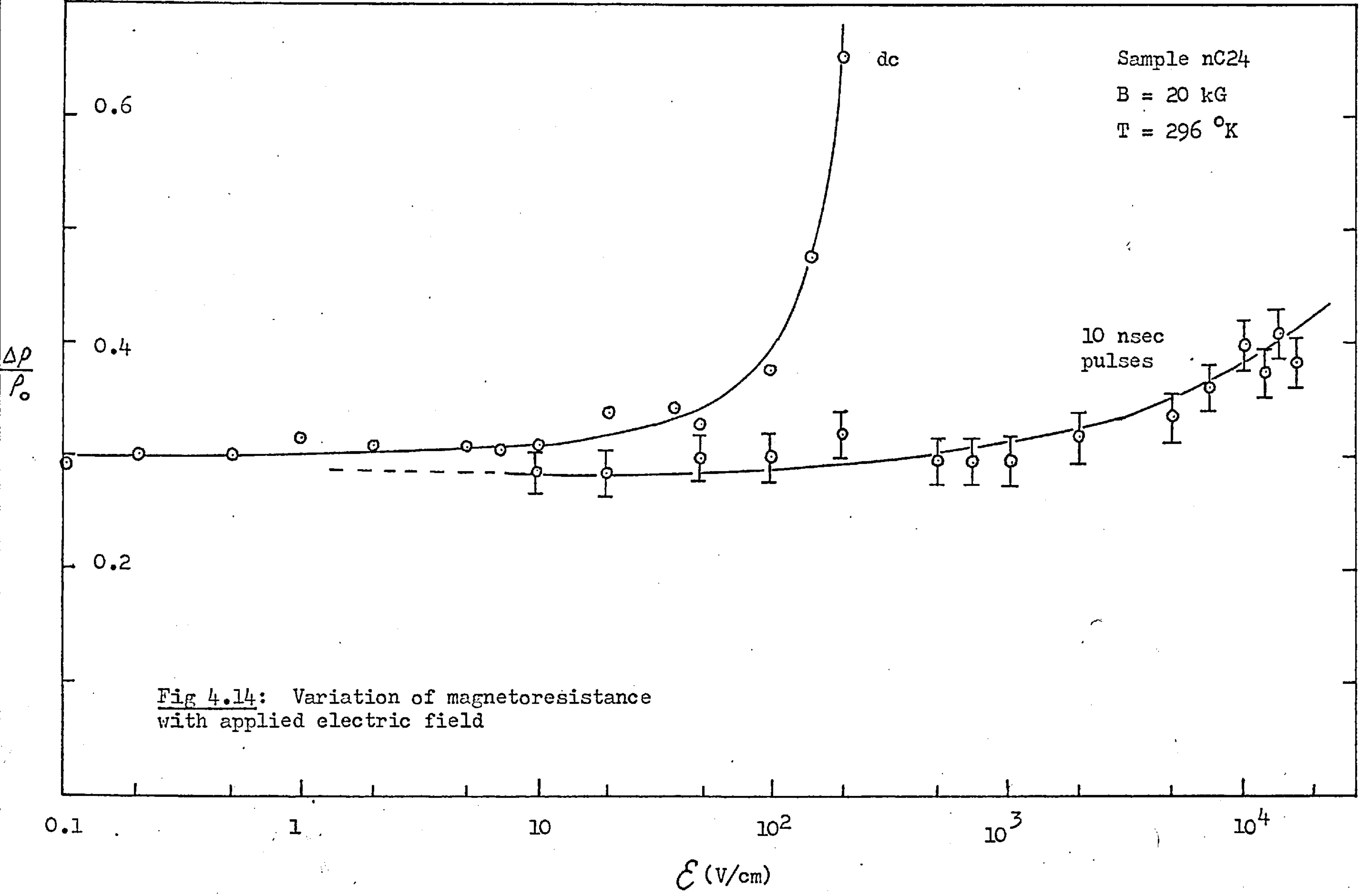

Fig 4.14: Variation of magnetoresistance with applied electric field

may therefore be assumed that the electron mobility is relatively independent of $\mathcal{E}$ up to about 10^4 V/cm.

CHAPTER FIVE: DC Field-Effect Measurements

5.1 Introduction

In Chapter Four, the mechanisms limiting electron mobility were discussed. While the physical grain boundaries are responsible to a large extent for reducing the mobility by limiting the electron mean free path to approximately half the mean crystallite size, the potential barrier associated with the boundaries is believed to be responsible for the exponential temperature variation. The exponential temperature dependence could be due to all kinds of scattering centres, and not necessarily due to the grain boundary potential alone. However, it will be shown that it is possible to modulate this potential by a constant gate field applied through the mica substrated. This is a dc field effect.

Electron mobility studies in metal gate-insulator-semiconductor structures have been made in CdS films by Waxman et al (W9) and in CdSe films by van Heek (H10). In both cases an increase in Hall mobility with gate voltage has been observed, contrary to the surface scattering theory of Schrieffer (S2). The observed increase has been attributed to inhomogeneity in these polycrystalline films. A model based on low-resistivity crystallites and high-resistivity crystallite barriers, was first proposed by Petritz (P9) to explain the photoconductivity in lead salt films.

It must be pointed out that CdS and CdSe films have accumulation surfaces and a positive gate field would merely bring the surface into greater accumulation. According to the theory of Schrieffer, surface scattering becomes significant only when electrons are strongly attracted to the surface. In InSb films, the surfaces are in depletion; and therefore scattering is not important. This has also been considered in Chapter Four. Consequently, any variation in carrier mobility as a result of a gate field may be attributed to grain boundary potential modulation.

In this chapter, low-field transport of carriers across grain boundaries in polycrystalline films will be examined. DC field-effect experiments are used to elucidate the effect of the potential barrier on the conduction process, while the already established theory of rectification of diodes and p-n junctions is modified to provide the theoretical background.

5.2 Grain boundary states

Consider a dislocation to be a negatively charged line, surrounded by a cylinder of positive space charge. Assume uniform charge density within the cylinder, equal to the ionised impurity concentration, N, and neglect free holes and electrons (their numbers being small compared with N). Under this assumption, the solution of Poisson's equation, $\underline{\nabla}.\underline{\mathcal{E}} = \rho/\epsilon = Ne/\epsilon$, leads to (M7)

$$\phi = \epsilon\,\mathcal{E}^2/2Ne \tag{5.1}$$

where $\mathcal{E}$ is the electric field at the top of the barrier, and ϕ is the barrier potential. The potential difference across the barrier from region 1 to region 2, with reference to Fig 5.1, when a voltage, V, is applied across the barrier, is

$$\phi_1 - \phi_2 = V = \epsilon(\mathcal{E}_1^2 - \mathcal{E}_2^2)/2Ne \tag{5.2}$$

The surface charge (per unit area of grain boundary surface)

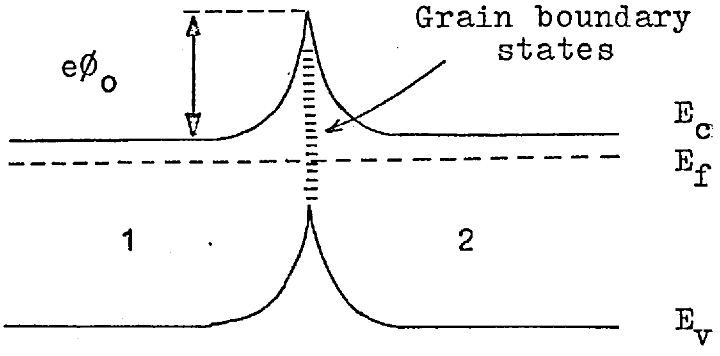

(a) No bias

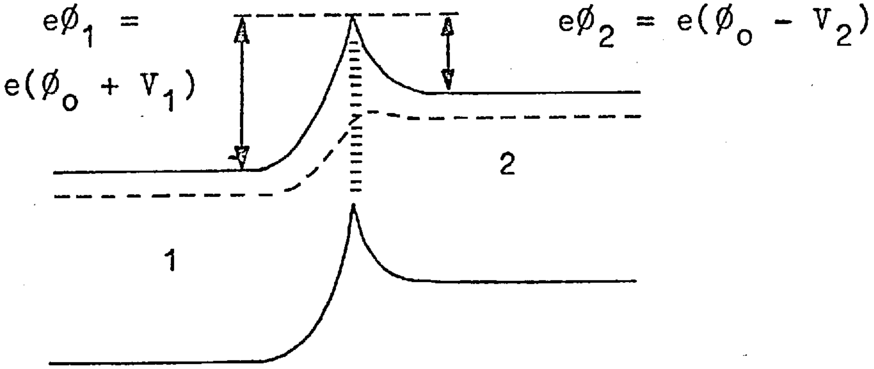

(b) With bias, V

Fig 5.1: Grain boundary potential barrier on the boundary states, q, can be obtained from Gauss Law, and is given by

$$q = \epsilon(\mathcal{E}_2 - \mathcal{E}_1) \tag{5.3}$$

In equilibrium, i.e. when $V = 0$,

$$\emptyset_1 = \emptyset_2 = \emptyset_o ;$$
$$\mathcal{E}_1 = -\mathcal{E}_2 = \mathcal{E}_0 = -q_o/2 \tag{5.4}$$

From Eqns (5.2) and (5.3)

$$\mathcal{E}_1 = -q/2 - eNV/q ;$$
$$\mathcal{E}_2 = q/2 - eNV/q \tag{5.5}$$

Substituting in Eqn (5.1),

$$\emptyset_1 = (\epsilon/2Ne)\left[q/2 + NeV/q\right]^2 ;$$
$$\emptyset_2 = (\epsilon/2Ne)\left[q/2 - NeV/q\right]^2 \tag{5.6}$$

$\mathcal{E}_2$ and $\emptyset_2$ reduce to zero if V reaches the critical value,

$$V_c = (1/2\epsilon Ne)q^2 \tag{5.7}$$

If q remains equal to q_o, then from Eqn (5.4),

$$V_c = 4\emptyset_o \tag{5.8}$$

Now

$$\emptyset_1 = \emptyset_o + V_1 ;$$
$$\emptyset_2 = \emptyset_o - V_2$$

where $V_1 + V_2 = V$. The applied voltage, V, contributes mainly to V_1, V_2 being much smaller than V_1 normally. $\emptyset_2$ is therefore practically constant for small applied voltages. Putting $\phi_2 = \phi_o$ or $\mathcal{E}_2 = -\mathcal{E}_o$ in Eqn (5.5), gives

$$q_o/2 = q/2\epsilon + 2\ NeV/q$$

i.e.

$$q = (q_o/2)\left[1 + (1 + V/\phi_o)^{\frac{1}{2}}\right] \qquad (5.9)$$

Eqn (5.9) shows that the surface charge at the boundary states actually increases with the applied field.

5.3 Grain boundary theory

The theory of activation of carriers over the potential barrier, such as existing across crystal rectifiers, metal-semiconductor diodes and p-n junctions, rests on two different assumptions:

(1) The diode theory

The underlying principle of the diode theory assumes a barrier width small compared with the carrier mean free path, so that carrier collisions within the barrier region can be neglected. More accurately, the mean free path should be compared with the distance within which the potential energy changes by kT near the top of the barrier width (H6, T3). Under the above assumption, the diode current is given by (W9, H10)

$$j = \tfrac{1}{4}ne\langle c\rangle\ \exp(-e\phi_o/kT)\left[\exp(eV/kT) - 1\right] \qquad (5.10)$$

where

n is the number of carriers,
$\langle c\rangle$ is the mean thermal velocity,
ϕ_o is the barrier height in the absence of an external field, and
V is the applied voltage.

Eqn (5.10) shows the forward current (for positive V's) to increase exponentially with applied voltage, whilst the reverse current (for negative V's) rapidly saturates to a constant value.

(2) The diffusion theory

Alternatively, the barrier thickness can be assumed to be large compared with the mean free path, so that numerous collisions take place within the barrier region. This leads to a more general formulation which includes contribution to the current due to both the local field as well as the local concentration gradient. The current can be obtained from solving the equation:

$$\begin{aligned} j &= en(x)\mu\mathcal{E} + D\frac{dn}{dx} \\ &= eD\left[-\frac{en(x)}{kT}\frac{d\emptyset(x)}{dx} + \frac{dn}{dx}\right] \qquad (5.11) \end{aligned}$$

where use has been made of the relations, $\mathcal{E} = -d\emptyset(x)/dx$ and $D = \mu kT/e$.

Assuming constant mobility, μ, and hence a constant diffusion constant, D^{4}, independent of the field, $\mathcal{E}$, Eqn (5.11) can be put into the integrable form, thus

$$j \exp\left(-\frac{e\emptyset(x)}{kT}\right) = eD\frac{d}{dx}\left[n(x)\exp\left(-\frac{e\emptyset(x)}{kT}\right)\right] \qquad (5.12)$$

To integrate Eqn (5.12), it is necessary to know the exact

---

[4] This assumption may not apply, since in high electric fields, μ is a function of $\mathcal{E}$; and, the local field, $\mathcal{E} = -d\emptyset/dx$, could exceed the critical field, above which carrier mobility is seriously affected. Moreover, parameters governing diffusion at the top of the barrier are not identical with those at the bottom, since the effective mass of the carriers may be different.

profile of $\phi(x)$, which in principle can be found by solving a Poisson's equation (S10), but is usually complicated. However, $\phi(x)$ has often been approximated to Mott and Schottky barriers (H6), though the simpler triangular barrier is also used (E1). All the three approximations give solutions that are basically the same as given in Eqn (5.10).

In polycrystalline films, the diode theory is usually assumed to apply (W9, H10, C1, C2). Unlike metal-semiconductor diodes, crystallite boundaries have symmetrical potential barriers and therefore behave like two diodes, mounted back to back. For this reason, Eqn (5.10) must be modified to give the symmetrical expression:

$$j = \tfrac{1}{4} n e \langle c \rangle \exp\left(-\frac{e\phi_o}{kT}\right)\left[\exp\left(+\frac{eV_2}{kT}\right) - \exp\left(-\frac{eV_1}{kT}\right)\right] \tag{5.13}$$

where

ϕ_o is the potential barrier in the absence of an external field, and

$V = V_1 + V_2$, is the voltage drop across one barrier (see Fig 5.1).

At this point, it would be appropriate to consider the applicablility of the equations, introduced so far, to the present study. Eqn (5.10) was derived under the assumption of a non-degenerate electron population, i.e. using Boltzmann statistics, which is strictly not valid for InSb. On the other hand, the use of degenerate statistics (Fermi-Dirac) is highly doubtful in the barrier region. Carrier trapping at dislocation dangling bonds (which are acceptors), in the grain boundaries, does not obey Fermi-Dirac statistics, since the number of charges trapped is limited by Coulomb interaction (M7). It is well established that the stress and strain around a dislocation site introduce distortions into the energy band, so that the band edge can not be known with certainty. If $(e\phi_o - E_f)/kT$ is greater than 2 or 3, then the conduction band edge within the barrier would be sufficiently remote from the Fermi level for the Boltzmann statistics to hold approximately. That high potential barriers are actually present, is probably a reasonable assumption and in fact, the diode theory is essentially one of high barriers (H6).

5.3.1 Application to InSb films

For low-field conduction, i.e. for $eV/kT \ll 1$, Eqn (5.13) approximates to

$$j = \tfrac{1}{4} ne\langle c\rangle (2eV/kT) \exp(-e\phi_o/kT) \qquad (5.14)$$

If there are N_1 crystallites in a length L_1, then the applied field, $\mathcal{E}$, is related to the barrier voltage by $\mathcal{E} = 2VN_1/L_1$. Substituting for V in Eqn (5.14) leads to

$$j = ne\mu\mathcal{E} \qquad (5.15)^4$$

where the effective mobility is given by

$$\mu = \mu_o \exp(-e\phi_o/kT) \qquad (5.16)$$

and $\mu_o = e\langle c\rangle L_1/N_1 kT$.

Consider a 2000 A° film. The mean crystallite size is just L_1/N_1 and is taken to equal the film thickness.

---

[4] Alternatively, it may be considered that only $n \exp(-e\phi_o/kT)$ carriers take part in the conduction, but with the diminished mobility, μ_o.

From Appendix C, the mean thermal velocity can be obtained, from which

$$\mu_o(300\ ^oK) \sim 1.84\times10^4\ cm^2/V\ sec$$

$$\mu_o(\ 77\ ^oK) \sim 3.62\times10^4\ cm^2/V\ sec$$

Taking $e\phi_o$ to be 0.04 eV,

$$\mu(300\ ^oK) \sim 1.84\times10^4\ \exp\ (-1.55) = 3860\ cm^2/V\ sec;$$

$$\mu(\ 77\ ^oK) \sim 3.62\times10^4\ \exp\ (-6.02) = 90\ cm^2/V\ sec.$$

These are typical mobilities observed at the two temperatures, although, in the calculation, there is no a priori justification for taking ϕ_o to be temperature independent. Physically, ϕ_o arises as a result of carrier trapping in the crystallite boundary. This produces a difference in the carrier densities, leading to a diffusion potential, which can be expressed as

$$e\phi_o = kT \log\ (n_1/n_2) \qquad (5.17)$$

where n_1 and n_2 are the carrier densities in the bulk and in the barrier, respectively. It must be pointed out that Eqn (5.17) is also derived under conditions of non-degeneracy.

The exponential temperature dependence, as expressed in Eqn (5.16), can alternatively be arrived at without resorting to assumptions, from an a posteriori argument provided by Hall measurements (Chapter Four).

5.3.2 The field effect

Consider now the application of a field, orthogonal to the film surface, from a gate electrode. A positive gate voltage, $+V_g$, induces a number, Δn, of carriers per unit area in the film, assumed to be equal in the crystallites as well as in the grain boundaries. This assumption would be reasonable, if the gate insulator is of uniform thickness, i.e. the gate electrode and the insulator form a uniform, parallel-plate capacitor, and furthermore, if an equipotential film surface is assumed[4]. The new diffusion potential can now be written as

$$\phi(V_g) = \phi_o + \Delta\phi = kT \log \left(\frac{n_1 + \Delta n/L_c}{n_2 + \Delta n/L_c} \right) \qquad (5.18)$$

where it is assumed that the induced charge penetrates a distance, L_c, into the semiconductor, L_c being the mean space-charge depth, as defined by Many et al (M4). It can be seen that $\phi(V_g)$ decreases, because the change (decrease) in E_c-E_f is smaller in the crystallites for a given change in n, than the corresponding change in the barrier region. Eqns (5.17) and (5.18) then yield

$$e\,\Delta\phi = kT \log \left(\frac{1 + \Delta n/n_1 L_c}{1 + \Delta n/n_2 L_c} \right) \qquad (5.19)$$

Expressing Δn in terms of V_g, Eqn (5.19) becomes

$$e\,\Delta\phi = kT \log \left(\frac{1 + \beta_1 V_g}{1 + \beta_2 V_g} \right) \qquad (5.20)$$

where $\beta_{1,2} = \theta_{1,2} C_g / e L_c n_{1,2}$. C_g is the capacitance of the gate insulator per unit area, and θ is the fraction of the total charge induced that is not trapped in the

---

[4] It must be appreciated that at sites along the grain boundaries, where the dislocation lines intersect the surface, there is a reduction in potential. However, this is of no significance, since the drop in potential is very much smaller than the applied gate voltage.

insulator and in the surface states. In the grain boundaries, the dangling bonds are additional trapping centres, since a decrease in ϕ, leads to an increase in the 'filling factor', according to $q = (q_0/2)\left[1 + (1 + V/\phi)^{\frac{1}{2}}\right]$, Eqn (5.9). Using Eqns (5.16) and (5.20), the effective mobility in the presence of a gate voltage can be written as

$$\begin{aligned} \mu(V_g) &= \mu_o \exp(-e\phi/kT) \\ &= \mu_o \exp(-e\phi_o/kT)\, G(V_g) \end{aligned} \qquad (5.21)$$

where

$$\begin{aligned} G(V_g) = {} & 1 + (\beta_2 - \beta_1)V_g - \beta_1(\beta_2 - \beta_1)V_g^2 \\ & + \beta_1^2(\beta_2 - \beta_1)V_g^3 - \dots \end{aligned} \qquad (5.22)$$

In this way, the effect of a gate voltage on the mobility can be represented as a multiplying factor, which is a polynomial in V_g.

To gain an idea of the relative magnitude of the coefficients in Eqn (5.22), the following typical values for the various parameters are used:

$C_g = 3.1\times10^{-10}$ F/cm^2, for a 40 µm thick mica,
$L_c = 500$ A^o,
$n_1 = 2\times10^{17}$ cm^{-3},
$n_2 = 2\times10^{16}$ cm^{-3} (taking $e\phi_o = 0.04$ eV).

From these figures,

$$\beta_1 \sim 10^{-2}\,\theta_1; \qquad \beta_2 \sim 10^{-1}\,\theta_2$$

Assuming equal trapping in both crystallites and barriers, i.e. $\theta_1 = \theta_2$, the following values are obtained:

Table 5.1

$\theta_{1,2}$	$(\beta_2 - \beta_1)$	$\beta_1(\beta_2 - \beta_1)$	$\beta_1^2(\beta_2 - \beta_1)$
10^{-2}	10^{-3}	10^{-7}	10^{-11}
5×10^{-2}	5×10^{-3}	2.5×10^{-6}	1.2×10^{-9}
10^{-1}	10^{-2}	10^{-5}	10^{-8}

The coefficients of the cubic and subsequent terms are seen to be much smaller than that of the quadratic term. Hence, for practical gate voltages, it is sufficient to take the expansion up to the third term.

5.4 Experimental details

Waxman et al and van Heek used a vacuum-deposited layer of SiO or CaF_2 to insulate the semiconductor from the metal gate. The thickness of the insulator could be made as small as 500 A°, so that only a low gate voltage is required. But this technique imposes a restriction on the size of the Hall sample, since it is difficult to eliminate 'pin-holes' from the insulator film and subsequent shorting out of the semiconductor and the gate. The present field-effect samples were prepared by first cleaving the mica substrate down to about 20 µm thick, followed by a deposition of a layer of Al to form the gate, on the opposite side of the substrate to that on which the InSb Hall sample was previously deposited. The mica substrate, therefore, also served as the gate insulator.

In view of the thickness of the mica substrate-insulator, a high voltage, provided by a Fluke 415B was employed. The voltage supply was capable of giving a maximum voltage of ±3 kV. The maximum gate voltage that could be applied is limited by the breakdown field strength of mica, which is around 10^6 V/cm. For a mica thickness of 20 µm, this implies a maximum gate voltage of 2 kV. If a surface trap density of 10^{12} cm^{-2} can be assumed, then the minimum gate voltage needed to produce any observable change in the Hall measurement would be ~0.25 kV.

The Hall measurements were carried out at room and liquid nitrogen temperatures, in the presence of a constant magnetic field of 2 kG and a variable gate voltage. All the Hall samples were n-type; measurements of p-type samples were not possible in the present study, because of the very high impedance of these samples at 77 °K. Because of trapping of induced carriers at slow surface states, all measurements were made after the gate voltage was applied for about 30 mins, when the slow states were almost completely filled.

5.5 Results

5.5.1 The decay pattern

Fig 5.2 shows a typical decay pattern of sample conductivity with time for various gate voltages. An application of a positive gate voltage induces electrons in an n-type sample, increasing the electron density. At the same time, the potential barrier is lowered and this leads to an increase in the electron mobility. But the increased conductivity does not remain constant with time, because of electron trapping, both at surface states and in the insulator.

Earlier, it has been assumed, as did Waxman et al, that the trapping factor is the same both in the crystallites and in the barriers. However, there is the serious objection

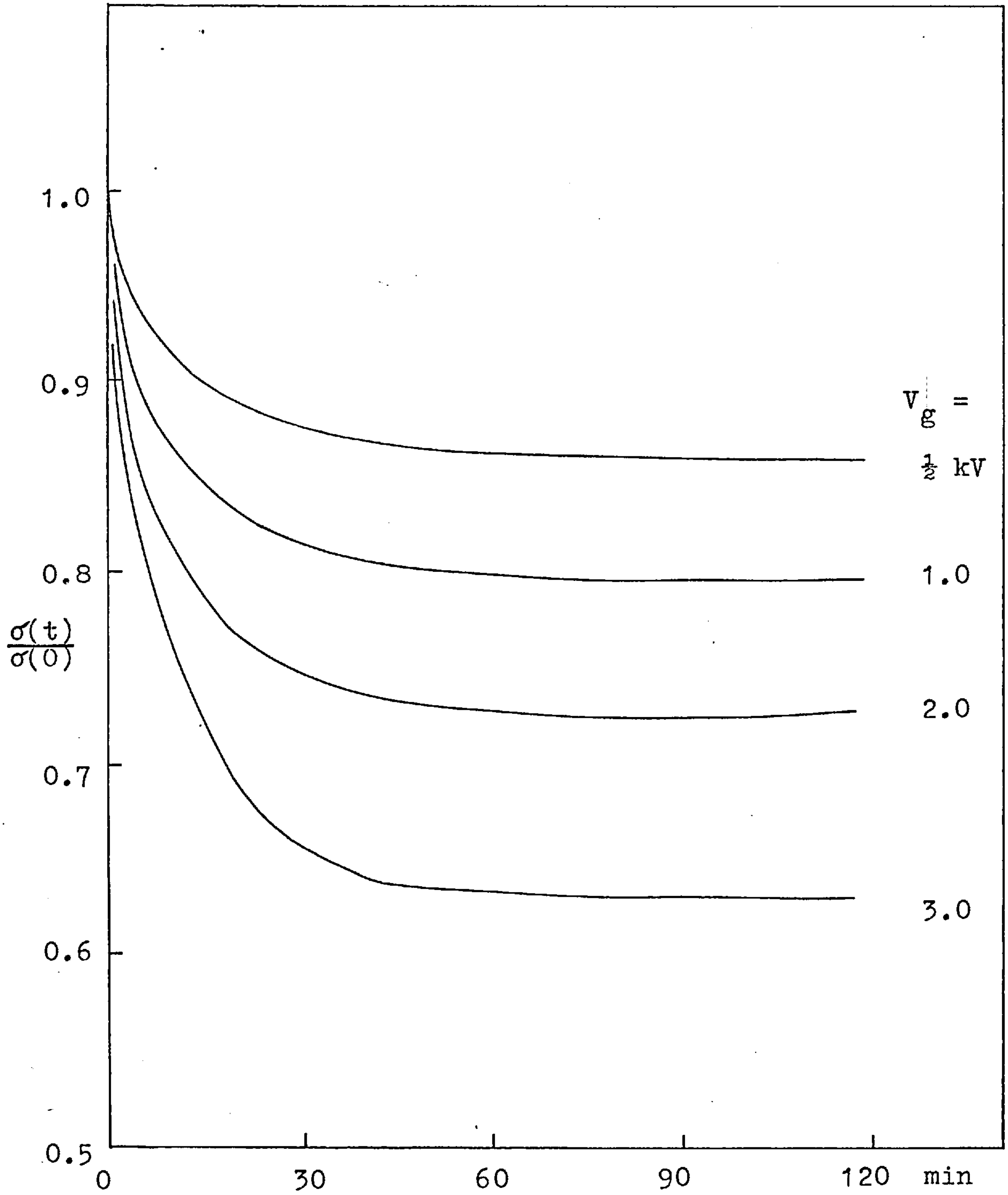

Fig 5.2: Decay Pattern of normalized conductivity with time for different gate voltages

to this assumption, as van Heek pointed out, that it would imply a fewer number of traps in the band gap (per unit energy-interval) in the barrier region than in the crystallites, since, initially, the conduction band-edge is nearer to the Fermi level in the crystallites than in the barriers. On the contrary, van Heek ignored trapping altogether in the crystallites and considered trapping to be important only in the barriers. This he justified by demonstrating the relative temperature independence of V_{g0}, the gate voltage at which all the induced charges go into traps.

van Heek's argument can be accomodated by the grain boundary dislocation model, since a gate voltage produces a lowering in the barrier potential and therefore an increased trapping at dangling bonds (see Eqn (5.9)). But the very slow decay time, of the order of several hours, casts doubt on this theory. Dangling bonds are located within the semiconductor and the associated trapping states and therefore in intimate communication with the charge carriers. Hence, the trapping process is expected to involve a short trapping time, which is particularly so in the case of a low band-gap semiconductor.

Slow states lying within the insulator might perhaps be responsible for the slow decay. Sewell (S11) found that the decay does not follow any simple exponential law. He introduced a decay time, τ^*, which is defined as the time taken for the conductivity to fall by 90% of its initial value and found that it fits an empirical equation of the form

$$\tau^* = \nu_0 \exp (E_t/kT) \tag{5.23}$$

where ν_0 is some time constant, and E_t is a trap energy, which he found to be $\sim 5\times10^{-3}$ eV. He obtained evidence to suggest that electrons from the semiconductor enter the insulator by some kind of 'tunneling' or 'hopping' mechanism.

More will be said of the slow surface trapping in Chapter Seven.

5.5.2 The barrier potential

Fig 5.3 is a plot of Hall mobility against 1/T for different gate voltages (only 3 values of V_g are shown) for sample nF20.3. The sample is 2100 A^o thick, having $\mu(V_g = 0) = 2530$ cm^2/V sec and $n(V_g = 0) = 5\times10^{16}$ cm^{-3}, at 296 ^oK. The exponential temperature variation for $T > 200$ ^oK, typical of polycrystalline films, is a strong evidence supporting the barrier model. From the linear portions of $\mu(1/T)$ curves, the barrier potential, $\emptyset$, is deduced, using Eqn (5.16). The variation of $\emptyset$ with $\mathcal{E}_g$ (gate field across mica = gate voltage/mica thickness), is also shown in the figure. For a positive gate field of 7.5×10^5 V/cm, the barrier potential decreases by $\sim$12% from its zero gate field value of $\sim$0.04 eV. However, for negative gate fields, $\emptyset$ shows a slight increase.

If Eqn (5.17) is assumed to apply to holes as well, then a negative gate field should also bring about a lowering of $\emptyset$, which has not been observed. For InSb, it has been shown by Lile (L6) and will also be demonstrated in Chapter Seven, that, even in the absence of an applied gate field, the surface is naturally depleted by the action of surface states to the point where the surface is quasi-intrinsic, with the Fermi level approximately two-thirds down the band gap. A positive gate voltage

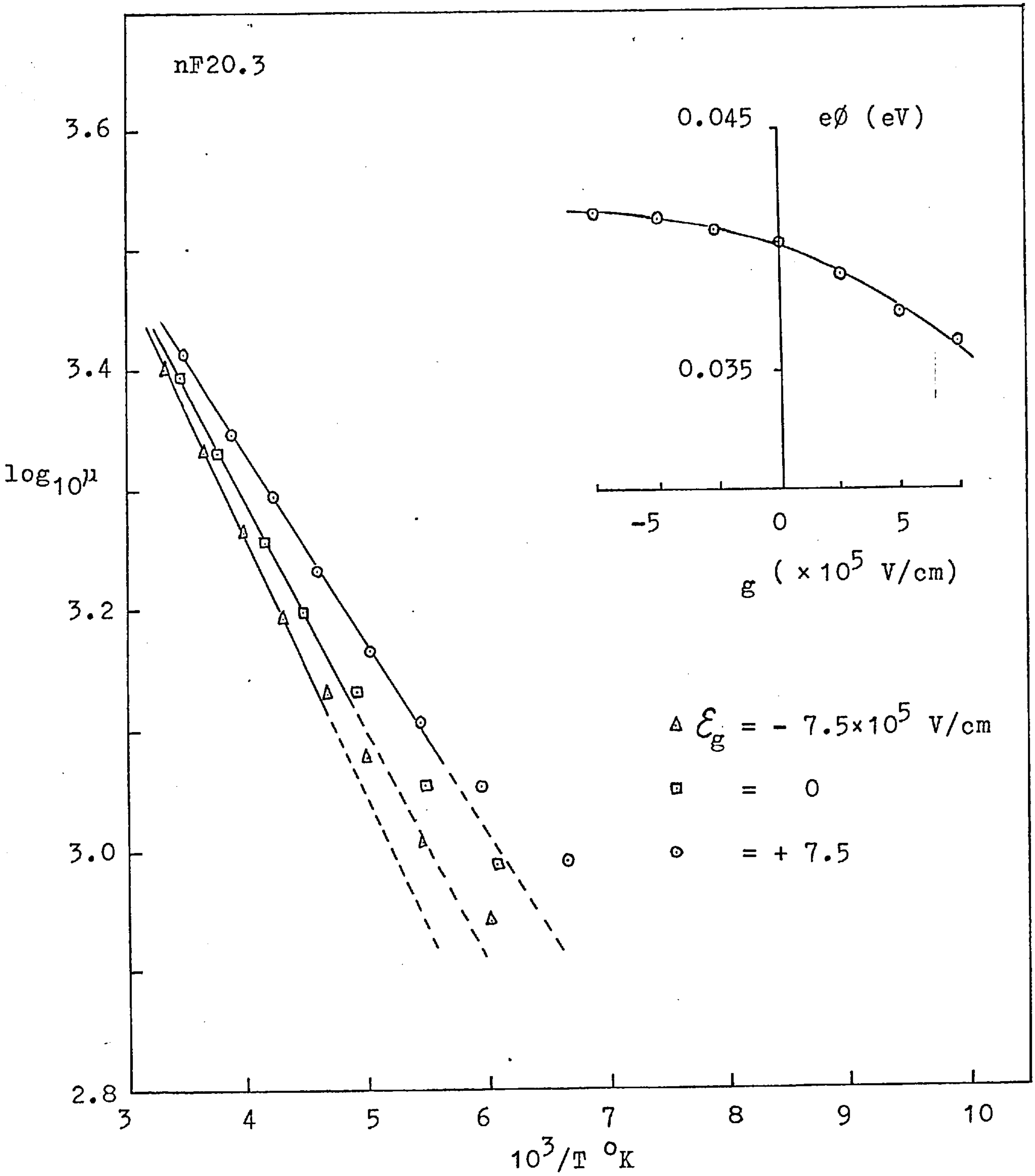
nF20.3
$\log_{10}\mu$
3.6
3.4
3.2
3.0
2.8
3
4
5
6
7
8
9
10
$10^3/T$ °K
0.045
0.035
eØ (eV)
−5
0
5
g (× 10^5 V/cm)
△ $\mathcal{E}_g$ = − 7.5×10^5 V/cm
⊡ = 0
⊙ = + 7.5

Fig 5.3

reduces the surface band bending[1], thereby extending the space charge deeper into the 'bulk' (M4), i.e. resulting in an increase in the space charge penetration depth, L_c. A negative gate voltage depletes the surface even further, drastically reducing L_c, so that any modulation effect due to holes would be confined to avery thin layer near the surface, the bulk conduction being still due to electrons. The negligible hole contribution to conduction could therefore account for the relative independence of ϕ on negative V_g.

The deviation from linearity for $T < 200$ °K, might indicate that the barriers are now no longer the dominating mechanism in determining the effective mobility. In bulk InSb, polar optical scattering dominates from high temperatures down to 200 °K (M1), and this would cause mobility to increase with $1/T$. But the main scattering mechanism at temperatures in the vicinity of 100 °K is by ionised impurities (F5), for which mobility varies as $T^{3/2}$ and would actually decrease with the increase in $1/T$. It seems unlikely, therefore, that the deviations observed can be accounted for in these terms.

An alternative explanation is possible. In InSb, the donor ionisation energy is not detectable over the temperature range investigated. It cannot, however, be assumed that the electron density, n_1, is equal to the impurity concentration, N_d, since in a low band-gap material such as InSb, the Fermi energy could rise above the conduction band edge for relatively low N_d[2]. Due to

---

[1] The surface band bending, v_s, is be convention, negative for a depleted surface, and positive for an enhanced surface (M4).

[2] The use of non-degenerate statistics would involve serious error here.

the markedly non-parabolic nature of the conduction band in InSb, the density of states in the vicinity of the band edge is low. Thus, as the temperature is lowered, the Fermi level moves into the conduction band and some de-ionisation of donors occurs, leading to a reduction in n_1. ϕ is therefore, expected to vary with T through n_1. Using Fermi-Dirac statistics for the carriers, a non-parabolic band and partial ionisation of impurities (see Appendix D), appropriate to InSb, E_f and n_1 have been numerically evaluated. For $N_d = 5\times10^{16}$ cm^{-3}, it was found that $E_f = -0.41$ kT (with respect to the conduction band edge) and $n_1 = 2.26\times10^{16}$ cm^{-3} at 300 °K, and $E_f = +0.66$ kT and $n_1 = 1\times10^{16}$ cm^{-3} at 100 °K. The decrease of n_1 with diminishing T therefore decreases ϕ provided that n_2 varies little with temperature.

The density of carriers, n_2, in the inter-crystalline boundary region will be determined by the filling of trapping states. Assuming a symmetrical potential about a dislocation line, Poisson's equation requires

$$p_2 + N_d^+ - n_2 - N_a^- - N_t^- = 0 \qquad (5.24)$$

where $N_t^- = N_t f$. N_t is the density of dangling bonds and f, the 'filling factor'. $N_a = 0$ in an n-type sample. If the Fermi level is sufficiently remote from either band edge, so that $p_2 \sim 0$ and $N_d^+ \sim N_d$, i.e. complete ionisation of donors, Eqn (5.24) approximates to

$$n_2 \sim N_d - N_t f \qquad (5.25)$$

Consider crystallite size of mean diameter, d, taken to equal 2000 A^o. Total effective surface area would be approximately $1/d = 5\times10^4\ \mathrm{cm}^2/\mathrm{cm}^3$ (area of grain boundary surface per unit volume of film). If the dangling bonds are c apart (on the same dislocation line), and if the dislocations are D apart (see Sec 4.3.2), then the boundary trap density would be $1/(D\times c)$. Hence, the volume trap density is roughly,

$$N_t \sim 1/(D\times c\times d) \sim 10^{18}\ \mathrm{cm}^{-3},$$

which is an order of magnitude larger than N_d.

According to Eqn (5.25), the temperature dependence of f would be reflected directly in n_2. Now, the function f has been treated by Read (R5) under two assumptions:

(1) <u>Read's minimum energy approximation</u>

This assumption assumes zero entropy in the system, the occupation probability being given by

$$E_f - E_t = (e^2/\epsilon c)\left[3 \log (f/f_c) - 0.232\right] \qquad (5.26)$$

where $f_c = c\pi^{\frac{1}{3}}(N_d - N_a)^{\frac{1}{3}}$.

(2) <u>Read's 'Fermi' approximation</u>

Maximum configuration entropy is assumed here. f is obtained from

$$E_f - E_t + kT \log \left(\frac{1-f}{f} \right) = \left(\frac{e^2\epsilon}{c}\right)\left[3 \log (f/f_c) - 0.232\right] \qquad (5.27)$$

E_f can be obtained for any T from a knowledge of the impurity concentration. If E_t, the dislocation trap energy is known, the f can be found as a function of T. Eqns (5.26) and (5.27) represent the upper and lower limits of f; the true value lies between these limits.

Willoughby (W8) was able to show that the function, f, increases rather slowly with the decrease of temperature, in bulk InSb. The trap occupation probability takes a value, which is of the order of 0.01 at room temperature and could go up to 0.1 at very low temperatures, so that in the temperature range considered (77 - 300 ^{o}K), N_tf is about an order of magnitude smaller than N_d. n_2 is therefore not expected to vary much with T. Hence, mobility would not decrease as rapidly as if ϕ were to remain a constant.

5.5.3 Hall coefficient and mobility

(1) T = 77 ^{o}K

The variation of Hall mobility and coefficient as a function of gate field at 77 ^{o}K is shown in Fig 5.4, for three typical n-type samples, having parameters listed in Table 5.2

Table 5.2

Sample	thickness (A^{o})	carrier conc (77 ^{o}K) ($\times 10^{16}$ cm^{-3})	mobility (77^{o}K) (cm^{2}/V sec)
nF5.3	2250	2.33 (6)*	78
nF16.3	2200	6.0 (14)*	200
nF18.3	1880	3.36 (10)*	90

* Figures in baracket are the (approximate) corrected carrier concentration.

The application of a negative gate field depresses the Fermi level at the surface towards the valence band edge and minority carriers (holes) are generated. These increase in number as the negative gate field increases. When the film is relatively thick and the carrier density, n_1, in the volume of the film is fairly large, the minority

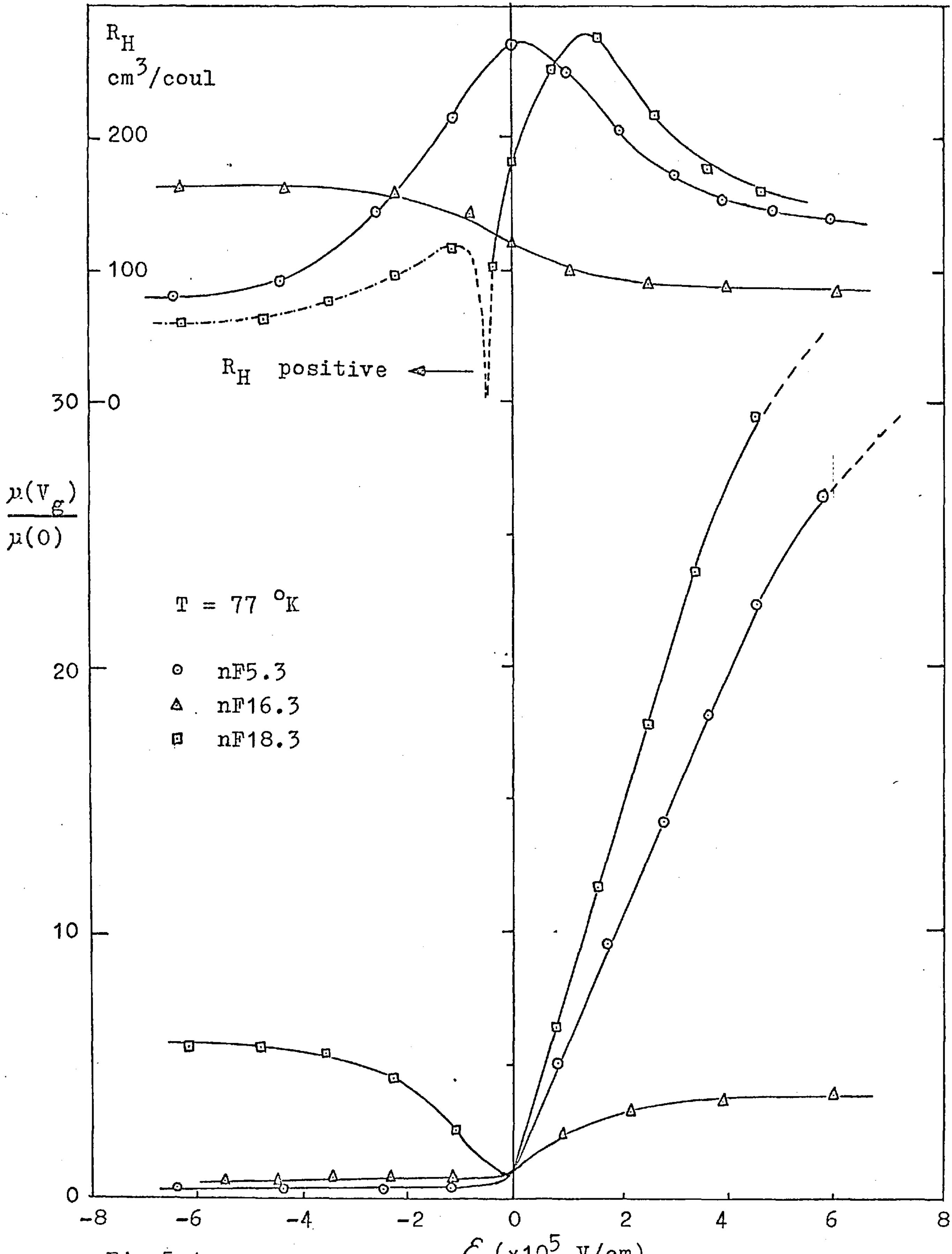

R_H
cm^3/coul
200
100
30–0
20
10
0
$\frac{\mu(V_g)}{\mu(0)}$
R_H positive
T = 77 °K
⊙ nF5.3
△ nF16.3
⊡ nF18.3
−8
−6
−4
−2
0
2
4
6
8
$\mathcal{E}_g$(×10^5 V/cm)

Fig 5.4

hole generation does not significantly affect n_1. This accounts for the relative independence of R_H on negative V_g for sample nF16.3. Likewise, the mobility varies little with negative V_g. For sample nF5.3, which has a low carrier density, R_H falls by a factor of 2.6 over a gate field range of $\sim 7.0\times10^5$ V/cm. The induced holes contribute significantly to the conduction process, in this case, and according to Eqn (4.1)[4], R_H should decrease due to the increased importance of bipolar conduction. The Hall coefficient for both the samples decreases with positive gate field, indicating an increased electron concentration.

Sample nF18.3 shows a very interesting behaviour. The film actually becomes p-type for negative gate fields, and this occurs at a rather low value of V_g. This is often observed in thinner films in the 1000 A° region. Because they are heavily depleted on either surface, only a low density of holes is needed to cause the entire film to become p-type. The conduction is then predominantly due to holes. As the Fermi level shifts towards the valence band edge, detrapping of charges at dangling bonds within the barrier occurs, leading to a reduction in ϕ. Hole mobility therefore increases and saturates when ϕ becomes negligible (for increasing negative gate field).

For positive gate fields, the linear relation as predicted by Eqn (5.22) for small V_g's, is clearly demonstrated for samples nF5.3 and nF18.3. An increase by a factor of 30 is seen. Such a large increase is usually associated with low carrier density films, in view

---

[4] i.e.

$$R_H = -(nb^2 - p)/(nb + p)^2 e \qquad (4.1)$$

of the fact that a higher change in carrier density can be induced. By the same reasoning, the mobility of sample nF16.3, which has a higher carrier density, does not change much from its zero gate field value.

Breakdown in the mica insulator limits the gate field to about 8×10^5 V/cm, when deviation from linearity begins to appear, due to the effects of higher order terms in Eqn (5.22). It should be interesting to investigate further. This would be possible if an insulator with a higher breakdown field is used.

(2) T = 296 °K

In Fig 5.5, Hall mobility and coefficient variation for T = 296 °K is shown for the following samples, in Table 5.3.

Table 5.3

Sample	thickness (A°)	carrier conc (296 °K) ($\times10^{16}$ cm^{-3})	mobility (296 °K) (cm^2/V sec)
nF14A.3	1500	4.45 (15)*	1880
nF20.3	2100	5.1 (13)*	2530
nF22.3	800	5.6 (24)*	460
nF27.3	1500	9.9 (20)*	3200

* Figures in brackets are the (approximate) corrected carrier concentration.

Generally, there is little change in R_H, since at this higher temperature, the electron concentration is much higher. The number of induced carriers (after trapping at surface states and dislocation dangling sites) is significant only in the barrier region, being small compared

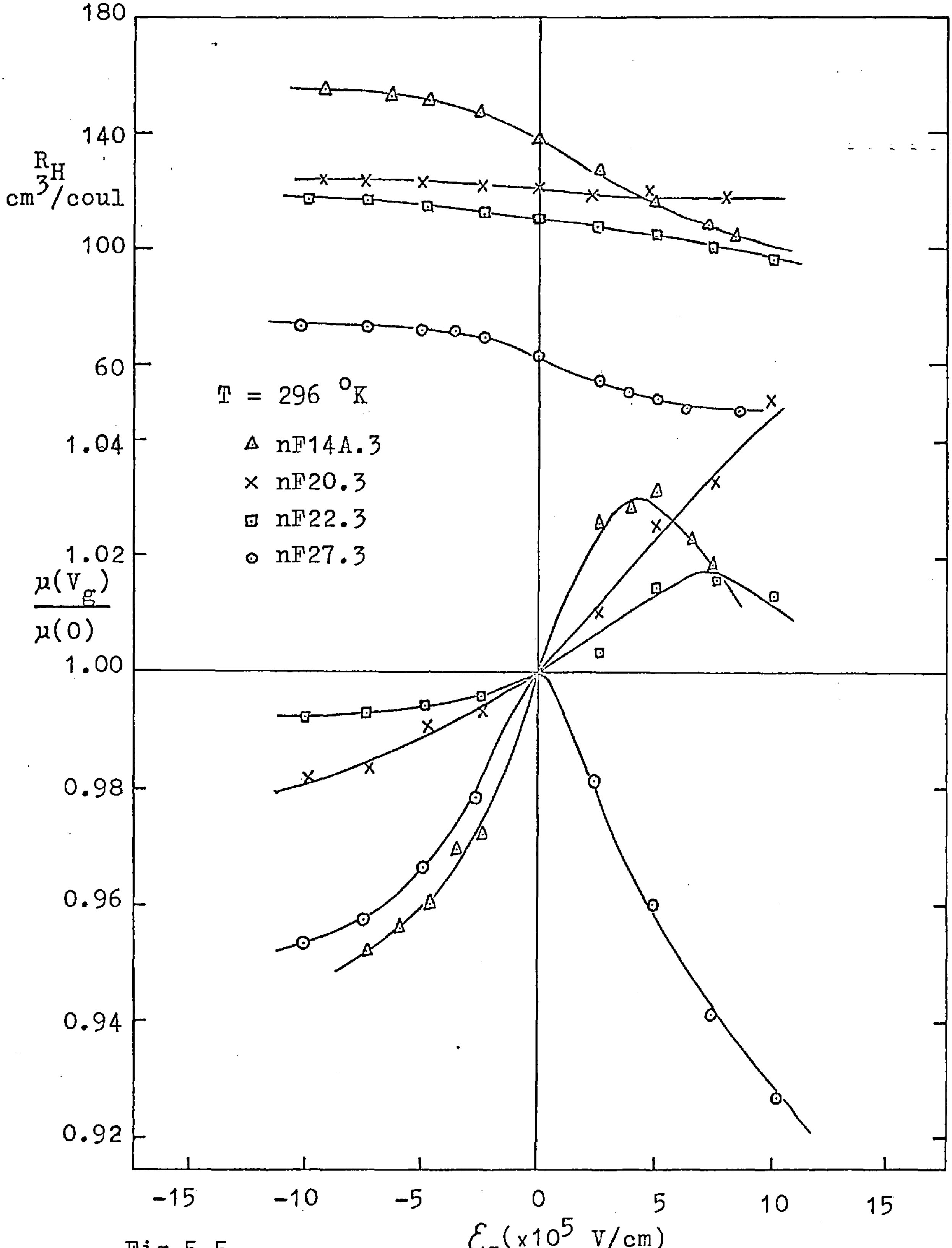
180
140
100
60
R_H $cm^3/coul$
1.04
1.02
1.00
0.98
0.96
0.94
0.92
$\frac{\mu(V_g)}{\mu(0)}$
T = 296 °K
△ nF14A.3
× nF20.3
⊡ nF22.3
⊙ nF27.3
-15
-10
-5
0
5
10
15
$\mathcal{E}_g(\times 10^5$ V/cm)

Fig 5.5

to the number of carriers n_1 already present in the crystallite. n_1 is therefore relatively constant, while n_2 increases to reduce ϕ. But because of the exponential dependence of μ on ϕ, a given change in ϕ produces a much smaller change in μ at 296 °K than if the change occurs at 77 °K. For this reason, mobility varies very little with V_g, to within ± 5% of its zero gate field value.

The decrease in mobility with positive gate field would mean a new scattering mechanism now being operative. A positive V_g results in (1) an increase in the electron concentration, and (2) a decrease in surface band bending. It has been seen that effect (1) produces only a mobility increase. It therefore remains to examine the effects due to a reduction in surface band bending. For a depleted surface, surface scattering is not important. This was demonstrated in Sec 4.3.2. However, as the surface is enhanced by a gate field, it attracts electrons, thereby increasing scattering. Based on such a model, Schrieffer's theory predicts a mobility reduction, which has since been substantiated by the experimental data of Waxman et al (W9) and van Heek (H10). It would appear that the theory could also provide an explanation for the observed mobility behaviour at 296 °K.

A tentative estimate of mobility reduction due to surface scattering can be obtained from the following equation (M4):

$$\mu_s/\mu_b \sim \left[1 + \lambda(1 + v_s)^{\frac{1}{2}}/L_c\right]^{-1} \qquad (5.28)$$

where s, b denote surface and bulk values, respectively. λ is the mean free path, taken to equal half the mean crystallite size. Since v_s is relatively independent of temperature (L6), the ratio of the relative mobility reduction at 296 °K and 77 °K is approximately equal to $L_c(296\ ^oK)/L_c(77\ ^oK)$, if $\lambda(1 + v_s)^{\frac{1}{2}}/L_c \gg 1$. The space charge penetration depth, L_c, for sample nF20.3 ($N_d \sim 1.3\times10^{17}$ cm^{-3}) is plotted in Fig 5.6, as a function of surface band bending, for 3 temperatures. The surface band bending for zero gate field will be seen to be around ~25 kT, and using this value of v_s, the ratio, $L_c(296\ ^oK)/L_c(77\ ^oK)$, is found to be 18. A qualitative conclusion, that surface scattering is much larger at room temperature than at liquid nitrogen temperature, is to be drawn here.

If the carrier mean free path is not governed by the crystallite size, then the potential barrier no longer controls mobility and the field-effect experiment would reveal the surface scattering effect only. It is of interest here to mention the work of Juhasz (J1) on InSb films, in the thickness range 5000 A° and with mobility ~10000 cm^2/V sec. His experimental results are in good agreement with the surface scattering theory.

5.6 Discussion

Returning to Chapter Four, it is now possible to explain the different slopes of the mobility-temperature curves (Fig 4.3). n_1 varies to a much larger extent from room temperature to liquid nitrogen temperature for films with low impurity concentration, $N_d \sim 5\times10^{16}$ cm^{-3}, than for films with high impurity concentration, N_d 1 - 2×10^{17} cm^{-3}. Since n_2 is rather temperature insensitive, a much larger mobility variation is therefore expected for low carrier density films.

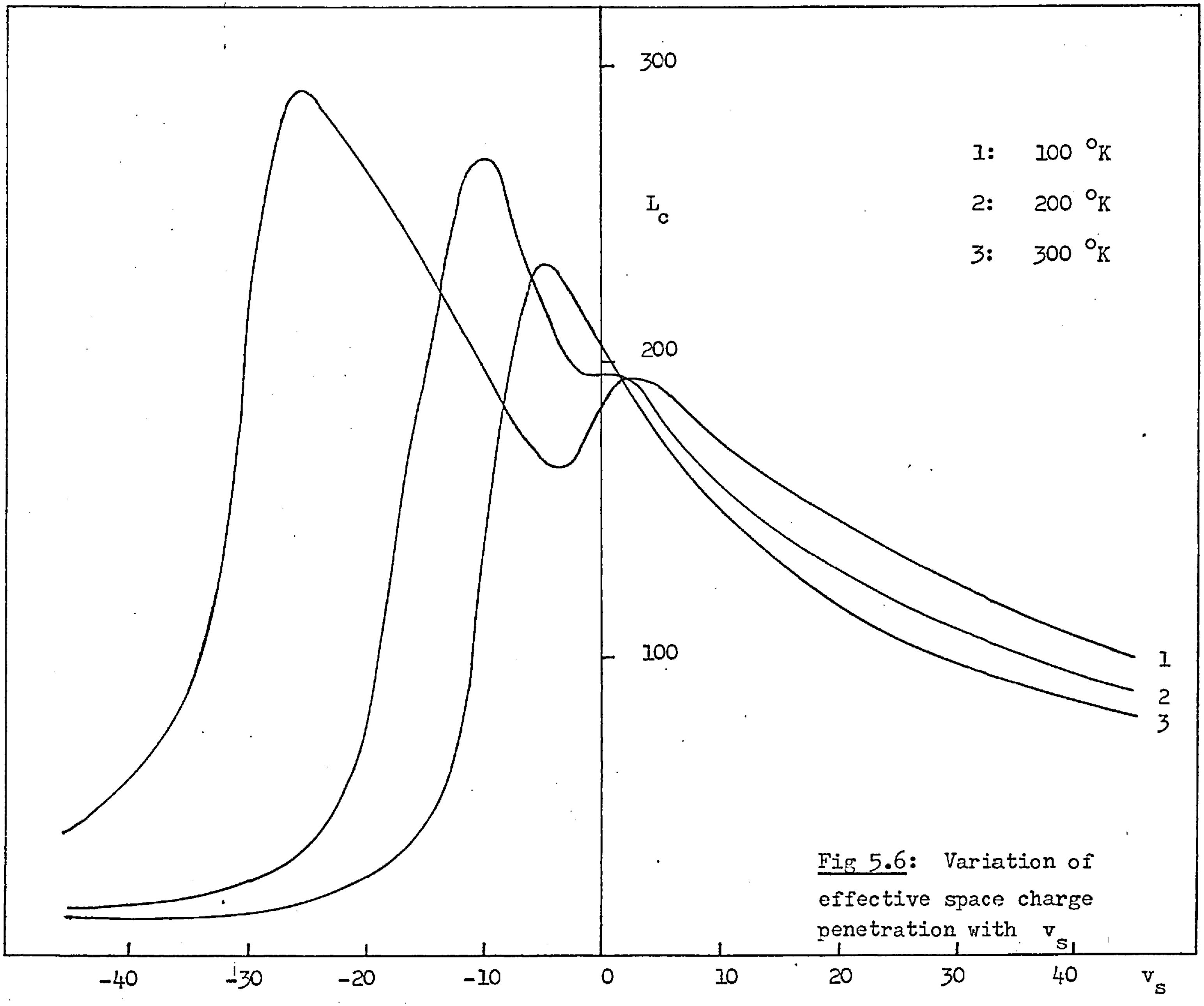

Fig 5.6: Variation of effective space charge penetration with v_s

The results of Hall and field-effect measurements have all been found to be in favour of the potential model proposed. The barrier potential associated with grain boundaries is attributed to dislocation dangling bonds, rather than to different impurity concentration due to stoichiometric variations, as suggested by previous workers. The exponential variation of mobility and the slight temperature dependence of ϕ can all be accomodated by the dislocation dangling bond model.

The 'barrier' effect has been observed in a number of semiconductor films. However, the work of Egerton (E1), on epitaxial lead salt films, shows that the effect is insignificant, i.e. the potential barrier scattering is unimportant. This, he attributes to the high static permittivity of the material.

It is possible to present a mathematical model. Combining Poisson's equation and the diffusion equation for carriers across the grain boundary, a second order differential equation is obtained, which can be numerically solved for $\mathcal{E}$ and ϕ (eg. by Runge-Kutta method). This would require a knowledge of

(1) the occupation statistics, different in the crystallites and in the barrier region,

(2) the trapping energy, E_t, which is different for In- and Sb-dislocations, and is also a function of the angle of misorientation, θ, and

(3) the change in band gap at the dislocation, due to the stress and the strain set up at the disrupted lattice. Furthermore, the variation of carrier concentration (and associated effects) across the thickness of the film makes the problem truly formidable, an will not be attempted here.

In Sec 5.5.2, the filling factor was taken to be 0.01. From Eqn (5.1) and (5.4), the trapped charge in the grain boundaries, $q_o = 2(2Ne\epsilon\phi_o)^{\frac{1}{2}} \sim 5\times10^{11}$ cm^{-2}, taking $\phi_o = 0.04$ eV and $N = 10^{17}$ cm^{-3}. From the angle of misorientation, the trap charge density was estimated at $\sim 3\times10^{13}$ cm^{-2} (see Sec 4.3.2). Hence, $f = 5\times10^{11}/3\times10^{13}$ ~ 0.02, justifying the earlier assumption.

Further information on the potential model is provided by conductivity measurements at high electric (measuring) fields. This will be the subject for the next chapter. The high breakdown fields in thin films, have often been ascribed to the high-resistivity grain boundaries. This hypothesis can be put to test by combining the high-field and the dc field-effect measurements.

CHAPTER SIX: High Field Measurements

6.1 Introduction

Interest in the high field effects on electrons in solids began with the study of breakdown in dielectrics (W11, F9, S13, S14). One of the earliest theories was due to Zener (Z2), who proposed a purely quantum mechanical 'tunnelling' process. He considered that, in the presence of an applied electric field, each energy band (defined for no external field) of a lattice of infinite extent becomes degenerate with every other band; consequently, an electron may pass from one energy band to another, which, if the external field were absent, would lie above the first band. Zener's theory predicts in particular, an abrupt change in the conductivity when the applied field reaches a certain critical value and this has been well borne out by experiments (W11).

Following the first successful investigation of the effects of high fields in homogenous semiconductors by Shockley and Ryder (S12), rapid development has since been made both theoretically and experimentally by many workers (K3, B11, C9). Semiconductors have the advantage that, at ordinary temperatures, a significant number of carriers is present, so that it is possible to observe the continuous change in the electrical behaviour from low fields up to breakdown, for readily attainable power densities.

The earliest reports on the non-linear behaviour in high electric fields were made on Ge and Si (M8, M9, M10, M11, W12, G6). Gunn (G6) shows that deviation from ohmicity in Ge starts at a field of $\sim 9\times10^{3}$ V/cm, and the dependence of drift velocity on $\mathcal{E}^{\frac{1}{2}}$, then considered to hold according to simple theory, was not observed. Shockley was able to account for this by a refined theory, which predicts among other things, a $\mathcal{E}^0$ field-dependence for a certain field range, i.e. a 'saturated drift velocity' effect. Breakdown at high fields was attributed to an avalanche process, in which carriers, accelerated to a high kinetic energy, are able to cause ionisation upon impact with the lattice. Multiplication rates for injected carriers were measured by McKay and McAfee (M10) in p-n junctions are found to be as high as 18, and a multiplication time of less than $\sim 2\times10^{-8}$ sec was also observed. These results were in excellent agreement with the theoretical predictions of Wolff (W12). Miller (M11) obtained a threshold for electron-hole pair production of approximately 1.5 eV in Ge ($E_g \sim 0.7$ eV) and a mean free path for electron (or hole) - phonon collision of about 130 A°; no internal field emission was observed, however, even for a field as high as $\sim 3.2\times10^5$ V/cm.

6.2 Survey of high-field effects in InSb

High-field effects have perhaps been most extensively studied in InSb among all semiconductors, because of its high electron mobility and consequently, the relative ease with which the electrons can be 'heated', i.e. can increase in energy. The first current-field, j-$\mathcal{E}$, characteristics were measured by Prior (P10), at room temperature. This was followed immediately by the work of other authors (G7, K4, K5, K6, S14, C10, A3, S15, G5), the subsequent work being all carried out at 77 °K. It has now been firmly established that carrier multiplication is due to electron-hole pair generation by across-the-gap ionisation, i.e. an avalanche process. Carrier generation as indicated by an increase in conductivity is clearly discernible even at a field as low as 50 V/cm. The critical field at which rapid rise of current occurs, i.e.

$dj/d\mathcal{E} \rightarrow \infty$, is observed to be in the vicinity of 350 V/cm for n-type InSb and some 1 - 2 times higher for p-type material.

The rise in current at the critical field is, however, not as rapid as anticipated, due to a 'self-pinch' effect. The presence of a sufficiently large number of generated electrons and holes, produces a self magnetic field which constricts ('pinches') the free carriers or plasma into a smaller volume, thereby increasing the resistivity.

In n-type InSb, electrons are obviously responsible for initiating the avalanche, since holes are present in fewer number and have lower mobility. In typical p-type InSb, the equilibrium electron concentration at 77 °K is negligible compared to hole population ($\sim 10^2 - 10^3$ electrons/cm^3 as against $\sim 10^{15} - 10^{16}$ holes/cm^3), and Kanai (K5) suggested that the presence of light holes, having mobilities 10 times larger than that of electrons might be responsible for the avalanche effect. Steele and Glicksman (S14) were quick to point out that such a light-hole, high-mobility concept was unrealistic; they suggested that both ordinary holes (heavy holes) and injected electrons (through contacts) could initiate avalanche. In either case, a critical field strength higher than 350 V/cm, is to be expected. They obtained a critical field of approximately 700 V/cm for a p-type sample containing $\sim 2.3 \times 10^{16}$ acceptors/cm^3 and having a low-field hole mobility of ~ 4000 cm^2/V sec.

For impact ionisation to occur, an electron must have an energy in excess of the energy gap of ~ 0.23 eV (at 77 °K). But because of electron-phonon interaction, a higher energy is needed. Tauc (T4) found that, on the average, approximately 0.5 eV is needed to generate one electron-hole pair. The generation rate, $g(\mathcal{E})$, in the presence of an electric field, has been studied by McGroddy and Nathan (M12), who applied short rectangular voltage pulses across a sample. After a formative lag time[4] of 0.4 ± 0.3 nsec (A4), the current pulse top was observed to rise linearly with time. Neglecting for the present the mobility variation, the slope of the current pulse top gives a measure of the carrier generation rate. The experimental data of McGroddy and Nathan fits well a function of the form

$$g(\mathcal{E}) = g_o \exp(\mathcal{E}/\mathcal{E}_o) \qquad (6.1)$$

where g_o and $\mathcal{E}_o$ were found to be approximately 5×10^3/sec and 30 V/cm, respectively at 77 °K.

As the electric field increases, the Hall drift velocity (Hall mobility x electric field) is observed to saturate with $\mathcal{E}$ (K6, G5), followed by a sharp drop at breakdown (at the critical field). Such mobility decrease can be due to several factors. Physically, as the electrons get heated, they occupy higher energy states in the conduction band. The markedly non-parabolic band rapidly increases the electron effective mass, so slowing down the carriers. To allow for the energy dependence of the effective mass, Glicksman and Hicinbothem (G5) obtained a mean value by averaging m*(E) over the appropriate electron distribution function. The chances of scattering by polar optical phonons increase as the electrons become more energetic. With the generation of carriers, electron-electron and electron-hole scattering must also be considered. Theoretical analyses (H11, L7, D3) also point to the presence of such a phenomenon, while Ikoma (I2) proposed a transverse breakdown model,

---

[4] The formative lag time is defined as the lapse between the start of the voltage pulse and the onset of plasma generation.

attributed (in the presence of a magnetic field) to the very strong Hall field developed, in the vicinity of breakdown, to account for the drift velocity saturation.

In addition to the above high-field-induced effects, hot electrons in InSb have produced other new phenomena, some of which well be briefly mentioned here. Plasma oscillations in the MHz - GHz frequency range, ascribed to the 'pinching' and 'unpinching' instabilities of electrons and holes, have been reported by various authors (I2, A4, E5). Steele and Glicksman (S14), and Tosima (T5) observed a current-controlled negative differential resistivity. The Gunn effect[‡], previously thought not possible, because the Gunn threshold (~600 V/cm) is higher than the breakdown field, has now been firmly established by Smith et al (S6). Microwave emission (B12) and non-linear galvanomagnetic effects in the quantum limit, at helium temperatures (K7), have also been reported.

6.3 Some theoretical consideration

Generally, Ohm's law for electronic conduction in semiconductors is strictly valid in the limit of vanishingly small fields, when carriers and lattice phonons are in thermal equilibrium. The application of a field produces heating in the carriers, i.e. raising their average kinetic energy. Under steady state conditions, the gain in energy is balanced by its loss due to carrier-phonon scattering. If the heating is sufficiently intense, the carriers become 'hot' and deviations from low-field values of carrier distribution and mobility (inter alia), are to be expected. Thus the current-field characteristics would exhibit three regions of interest:

[‡] Due to an intervalley transfer of electrons from the main valley to a satellite valley, whose minimum is ~0.45 eV above the band edge, and lies along a ⟨111⟩ direction.

(1) The ohmic region, where the current and field relationship is linear;

(2) The 'warm' carrier region where deviation from ohmicity starts to set in; and

(3) The 'hot' carrier region where significant changes in the conduction behaviour occur, culminating in breakdown.

6.3.1 Distribution function

A rigorous approach to the high-field problem of interaction between carriers and lattice phonons, involves the exact solution of Boltzmann's equation. The thermal equilibrium distribution function of phonons with wave vector $\underline{q}$ is given by

$$\overline{N}_q = \frac{1}{\exp(\hbar\omega_q/kT) - 1} \qquad (6.2)$$

where $\hbar\omega_q$ is the energy of a phonon, characterised by $\underline{q}$.

The distribution function for the carriers has an analytic form only in the case of pure acoustic scattering (Y1); the distribution can only be evaluated numerically or analytically over a limited range of energy, ~~for~~ other scattering mechanisms, alone or in combination with acoustic phonons (C9).

In situations in which electron-electron interactions play a negligible role (for $n < 10^{14}$ cm^{-3}), the velocity distribution of electrons under the influence of a dc electric field may become highly peaked along the field direction. Since the probability of an electron being scattered from a state $\underline{k}$ into a state $\underline{k}'$, is proportional to $|\underline{k} - \underline{k}'|^{-2}$, small-angle scattering is strongly favoured over large-angle scattering. Hence, in the presence of a field, electrons tend to scatter into a narrow cone, after successive collisions with the lattice phonons. This 'focusing' effect results in a highly anisotropic distribution (D3). Baraff (B13) used the conventional spherical harmonics expansion of the electron distribution but under conditions of 'maximum anisotropy approximation' to obtain solutions to the Boltzmann equation.

Phonon scattering is usually assumed to be of the polar-optical-mode (D3, M2, M3, L5). Acoustic mode scattering in low carrier density InSb is rather improbable, since the acoustic scattering time is approximately two orders of magnitude longer than those for optical-mode scattering (D3). The low effective mass also makes acoustic scattering ineffective (Chapter Two).

In the calculation of the distribution function, the effect of non-parabolicity of the conduction band is of great significance. The distribution function for parabolic bands is not normalisable, and a condition known as carrier 'run away' arises (F9, S13). This, however, is prevented, if non-parabolicity is included in the analysis. The deviation from a standard band, therefore, produces a 'cooling effect' on the carriers, in particular, the energetic ones (M3).

In the case where the carrier concentration is high ($n \sim 2\times10^{16}$ cm^{-3}), for example in thin films, carrier-carrier scattering might dominate the scattering process. The critical concentration for this to occur, has been considered by Fröhlich and Parajape (F9), and by Stratton (S13). Under this situation, the distribution is usually assumed to be a drifted Maxwellian, which is of the form

$$f^*(\underline{k}) = f_o(\underline{k}, \underline{\mathcal{E}}) - \underline{k}_d \cdot \frac{df_o}{d\underline{k}} \qquad (6.3)$$

where the symmetric part of the distribution has been allowed to vary with the applied field, $\mathcal{E}$. $\hbar\underline{k}_d$ is the drift momentum. The concept arises from the energy-randomising nature of the carrier-carrier scattering, which causes the distribution to be Maxwellian, but because of the higher energy the carrier now possesses, the distribution is characterised by a 'carrier temperature', T_e (S13, L8), which is higher than the lattice temperature, T_o. Eqn (6.3) can be written in an alternative form, centred about the drift momentum, $\hbar\underline{k}_d$, thus

$$f^*(\underline{k}) = \exp\left(-\frac{E}{kT_e}\right)\left[1 + (1/kT_e)\,\underline{k}_d \cdot \frac{dE}{d\underline{k}}\right] \qquad (6.4)$$

6.3.2 The energy and momentum conservation method

Much of the theoretical work on high-field effects is devoted to the study of the variation of carrier mobility. Under steady state conditions, balance of energy gives (C9, H12),

$$\left\langle \frac{dE}{dt} \right\rangle = e\mu(\mathcal{E})\mathcal{E}^2 \qquad (6.5)$$

whereas, conservation of momentum requires

$$\left\langle \frac{d(\hbar k_\alpha)}{dt} \right\rangle = e\mathcal{E}_\alpha \qquad (6.6)$$

where $\hbar k_\alpha$ is the momentum component in the α direction. The differentials are with respect to time, t, and angular brackets denote the average over the chosen distribution function (K8, K9), thus,

$$\langle A(E)\rangle = \int_0^\infty \left(-\frac{df_o}{dE}\right) A(E)\,\gamma^{3/2}\,d\gamma \qquad (6.7)$$

where $A(E)$ is any arbitrary function of energy, and $\gamma(E) = E + E^2/E_g$, as defined by Eqn (2.3).

Eqns (6.4), (6.5) and (6.6) are sufficient to enable mobility to be found as a function of applied field (H12, L8, W13, S16). $\langle dE/dt\rangle$ and $\langle d(hk_\alpha)/dt\rangle$ are the scattering integrals that can be obtained through standard time-dependent quantum mechanical treatment (C9, Z3) and have been considered by many authors for InSb under a diversity of assumptions.

6.3.3 Application to thin films

Whilst the preceding ideas can be utilized to predict high-field effects in bulk material, a mathematical model developed along similar lines for thin films, would present serious difficulties, in view of the presence of grain boundaries and other scattering centres. Up to date, there has been very little work done in this field (C1, C2, I1, P11). The only j-$\mathcal{E}$ measurement in InSb films, that the author is aware of, is due to Červenák (C1, C2); however, there is serious objection to his work on the following grounds:

(1) Au or Al contacts were used. These contacts have been found to be highly non-ohmic (Chapter Three) and Červenák's data might reflect the behaviour of the contacts and not of the semiconducting film; and

(2) There was no mention of the way the high field was achieved. Presumably, dc voltages were employed; sample heating at high fields, would cause the measurement to lose much of its meaning.

A typical film of thickness 2000 A^o ($\mu \sim 2000$ cm^2/V sec and $n \sim 1\times10^{17}$ cm^{-3}) has a resistivity of 0.03 Ω-cm. In order to achieve a high field and yet a low enough power density, it is necessary to reduce the sample length to approximately $2 - 5\times10^{-3}$ cm. In bulk InSb, the drift velocity of electrons near the critical field is of the order of 10^8 cm/sec (I2). Since the electrons have an avalanche time[4] of 2 - 3 nsec (A4), an electron injected at the cathode travels a distance of 2 - 3 mm before undergoing an impact ionisation. That an electron must travel this uninterrupted distance, has been confirmed beyond any doubt by Tosima (T5), who made a study of the spatial dependence ofthe avalanche process and found that within some 3 mm of the cathode, no ionization took place. In the light of this and in view of the small crystallite size, it would appear that avalanche cannot occur in polycrystalline films, even if the sample length exceeds 3 mm.

In the previous chapter, grain boundaries were shown to be very effective scattering centres for carriers at low electric fields, and probably, the same also applies at high fields. The barrier model is again used to interpret the experimental data.

Referring to Chapter Five, it was shown that the critical voltage, V_c, at which $\emptyset_2$ (the potential associated with the forward biased side of the barrier) tends to zero, is $4\emptyset_o$, if the grain boundary state density, q, remains constant at q_o (i.e. the zero bias value). $\emptyset_o$ was found to be approximately 0.04 V, and the critical

---

[4] The avalanche time is defined as the time between the onset of plasma generation and the occurence of an increasing current independent of the applied field.

voltage is therefore 0.16 V. In the high-field measurement, $\mathcal{E} \sim 2 \times 10^4$ V/cm is often encountered. For a film of crystallite size equal to 2000 A°, this would mean a voltage drop of ~ 0.4 V across each barrier, which is approximately $2.5V_c$. Hence, it is conceivable that, in the presence of a field of this magnitude, $\emptyset_2$ could indeed become very small, even though the assumption of a constant q (independent of applied field) is not strictly valid (see Eqn (5.9)). The low-field linear relation is thus expected not to hold, since eV/kT is now much larger than 1. A deviation in the j-$\mathcal{E}$ characteristic from linearity may, intuitively, be interpreted as an increase in the electron mobility, physically compatible with the reduced barrier model. Putting $\emptyset_2 \rightarrow 0$, i.e. $V_2 \rightarrow \emptyset_o$ and $V_1 \rightarrow V$, Eqn (5.13) reduces to the form[4],

$$j = \tfrac{1}{4} en \langle c \rangle \left[1 - \exp\left(- eV/kT\right) \right] \qquad (6.8)$$

where the applied voltage now appears entirely across region 1 (see Fig 5.1), there being no potential drop associated with region 2. One important difference between Eqn (6.8) and that derived previously, is the absence of the initial barrier height, $\emptyset_o$, in the expression. The significance of this independence will be demonstrated.

At fields for which Eqn (6.8) is valid, i.e. when $\emptyset_2 \rightarrow 0$, the variation of conductivity with temperature and field can be obtained by taking partial derivatives of j. Differentiating with respect to $\mathcal{E}$ gives the conductivity,

$$\sigma = \left(\frac{\partial j}{\partial \mathcal{E}} \right)_T = \tfrac{1}{4} ne \langle c \rangle \left(\frac{ed}{kT} \right) \exp\left(- e\mathcal{E} d/kT\right) \qquad (6.9)$$

and

---

[4] Assuming, of course, the diode theory to be still valid.

$$\left(\frac{\partial\sigma}{\partial\mathcal{E}}\right)_T = -\tfrac{1}{4}ne\langle c\rangle\left(\frac{ed}{kT}\right)^2 \exp\left(-e\mathcal{E}d/kT\right)$$

$$= -(ed/kT)\,\sigma < 0 \qquad (6.10)$$

where use has been made of the relation, $V = \mathcal{E}d$, d being the mean crystallite size. Eqn (6.10) predicts negative differential conductivity, an effect, which in bulk InSb, is attributed to a mobility decrease (S6, H11, C11, D4) due to (1) single-valley carrier heating at moderate fields, and (2) intervalley transfer of carriers to low-mobility, high-mass states, near the critical field. The negative differential conductivity here is a purely barrier effect and a physical interpretation will be attempted in what follows.

Differentiating with respect to T leads to

$$\left(\frac{\partial\sigma}{\partial T}\right)_{\mathcal{E}} = \tfrac{1}{4}nea\left(\frac{ed}{kT}\right)\exp\left(-\frac{e\mathcal{E}d}{kT}\right)T^{-\frac{1}{2}}\left[\frac{e\mathcal{E}d}{kT} - \tfrac{1}{2}\right] \qquad (6.11)$$

where the mean thermal velocity is taken to be roughly $aT^{\frac{1}{2}}$. For the electric fields considered, $(e\mathcal{E}d/kT) \gg 1$. Eqn (6.11) can be approximated to

$$\left(\frac{\partial\sigma}{\partial T}\right)_{\mathcal{E}} \sim T^{-5/2}\exp\left(-e\mathcal{E}d/kT\right) \qquad (6.12)$$

from which it follows that non-linearity in the j-$\mathcal{E}$ characteristics is greater at higher temperatures.

6.4 Experimental technique

A block diagram of the apparatus used in the high-field experiment is shown in Fig 6.1. The voltage pulses generated by a Tektronix pulse generator (type 109), had a duration of 10 nsec, a rise-time of ~0.25 nsec and a maximum amplitude of 50 V. However, with an external

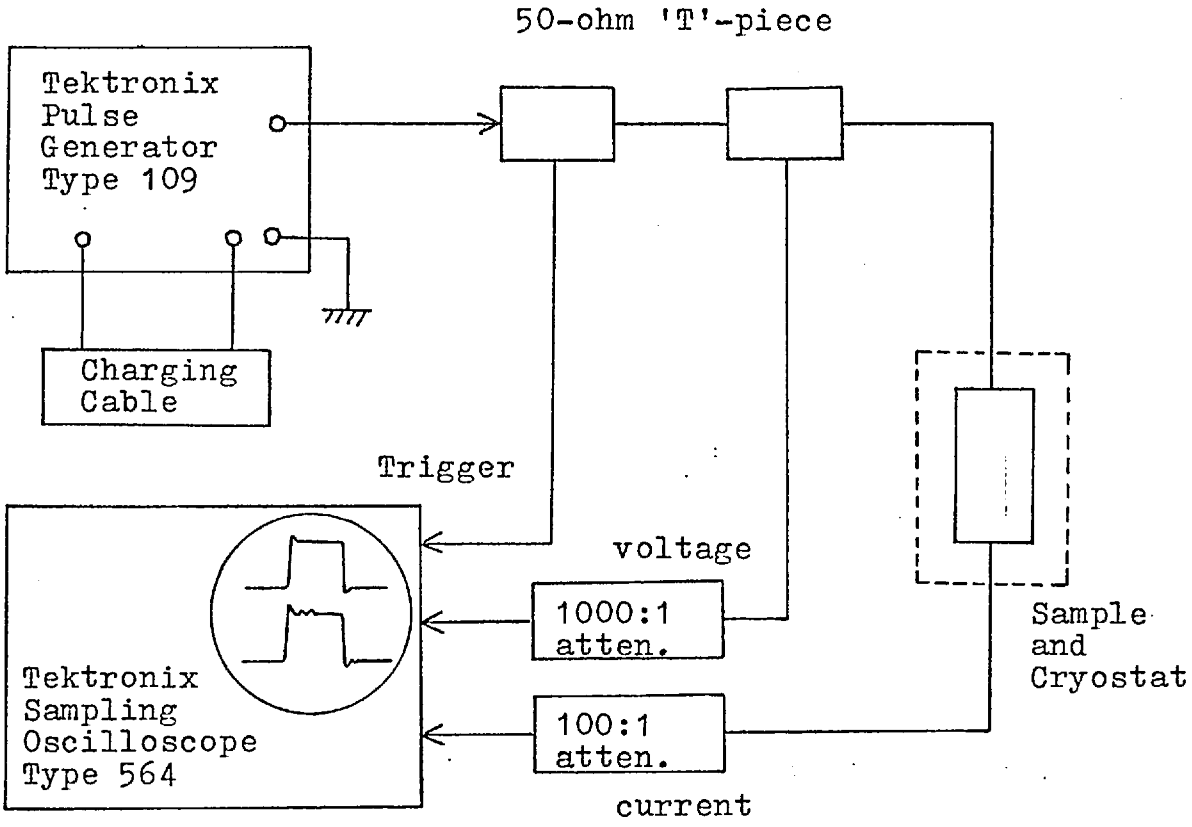

(a) Block diagram of apparatus

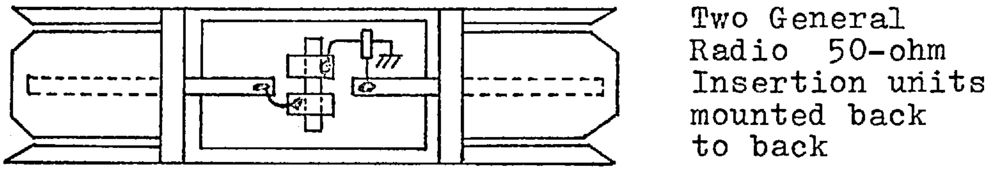

(b) Sample mounting unit, showing current-monitoring ferrite ring (not to scale)

Fig 6.1: Apparatus for high-field experiment dc voltage supply, the maximum amplitude could be increased to 300 V. The pulse duration could be altered by changing the actual physically length of the charging cable (General Radio 50 ohm co-axial cable). The generator had an output impedance of 50Ω and a repetition frequency of 550 Hz.

The voltage and current waveforms were displayed simultaneously on a Tektronix sampling oscilloscope (type 564) which had a matching input impedance of 50Ω and a rise-time of ~0.25 nsec. All connecting cables had a matching characteristic impedance of 50Ω (General Radio cables).

The sample was prepared by evaporating a layer of In or Ag contacts through a wire mask (diameter 0.001 - 0.005") on to an InSb film. The gap was so chosen as to give the sample an impedance of as near 50Ω as possible. This was necessary for impedance matching. The current waveforms became noisy when the sample impedance was less than about 30Ω or greater than about 300Ω. For high-resistivity samples (at 77 °K), a number of gaps were connected in parallel to achieve a manageable impedance.

In view of the above requirement, the current could not be measured in the usual way by monitoring the voltage drop across a small resistance in series with the sample. The difficulty was overcome by using a pulse transformer[4], which was in the form of a ferrite ring (from Mullard), with a coil of N turns, uniformly spaced round it to form the secondary. The primary was just a thick copper wire, threading the ring and carrying the sample current. If the total impedance in the secondary coil is R, then only a fraction of this, R/N^2, is reflected

---

[4] The author is indebted to Dr T. O'dell for the suggestion.

in the primary. For N = 20, the reflected impedance was found to be $\sim 0.13\,\Omega$, small compared to the sample impedance. The frequency response of such a pulse transformer is remarkably good (R6).

6.5 Results

6.5.1 j-$\mathcal{E}$ characteristics

The j-$\mathcal{E}$ characteristics for two typical samples are shown in Fig 6.2 and 6.3 for a few temperatures. Three field regions will now be examined.

(1) The ohmic region

For $\mathcal{E}$ less than about 5×10^3 V/cm, the current is proportional to the applied field. The j-$\mathcal{E}$ characteristics can be described by the relation as given in Eqn (5.14), which is valid for low fields or rather when the external voltage produces only a small change in the barrier height.

(2) The non-ohmic region

Beyond about 5×10^3 V/cm, deviation from linearity appears. Sample nC41.4 (with $n \sim 7.2\times10^{16}$ cm^{-3}) shows an increase in conductivity with $\mathcal{E}$, though this was not predicted by the diode theory, and the increase is greater for lower temperatures. The conductivity increase might be interpreted as an increase in carrier mobility due to a lowering of the barrier height (on the forward-biased side of the barrier), while the carrier concentration remains constant. Any carrier multiplication at this stage can be ruled out, since the top of the current pulse remains essentially flat.

Sample nC24.4 shows that, whilst the differential conductivity increases with field for temperatures above room temperature, the reverse is true for lower temperatures,

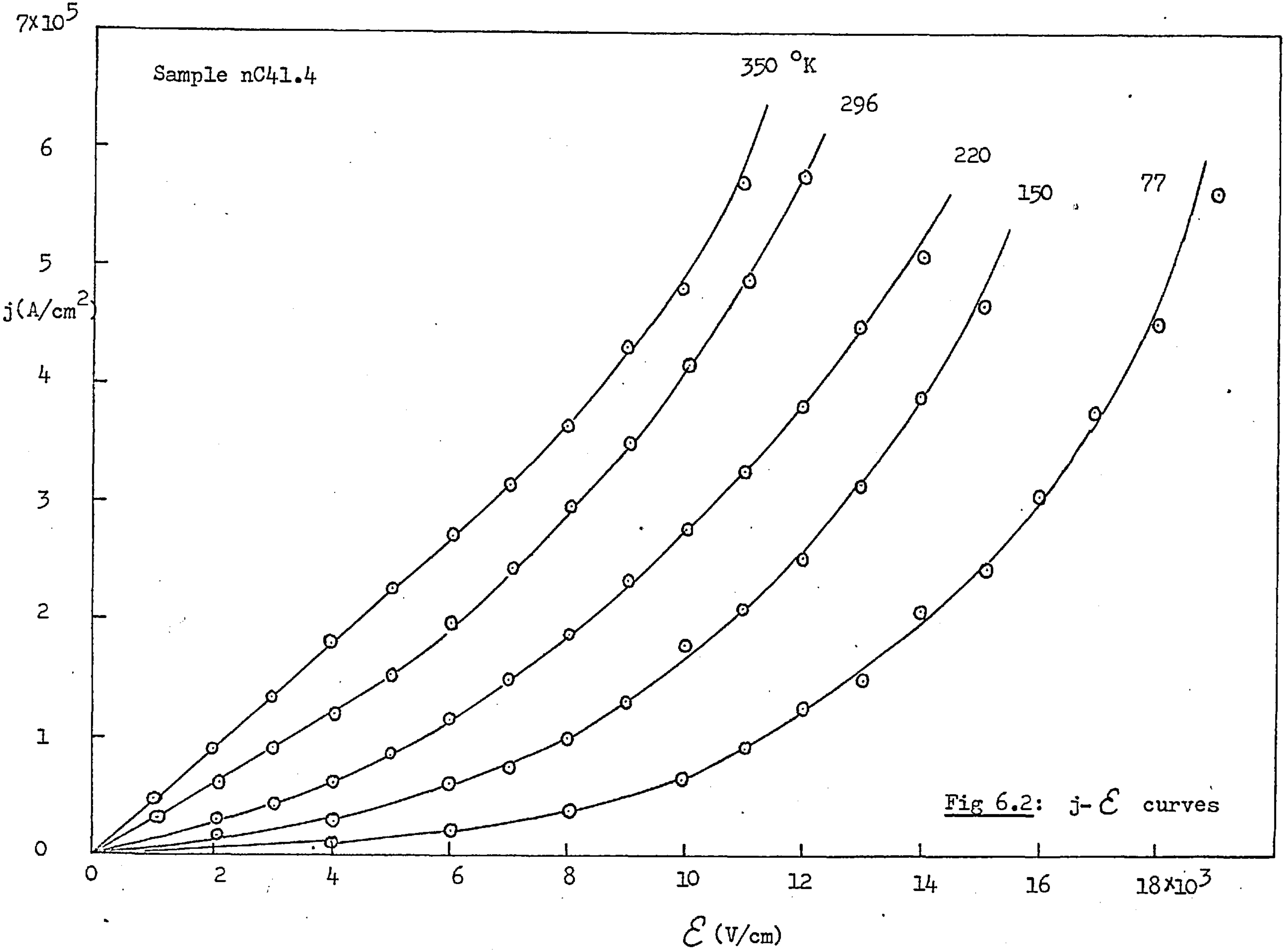

Fig 6.2: j-ℰ curves

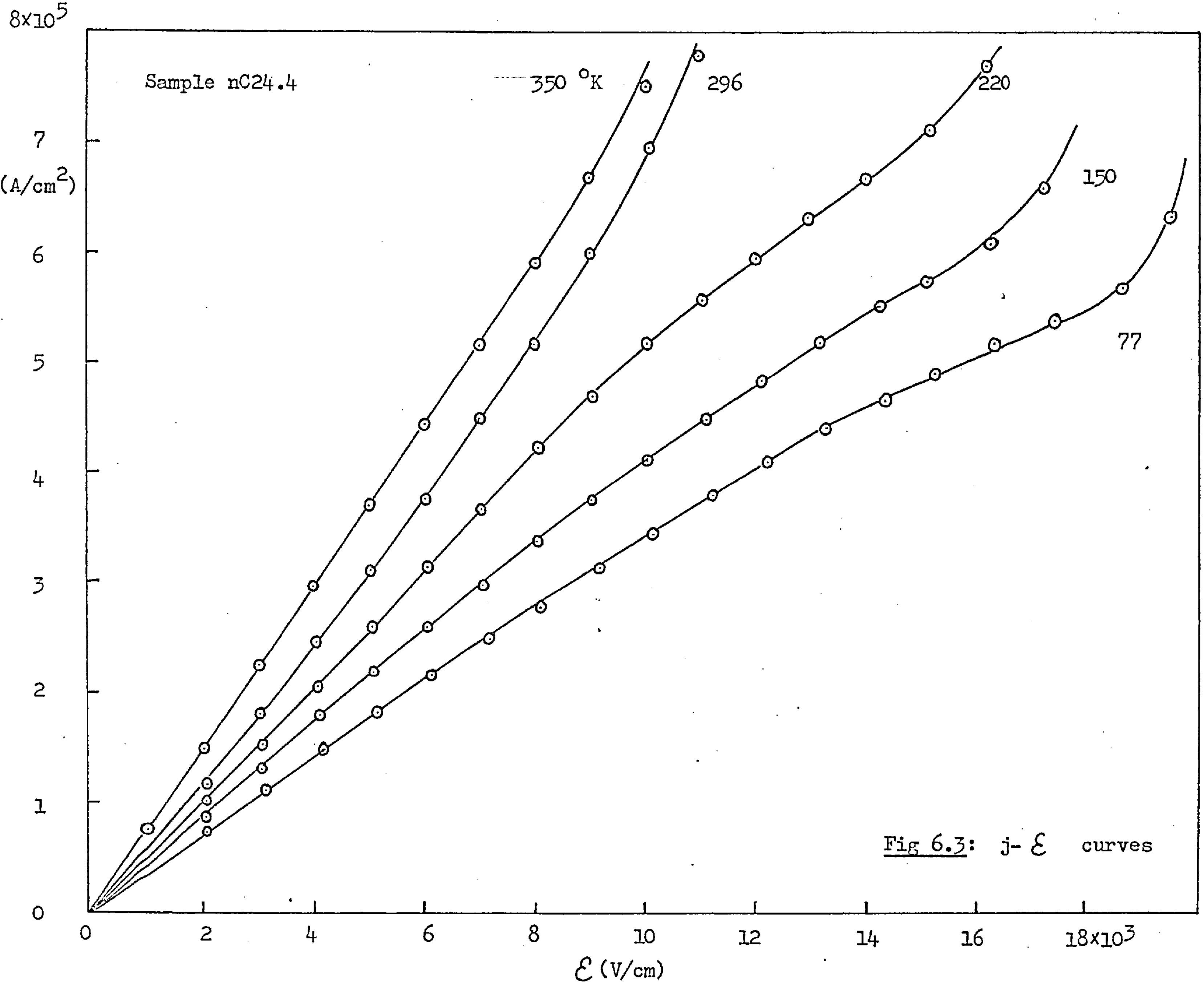

Fig 6.3: j- ℰ curves

now in agreement with Eqn (6.8). Since the electron concentration does not decrease with $\mathcal{E}$, this would imply a fall in mobility, contradicting the previous argument. However, it has been observed that this is typical behaviour, the former being associated with low carrier density films, and the latter, with high carrier density films. It may be inferred tentatively, that the difference in the conductivity behaviour, is another manifestation of the barrier effect, being related to the initial barrier height, ϕ_o.

Eqn (5.9) expresses the trapped charge density at boundary states, as a function of the barrier voltage, V, thus,

$$q = (q_o/2)\left[1 + (1 + V/\phi_o)^{\frac{1}{2}}\right] \qquad (5.9)$$

where q_o is the equilibrium trapped charge density, i.e. when $V = 0$. Clearly, q is also dependent on the initial barrier height, ϕ_o. When $V/\phi_o < 1$, $q/q_o \sim 1$; there is therefore negligible additional carrier trapping at the boundary states[+]. This leads to a constant n and a constant μ, since the latter depends on $\exp(-e\phi_o/kT)$, and ϕ_o is also constant in this case. Hence, under this condition of negligible trapping, the j-$\mathcal{E}$ characteristic is ohmic.

As V becomes comparable with or larger than ϕ_o, appreciable additional trapping results. This has the effect of lowering n, but increasing μ, which now depends on $\exp\left[-e(\phi_o - V_2)/kT\right]$ (see Fig 5.1). Since conductivity, $\sigma = ne\mu$, the fractional change in σ as a

---

[+] It must be pointed out, that trapping also occurs, at the same time, at the surface states, and is a function of V (or $\mathcal{E}$) as well. This will be taken up in the next chapter.

result of changes in n and μ, can be written as

$$\frac{\Delta\sigma}{\sigma} = \frac{\Delta n}{n} + \frac{\Delta\mu}{\mu} \tag{6.13}$$

$\Delta n/n$ is negative and is given by $(q - q_o)/q_o$; $\Delta\mu/\mu$, on the other hand, is positive, and is approximately given by

$$\frac{\exp\left[- e(\phi_o - V_2)/kT\right] - \exp(- e\phi_o/kT)}{\exp(- e\phi_o/kT)}$$

Eqn (6.13) becomes

$$\frac{\Delta\sigma}{\sigma} = \exp(eV_2/kT) - \tfrac{1}{2}\left[1 + (1 + V/\phi_o)^{\frac{1}{2}}\right] \tag{6.14}$$

Depending on T, V_2, V, or ϕ_o, $\Delta\sigma/\sigma$ can be positive or negative. Consider a field of $\sim 10^4$ V/cm in a film of mean crystallite size 2000 A^o. The voltage drop, V, across each barrier is ~ 0.2 V.

For low carrier density films:

Initial barrier height, $\phi_o \sim 0.04$ V.

Since $V(= 0.2\ V) > 4\phi_o(= 0.16\ V)$, $\phi_2 \rightarrow 0$, or $V_2 \rightarrow \phi_o$.

At room temperature, $eV_2/kT \sim 0.04/0.025 \sim 1.6$.

Hence,

$$\Delta\sigma/\sigma \sim \exp(1.6) - \tfrac{1}{2}\left[1 + (1 + 0.2/0.04)^{\frac{1}{2}}\right]$$
$$\sim 5 - 1.7, \quad \text{which is positive.}$$

For high carrier density films:

$\phi_o \sim 0.003$ V, typically (see Fig 4.3).

V is now much larger than $4\phi_o$, the critical voltage.

Again, at room temperature, $eV_2/kT \sim 0.003/0.025 \sim 0.12$, giving $\Delta\sigma/\sigma$ now negative.

It does appear that the conductivity behaviour in this field range can be accounted for in terms of barrier trapping, for temperatures below about 300 °K. For high temperatures, Eqn (6.14) would always give a negative $\Delta\sigma/\sigma$, contrary to what is observed (see j-$\mathcal{E}$ characteristics at 296 and 350 °K, Fig 6.3). As discussed in Chapter Five, a high density of carriers is present at high temperatures, and the barriers cease to be important, since bulk behaviour (as suggested by the mobility peak) begins to play a role. Eqn (6.14) is therefore expected not to hold, and the discrepancy must be considered in the light of effects other than that due to the barriers.

(3) The breakdown region

In this region, generally for $\mathcal{E} > 15\times10^3$ V/cm, conductivity increases very rapidly. Prior to this rapid increase, certain samples exhibit a saturation region, due to the filling up of boundary states, similar to that observed in Ge bicrystals (M7). The current pulse begins to assume a rising top, indicating electron-hole pair generation. Whereas, previously, the increase in conductivity was due to a mobility increase (for low carrier density films), there is now the additional increase of carriers. A further increase in the applied field would cause the current to rise vertically. This usually leads to the destruction of the film by evaporation.

Fig 6.4 is an oscilloscope picture (typical) of a sample about to breakdown. The current top rises linearly with time, indicating an exponential increase in electron population, while the voltage top falls slightly as sample resistance decreases. The applied field in the sample was about $\sim 15\times10^3$ V/cm and the generation rate was estimated at $\sim 2.5\times10^7$ electron-hole pairs/sec. This generation

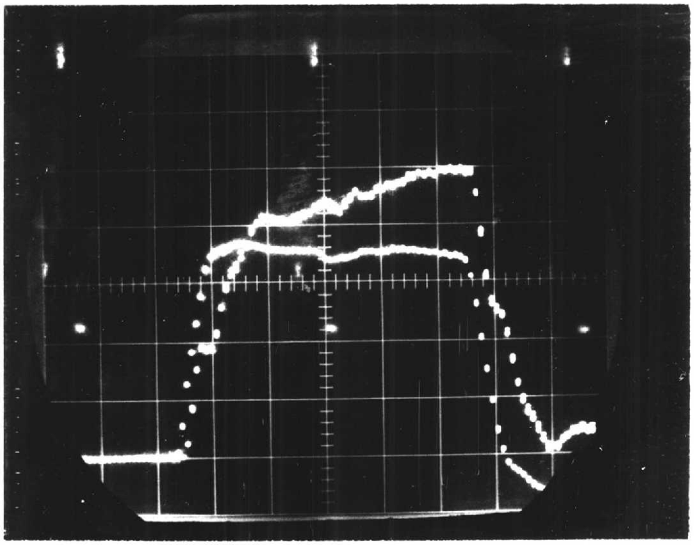

Fig 6.4: Current and voltage waveform across a 0.002"-gap sample. The rising current top indicates carrier multiplication.

Applied field - 1.5×10^4 V/cm

Current - 5×10^5 A/cm^2

Pulse duration - 10 nsec

rate is only an apparent one, since carrier trapping at boundary states and surface states has not been allowed for. In bulk InSb, McGroddy and Nathan (M12) obtained a figure of 2×10^7 electron-hole pairs/sec at $\mathcal{E} = 300$ V/cm.

For voltage pulses of the micro-second duration and longer, rising current tops at relatively low fields, $\sim5\times10^3$ V/cm have been observed. This was attributed to carrier multiplication due to Joule heating. Fig 6.5 shows the variation of the breakdown field, $\mathcal{E}_{crit}$, with pulse duration. Heating effects can be ruled out from 10 nsec pulses. Consequently, rising current tops must be due to genuine high-field-induced carrier generation. Some possible mechanisms will now be considered.

(1) Impact ionisation of donor impurities

In InSb, because of the proximity of the Fermi level to the conduction band edge, a certain amount of deionisation is always associated with the donor impurities (Sec 5.5.2). Since there is no energy requirement, due to the fact that the donor level is located at the conduction band edge, the breakdown field (should this be the mechanism) is expected to be low. Although impact ionisation of shallow acceptors (0.005 eV) in p-type bulk InSb has been observed (G8), it seems rather unlikely that this is the mechanism in thin films.

(2) Zener breakdown

Though Zener breakdown is confined essentially to dielectrics (Z2), such a mechanism has been found to operate in very thin p-n junctions of Si and Ge (M8, M10). Although the overall field is well below the critical field needed for Zener breakdown, the local field across the junction may be sufficiently high to make internal

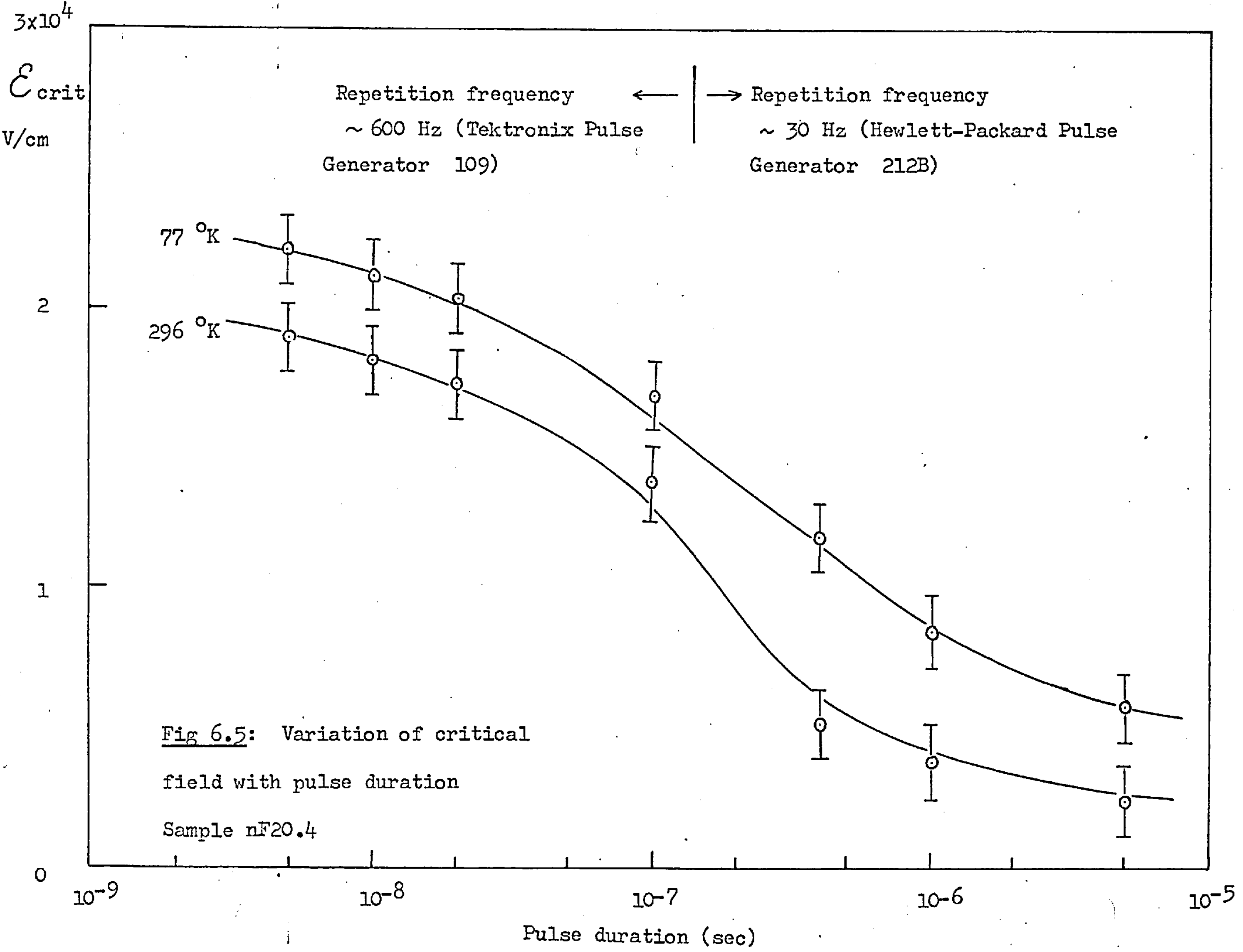

Fig 6.5: Variation of critical field with pulse duration

Sample nF20.4

field emission possible. According to Zener, the transition rate for an electron to pass from the valence band to the conduction band, for InSb, is

$$\gamma = 1.56 \times (10^7 - 4.8\times10^7/\mathcal{E}) \tag{6.15}$$

where the electric field, $\mathcal{E}$, is in V/cm. It is obvious from the equation that for any significant generation of electron-hole pairs, the electric field, $\mathcal{E}$, has to be of the order of 10^6 V/cm. The highest field experienced in the investigation is two orders of magnitude down; it is conceivable that the local field at the potential barrier, $\mathcal{E} = -d\phi(x)/dx$, could reach the critical value, just as in the case of very narrow p-n junctions.

From Eqn (4.30), taking a filling factor of 0.01, the barrier depth is estimated at ~ 100 A°, which gives a maximum field across the grain boundary of approximately 0.4 V/100 A° = 4×10^5 V/cm.

(3) Avalanche breakdown

Earlier, it was pointed out avalanche cannot take place in a sample less than about 3 mm in length, because the multiplication process involves a time of some 2 - 3 nsec. In bulk InSb, with a field of about 300 V/cm, this consideration ensures that the electrons would be able to accelerate and gain sufficient kinetic energy to bring about impact ionisation. In thin films, a field of $\sim 2\times10^4$ V/cm produces a voltage drop of ~ 0.4 V across each potential barrier (in a film of 2000 A°). From the energy point of view, an electron dropping through such a potential should be able to impact ionise (T4).

Both Zener and avalanche mechanisms could probably account for the breakdown. It is difficult to identify them separately, since both of them arise as a result of the presence of the grain boundaries. There is, however, stronger evidence pointing to the avalanche process, since the critical (breakdown) field strength corresponds to the 'necessary' voltage drop across each barrier for this process. Fig 6.6 is a plot of the critical field as a function of film thickness. There is a definite trend for thinner films to exhibit higher breakdown field. Ideally, $\mathcal{E}_{crit}$ should be shown as a function of the mean crystallite size, d. This would reduce the large scatter. If the critical voltage, V, does in fact determine the breakdown strength, then ($\mathcal{E}_{crit} \times d$) should be a constant equal to V. It should be interesting to verify this by more careful experiments. The local field, $-d\phi/dx$, responsible for Zener breakdown, should not be too highly dependent on the applied field and for this reason (as well as for the reason given above), this mechanism can be dismissed.

One notable difference between the thin film and the bulk characteristics is that, while the breakdown current in bulk is of the order of 10^4 A/cm^2, that in thin films is of the order of 10^5 A/cm^2. The data represents a difference of 10^3 times in the respective power dissipation ($\sim 10^6$ W/cm^3 in bulk and $\sim 10^9$ W/cm^3 in films). From theoretical considerations, Pinsker and Sandomirskii (P11) have shown that for the same electric field, heating occurs to a lesser extent in thin films than in bulk, due to a greater energy loss from the larger surface area associated with thin films. Other hot electron effects, such as plasma oscillation, Gunn effect, etc, appear to be absent.

Measurements were also made on p-type films

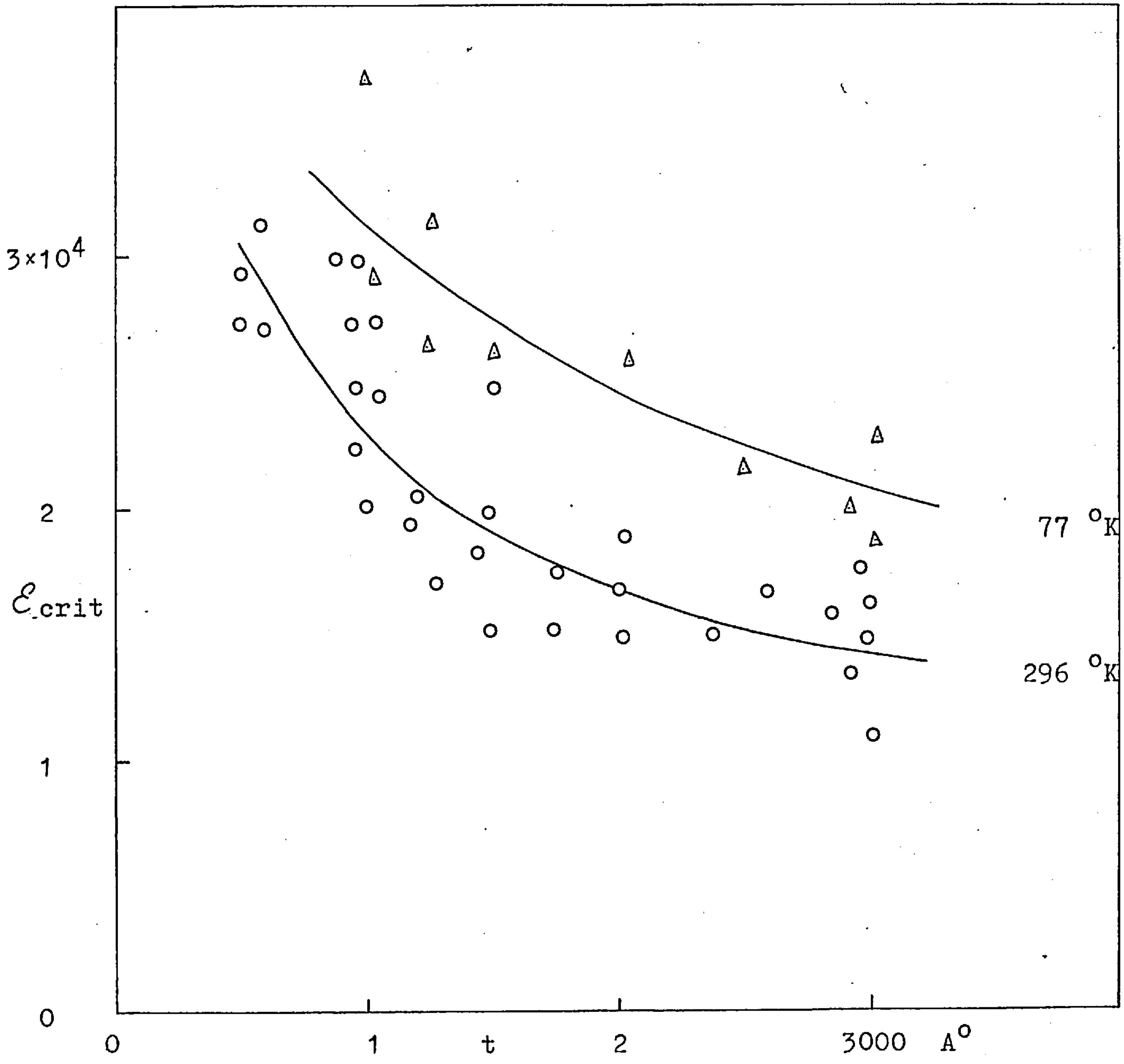

<u>Fig 6.6</u>: Breakdown field as a function of film thickness

using rather unsatisfactory contacts. j-$\mathcal{E}$ characteristics, similar to those given in Fig 6.2, were obtained. The breakdown field was found to be somewhat higher ($2 - 3\times10^4$ V/cm), which might be due to non-ohmic contact resistance. A hole-initiated avalanche gives a higher breakdown field in bulk (S14), but is not expected to alter the breakdown field strength in films, since in the latter case, the breakdown process depends possibly, again, on a hole falling through the 'necessary' potential. The experimental data are doubtful, until the effects of the non-ohmic contacts can be eliminated.

6.5.2 The field effect

It has been demonstrated in Chapter Five, that for low fields, a positive gate voltage enhances the electron mobility. This was interpreted as an increase in the electron mean free path, brought about by a lowering of the potential barrier. If the potential barriers are truly responsible for the increase in the breakdown field, by limiting the mean free path through which the carriers must accelerate (as in bulk), then it should be possible to alter $\mathcal{E}_{crit}$ by modulating the barriers with a dc gate field, applied orthogonally.

Fig 6.7 shows the j-$\mathcal{E}$ characteristics, at 77 °K, with $V_g = -1$, 0 +1 kV. The sample was 2100 A° thick with a room temperature mobility of $\sim$2500 cm^2/V sec and a barrier height, $\phi_o \sim 0.04$ V. But for a difference in the slope of these curves, due to a change in mobility and carrier concentration, the gate field does not appear to produce any significant change in $\mathcal{E}_{crit}$. It can be inferred from this, if it is true, that the critical field is independent of the barrier height, modulated or not modulated by a gate field. Such a ϕ-independence would

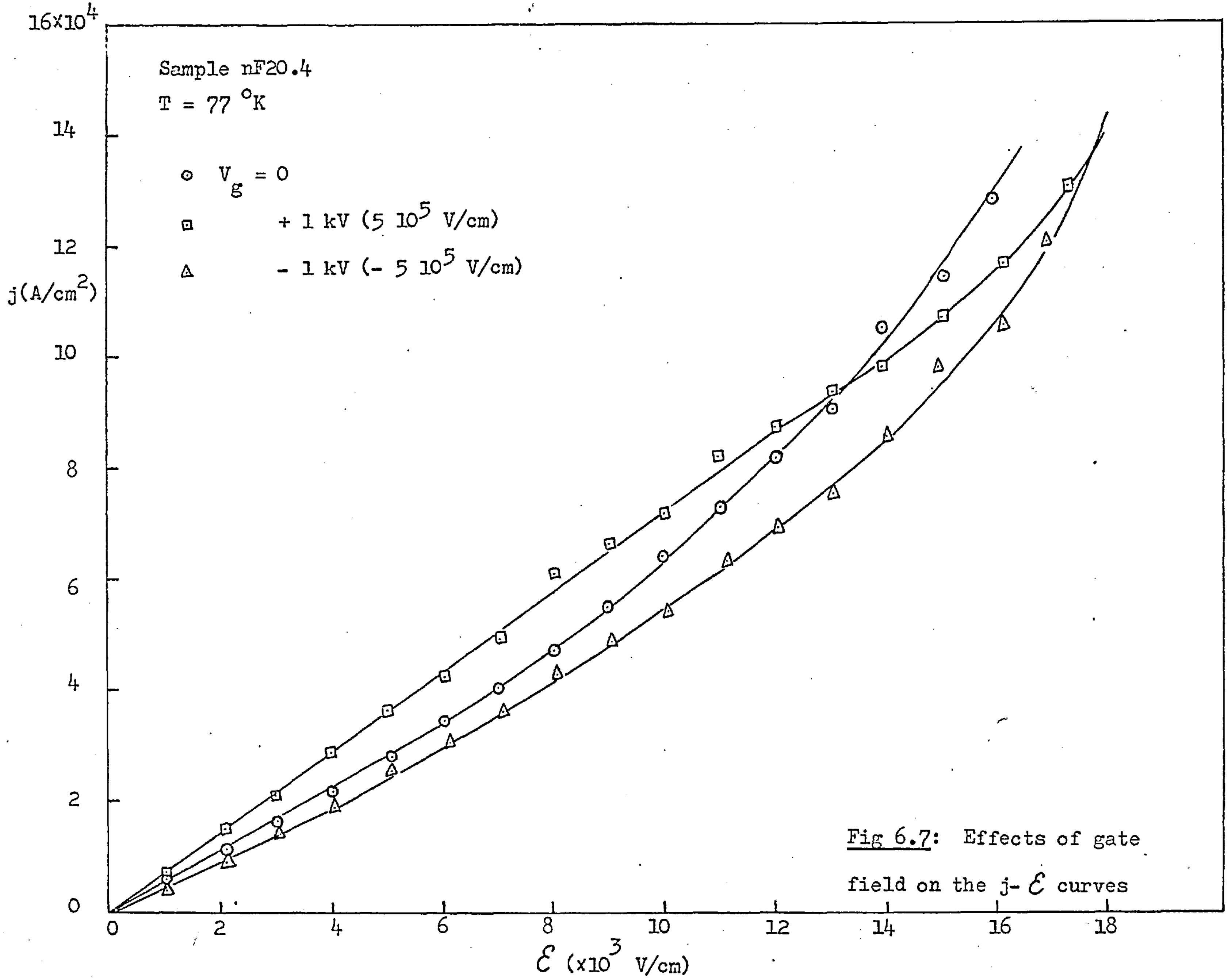

Fig 6.7: Effects of gate field on the j-$\mathcal{E}$ curves

arise because the applied voltage is in excess of the critical voltage, $4\phi_o$, as discussed previously, and this would support Eqn (6.8).

If avalanche does in fact occur, the distance through which the carriers accelerate before impact, must be shorter than the low-field mean free path, and therefore independent of the actual crystallite size. $\mathcal{E}_{crit}$ depends on the crystallite size only to the extent that the size determines the voltage drop across each boundary for a given field; carrier multiplication is still determined by the critical voltage drop across each barrier of approximately 0.4 V.

6.5.3 Field-dependent resistivity

High-field pulse measurement of thin films at liquid nitrogen temperature presents impedance matching difficulties as a result of increased sample resistivity. This could be overcome by increasing the sample width and decreasing the length. As the field increases, it was found that while the current pulse maintained a flat top for most of the duration, 'ringing' for the first 2 - 3 nsec appeared. This was also accompanied by a train of reflected pulses (much attenuated) after the main pulse. Similar observation was made when the sample resistance was much higher than 50Ω, eg 1 kΩ. The tentative inference was that resistivity increased after the application of a pulse, so that the sample presented a higher resistance to the subsequent pulses. A low dc measurement made about 5 sec after the removal of the pulse, indeed confirmed the increase. It was also noted that the sample resistance decayed back to its initial value (before the application of a voltage) after several hours. At room temperature, no 'ringing' was observed and resistance measurement some 5 sec after application of a field did not indicate any resistivity change. This does not mean that a resistivity change did not in fact occur, but probably the decay time is short. Since the current monitor has a rise-time of about 2 nsec, a decay time shorter than this can not be recorded on the oscilloscope. Furthermore it was also found that such field-dependent resistivity could be controlled by a gate field. Fig 6.8 shows the variation of sample resistance with applied field for both positive and negative gate fields.

For positive V_g, $R(\mathcal{E})$ increases with $\mathcal{E}$ and saturates around the breakdown field. For negative V_g the increase is much less. And in fact, for $V_g = -1.5$ kV (corresponding to a gate field of $\sim 4.2 \times 10^5$ V/cm), $R(\mathcal{E})$ is practically independent of $\mathcal{E}$.

Fig 6.9 shows the variation of resistivity, $\rho(\mathcal{E})$, for four n-type samples and one p-type sample[+]. All the n-type samples show resistivity increase with $\mathcal{E}$, except nF22.4, which shows a decrease. All p-type samples, however, exhibit resistivity decrease.

The increase in resistivity after the application of a voltage pulse, of 2 orders of magnitude, from $\mathcal{E} = 0$ to $\mathcal{E} \sim 2 \times 10^4$ V/cm, would suggest carrier depletion from the crystallite bulk. Trapping at dangling bonds at dislocations may be neglected, since this occurs only during the period of the pulse, and the accepted electrons would probably have completely detrapped by the time the resistivity observation was made. The long decay time indicates some very slow trapping mechanism, such as due to slow states, possibly located at the oxide or the semiconducto

---

[+] The effects of the non-ohmic contacts are assumed to be constant, so that $\rho(\mathcal{E})$ variation could reflect p-type behaviour.

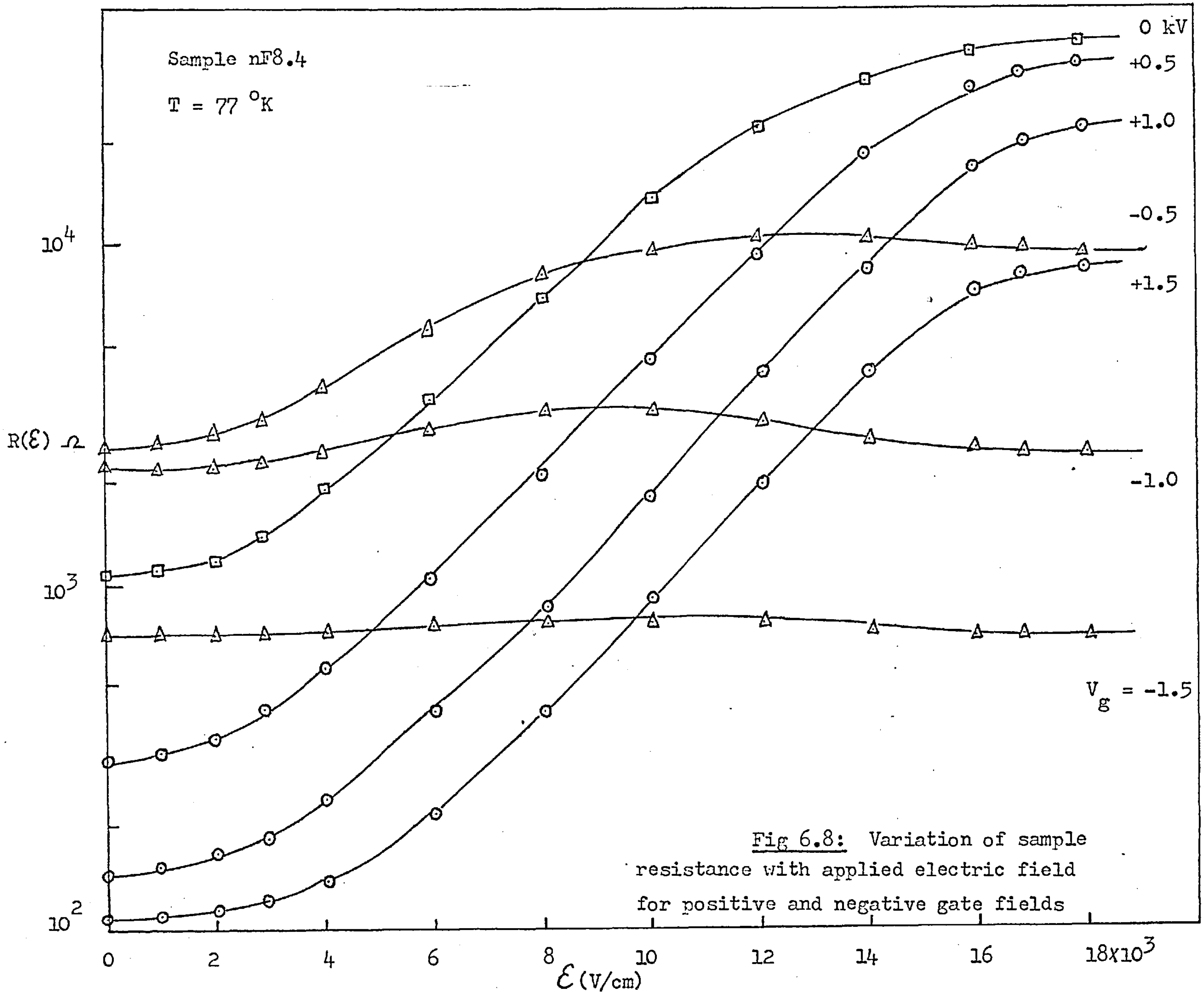

Fig 6.8: Variation of sample resistance with applied electric field for positive and negative gate fields

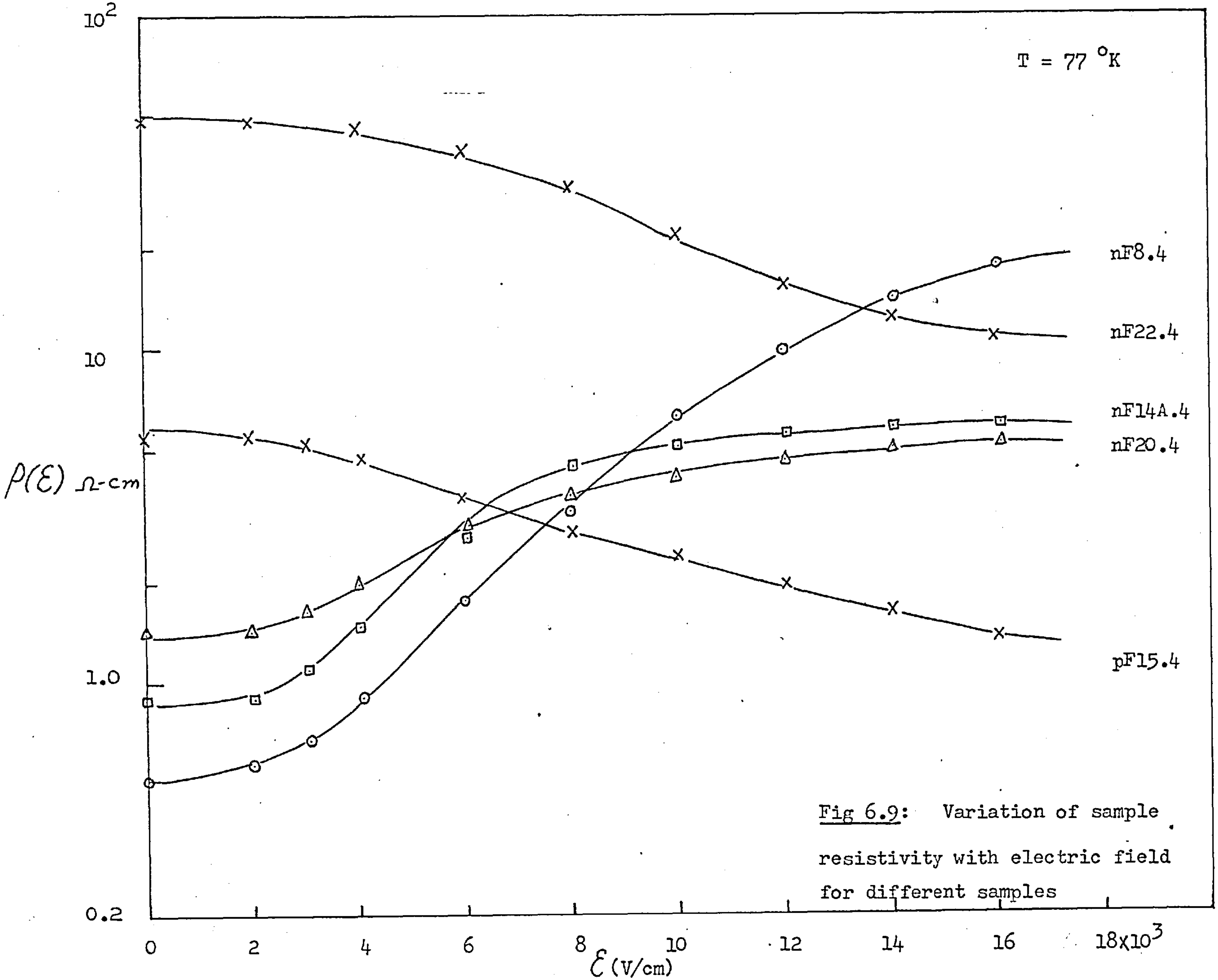

Fig 6.9: Variation of sample resistivity with electric field for different samples

-insulator interface.

For low fields, resistivity does not change; there is no trapping. Under moderate fields, a lowering of barrier potential leads to enhanced injection lf electrons from the contact. At higher fields, carrier multiplication makes trapping even more favourable. Trapping of excess electrons takes place in a time small compared to 10 nsec. When the field is removed, the trapped electrons detrap but at a very slow rate. It may be assumed that the traps are energy wells into which the excess electrons fall. The probability of detrapping would be proportional to exp (E_t/kT), where E_t is some trap energy. The exponential temperature dependence might account for the fact that no resistivity change could be detected at room temperature, i.e. the decay time, if trapping does occur, is short (much less than 5 sec). In fact, the sample resistivity (at 77 $^{\circ}$K) can be brought back to 'normal' by warming the sample to room temperature and cooling it back again.

This model would also explain the gate field dependence of the $R(\mathcal{E})$ curves in Fig 6.8. A positive V_g, decreases the surface potential, enhancing trapping. Saturation is reached when the slow states are filled up, which occurs in the vicinity of the breakdown field (when carrier multiplication increases the excess electrons rapidly). A negative V_g, on the contrary, increases the surface band bending, making trapping more unlikely.

The preceding argument applies to n-type films. For p-type samples, assuming a downward band bending at the surface (to the upward bending in n-type films), the same argument would lead to a rsisitivity decrease. This behaviour is often shared by very thin n-type films (nF22.4) less than 1000 A$^{\circ}$, which will be shown later to have p-type surface.

It will be appreciated that electron depletion alone is not the sole cause of the resistivity increase. Mobility reduction due to the barrier effect plays just as important a role, if not more. The evidence available at this stage does not justify a more detailed treatment of this problem. In the next chapter, the surface band bending and the trapped electron density measured as a function of the applied field are given. These allow a more quantitative picture of the slow state trapping model to be presented.

6.6 Discussion

Unlike in bulk single crystals, where carriers accelerate to high energy over a distance of 2 - 3 mm to achieve impact ionisation, avalanche in polycrystalline films involves carriers dropping through the 'necessary' potential. The distance through which carriers travel in this case is probably of the order of the barrier width, perhaps ~ 100 A^{o}. Near breakdown, trapping of generated carriers could explain why the slope of the $j - \mathcal{E}$ curve is not as steep as it should be. In bulk, this is due to the pinch effect, which can be ignored here, since this process involves a time of the order of 10^{-7} sec (S14).

The recent work of Lile (L2) on the carrier generation rate and effective lifetime in InSb films, several μm thick, attributes the higher breakdown field (in this case, ~ 600 V/cm) to surface recombination. A recombination time of $\sim 10^{-10}$ sec has been measured. The recombination times in the present films are expected to be even shorter, and this might also contribute to some extent to determining the breakdown field strength.

It has been demonstrated by many authors (C10, A3, G5) that for plasma oscillation to occur, sufficient electron-hole pairs must be present. In thin films, excessive recombination and trapping at the surface might preclude the onset of this effect and possibly other high-field effects as well.

Measurements of $\rho(\mathcal{E})$ have also been made of a 1 µm film[4] ($\mu \sim 8000$ cm^2/V sec, $n \sim 10^{17}$ cm^{-3} at room temperature) at 77 °K. Resistivity varied very slightly with $\mathcal{E}$. In films of this thickness, the barrier effect is expected to be negligible and the space charge region comparatively small.

The conductivity, σ and σ^*, before and after the application of $\mathcal{E}$, is given by

$$\sigma = ne\mu \quad ; \qquad \sigma^* = n^* e \mu^* \tag{6.16}$$

where the asterisk denotes values after the application of a field. Now,

$$n = f_1(\phi_0, n_2) \quad ; \qquad \mu = f_2(\phi_0) \tag{6.17}$$

and

$$n^* = f_1(\phi_0^*, n_2^*) \quad ; \qquad \mu^* = f_2(\phi_0^*) \tag{6.18}$$

where n and n^* are related to $T(\mathcal{E})$, the rate of surface trapping. This rate can be obtained from the following equation

$$g(\mathcal{E}) = g_{obs}(\mathcal{E}) + r(\mathcal{E}) + T(\mathcal{E}) \tag{6.19}$$

---

[4] Prepared by A.M. Gulyaev (G4).

where

$g(\mathcal{E})$ is the actual generation rate,

$g_{obs}(\mathcal{E})$ is the observed generation rate (see Fig 6.4),

$r(\mathcal{E})$ is the surface recombination rate (bulk recombination rate may be assumed to be much smaller).

There is some uncertainty in $g(\mathcal{E})$. However, to the first approximation, Lile's expression may be applicable here. The surface recombination time of $\sim 10^{-10}$ sec, obtained by Lile for μm films, provides some idea of the magnitude of $r(\mathcal{E})$. The above equations, would in principle, allow the trapping rate to be calculated. Further work on carrier life-time, obtained from, for example, measurements of photoelectromagnetic and photoconductive currents (radiation-induced), is required.

CHAPTER SEVEN: AC Field-Effect Measurements

7.1 Introduction

The abrupt termination of the crystal lattice at the surface, results in a loss of periodicity. In crystals where the surface to volume ratio is high, the electronic properties of the material may be completely masked by the surface. This chapter is devoted to examining some of the surface properties. The surface conductance is measured as a function of a sinusoidal gate voltage, and by comparing the experimental data with theory, the surface band bending and surface trapped charge can be deduced. The experiment is carried out in conjunction with the high-field measurements, described in the last chapter, and the results provide a further insight into the breakdown mechanism.

7.2 Surface states

The solutions of the Schrödinger equation in a periodic lattice potential are in the form of Bloch functions, in which allowed electron energy levels corresponding to real $\underline{k}$ values are grouped into bands, separated by forbidden energy gaps. Tamm (T6) was the first to realize that in the presence of the surface, complex $\underline{k}$ values may describe quantum states that are physically possible. Treating a one-dimensional Kronig-Penney model and its subsequent extension to a three-dimensional lattice, he was able to predict the presence of localised states at the surface, whose energies lie within the forbidden energy gap of the material. Such surface states owe their origin solely to the termination of the crystal potential and are thought of as being due to unsatisfied 'dangling bonds'. Whilst Tamm considered an asymmetrical termination of the periodic potential, Shockley (S17) assumed a model that maintains perfect periodicity right up to the surface, at which point it is terminated symmetrically. Tamm and Shockley states constitute the so-called 'intrinsic' states.

If each surface atom is assumed to have one dangling bond, then the maximum density of surface states in a 'clean' surface is expected to be around 10^{15} cm^{-2}. Photoelectric measurements on cleaved silicon (in vacuum) have confirmed this figure (F7).

In thin-film transistors (TFT) and other devices, in which a change in conductivity is achieved by the application of an external electric field, the maximum charge density that can be induced is approximately 10^{13} cm^{-2}. Hence, in truly clean surfaces, conductivity modulation is unbotainable. In practice, however, the real surface is invariably covered with several atomic layers of foreign matter, or intentionally coated with an oxide layer. These surface impurities constitute the 'extrinsic' surface states, which together with the 'intrinsic' surface states, give rise to 'fast' states, characterised by time constants of $\sim 10^{-2}$ sec or less. In contrast to 'fast' states, 'slow' states are believed to be associated with impurities or charges (ions) within the oxide layer or remote from the semiconductor-oxide or semiconductor-mica interface. These states do not communicate readily with the semiconductor and have time constants ranging from seconds to hours.

Fast states can give rise to degradation in the performance of thin-film devices, while the slow states are responsible for the time dependence of the device characteristics (M4).

7.3 Definition of surface parameters

Like impurity levels in bulk crystals, surface states can donate or accept one or more electrons. This gives rise to a space-charge region beneath the surface and subsequent band bending. The various surface parameters associated with this charge transfer from bulk to surface are defined with reference to Fig 7.1.

The potential ϕ is defined by the equation

$$e\phi = E_f - E_i(z) \qquad (7.1)$$

where E_f is the Fermi level and $E_i(z)$ is the intrinsic Fermi level at a distance z beneath the surface, which is at $z = 0$. $E_i(z)$ runs parallel to the band edges and is usually near the mid-gap[+]. The potential barrier V is defined by

$$V(z) = \phi(z) - \phi_b \qquad (7.2)$$

and is the potential at the point z with respect to the bulk potential, i.e. at $z = \infty$. The total barrier height, which occurs at the surface, is given by

$$V_s = \phi_s - \phi_b \qquad (7.3)$$

where the subscripts b, s denote respectively bulk and surface values. It is useful to define dimensionless potentials by

$$u = e\phi/kT \quad ; \quad v = eV/kT \qquad (7.4)$$

[+] For parabolic bands and non-degenerate statistics, the intrinsic Fermi level is given by $E_i = \frac{1}{2}(E_c+E_v) - \frac{1}{2}kT \log(\frac{N_c}{N_v})$, all symbols having usual meaning.

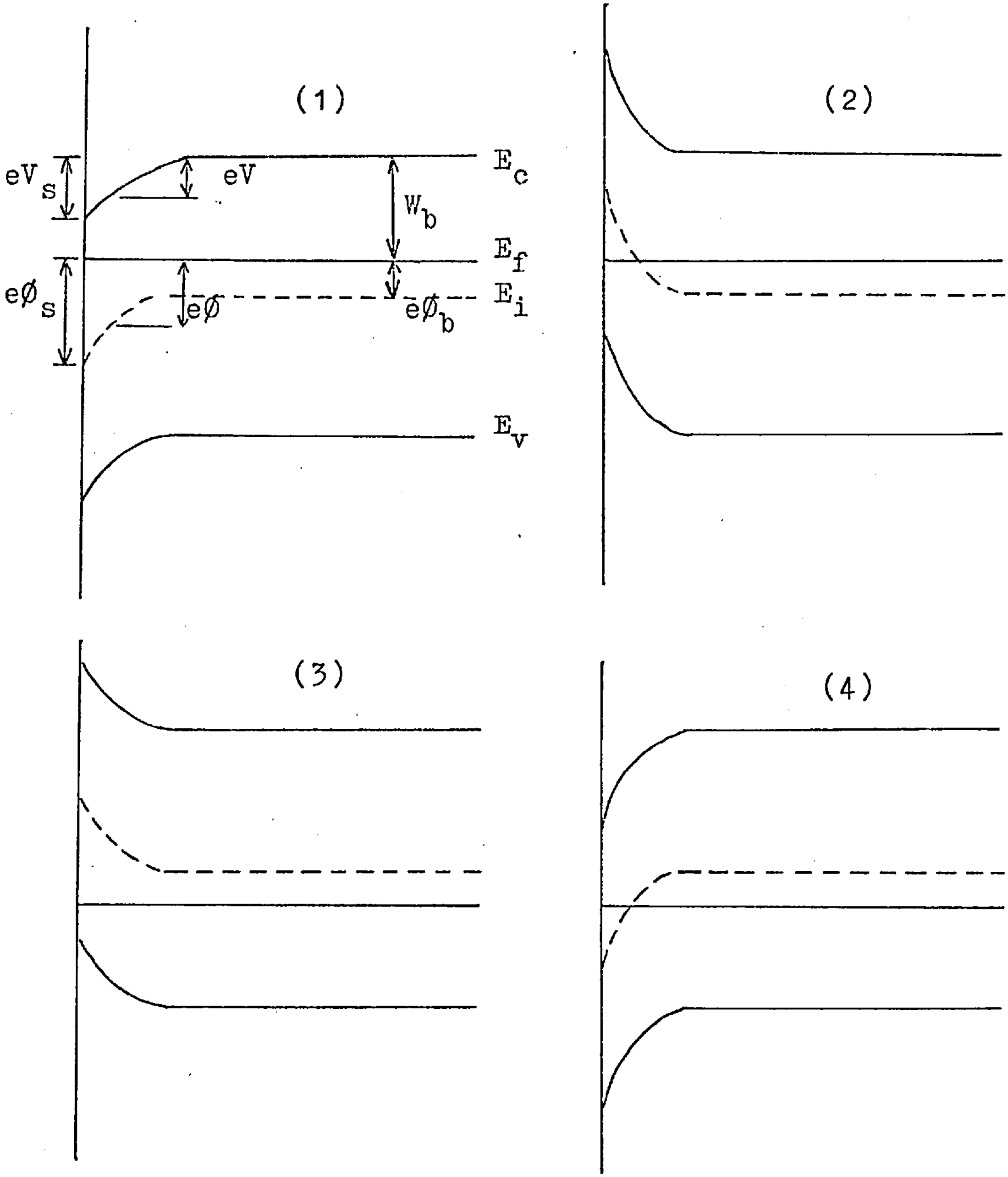

n-type semiconductor

(1) Accumulation

$V_s = \phi_s - \phi_b > 0$

(2) Inversion

$V_s = \phi_s - \phi_b < 0$

p-type semiconductor

(3) Accumulation

$V_s = \phi_s - \phi_b < 0$

(4) Inversion

$V_s = \phi_s - \phi_b > 0$

Fig 7.1: Surface parameters characterising the space-charge region and from Eqn (7.3), $v = u - u_b$.

At $u(z) = 0$, the carrier densities are intrinsic; $u_b = 0$ corresponds to an intrinsic bulk whilst $u_s = 0$ corresponds to an intrinsic surface. $v_s = 0$ means an absence of band bending at the surface, i.e. a flat-band condition.

When the majority carrier density in the space-charge region exceeds that in the bulk, the space-charge is termed an accumulation layer. For this to occur, v_s and u_b must have the same sign, i.e. both positive for n-type or both negative for p-type material. When v_s and u_b have opposite signs, a depletion or an inversion layer results; the majority carrier density in the space-charge region is now less than that in the bulk.

7.4 Theory

7.4.1 Poisson equation

If the donor and the acceptor surface states are assumed to exist in approximately equal numbers, then at thermal equilibrium, surface band bending would invariably result in a depletion layer, i.e. bands bend upwards for n-type 'bulk' and downwards for p-type 'bulk' as charges get trapped. Since overall charge neutrality must prevail, an equal but opposite charge is built up in the semiconductor. In metals, the space charge penetrates but a small depth, typically one atomic layer; in semiconductors, however, because of the considerably fewer free carriers, the penetration is appreciably more. The space charge gives rise to a potential whose variation with distance can be obtained by solving a Poisson equation, which in one dimension, takes the form

$$\frac{d^2V}{dz^2} = - \frac{\rho(z)}{\epsilon\epsilon_o} \qquad (7.5)$$

where V is the electrostatic potential defined by Eqn (7.2), and $\epsilon\epsilon_o$ is the constant of permittivity of the semiconductor. $\rho(z)$ is the net space charge density, within the crystallites, due to mobile carriers and static ionised impurity atoms, and is given by[4]

$$\rho(z) = e(p + N_d^+ - n - N_a^-) \tag{7.6}$$

where p, n are the mobile holes and electrons in the valence and conduction bands, respectively, and N_d^+, N_a^- are the ionised donors and acceptors. Solution of the Poisson equation at the grain boundary region is a formidable two-dimensional problem, which will not be considered here. As far as ac field-effect experiments are concerned, it might be reasonable to assume that the charges induced are negligible at the grain boundaries, in view of the fact that the grain boundary surface is much smaller than the crystallite surface. The effect of the grain boundaries will be reflected in a change in the mobility of these induced carriers, as expressed in Eqns (5.11) and (5.12).

Eqn (7.5) has been solved by Kingston and Neustadter (K11) and also independently by Garrett and Brattain (G9), assuming complete ionisation of impurities, i.e. $N_d^+ = N_d$ and $N_a^- = N_a$, and a non-degenerate Boltzmann statistics. Seitwatz and Green (S18) extended the treatment further to include degenerate statistics and partial ionisation of impurities. The above treatment cannot be applied to InSb in view of its highly non-parabolic conduction band, and a usually degenerate electron population (J1). With an electron concentration of 10^{17} cm^{-3}, the Fermi level lies close to the conduction band edge and deionisation

---

[4] Deep traps, which usually dominate the characteristics of the space-charge region in wide-gap semiconductors (M4), are neglected here.

of impurities must certainly be taken into account. Substituting for the mobile and static charges in Eqn (7.6) with known expressions (which are functions of v and therefore of z), as given in Appendix D, Eqn (7.5) can be integrated once with respect to z to give

$$\frac{dv}{dz} = \pm \frac{F(v)}{F} \tag{7.7}$$

where the plus sign refers to a negative $v(z)$ and the minus sign refers to a positive $v(z)$. The effective Debye length L is given by

$$L = \left[\frac{\epsilon\epsilon_0 kT}{e^2(n_b + p_b)}\right]^{\frac{1}{2}} \tag{7.8}$$

where n_b, p_b are respectively the bulk electron and hole concentrations. The F function is defined by

$$\begin{aligned} F(\pm v) = \pm 2^{\frac{1}{2}} \Bigg\{ & A_d\left[\log \frac{1 + \frac{1}{2}\exp(-x_{fd} - v)}{1 + \frac{1}{2}\exp(-x_{fd})}\right] \\ & + A_a\left[\log \frac{1 + \frac{1}{2}\exp(+x_{fa} + v)}{1 + \frac{1}{2}\exp(+x_{fa})}\right] \\ & + \frac{2}{3} A_p\left[F_{3/2}(-v - x_{fv}) - F_{3/2}(-x_{fv})\right] \\ & + \frac{2}{5} aA_p\left[F_{5/2}(-v - x_{fv}) - F_{5/2}(-x_{fv})\right] \\ & + \frac{2}{3} A_n\left[F_{3/2}(+v - x_{cf}) - F_{3/2}(-x_{cf})\right] \\ & + \frac{2}{5} aA_n\left[F_{5/2}(+v - x_{cf}) - F_{5/2}(-x_{cf})\right]\Bigg\}^{\frac{1}{2}} \end{aligned} \tag{7.9}$$

where all symbols are defined in Appendix D. The complex

F-function, analogous to that given by Many et al (M4), is numerically evaluated.

The space-charge density, Q_{sc}, is defined as the total charge per unit surface area, which can be found by applying Gauss law at the surface, i.e.

$$Q_{sc} = \epsilon\epsilon_o \mathcal{E}_s \qquad (7.10)$$

where $\mathcal{E}_s = -dV/dz$, is the electrostatic field just beneath the semiconductor surface, being positive when directed from the surface outwards. Using Eqns (7.7) and (7.8),

$$Q_{sc} = (kT/e)\,\frac{dv}{dz}\,, \quad \text{ignoring the minus sign}$$

$$= e(n_b + p_b)\,LF_s \qquad (7.11)$$

where F_s is the F-function evaluated at $v = v_s$ or $z = 0$.

A useful parameter is the effective charge distance, L_c, defined as the position (measured from the surface) of the centre of the space charge and is given by the equation,

$$L_c = \int_0^\infty \rho(z) z\,dz \Big/ \int_0^\infty \rho(z)\,dz \qquad (7.12)$$

$\int_0^\infty \rho(z)\,dz$ is just the space charge density, Q_{sc}. Integrating Eqn (7.12) by parts and using Eqns (7.5), (7.7) and (7.11), it can be shown as by Many et al that

$$L_c = |v_s| L/F_s \qquad (7.13)$$

7.4.2 Excess surface-carrier densities

The excess surface-carrier densities are defined as the number of carriers per unit surface area in the space-charge region, with respect to their numbers at flat bands (i.e. for $v_s = 0$). The excesses, ΔN of electrons and ΔP of holes are given by the equations:

$$\Delta N = \int_0^\infty \left[n(z) - n_b \right] dz \tag{7.14}$$

and

$$\Delta P = \int_0^\infty \left[p(z) - p_b \right] dz \tag{7.15}$$

ΔN and ΔP are the changes in the carrier densities in the space-charge region and could therefore be positive or negative, but they must have opposite signs. Changing the variable of integration from z to v, Eqns (7.14) and (7.15) become

$$\Delta N = \int_0^\infty \frac{\left[n(z) - n_b \right]}{F} dv \tag{7.16}$$

and

$$\Delta P = \int_0^\infty \frac{\left[p(z) - p_b \right]}{F} dv \tag{7.17}$$

These integrals correspond to the G-integrals of Many et al, and because of their complexities, can only be numerically evaluated.

Juhasz (J1) defines two other excesses due to ionised impurities. These are the changes in the number of ionised donors, N_d^+, and acceptors, N_a^-, with respect to their numbers at flat bands, being given by

$$\Delta N_a^- = \int_0^\infty \left[N_a^-(z) - N_a^-(\infty) \right] dz \tag{7.18}$$

and

$$\Delta N_d^+ = \int_0^\infty \left[N_d^+(z) - N_d^+(\infty) \right] dz \tag{7.19}$$

where $N_a^-(\infty)$ and $N_d^+(\infty)$ are the flat-band values of the ionised acceptor and donor concentrations.

In terms of the surface excesses, the space-charge density, Q_{sc}, can now be written as

$$Q_{sc} = e(\Delta P + \Delta N_d^+ - \Delta N - \Delta N_a^-) \tag{7.20}$$

The surface conductance, $\Delta\sigma(v_s)$, defined as the change in sample conductance per square area of its surface resulting from a change in surface potential from 0 to v_s, is given by

$$\Delta\sigma(v_s) = e\left[\mu_{ns}(v_s)\,\Delta N(v_s) + \mu_{ps}(v_s)\,\Delta P(v_s)\right] \tag{7.21}$$

where now the surface mobilities of electrons and holes are functions of the surface band bending.

7.4.3 The field effect

In the field-effect experiment, a gate voltage, V_g, induces a charge, $Q_g(V_g)$, which is distributed between the space-charge region and the surface states, i.e.

$$- Q_g(V_g) = Q_{sc}(v_s) + Q_{ss}(v_s) \tag{7.22}$$

The space charge, Q_{sc}, is a function of v_s, through the surface excesses (Eqn (7.20)). The gate charge, Q_g, is known from the geometric capacitance of the insulator. Experimentally, the surface conductance, $\Delta\sigma$, can be measured as a function of Q_g. Since the conductance minimum is a unique function of v_s (M4, F7), then by aligning the experimental and theoretical surface conductance curves so that the minima coincide as in Fig 7.2, $Q_g(V_g)$

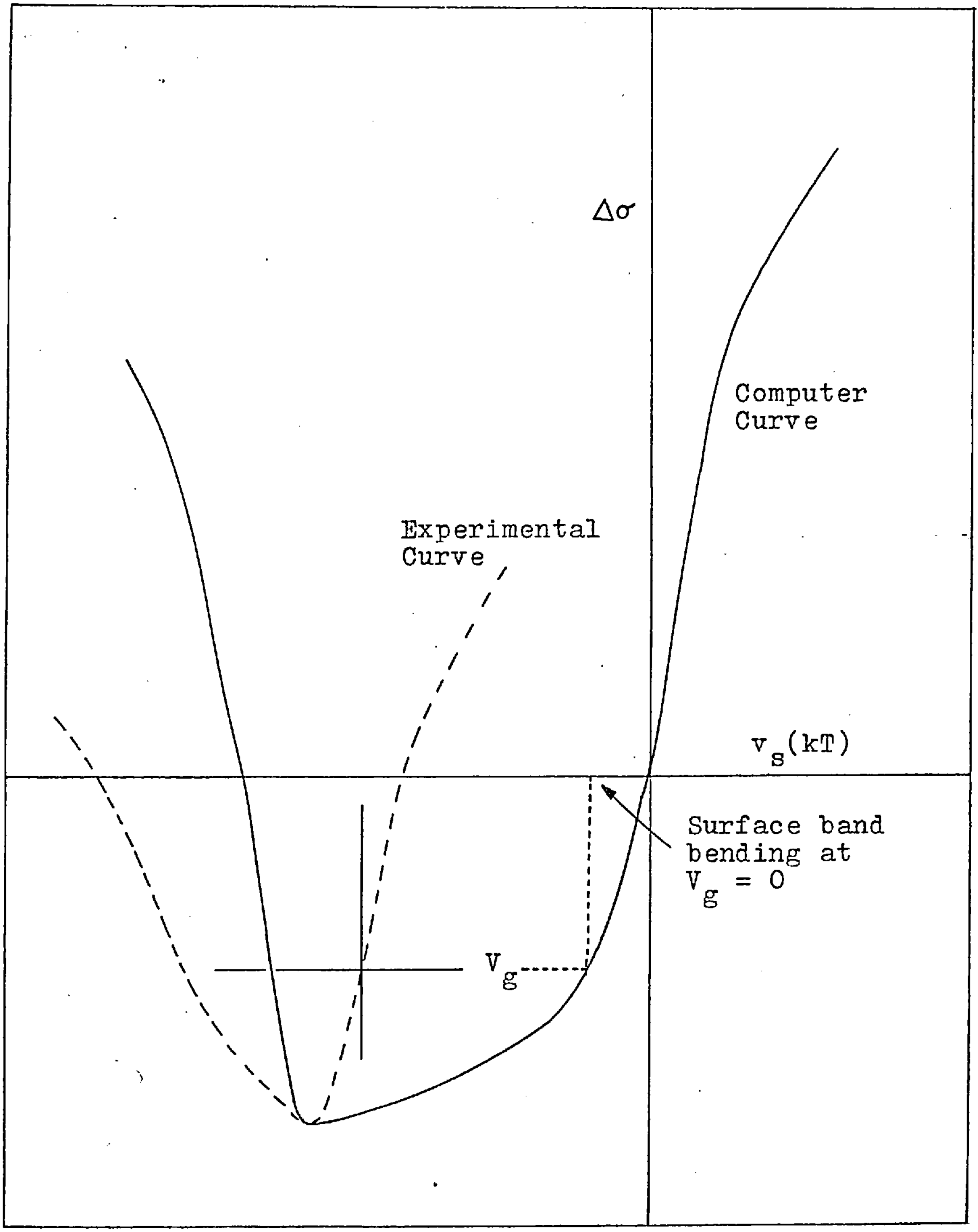

Fig 7.2: 'Aligning the conductance minima'

is thus calibrated (against Eqn (7.21)) as a function of v_s. From Eqn (7.22), the trapped surface charge, given by the horizontal difference between the two curves, can therefore be found as a function of v_s.

Putting $V_g = 0$, i.e. at quiescent condition, in Eqn (7.22), leads to

$$Q_{sc}(v_s^o) + Q_{ss}(v_s^o) = 0 \tag{7.23}$$

where v^o is the initial band bending; the trapped charge at the surface states now equals the space charge (charges have opposite signs).

7.5 Experimental technique

In the dc field-effect experiments (Chapter Five), all surface states participate, whatever their time constants, which may range from microseconds or less (fast states) to even several hours (slow states). Since slow states are present in much higher density than fast states (M4), they dominate the trapping mechanism and effectively determine the surface band bending, v_s^o, and the surface charge density, N_{ss}^o (= $Q_{ss}(v_s^o)/e$). DC fields are therefore not practical as a means of varying the surface potential. However, because of the long time constants associated with the slow states, their effect can be eliminated by using an ac gate field. Only those states would now actively participate in the trapping process, whose time constants are less than the periodic time of the ac field.

A block diagram of the field-effect circuit is given in Fig 7.3, and the actual set-up in Fig 7.4. The preparation of the sample has been described in Chapter

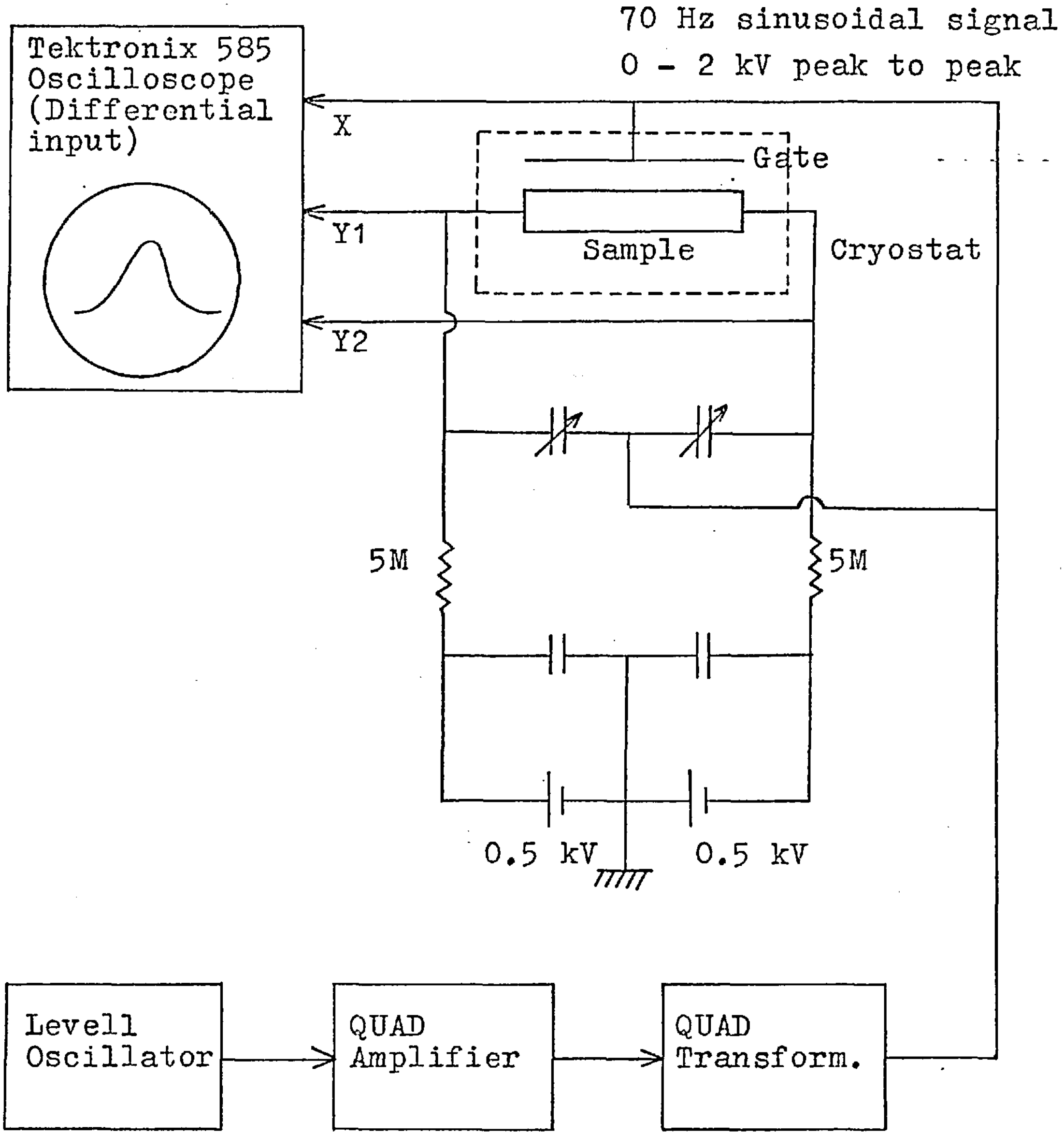

Fig 7.3: Block diagram of field-effect circuit

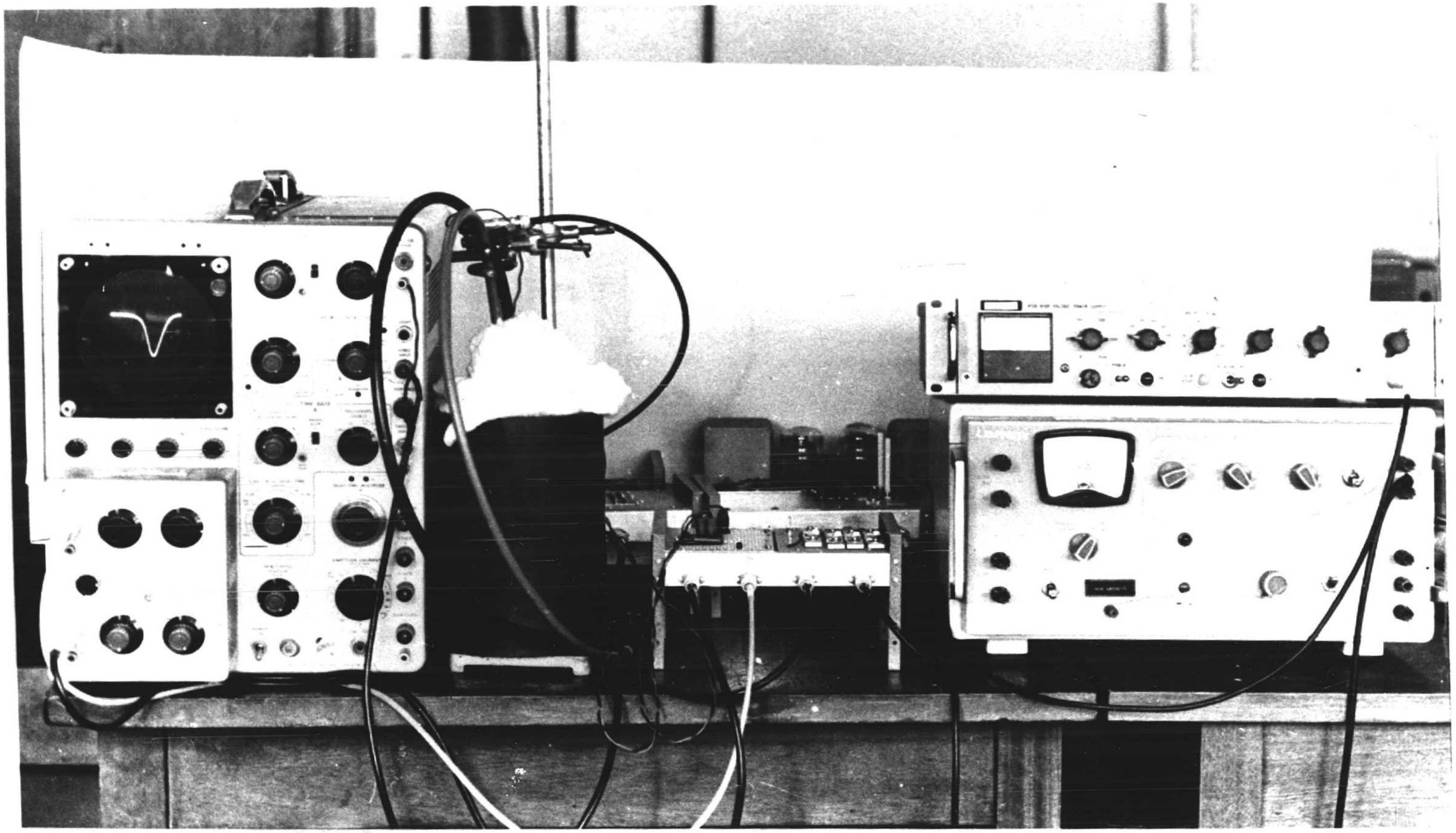

Fig 7.4: Apparatus for the Field-Effect Experiment

Five. Two power supplies (± 0.5 kV), in series with 10 MΩ, provide a constant measuring current, I_o, through the sample. The gate voltage is a 70 Hz sinusoidal signal with a variable peak-to-peak amplitude of 0 - 2 kV, produced by an oscillator-amplifier-transformer system. The gate voltage (properly attenuated) also forms the X-input to the Tektronix oscilloscope (type 585). The voltages at the ends of the sample are fed into the differential amplifier (Y1, Y2) to display the 'conductance' voltage as a function of the applied gate voltage.

One of the difficulties encountered was to prevent the induced voltage drop (produced by the gate voltage) from appearing in the output. This was achieved by adjusting the capacitor 'bridge' for minimum output with the power supplies shorted out. When the measuring current was switched on, the output was very nearly the field-effect signal. The induced gate signal can be further reduced by the use of a large measuring current, which in this case was 100 μA.

Facilities were also provided for the sample to be switched into the high-field measuring circuit of Fig 6.1, so that the field-effect characteristics could be measured after the application of a high voltage pulse.

The surface conductance, $\Delta\sigma$, is calculated from the formula

$$\Delta\sigma = \frac{l}{w} I_o \left(\frac{1}{V_\sigma} - \frac{1}{V_{\sigma 0}} \right) \qquad (7.24)$$

where

I_o is the constant measuring current, and

l, w are respectively the length and width of the sample.

V_σ is the 'conductance' voltage across the sample, at any gate voltage, and $V_{\sigma 0}$ is the value at $V_g = 0$.

7.6 Results

7.6.1 The field-effect curves

The field-effect curves for a typical n-type film, as a function of $\mathcal{E}$ (from low field up to breakdown) are shown in Fig 7.5; that for a p-type film and a very thin n-type film (less than 1000 A^o) are shown in Fig 7.6. What is shown in the oscilloscope pictures is the variation of the 'conductance' voltage with gate field. Eqn (7.24) must be invoked to find the surface conductance. Evaluating $\Delta\sigma$ for various V_g, and comparing the experimental data with the theoretical curve (given by Eqn (7.21)) as in Fig 7.2, $\Delta\sigma(V_g)$ was thus calibrated against the surface band bending, v_s (see Fig 7.7). From this calibrated curve, the surface charge density, N_{ss} and the field-effect mobility, μ_{fe} (given by the slope of the conductance curve), as a function of v_s could be obtained. However, what is of interest here, is the initial surface band bending and surface charge density at $V_g = 0$, v_s^o and N_{ss}^o. Typical values of v_s^o and N_{ss}^o at $\mathcal{E} = 0$ and $T = 77\ ^oK$ were found to be respectively -25 kT and 5.5×10^{11} electron traps/cm^2, for n-type films.

After subjecting the sample to successive high voltage pulses, the surface conductance minimum was observed to shift towards V_g positive, indicating a more negative v_s, and therefore an increased trapping of electrons in the surface states. n-type samples usually exhibit a surface conductance minimum in the negative V_g region for $\mathcal{E} = 0$; the minimum gradually shifts to the positive

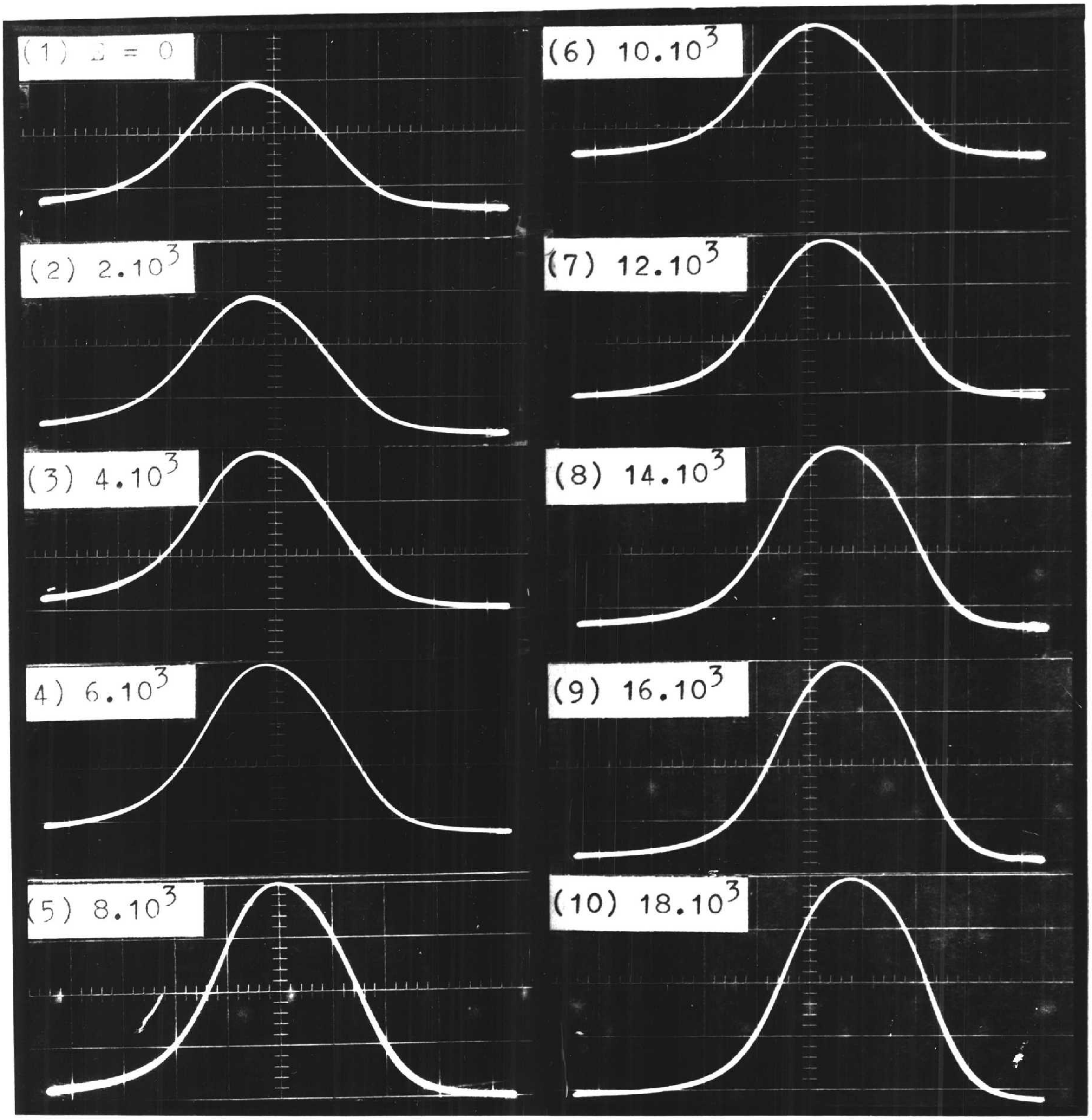

Fig 7.5: Field-effect curves, measured after application of 10 nsec voltage pulses. The applied field in V/cm is indicated in each picture, (1) - (10).

Horizontal axis - Sinusoidal signal approximately 1 kV peak to peak, at 70 Hz.

Vertical axis - Conductivity voltage
(1) - (5) 1 V/cm
(6) - (10) 2 V/cm

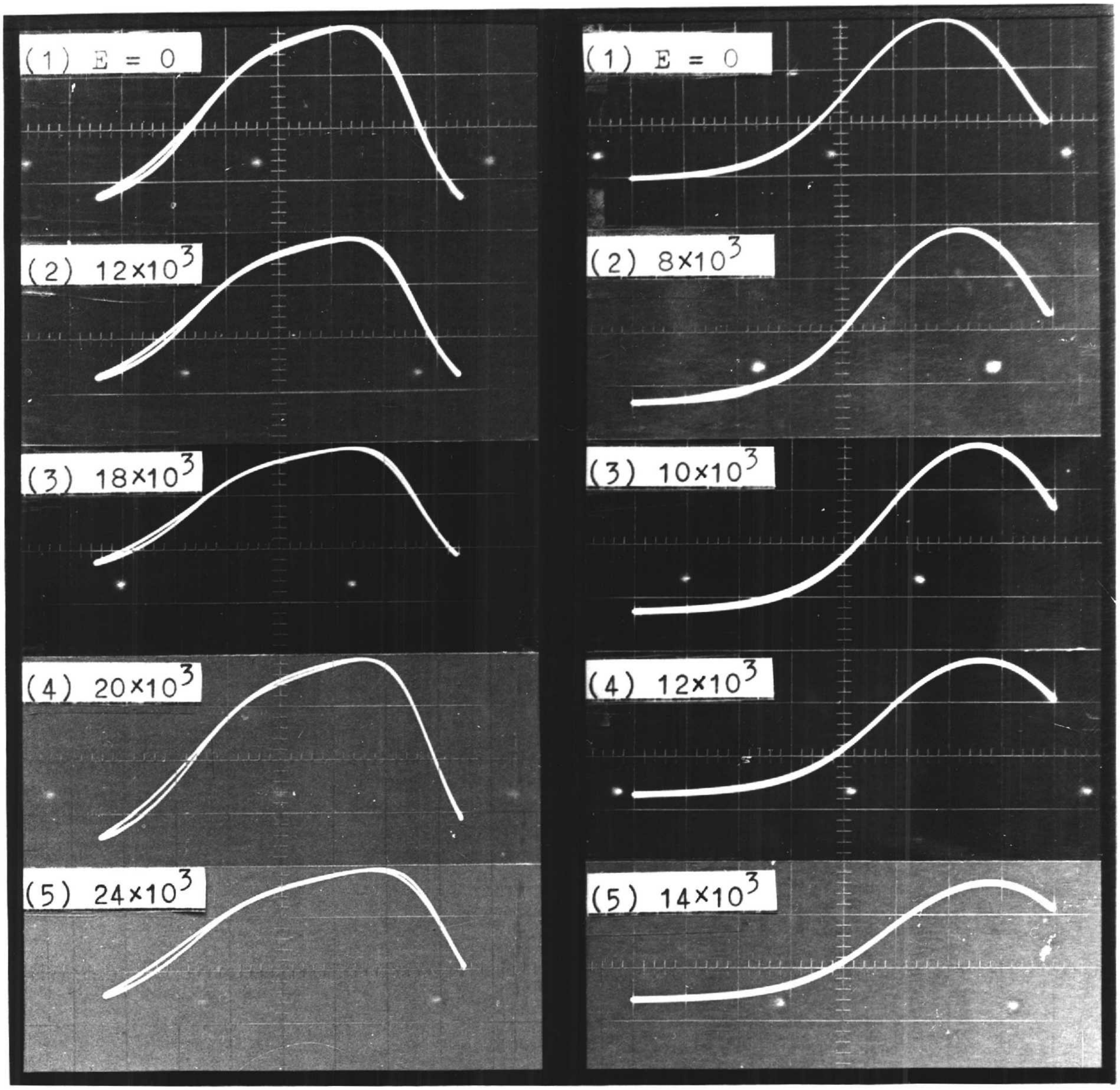

(1) p-type sample, pF15

Gate signal (horizontal)
- 0.8 kV peak to peak

Vertical Axis -
(1) - (3) 0.2 V/cm
(4) - (5) 0.1 V/cm

(2) Very thin n-type sample, nF22

Gate signal (horizontal)
- 1 kV peak to peak

Vertical Axis -
(1) - (5) 5 V/cm

Fig 7.6: Field-effect curves, at 77 °K

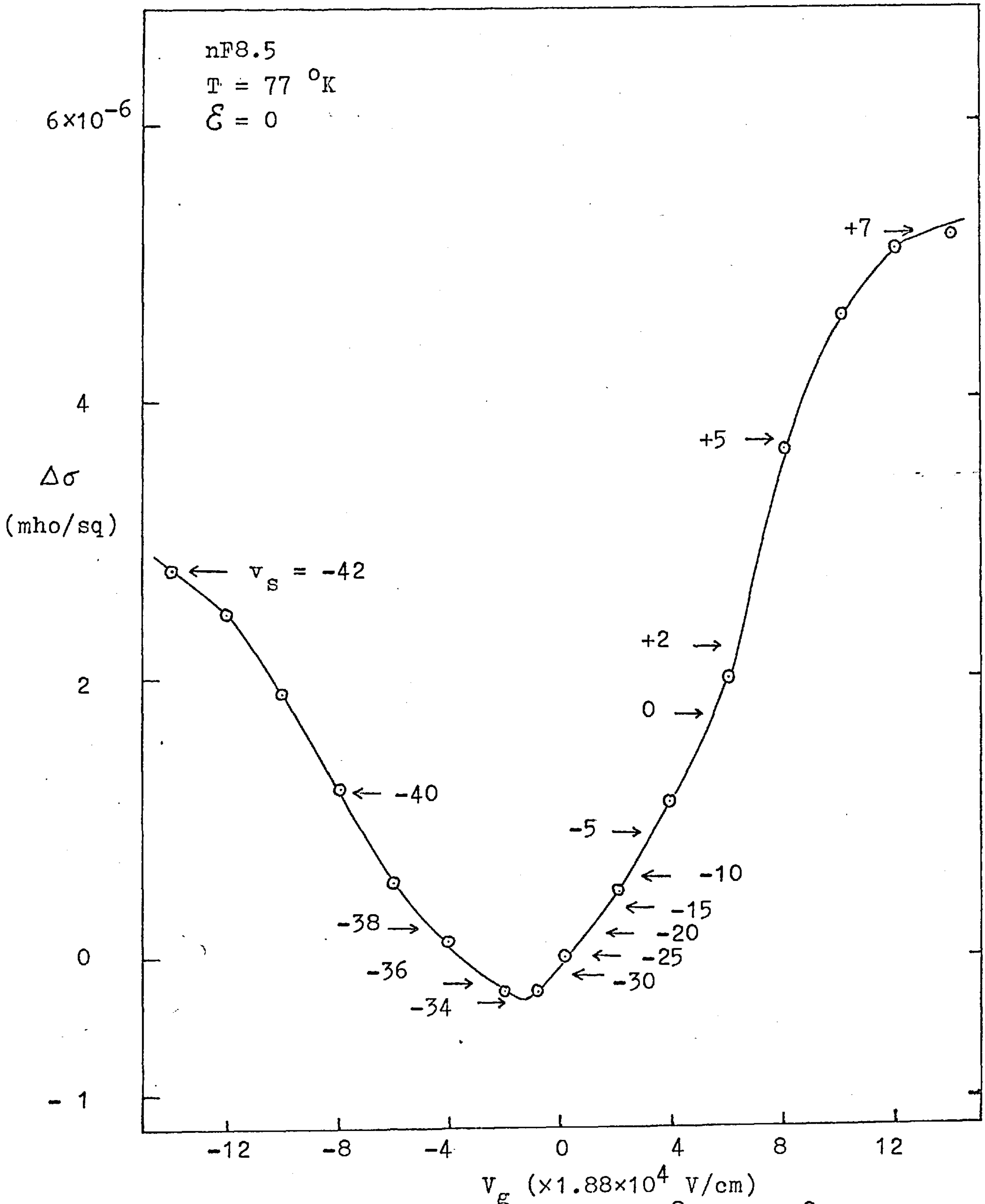

Fig 7.7: 'Conductance' curve (calibrated)

region near the breakdown field. This is clearly visible from Fig 7.5, for sample nF8.5. p-type films, on the contrary, have their minima in the positive V_g region and move into even more positive region as $\mathcal{E}$ increases. This behaviour is also shared by very thin n-type films, obvious from Fig 7.6. For the latter two cases, the minima shift could also be interpreted as an increase in electron trapping at the surface.

The variation of the surface conductance with V_g for various electric fields are shown in Fig 7.8 for an n-type sample and in Fig 7.9 for a p-type sample. From these curves, v_s^o and N_{ss}^o as a function of $\mathcal{E}$, are plotted in Fig 7.10 and 7.11. Samples nF8.5, nF14A.5, and nF20.5 have an initial band bending of about -25 kT, which increase to about -35 kT, when $\mathcal{E}$ reaches the breakdown field. Sample pF15.5 (p-type) has an initial positive bending of $+14$ kT and this changes to -2 kT in the vicinity of breakdown. Sample nF22.5 (~ 800 A^o) has an unusually high initial band bending of -37 kT and shows only a slight increase with $\mathcal{E}$. All n-type films show an increase in the surface charge density (negative) with $\mathcal{E}$. Sample pF15.5 has an initial positive charge in the surface states; however, near breakdown, this charge becomes negative.

The above results can be accomodated in a slow surface-state trapping model, with reference to the band diagram of Fig 7.12.

7.6.2 <u>Slow surface-state trapping model</u>

(1) n-type sample

Consider first a fairly thick n-type sample (~ 2000 A^o), so that a sizable 'bulk' region is present.

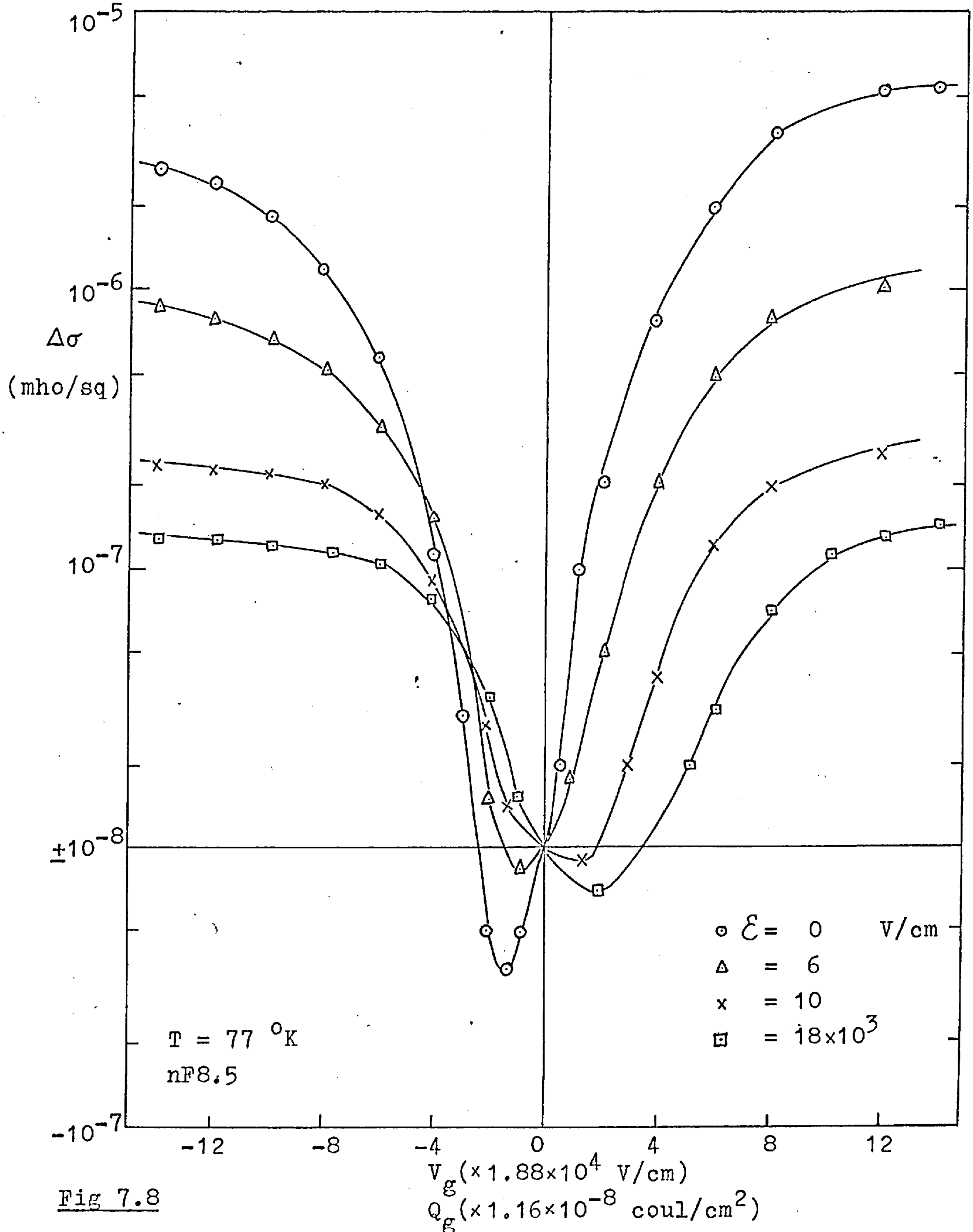

10^{-5}
10^{-6}
10^{-7}
$\pm 10^{-8}$
-10^{-7}
$\Delta\sigma$
(mho/sq)
-12
-8
-4
0
4
8
12
$V_g(\times 1.88\times10^4$ V/cm)
$Q_g(\times 1.16\times10^{-8}$ coul/cm^2)
⊙ $\mathcal{E}$ = 0 V/cm
△ = 6
× = 10
⊡ = 18×10^3
T = 77 °K
nF8.5

Fig 7.8

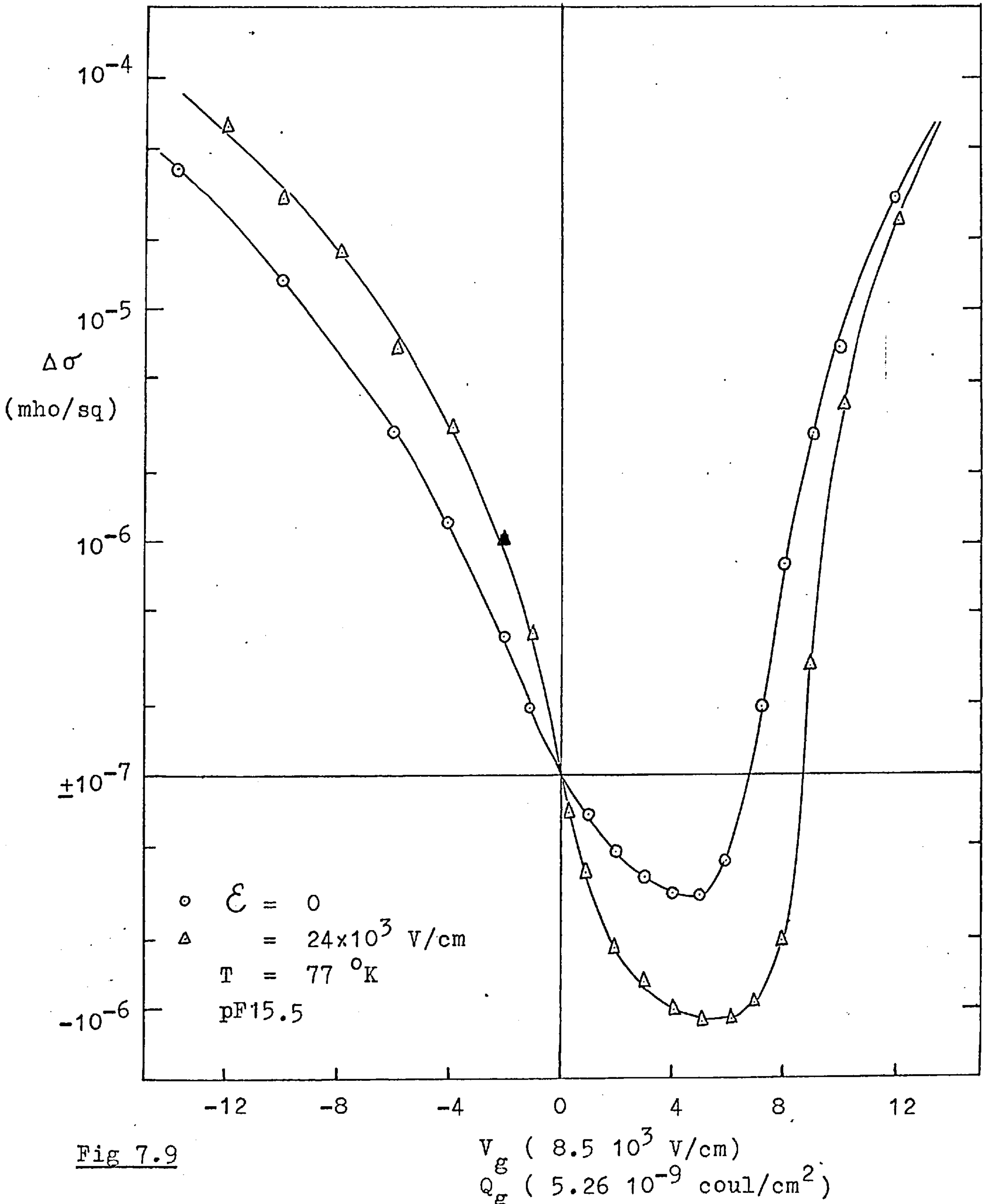
10^{-4}
10^{-5}
10^{-6}
$\pm10^{-7}$
-10^{-6}
$\Delta\sigma$
(mho/sq)
○ $\mathcal{E}$ = 0
△ = 24×10^{3} V/cm
T = 77 °K
pF15.5
-12
-8
-4
0
4
8
12
V_g (8.5 10^{3} V/cm)
Q_g (5.26 10^{-9} coul/cm^{2})

Fig 7.9

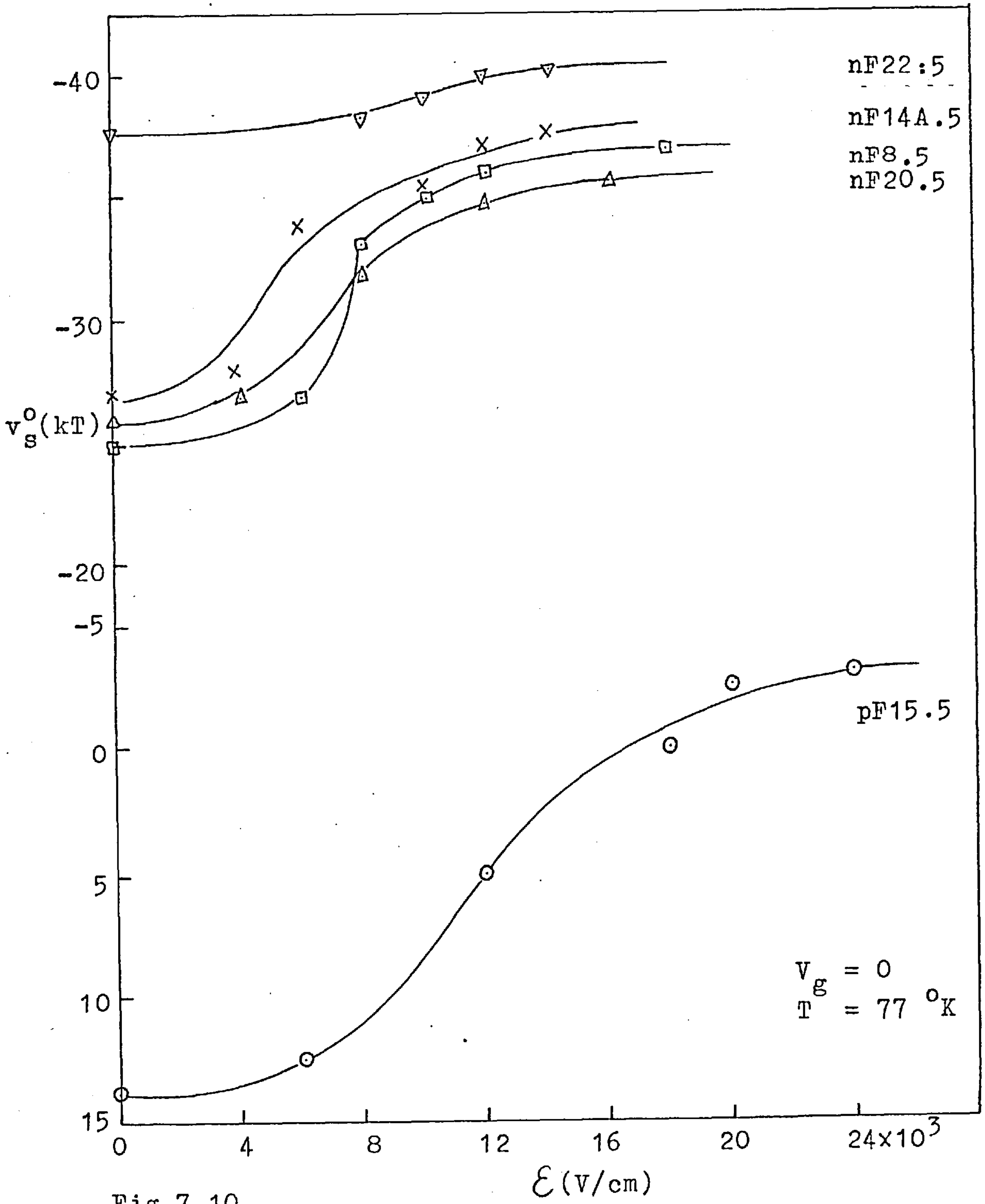
nF22.5
nF14A.5
nF8.5
nF20.5
pF15.5
V_g = 0
T = 77 °K
-40
-30
v_s^o(kT)
-20
-5
0
5
10
15
0
4
8
12
16
20
24×10^3
$\mathcal{E}$(V/cm)

Fig 7.10

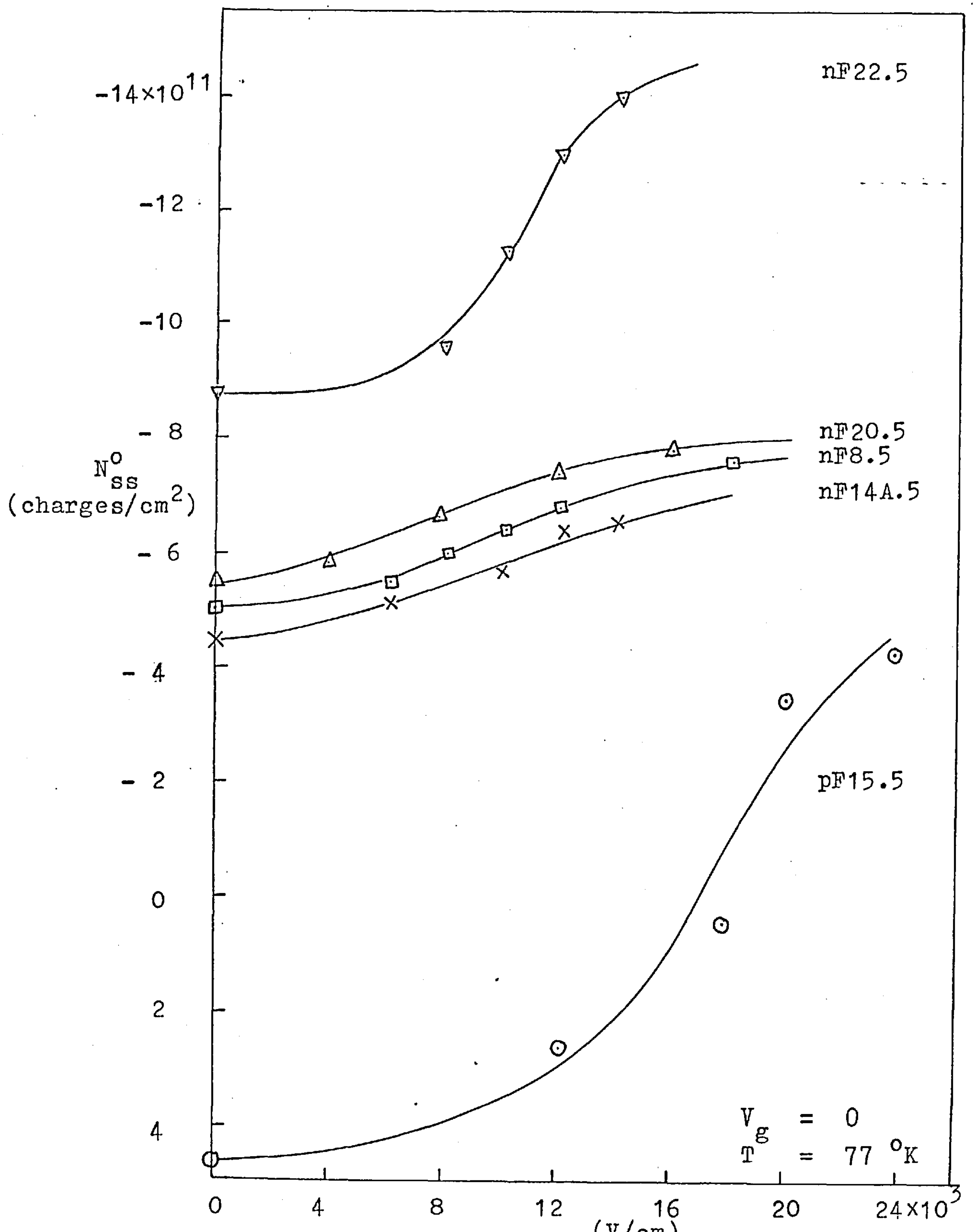
-14×10^11
-12
-10
- 8
- 6
- 4
- 2
0
2
4
N^o_ss (charges/cm^2)
0
4
8
12
16
20
24×10^3
(V/cm)
nF22.5
nF20.5
nF8.5
nF14A.5
pF15.5
V_g = 0
T = 77 °K

Fig 7.11

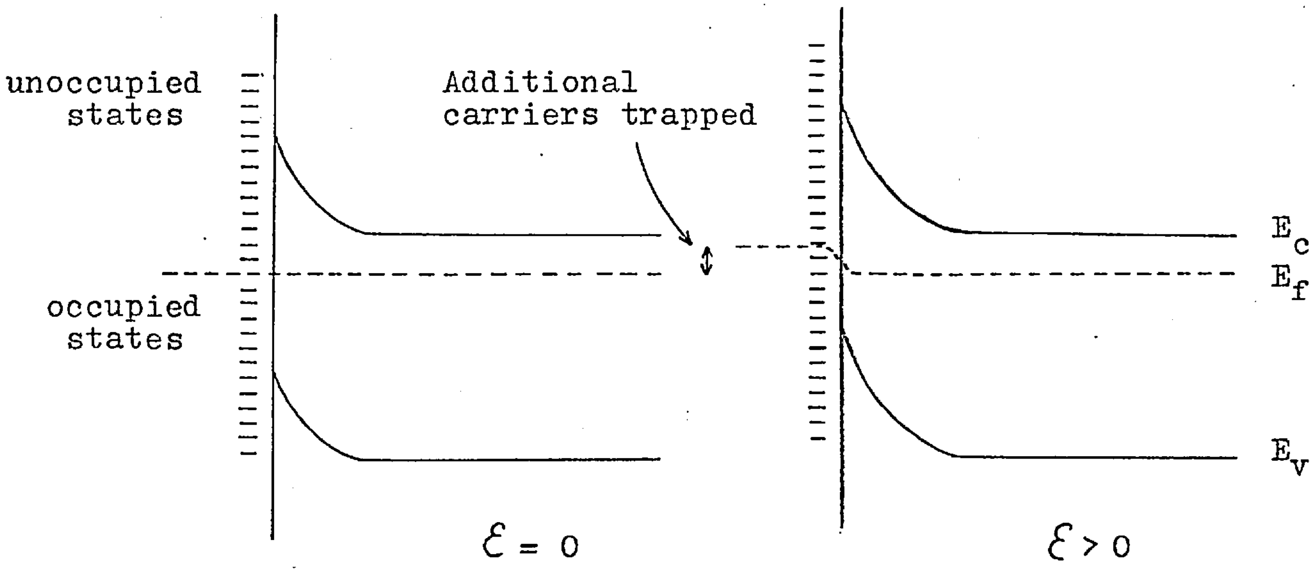

(1) n-type bulk

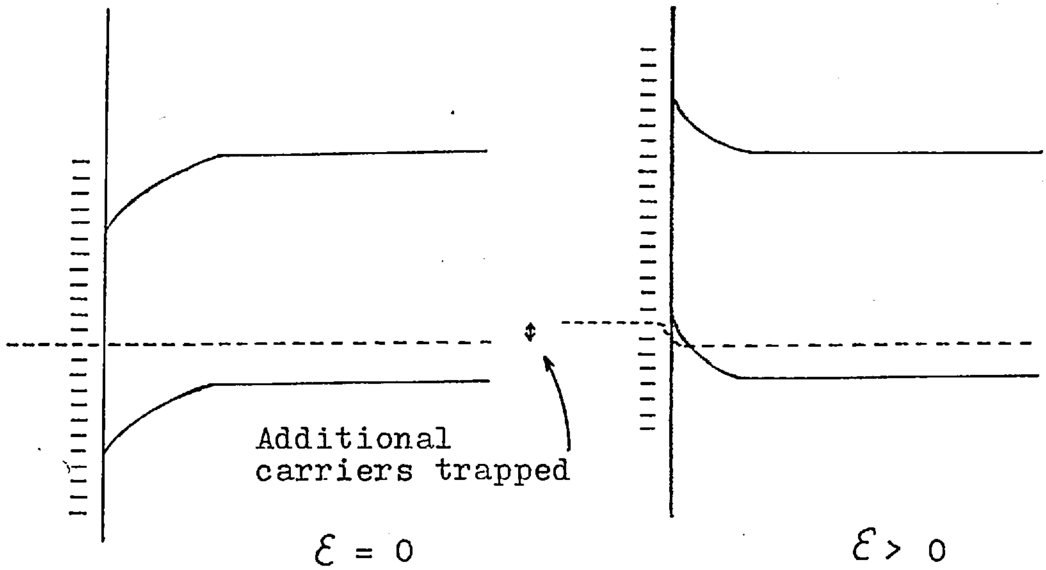

(2) p-type bulk

Fig 7.12: Band diagram to illustrate surface trapping of carriers

The initial surface band bending, $v_s^o(\mathcal{E} = 0)$ is approximately $- 25$ kT at liquid nitrogen temperature. Now $v_s^o(\mathcal{E})$ is determined by the trapping of electrons mainly at the slow states, below the Fermi level. For low $\mathcal{E}$, there is little change in the electron density in the crystallite bulk. There is, therefore, negligible additional trapping at the surface states; hence, $v_s^o(\mathcal{E})$ remains essentially constant. This result is consistent with the relative independence of sample resistivity, $\rho(\mathcal{E})$, for low $\mathcal{E}$ (see Fig 6.9).

With increasing $\mathcal{E}$, injection of excess electrons becomes appreciable, resulting in trapping through electrons surmounting the surface potential barrier and dropping into surface states. On removal of the field, the electron density within the crystallite bulk reverts back to its pre-field value. This requires E_f in the bulk to remain constant with respect to the conduction band edge, E_c, as before. In the space-charge region, the extra electron depletion is met with an increase (negatively) in the surface band bending (actually, an increase in dV/dz). This results in the Fermi level at the surface, being depressed downwards relative to the conduction band edge, i.e. an increase in $(E_c - E_f)$ at the surface. In the insulator (at the surface states), however, the Fermi level must move upwards to accomodate the additional trapped charges. Because of the high density of slow states, only a slight upward shift is needed (see Fig 7.12).

At a trap energy level, E_t[4], a number of donor and acceptor traps exists. Donor traps are neutral when full and positively charged when empty, whilst acceptor traps are neutral when empty, but negatively charged when

---

[4] Both discrete and continuous energy levels have been considered, but there is stronger evidence supporting the former (M4, F7, J1).

full. The surface states would thus be positively or negatively charged, depending on the probabilities, $f_n(E_t)$ and $f_p(E_t)$ of electron- or hole-trapping, as well as on the acceptor and donor trap densities, N_{ta} and N_{td}[4], at the given energy. $v_s^o(\mathcal{E})$ would increase (negatively) as long as $\Sigma N_{ta} f_n(E_t) \gg \Sigma N_{td} f_p(E_t)$. Saturation appears when the two quantities are equal and this is expected to occur near the breakdown field, when electron trapping has to compete with hole trapping, since, at avalanche, electrons and holes are present in almost equal numbers. This explanation is compatible with the observed saturation of $\rho(\mathcal{E})$.

From the variation of $v_s^o(\mathcal{E})$ with $\mathcal{E}$, it is noted that saturation sets in when the Fermi level at the surface lies a few kT below the valence band edge, when $f_n \ll f_p$. It may be inferred from this that the acceptor density at the mica/InSb interface is much higher than the donor trap density.

(2) p-type sample

Field-effect curves show that as in n-type samples, p-type films show a depletion surface, now with a positive band bending at $\mathcal{E} = 0$. From the above discussion, it is expected that electrons will be preferentially trapped in acceptor surface states as $\mathcal{E}$ increases. This reduces the initial positive bending and drives it eventually negative. Saturation occurs when the Fermi level sinks 2 or 3 kT below the valence band edge at the surface, a condition determined as in n-type films, by the surface trap densities and their trapping probabilities.

---

[4] Fermi-Dirac statistics are usually employed, but this is rather questionable (L6).

The trap energy, E_t, must be replaced by an effective energy to allow for possible multiplicity of surface states (M4).

The change from a depleted surface to an enhanced surface is expected to be accompanied by a resistivity reduction in the sample. This was in fact observed for p-type films (see Fig 6.9).

(3) Very thin n-type films

In Chapter Five, it was observed in the dc field-effect measurements that the Hall coefficient in very thin n-type films (less than 1000 A^o) turns positive for negative V_g. This was attributed to a highly depleted surface. Direct evidence is provided by the field-effect measurement of sample nF22.5 ($\sim$800 A^o) which has a $v_s^o(0)$ of $-$ 37 kT. The decrease of $\rho(\mathcal{E})$ with $\mathcal{E}$ is accompanied by a further increase (negative) in surface bending, v_s^o near breakdown being around $-$ 40 kT. The space-charge region is greatly reduced in view of the strong inversion. This would explain the fall in the sample resistivity and the p-like behaviour.

The resistivity change with electric field has been interpreted in terms of preferential electron trapping at the surface states. In each case, the Fermi level at the semiconductor side of the interface, is depressed downwards to accomodate the additional negative charges in the slow surface states. Fast states, which communicate readily with the semiconductor and owe their origin to abrupt lattice termination at the surface, have their energies rigidly fixed with respect to the conduction and valence band edges (M4). Hence, as the band bends upwards and downwards, these states move $- v_s$ and $+ v_s$ respectively. Since, the Fermi level in the space charge always moves downwards after successive voltage pulses, it must be assumed that the fast surface states detrap. This is of no significance, since it is the trapping at the slow states that determines the overall surface charge.

7.6.3 The charge-transfer mechanism

The charge-transfer mechanism between the slow states (located in the insulator) and the underlying semiconductor, which gives rise to the decay characteristics, is still a highly speculative issue. However, it has been reasonably well established (M4, F7), that, in the presence of an external excitation, trapping of carriers takes place in a relatively short time, whilst detrapping involves a much longer time. This asymmetry in the carrier relaxation leads to the 'storage' effect, which, in thin insulating layers (50 A^{O}), is also dependent on ambient conditions.

Trapping occurs when carriers have sufficient energy to surmount the surface potential, v_s. At quiescent conditions, carriers in the respective bands do not enter the insulator, since the diffusion forces are just balanced by the electrostatic field force (- e dV/dx) of the surface potential. As the carrier densities increase, a certain number succeeds in overcoming the barrier, resulting in trapping. This is greatly facilitated by the presence of a strong excitation, eg high electric (measuring) fields. Near avalanche breakdown, appreciable numbers of carriers possess energies of approximately 0.4 eV ($\sim$60 kT at 77 ^{O}K), which is far in excess of v_s.

In the high-field measurements, the voltage pulses are of 10 nsec duration. It must therefore be assumed that trapping takes place in a time short compared to this. The trapped carriers communicate first with the fast states, that lie close to the respective band edges near the surface. From these states, they cascade into the 'ground' states near the Fermi level, by a series of trapping and detrapping of lower energy states, accompanied by phonon emissions. The surface states involved are fast states located next to the semiconductor, and the process is expected to take a short time. An accumulation of carriers in the potential well builds up near the surface, from where they are assumed to migrate, under the influence of diffusion forces, into the insulator, to be trapped at slow states. The time involved in this redistribution of trap occupation is expected to be considerably longer, but as far as the semiconductor is concerned, the trapping ceases at the end of the excitation.

As mentioned earlier, the high-field data were recorded after the application of 10 nsec pulses for about 5 sec, i.e. about 3000 pulses. Carrier accumulation will be assumed to occur continuously, which becomes negligible after about 5 sec, since no noticeable change in $\rho(\mathcal{E})$ for a given $\mathcal{E}$ were observed for a longer application time. It is obvious from this, that the trapping is a function of the duration as well as the intensity of excitation. The previous assumption that trapping (at the fast states) occurs in a time less than 10 nsec, is strongly supported by the evidence shown in Fig 7.13. Pulses of different durations were used in the measurement of $\rho(\mathcal{E})$. It was found that for pulse duration greater than about 10 nsec, all experimental points lie within reasonable limits of a well-defined curve. But the 1 nsec points lie on a curve which is well below the previous curve. However, it was possible to shift this curve upwards by a continuous application of pulses for some 600 secs, this being apparently the upper limit. The result leads to the conclusion that the trapping time is comparable with 1 nsec, probably of the same order as the surface recombination time of 0.1 nsec, obtained by Lile (L2).

During the period of the pulse, carrier migration

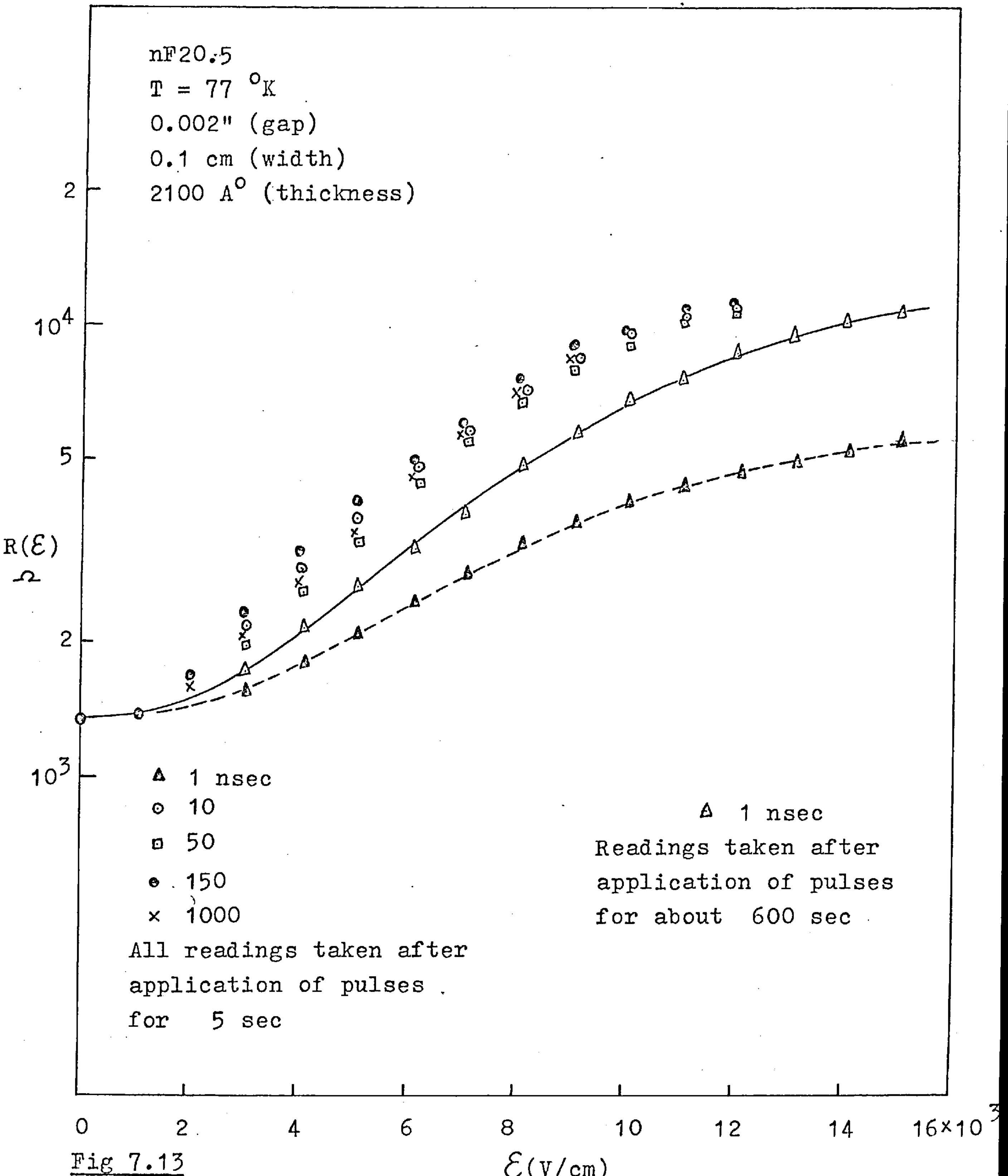
nF20.5
T = 77 °K
0.002" (gap)
0.1 cm (width)
2100 A° (thickness)
R(ℰ)
Ω
2
10^4
5
2
10^3
Δ 1 nsec
○ 10
□ 50
● 150
× 1000
All readings taken after application of pulses for 5 sec
Δ 1 nsec
Readings taken after application of pulses for about 600 sec
0
2
4
6
8
10
12
14
16×10
ℰ(V/cm)

Fig 7.13

into the insulator when the gate is earthed, will be enhanced or retarded, depending on the polarity of the pulse. An orthogonal field exists (between the semiconductor and the gate), which provides the driving force. The field is approximately linearly distributed along the semiconductor film, being highest near the anode contact. The effect is similar to an applied gate field, when the semiconductor film is at a low potential. Evidence of carrier migration, has been demonstrated by Sewell (S11), who found the decay time to be an increasing function of the gate voltage. The maximum field across the mica, due to the voltage applied between the two contacts, in the present films, is of the order of 5×10^4 V/cm, which is low and the effect is probably insignificant.

The 'spreading' out of the trapped carriers has the effect of raising the Fermi level in the insulator relative to its position in the semiconductor. The tendency to equalise the Fermi levels leads to detrapping. Most of the trapped carriers are bound to slow states, situated at varying depths in the insulator, which are determined by the degree of excitation. The detrapping process requires a carrier (1) migrating to the edge of the potential well (at the same energy level) - a necessarily slow process, in view of the low mobility of carriers in insulators, and (2) surmounting the potential barrier ($E_c - E_f$ for electrons, and $E_f - E_v$ for holes), which is now much larger than the previous 'trapping' barrier, v_s. The process is therefore a very slow one, and as carriers empty from different depths, will not be characterised by a single time constant.

A number of physically possible processes has been proposed to explain the detrapping mechanism.

(1) If the decay is independent of temperature,

quantum mechanical tunnelling might account for the release of carriers from surface states.

(2) If the decay time is temperature dependent, a thermally activated process is responsible, the decay time in this case, being proportional to $\exp(E_t/kT)$.

(3) The possibility of high-field induced tunnelling (M4) and phonon-assisted tunnelling (K12) have also been considered.

Koelmans and de Graaff (K12) pointed out that for a measurable tunnelling current, the tunnelling distance must be less than about 100 A°, since the tunnelling probability diminishes rapidly (exponentially) with tunnelling distance (M4). The process is therefore only appreciable for trapped carriers at surface states very near to the insulator/semiconductor interface, eg in strongly enhanced or inverted surface. A natural depletion of - 25 kT at the surface of a typical film, makes tunnelling unlikely, since the effective charge penetration is some 300 - 400 A° (see Fig 5.6). If tunnelling is the dominant transport mechanism, the time constant, $\tau \sim \exp(d_{tf})^{\frac{1}{2}}$, where d_{tf}, is the distance between the surface trap and interface (F7).

In view of the above length requirement, migration in the insulator by tunnelling from trap to trap is only possible if the trap density exceeds $\sim 10^{18}$ cm^{-3}. A model, which assumes the charge transfer between the insulator and the semiconductor to be of an ionic rather than an electronic nature, has been advanced by Pilkuhn (P12). The slow decay in the charge initially induced in the semiconductor space-charge region is attributed to the drift of ions in the insulator. On this basis, the time constant should be inversely proportional to the mobility and to the density of the ions. Thus both electron (or hole) and ion migration in the insulator could account for the charge transfer, from slow states (deep in the insulator) to fast states (located near the semiconductor surfaces).

The possibility of completely detrapping the surface charge by heating from liquid nitrogen temperature to room temperature (Chapter Six) affords by far the best indication of a thermally activated process. τ increases rapidly with decreasing temperature and increasing energy separation between E_t and the band edges.

7.7 Discussion

The theoretical conductance curve was numerically computed from Eqn (7.21), assuming a constant electron surface mobility and a constant mobility ration, $\mu_{ns}/\mu_{ps} = 10$. As is known from dc field-effect measurements, electron mobility varies considerably with V_g; consequently, errors involved in taking μ_{ns} and μ_{ps} to be independent of V_g and hence of v_s, are expected to be large, particularly at high positive v_s. In the ac field-effect measurements, V_g was restricted to roughly 1 kV peak to peak, i.e. a maximum V_g of $\pm$ 0.5 kV. Since the conductance minima usually lie within $V_g = \pm 0.1$ kV, the theoretical curves around the minima are reasonably accurate. v_s^o and N_{ss}^o are therefore fair estimates. Deductions of $\mu_{fe}(v_s)$ and $N_{ss}(v_s)$ from other parts of the curve remote from the minimum must be viewed with caution.

Returning to Fig 6.8, the variation of $R(\mathcal{E})$ with dc gate voltage, V_g, can now be better understood. For positive V_g's, $R(\mathcal{E})$ curves are very similar except that they are displaced vertically. This is to be expected, since what a positive gate voltage does is to produce a reduction in the surface band bending, so that saturation occurs at a higher $\mathcal{E}$ for a more positive V_g. This, however, is not very well borne out. A negative V_g, on the other hand, produces an increase in the surface bending (negative), and saturation is expected at a lower $\mathcal{E}$. Further increases in $\mathcal{E}$, would lead to a reduction in sample resistance, since the surface is tending towards strong inversion. This is clearly the case for V_g equal to -0.5 and -1.0 kV. For $V_g = -1.5$ kV, there is hardly any change at all. It must now be assumed that carrier trapping does not take place, because the initial surface bending is too large.

From Fig 6.8, sample resistance for $V_g = 0$, increases from $R(0) = 1.1\times10^3\Omega$, to $R(\mathcal{E}) = 5.1\times10^4\Omega$ at breakdown. This is a 46-fold increase in resistivity. From Fig 7.11, the surface trapped charge, again for $V_g = 0$ is $N_{ss}^{o}(0) = -5.5\times10^{11}$ cm^{-2} at $\mathcal{E} = 0$, and $N_{ss}^{o}(\mathcal{E}) = -7.5\times10^{11}$ cm^{-2} at breakdown. Translated into volume density, these figures represent a loss of $\sim1.8\times10^{16}$ mobile electrons/cm^3 from the film. Assume that the loss is uniformly felt over the entire bulk of the film, and that it is solely responsible for the increase in resistivity. Taking the electron density to be 1×10^{17} cm^{-3}, the increase is expected to be a mere 12%, or at the most twice this figure, considering equal trapping at the InSb/oxide interface as well. The barrier effect is again clearly evident here: such a high resistivity increase is due not so much to a decrease in the electron density, rather to the increase in the crystallite barrier height.

There is considerable room for future work. The use of nanosecond and subnanosecond voltage pulses appears to hold great promise in determining the surface trapping time, bearing in mind that this might also be complicated by surface recombination. The study of transient behaviour of the induced charge and the interaction processes leading up to steady-state conditions, by means of pulsed field effect (applying high voltage pulses to the gate plate), could be of great importance in the understanding of the detrapping mechanism. Measurement of the decay time over different temperatures, would also yield valuable information.

CHAPTER EIGHT: Conclusions

On the evidence obtained in the present study, the following conclusions are drawn.

Flash-evaporated thin films of InSb, in the thickness range 1000 - 3000 A^o, are found to be highly polycrystalline. The crystallite size distribution, however, is not an important parameter here, since the electron mobility is governed almost entirely by the mean crystallite size. In well-annealed, good-mobility films, a linear relation between the electron mobility and the mean crystallite size has been found, which strongly supports the view, that crystallite boundaries reduce carrier mobility by limiting the carrier mean free path to half the crystallite size.

The temperature-dependence of the electron mobility is found to be exponential. This behaviour, common in polycrystalline films, has been interpreted in terms of a barrier potential, ϕ_o, which is associated with the crystallite boundaries. The presence of crystallite boundaries not only accounts for the greatly reduced electron mobility of these films, but also for the temperature dependence.

ϕ_o is a quantity which depends on the free (mobile) electron concentrations in the crystallites and in the boundaries; its presence has been demonstrated by the dc field-effect experiment. Contrary to the work of previous workers, who ascribed the physical origin of ϕ_o to stoichiometric variations across the boundaries, ϕ_o is attributed here to dislocation dangling bonds.

Mobility changes of a factor of 1 - 2, in surface conductivity modulation (field-effect) experiments, are often interpreted in the light of Schrieffer's surface scattering model. This effect must now be considered to be small, since mobility changes of a factor of 30 have been recorded in the present films. This discrepancy can be reconciled: in the previous works, the crystallites are generally larger due either to thicker films (μm) or superior annealing techniques (eg protective annealing), so that electron mobility is not so much limited by the crystallite size as by other scattering centres. A lowering of barrier potential by a gate field, therefore, produces little or no increase in the electron mean free path.

The barrier potential model is attractive, since it can also explain the high-field effects. Breakdown, under the influence of a high electric field, has been attributed to an avalanche process as in bulk. But unlike bulk single crystals, carriers do not accelerate to high energies to achieve impact ionisation. Rather, carriers depend on falling through the 'necessary' potential - a different process, leading however to the same result. The independence of the critical breakdown field on the initial barrier height, as predicted by the modified diode theory, has one important significance: that the high breakdown field (approximately two orders of magnitude up on bulk) is not due to a large voltage drop across the high-resistivity crystallite boundaries, per se, as is generally believed.

Under high fields, polycrystalline InSb films exhibit both positive and negative differential conductivity; the effects have been interpreted purely as thin film phenomena. In bulk material, a decrease in carrier mobility with applied field is due to the Gunn effect, i.e. intervalley transfer of carriers. This cannot be excluded in the present case, since carriers near the breakdown field have sufficient energy to undergo an intervalley transition. Possibly, information can be obtained by studying this phenomenon under high hydrostatic pressure, since the energy difference between the main valley minimum (at $\underline{k} = 0$) and the satellite valley minimum (along a $\langle 111 \rangle$ direction) is decreased in this case, making intervalley transfer of carriers more probable.

In the ac field-effect experiments, depleted surfaces are found to exist in the InSb/mica interface, i.e. $+v_s$ for p-type films and $-v_s$ for n-type films at quiescent conditions. The surface band bending is a function of the applied electric field, as a result of preferential trapping of electrons at acceptor surface states. The surface thus acts as a 'sponge' leading to two important consequences: (1) trapping of high-field-induced carriers in a time short compared to the pulse duration, so that 'carrier run-away' is prevented, and (2) preclusion of high-field effects, such as plasma and Gunn oscillations, microwave emissions, etc, in the absence of a high density of electron-hole pairs.

Carrier transfer between the surface states and the underlying semiconductor is interpreted using a slow surface-state trapping model. In contrast to the fast trapping of carriers, the reverse process (detrapping) involves a very much longer time, resulting in a 'storage' effect, i.e. an accumulation of charge carriers in the insulator side of the interface. The strong temperature-dependence of detrapping points to a thermally activated process; however, migration of carriers from deep in the insulator to the edge of the interface, via some tunnelling or hopping mechanism, would be most consistent with the very slow detrapping time.

The field-dependent resistivity is a direct consequence of surface trapping. Carrier depletion from the crystallite bulk leads to an increase (negatively) in the surface band bending, leading to an overall decrease in the number of conduction carriers. In n-type films (reasonably thick), this results in a large increase in resistivity, larger than anticipated if the loss of carriers is solely held responsible. A mobility reduction, as a consequence of the barrier effect, can easily account for the resistivity increase.

APPENDIX A: Equivalent Circuit for a Metal-InSb-Metal Structure

The equivalent circuit for a symmetrical metal-InSb-metal structure is assumed as shown in Fig 3.9. C and R are the capacitance and the resistance, respectively, of the metal contacts. C_1 and R_1 are the combined capacitance and resistance of all the barriers, neglecting the contribution due to the body of the crystallites. If each barrier has a resistance, R_o, and a parallel capacitance, C_o, then

$$R_1 = N_1 R_o \quad ; \tag{A.1}$$

$$C_1 = C_o/N_1 \tag{A.2}$$

where N_1 is the total number of crystallites.

The impedance, Z, can be written down as

$$\begin{aligned} Z &= \left[\frac{2R}{1 + j\omega CR} + \frac{R_1}{1 + j\omega C_1 R_1} \right] \\ &= \left[\frac{2R}{1 + \omega^2 C^2 R^2} + \frac{R_1}{1 + \omega^2 C_1^2 R_1^2} \right. \\ &\quad \left. - \frac{2\omega CR^2}{1 + \omega^2 C^2 R^2} + \frac{C_1 R_1^2}{1 + \omega^2 C_1^2 R_1^2} \right] \end{aligned} \tag{A.3}$$

where ω is the frequency of the measuring signal and $j = \sqrt{-1}$.

(1) Series equivalent - Let the circuit in the figure be represented by a resistance, R_s, in series with a capacitance, C_s. Then, the impedance, in the series

equivalent, can be written as,

$$Z = R_s + 1/j\omega C_s$$

$$= R_s - j/\omega C_s \qquad (A.4)$$

From Eqns (A.3) and (A.4) to be equivalent, then, equating real and imaginary parts,

$$R_s = \left[\frac{2R}{1 + \omega^2 C^2 R^2} + \frac{R_1}{1 + \omega^2 C_1^2 R_1^2} \right] ;$$

$$C_s = \left[\frac{2\omega^2 C R^2}{1 + \omega^2 C^2 R^2} + \frac{\omega^2 C_1 R_1^2}{1 + \omega^2 C_1^2 R_1^2} \right]^{-1} \qquad (A.5)$$

Considering the limiting cases:

For $\omega \longrightarrow 0$,

$$R_s \longrightarrow 2R + R_1 \quad ;$$

$$C_s \longrightarrow \infty \qquad (A.6)$$

For $\omega \longrightarrow \infty$,

$$R_s \longrightarrow 0 \quad ;$$

$$C_s \longrightarrow CC_1/(C + 2C_1) \qquad (A.7)$$

(2) <u>Parallel equivalent</u> - If the circuit is considered to be a resistance, R_p, in parallel with a capacitance, C_p, then the impedance,

$$Z = \frac{R_p}{1 + j\omega C_p R_p}$$

$$= \left[\frac{R_p}{1 + \omega^2 C_p^2 R_p^2} - \frac{j\omega C_p R_p^2}{1 + \omega^2 C_p^2 R_p^2} \right] \qquad (A.8)$$

Again, equating real and imaginary parts,

$$R_p = A(1 + \omega^2 C_p^2 R_p^2) \quad ;$$

$$\omega C_p R_p^2 = B(1 + \omega^2 C_p^2 R_p^2) \tag{A.9}$$

where

$$A = \frac{2R}{1 + \omega^2 C^2 R^2} + \frac{R_1}{1 + \omega^2 C_1^2 R_1^2}$$

$$B = \frac{2\omega C R^2}{1 + \omega^2 C^2 R^2} + \frac{\omega C_1 R_1^2}{1 + \omega^2 C_1^2 R_1^2} \tag{A.10}$$

From Eqns (A.9) and (A.10),

$$R_p = (A^2 + B^2)/A \quad ;$$

$$C_p = B/\omega(A^2 + B^2) \tag{A.11}$$

In the limit, as $\omega \longrightarrow 0$,

$$A \longrightarrow 2R + R_1,$$
$$B \longrightarrow 0,$$
$$B/\omega \longrightarrow 2CR^2 + C_1R_1^2$$

Hence,

$$R_p \longrightarrow 2R + R_1 \quad ;$$

$$C_p \longrightarrow (2CR^2 + C_1R_1^2)/(2R + R_1)^2 \tag{A.12}$$

And for $\omega \longrightarrow \infty$,

$$A \longrightarrow 0,$$
$$B \longrightarrow 0,$$
$$\omega B \longrightarrow 2/C + 1/C_1,$$
$$\omega A^2/B \longrightarrow 0,$$
$$B^2/A \longrightarrow RR_1(C + 2C_1)^2/(RC^2 + 2R_1C_1^2)$$

Hence,

$$R_p \longrightarrow RR_1(C + 2C_1)^2/(RC^2 + 2R_1C_1^2) \quad ;$$

$$C_p \longrightarrow CC_1/(C + 2C_1) \qquad (A.13)$$

The results are summarised in the following tables:

Table A.1

	$\omega \longrightarrow 0$	$\omega \longrightarrow \infty$
R_s	$2R + R_1$	0
C_s	∞	$CC_1/(C + 2C_1)$
R_p	$2R + R_1$	$RR_1(C + 2C_1)^2/(RC^2 + 2R_1C_1^2)$
C_p	$(2CR^2 + C_1R_1^2)/(2R + R_1)^2$	$CC_1/(C + 2C_1)$

Table A.2: For $C_1 = 0$

	$\omega \longrightarrow 0$	$\omega \longrightarrow \infty$
R_s	$2R + R_1$	R_1
C_s	∞	$C/2$
R_p	$R_1 + 2R$	R_1
C_p	$2CR^2/(2R + R_1)^2$	0

APPENDIX B: Surface Transport Theory

In films, carriers suffer a scattering due to the boundary surfaces, in addition to the normal bulk scattering. A carrier making a collision with the surface could emerge either with the normal component of its thermal velocity reversed (but otherwise unaltered), or with its velocity completely randomised. These two cases are termed respectively 'specular' or 'diffuse'. However, surfaces usually possess a certain degree of specularity, exhibiting a mixed scattering. When carriers have a net drift momentum (eg, due to an external electric field) parallel to the surface, this is partially or completely destroyed after a collision with the surface, leading to a mobility reduction for carriers near the surface.

Early investigations revealed that thin metal films have higher electrical resistivity than the same metal in bulk. Thomson was the first to suggest that the effect arose from the limitation of electron free path (see S1). Using Drude's theory of conduction (W14), he obtained the following equation for the conductivity of a metal film, of thickness, 2d, and bulk free path, λ ,

$$\sigma/\sigma_b = 3d/2\lambda + (d/\lambda) \log (d/2\lambda) \tag{B.1}$$

where σ_b is the bulk conductivity.

Thomson's theory does not allow for free paths starting at the surface, and these become significantly important as the film thickness is reduced. A more rigorous treatment of the problem was carried out (for metal films) by Fuchs (F1), and refined by Sondheimer (S1) and Lucas (L3). The treatment has since been modified for semiconductors by various authors (A1, S2, Z1, G1, H13).

(1) The flat-band model

The following treatment may be applicable to semiconductor films with flat bands at the surface, i.e. $v_s = 0$. Under steady state conditions, the distribution function for electrons (or holes) is determined by Boltzmann transport equation:

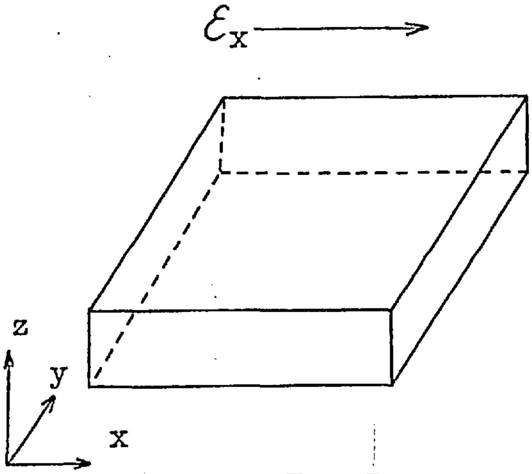

Fig B.1

$$\underline{c}.\mathrm{grad}_{\underline{r}} f + \underline{a}.\mathrm{grad}_{\underline{c}} f = -(f - f_o)/\tau \qquad (B.2)$$

where $\underline{a}$, $\underline{c}$ are the acceleration and velocity of the electrons, τ, the relaxation time, which is assumed to be independent of energy, and $f = f_o + f_1$. f_o is the equilibrium distribution function, and f_1 is a small perturbing function.

Consider now a film of finite thickness, 2d, in the z-direction and of semi-infinite extent in the x- and y-directions, as in Fig B.1. A small electric field, $\mathcal{E}_x$, is applied in the x-direction, so that $f_1 = f_1(c_z, z)$. Taking

$$\underline{a} = (-e\,\mathcal{E}_x/m_i,\ 0,\ 0),$$

$$\underline{c} = (c_x,\ c_y,\ c_z),$$

and neglecting products of f_1 and $\mathcal{E}_x$, Eqn (B.2) reduces to

$$c_z \frac{\partial f_1}{\partial z} + \frac{f_1}{\tau} = (e\,\mathcal{E}_x/m_i)\frac{\partial f_o}{\partial c_x} \tag{B.3}$$

The general solution of Eqn (B.3) is of the form

$$f_1 = \frac{e\,\mathcal{E}_x}{m_i}\frac{\partial f_o}{\partial c_x}\left[1 + h(\underline{c})\exp\left(-z/\tau c_z\right)\right] \tag{B.4}$$

where $h(\underline{c})$ is an arbitrary function of $\underline{c}$, to be determined by the boundary conditions. Let $\left[f_o + f_1^+(+c_z,\ z = 0)\right]$ and $\left[f_o + f_1^-(-c_z,\ z = 0)\right]$ be the respective electron distribution leaving and approaching the surface, $z = 0$. Assuming a fraction P of the electrons undergoes specular scattering, the following equations, must be satisfied:
At $z = 0$,

$$f_o + f_1^+(+c_z,\ z = 0) = P\left[f_o + f_1^-(-c_z,\ z = 0)\right] + (1 - P)f_o \tag{B.5}$$

and similarly, at $z = 2d$,

$$f_o + f_1^-(+c_z,\ z = 2d) = P\left[f_o + f_1^+(-c_z,\ z = 2d)\right] + (1 - P)f_o \tag{B.6}$$

These two equations are sufficient to determine $h(\underline{c})$. Using the symmetry requirement that $f_1(+c_z,\ z) = f_1(-c_z,\ 2d-z)$, two solutions to Eqn (B.3) are possible, thus,
for $c_z > 0$,

$$f_1(c_z,\ z) = \frac{e\,\mathcal{E}_x\tau}{m_i}\frac{\partial f_o}{\partial c_x}\left[1 - \frac{(1 - P)\exp\left(-z/\tau c_z\right)}{1 - P\exp\left(-2d/\tau c_z\right)}\right]$$

and for $c_z < 0$

$$f_1(c_z, z) = \frac{e\mathcal{E}_x\tau}{m_i}\frac{\partial f_o}{\partial c_x}\left[1 - \frac{(1 - P)\exp(2d - z)/\tau c_z}{1 - P\exp(2d/\tau c_z)}\right] \tag{B.7}$$

To see the effect of surface scattering on the contribution of all the carriers to the current parallel to the surface, an average electron mobility is calculated from the relation,

$$I_x = ne\bar{\mu}\mathcal{E}_x = -e\int_0^{2d}\iiint_{-\infty}^{+\infty} c_x N(\underline{c})\, f_1\, dc_x dc_y dc_z dz \tag{B.8}$$

where $\bar{\mu}$ is the average electron mobility, and $N(\underline{c}) = 2(m_i/h)^3$ is the density of states in velocity space. The solution depends on the equilibrium distribution function used; in degenerate semiconductors, this is given by the Fermi-Dirac statistics. Eqn (B.8) was solved by Sondheimer, who obtained the result,

$$\bar{\mu}/\mu_b = K/Y(K) \tag{B.9}$$

where

μ_b is the bulk electron mobility,

$K = 2d/\lambda$, (λ being the mean freepath) and

$$\frac{1}{Y(K)} = \frac{1}{K} - \frac{3(1 - P)}{2K^2}\int_1^{\infty}(t^{-3} - t^{-5})\left[\frac{1 - \exp(-Kt)}{1 - P\exp(-Kt)}\right]dt \tag{B.10}$$

Eqn (B.10) can be approximated to

$$1/Y(K) = 1/K - 3(1 - P)/8K^2 \qquad \text{for } K \gg 1 \tag{B.11}$$

and

$$1/Y(K) = 3(1 + P)4(1 - P) \log (1/K) \quad \text{for } K \ll 1 \qquad (B.12)$$

Perfectly specular scattering, i.e. $P = 1$.
In this case, $\bar{\mu} = \mu_b$ and Sondheimer's theory does not predict any mobility reduction. This, however, is valid only if spherical energy surfaces are assumed. In the absence of such an assumption, the electron effective mass becomes a tensor quantity, and even perfectly specular scattering may result in a mobility reduction (H13).

Perfectly diffuse scattering, i.e. $P = 0$.
Using Eqns (B.11) and (B.12), $\bar{\mu}/\mu_b$ is seen to vary from $3/4 \log (1/K)$ for thin films, to $(1 - 3K/8)$ for thicker ones.

The above theory concerns solely the geometrical limitation of electron free path. Experimental observations consequently have to be made on very thin films. But thin films are usually associated with a high density of defects, the effects of which are difficult to eliminate. This difficulty, however, can be diminished if the measurements are carried out at low temperatures since the mean free paths are now much longer and thicker films can be used. Andrew (A5), working on tin foils at 3.8 °K, obtained experimental data in excellent agreement with the above theory, if a perfectly diffuse surface is assumed. He obtained similar results for mercury wires at 2.5 °K. Experiments of Lovell on alkali metal films (L9), and of Macdonald and Sarginson (M15) on thin wires of sodium also support the theory.

(2) The band-bending model

The flat-band model has rather restricted applications since, in semiconductors, the energy bands almost invariably bend, as a result of trapping of free carriers at surface states or of an external electric field applied normal to the surface. The following treatment considers an accumulation layer in an n-type semiconductor. Because of the presence of an electric field, $\mathcal{E}_z$, in the z-direction, the Boltzmann equation has an additional term and is of the form

$$c_z \left[\frac{\partial f_1}{\partial z}\right]_{c_z} - \frac{e\mathcal{E}_x}{m_i}\left[\frac{\partial f_o}{\partial c_x}\right]_x - \frac{e\mathcal{E}_z}{m_i}\left[\frac{\partial f_1}{\partial c_z}\right]_z = - \frac{f_1}{\tau} \qquad (B.13)$$

Schrieffer pointed out (S2) that Eqn (B.13) can be simplified by a change of the independent variables from (c_z, z) to (c_z, w^*), where

$$w^*(z, c_z) = (m_i c_z^2/2kT) - v(z) \qquad (B.14)$$

is the part of the electron's total energy that is associated with its motion in the z-direction. $v(z)$ is the potential energy (see Fig 7.1). In terms of the new variables, Eqn (B.13) becomes

$$- \frac{e\mathcal{E}_z}{m_i}\left[\frac{\partial f_1}{\partial c_z}\right]_{w^*} + \frac{f_1}{\tau} = \frac{e\mathcal{E}_x}{m_i}\left[\frac{\partial f_o}{\partial c_x}\right] \qquad (B.15)$$

which can now be solved for f_1, given the appropriate boundary conditions and a knowledge of the potential distribution, $v(z)$.

Schrieffer assumes a parabolic band with spherical constant-energy surfaces, a constant relaxation time, τ, and a non-degenerate Maxwellian distribution of the form,

$$f_o = C \exp - \left[\frac{m_i(c_x^2 + c_y^2 + c_z^2)}{2kT} - v(z) \right] \qquad (B.16)$$

where C is a constant. The electron current per unit width parallel to the surface is given by (using Eqn (B.8))

$$I_x = \left[\frac{CkT}{e\mathcal{E}_{zs}} \left\{ \frac{2\pi kT}{m_i} \right\}^{3/2} \exp v_s \right] e \, \mathcal{E}_x \frac{e\tau}{m_i} \left[1 - \exp \alpha^2 \operatorname{erf} \alpha \right] \qquad (B.17)$$

where a constant $\mathcal{E}_z = \mathcal{E}_{zs}$ has been assumed, i.e. v(z) varies liearly from v_s at the surface to ∞ in the bulk, and

$$\alpha = (2m_i kT/e\tau \, \mathcal{E}_{zs})^{\frac{1}{2}}$$

$$\operatorname{erf} \alpha = (2/\pi^{\frac{1}{2}}) \int_{\alpha}^{\infty} \exp(-x^2) \, dx$$

The first factor in square bracket is just the number of electrons in the potential well. Because of the infinite bulk potential assumed, all the electrons can be regarded as residing near the surface, so that an effective surface mobility can be defined thus,

$$\mu_s = \mu_b \left[1 - \exp \alpha^2 \operatorname{erf} \alpha \right] \qquad (B.18)$$

where the bulk mobility is given by $\mu_b = e\tau/m_i$. In the limit for large $\mathcal{E}_{zs}$, μ_s reduces to $(2\alpha/\pi^{\frac{1}{2}})\mu_b$. Schrieffer has also attempted a more accurate approximation of the potential distribution by solving a Poisson equation for the space-charge region.

Following the poineer work of Schrieffer, many attempts have since been made to improve on his theory. A discussion of the more important results is now presented. Zemel (Z1) includes a magnetic field in the Boltzman equation and obtains an effective (Hall) mobility for a linear potential distribution of the form,

$$\frac{\mu_{\text{eff}}}{\mu_b} = \left[1 - \frac{2}{\pi^{\frac{1}{2}}} - (1 - 2\alpha^2) \exp \alpha^2 \operatorname{erf} \alpha \right]^{\frac{1}{2}} \tag{B.19}$$

which for large $\mathcal{E}_{zs}$, approximates to α . Compared to the (conductivity) mobility of Eqn (B.18), the effective (Hall) mobility is seen to be some 13% lower. This problem has also been considered by Flietner (F10), using a truncated linear potential. Greene, Frankl, and Zemel (see M4, F7) solved the Boltzmann equation for a non-degenerate statistics, and obtained a surface mobility as a function of the surface potential. Their results can be summarised as follows:

(1) for a deep potential well, the mobility is strongly reduced. This is to be expected, since the carriers are now attracted to the surface, thereby enhancing surface scattering.

(2) An anomaly occurs in the $\mu_s(v_s)/\mu_b$ curves, ranging from a slight discontinuity to a strong downward cusp at $v_s = 0$. This is also to be expected, because as the surface goes from accumulation to inversion, the carriers are first attracted and then repelled.

Recently, Juhasz (J1) has extended the problem further to include a degenerate Fermi-Dirac distribution and a non-parabolic conduction band, with special reference to InSb. The analysis remains basically similar to Schrieffer's treatment. He obtains the following expression for the surface mobility:

$$\mu_s/\mu_b = 1 - (n_b\lambda/\Delta N)\, H_{na,\, nd} \tag{B.20}$$

where

n_b	is the bulk electron concentration,
na	refers to accumulation layer,
nd	refers to depeltion layer, and
	is the electron mean free path.

ΔN is the excess surface-carrier density, defined by Eqn (7.14)

The H functions depend basically on v_s, being analogous to similar functions, previously obtained for non-degenerate statistics (M4). Eqn (B.20) predicts a mobility cusp for a degenerate statistics and a non-parabolic conduction band (appropriate to InSb), which Juhasz has confirmed experimentally. However, the equation does not give a mobility cusp if a non-degenerate statistics and a parabolic conduction band are used.

APPENDIX C: Electron Mean Free Path

The electron mean free path, λ , is given by $\lambda = \langle c \rangle \tau$, where the mean thermal velocity is defined by (J1)

$$\langle c \rangle = \int_0^\infty c(E)f(E)g(E)\,dE \Bigg/ \int_0^\infty f(E)g(E)\,dE$$

$$= (2kT/m_i)^{\frac{1}{2}}\, T_L(x_f - x_c)/D_{\frac{1}{2}}(x_f - x_c) \qquad (C.1)$$

and the relaxation time by

$$\tau = (3\mu_n m_i/2e) D_{\frac{1}{2}}(x_f - x_c)/T_{\frac{1}{2}}(x_f - x_c) \qquad (C.2)$$

The integrals are defined by

$$T_L(x_{fc}) = \int_0^\infty \frac{(x + ax^2)}{1 + \exp\,(x - x_{fc})}\,dx \qquad (C.3)$$

$$D_{\frac{1}{2}}(x_{fc}) = \int_0^\infty \frac{(x + ax^2)^{\frac{1}{2}}(1 + 2ax)}{1 + \exp\,(x - x_{fc})}\,dx \qquad (C.4)$$

$$T_{\frac{1}{2}}(x_{fc}) = \int_0^\infty \frac{(x + ax^2)\ \exp\,(x - x_{fc})}{\left[(1 + 2ax)(1 + \exp\left\{x - x_{fc}\right\})\right]^2}\,dx \qquad (C.5)$$

where

$x = E/kT$,

$a = kT/E_g$,

$x_{fc} = x_f - x_c = (E_f - E_c)/kT$

(f, c refer to the Fermi level and the conduction band edge, respectively.)

Evaluation of the integrals, (C.3), (C.4) and (C.5) is straight forward, using the standard Simpson's rule. The calculation was carried out on the CDC 6600 computer, and the following is a sample of the print-out.

Computer print-out: $T = 300\ ^oK$

Fermi energy (x_{fc})	Mean velocity	τ/μ_n	m.f.p.*
5.00	1.4362×10^6	8.3295×10^{-14}	3580
4.00	1.3376	8.1995	3280
3.00	1.2372	8.0803	3000
2.00	1.1400	7.9773	2720
1.00	1.0551	7.8964	2450
0.50	1.0206	7.8657	2400
0.00	9.9251×10^5	7.8422	2340
-0.50	9.7108	7.8246	2280
-1.00	9.5563	7.8122	2240
-2.00	9.3805	7.7983	2190
-3.00	9.3078	7.7927	2180
-4.00	9.2797	7.7907	2170
-5.00	9.2692	7.7899	2165
-10.00	9.2631	7.7894	2160
	(cm/sec)	($V\ sec^2/cm^2$)	(A^o)

* The mean free paths are calculated, using a bulk electron mobility, $\mu_n \sim 3\times10^4\ cm^2/V\ sec$.

APPENDIX D: The Poisson Equation

(1) Formulation

The treatment of Poisson equation in the surface space-charge region, has been considered by Juhasz (J1), for a degenerate electron population and a non-parabolic conduction band, under the following assumptions:

(1) The potential within the space-charge region does not have any significant effect on the band structure;

(2) Fermi-Dirac statistics is applicable; and

(3) The impurities are uniformly distributed and they do not mutually interact.

Poisson equation[4] in one dimension is of the form

$$\frac{d^2V}{dz^2} = - \frac{\rho(z)}{\epsilon\epsilon_o} \qquad (D.1)$$

where V is the electrostatic potential defined in Chapter Seven (with reference to Fig 7.1), and $\epsilon\epsilon_o$ is the constant of permittivity of the semiconductor. $\rho(z)$ is the net space charge density due to mobile carriers and static ionised impurity atoms, given by

$$\rho(z) = e(p + N_d^+ - n - N_a^-) \qquad (D.2)$$

where p, n are the mobile holes and electrons in the respective band, and N_d^+, N_a^- are the ionised donor and acceptor impurities, respectively.

The number of mobile electrons at the point z in the conduction band (in the space-charge region) is

---

[4] In the bulk, charge neutrality equation replaces Poisson equation, when $\rho(z) = 0$.

given by

$$n(z) = \int_{x_c}^{\infty} \frac{g_c(x)\, dx}{1 + \exp\left[x + x_{cf} - v(z)\right]} \qquad (D.3)$$

and similarly for holes in the valence band, by

$$p(z) = \int_{x_v}^{\infty} \frac{g_v(x)\, dx}{1 + \exp\left[x + x_{fv} + v(z)\right]} \qquad (D.4)$$

where $g_c(x)$, $g_v(x)$ are the density of states functions in the conduction and valence bands respectively, and the dimensionless quantities are defined by $x_{pq} = x_p - x_q = (E_p - E_q)/kT$. c, v, f refer to the conduction band, the valence band and the Fermi level, respectively. In general, the density of electron states is given by (taking into account electrons of both spins) (B14),

$$g(E)\, dE = (k^2/\pi^2)\, dk \qquad (D.5)$$

Using the E-k relationship of Kane's model for the conduction band (see Eqn (2.3)), the electron density of states function can be shown (in reduced energy, x), to be of the form

$$g_c(x) = 2 \frac{(2\pi m_n^* kT)}{h^3} \frac{2}{\pi^{\frac{1}{2}}} x^{\frac{1}{2}}(1 + x/x_g)^{\frac{1}{2}}(1 + 2x/x_g) \qquad (D.6)$$

where $E_g = x_g kT$ is the 'density-of-states' band gap, introduced by Ehrenreich (see Sec 2.5.1). Hence

$$n(z) = \frac{2(2\pi m_n^* kT)}{h^3} \frac{2}{\pi^{\frac{1}{2}}} D_{\frac{1}{2}}\left[v(z) - x_{cf}\right] \qquad (D.7)$$

where the integral $D_{\frac{1}{2}}$ has been defined by Eqn (C.4).

Eqn (D.6) can be approximated by expanding the factor $(1 + x/x_g)^{\frac{1}{2}}$ and truncating the Taylor polynomial at the linear term. The expression for the electron concentration then simplifies to

$$n(z) \;=\; \frac{2(2\pi m_n^* kT)}{h^3}\,\frac{2}{\pi^{\frac{1}{2}}}\left\{F_{\frac{1}{2}}\left[v(z) - x_{cf}\right] + \frac{5}{2}a\,F_{\frac{3}{2}}\left[v(z) - x_{cf}\right]\right\} \tag{D.8}$$

where $a = 1/x_g$ and the Fermi integral F_j is defined by (B14)

$$F_j(y) \;=\; \int_0^{\infty} \frac{x^j\,dx}{1 + \exp\,(x - y)} \tag{D.9}$$

Taking a parabolic valence band, the density of states is

$$g_v(x) \;=\; \frac{2(2\pi m_p^* kT)}{h^3}\,\frac{2}{\pi^{\frac{1}{2}}}\,x^{\frac{1}{2}} \tag{D.10}$$

giving

$$p(z) \;=\; \frac{2(2\pi m_p^* kT)}{h^3}\,\frac{2}{\pi^{\frac{1}{2}}}\,F_{\frac{1}{2}}\left[x_{vf} - v(z)\right] \tag{D.11}$$

For partial ionisation of impurities, which depends on $v(z)$ as well as on the position of the Fermi level, the number of positively charged donors, N_d^+, is the difference between the number of donors, N_d, and the fraction that still remains neutral, i.e.

$$\begin{aligned} N_d^+ &= N_d - N_d\left[1 + \tfrac{1}{2}\exp\left\{-\,x_{fd} - v(z)\right\}\right]^{-1} \\ &= N_d\left[1 + 2\exp\left\{x_{fd} + v(z)\right\}\right]^{-1} \end{aligned} \tag{D.12}$$

Similarly for the negatively charged acceptors,

$$N_a^- = N_a \left[1 + 2 \exp\left\{ - x_{fa} - v(z) \right\} \right]^{-1} \qquad (D.13)$$

where d, a refer to the donor and acceptor levels, respectively, and the spin degeneracy is accounted for in the factor 2.

In terms of the dimensionless potential, $v(z)$ Eqn (D.1) can be written as

$$\frac{d^2v}{dz^2} = - \frac{e}{\epsilon\epsilon_o kT} \rho(z) \qquad (D.14)$$

Multiplying both sides by dv/dz, Eqn (D.14) can be integrated once, using the boundary condition that $dv/dz = 0$, when $v(z) = 0$ or $z = \infty$, to give

$$\tfrac{1}{2}\left(\frac{dv}{dz}\right)^2 = \int_{\infty}^{z} - \frac{\rho(z)}{\epsilon\epsilon_o} \frac{dv}{dz} \, dz$$

$$= \int_{o}^{v} - \frac{\rho(z)}{\epsilon\epsilon_o} \, dv \qquad (D.15)$$

Now, $\rho(z)$ has been expressed as a function of $v(z)$ through Eqns (D.8), (D.11), (D.12) and (D.13), which all involve Fermi integrals. Eqn (D.15) can be evaluated analytically with the help of the recurrence relationship

$$\frac{\partial}{\partial y} F_j(y) = j \, F_{j-1}(y), \qquad \text{for} \quad j > 0 \qquad (D.16)$$

to

$$\frac{dv}{dz} = \pm F/L \qquad (D.17)$$

where the plus sign refers to a negative $v(z)$ and the minus sign refers to a positive $v(z)$. The effective Debye length L is given by

$$L = \left[\frac{\epsilon\epsilon_o kT}{e^2(n_b + p_b)}\right]^{\frac{1}{2}} \tag{D.18}$$

and the F function by

$$\begin{aligned} F(\pm v) = \pm\, 2^{\frac{1}{2}} \Bigg\{ & A_d \log\left[\frac{1 + \frac{1}{2}\exp(-x_{fd} - v)}{1 + \frac{1}{2}\exp(-x_{fd})}\right] \\ & + A_a \log\left[\frac{1 + \frac{1}{2}\exp(+x_{fa} + v)}{1 + \frac{1}{2}\exp(+x_{fa})}\right] \\ & + \frac{2}{3} A_p \left[F_{3/2}(-v - x_{fv}) - F_{3/2}(-x_{fv})\right] \\ & + \frac{2}{5} a A_p \left[F_{5/2}(-v - x_{fv}) - F_{5/2}(-x_{fv})\right] \\ & + \frac{2}{3} A_n \left[F_{3/2}(+v - x_{cf}) - F_{3/2}(-x_{cf})\right] \\ & + \frac{2}{5} a A_n \left[F_{5/2}(+v - x_{cf}) - F_{5/2}(-x_{cf})\right]\Bigg\}^{\frac{1}{2}} \end{aligned} \tag{D.19}$$

where

$$A_{d,a} = \frac{N_{d,a}}{n_b + p_b}$$

$$A_{p,n} = \frac{n_o}{n_b + p_b}\,(m^*_{p,n}/m_o)^{3/2}$$

$$n_o = \frac{2(2\ m_o kT)^{3/2}}{h^3}\ \frac{2}{\pi^{\frac{1}{2}}}$$

$$a = kT/E_g = 1/x_g$$

$$n_b = n_o (m_n^*/m_o)^{3/2} \left[F_{\frac{1}{2}}(x_{fc}) + \tfrac{5}{2} a \, F_{3/2}(x_{fc}) \right] ,$$

the bulk electron concentration, Eqn (D.8)

$$p_b = n_o (m_p^*/m_o)^{3/2} \; F_{\frac{1}{2}}(- x_{fv}),$$

the bulk hole concentration.

(2) Numerical evaluation

The complex F-function is evaluated on the CDC 6600 computer. The Fermi level, x_{cf}, in the bulk (where $v(z) = 0$) is obtained first iteratively, from a knowledge of the doping level (obtained from Hall measurement). Then for a given value of v, the corresponding value of F can be found from Eqn (D.19). Other quantities, such as space charge (Eqn (7.20)), surface conductance (Eqn (7.21)), etc, can all be evaluated. The following is a brief set-up of the programme; further details can be obtained from Ref. (J1).

Data Input

$N_{d,a}$: impurity concentrations
$E_{d,a}$: impurity levels
T : temperature
$\epsilon\epsilon_o$: constant of permittivity
a : constant of non-parabolicity, from Eqn (2.10)
μ_{ns} : electron surface mobility, taken to equal the measured Hall mobility
b : electron to hole mobility ratio, taken to equal 10 (see Sec 4.3.3)
$m^*_{n,p}$: electron and hole effective masses

Computer Print-out

n_b, p_b : bulk electron and hole density, from which the effective space-charge penetration, L_c is obtained (see Fig 5.6)

x_{cf} : the dimensionless Fermi energy

$\Delta\sigma(v_s)$: surface conductance as a function of surface band bending, i.e. the conductance curve

$Q_{sc}(v_s)$: the space charge as a function of v_s, from which the net charge density is obtained.

REFERENCES

A

(1) J.C. Anderson,
Advances in Physics, 19, 79, 311, 1970.

(2) J.C. Anderson,
Electronics and Power, 15, 90, 1969.

(3) B. Ancker-Johnson, R.W. Cohen and M. Glicksman,
Phys. Rev., 124, 6, 1745, 1961.

(4) B. Ancker-Johnson,
Proc. Int. Conf. Phys. of Semicond., Kyoto, 1966, p694.
(J. Phys. Soc. Jap., 21, Suppl., 1966.)

(5) E.R. Andrew,
Proc. Phys. Soc., A, 62, 77, 1949.

B

(1) K. Berchtold and D. Huber,
Phys. Stat. Sol., 33, 425, 1969.

(2) D.M.S. Bagguley, M.L.A. Robinson and R.A. Stradling,
Phys. Letts., 6, 143, 1963.

(3) L.P. Boishakov, A.S. Filipchenko, D.N. Nasledov and
L.N. Radoikina,
Phys. Stat. Sol., 32, K135, 1969.

(4) R.F. Broom and A.C. Rose-Innes,
Proc. Phys. Soc., 69B, 1269, 1956.

(5) F. Bardeen and W. Shockley,
Phys. Rev., 77, 407, 1950.

(6) H. Brooks,
Advances in Electronics and Electron Physics, 7, 85, 1955.

(7) D.M. Brown and R. Bray,
Phys. Rev., 127, 1593, 1962.

(8) R.L. Bell, L. Latkowski and A.F.W. Willoughby,
J. Mat. Sc., 1, 66, 1966.

(9) R.L. Bell and A.F.W. Willoughby,
J. Mat. Sc., 5, 198, 1970.
(10) R.L. Bell and A.F.W. Willoughby,
J. Mat. Sc., 1, 219, 1966.
(11) P.N. Butcher and C.J. Hearn,
Sci. Prog. Oxf., 57, 229, 1969.
(12) E. Bonek and R. Albert,
J. Appl. Phys., 41, 12, 4970, 1970.
(13) G.A. Baraff,
Phys. Rev., 133, 1A, A26, 1964.
(14) J.S. Blackmore,
'Semiconductor Statistics', Pergamon Press, 1962.

<u>C</u>

(1) J. Červenák,
Czech. J. Phys., B18, 1629, 1968.
(2) J. Červenák,
Thin Solid Films, 5, 277, 1970.
(3) C.A. Coulson, L.B. Redei and D. Stocker,
Proc. Roy. Soc., 270, 357, 373, 383, 397, 1962.
(4) C.H. Champness,
Phys. Rev. Letts., 1, 439, 1958.
(5) R.W. Cunningham, E.E. Harp and W.M. Bulling,
Proc. Int. Conf. in Semicond. Phys., Exeter, 732, 1962.
(6) J. Červenák, A. Živčáková and J. Buch,
Czech. J. Phys., B, 20, 84, 1970.
(7) B.K. Chakraverty,
J. Phys. Chem. Solids, 28, 2401, 1967.
(8) J. Cervenak,
Czech. J. Phys., B18, 1449, 1968.
(9) E.M. Conwell,
'High Field Transport in Semiconductors',
Academic Press, 1967.

(10) A.G. Chynoweth and A.A. Murray,
Phys. Rev., 123, 2, 515, 1961.

(11) R.C. Curby and D.K. Ferry,
Phys. Letts., 32A, 4, 236, 1970.

(12) R.C. Chambers,
Pro. Phys. Soc., A, 65, 903, 1952.

D

(1) G. Dresselhaus, A.F. Kip, C. Kittel and C. Wagoner,
Phys. Rev., 98, 556, 1955.

(2) G. Dresselhaus,
Phys. Rev., 100, 580, 1955.

(3) W.P. Dumke,
Phys. Rev., 167, 3, 783, 1968.

(4) C.L. Dick and B. Ancker-Johnson,
Appl. Phys. Letts., 18, 4, 124, 1971.

(5) D.L. Dexter and F. Seitz,
Phys. Rev., 86, 6, 964, 1952.

(6) E.B. Dale and G. Senecal,
J. Appl. Phys., 33, 2526, 1962.

E

(1) R. Egerton,
PhD Thesis, London University, 1968.

(2) H. Ehrenreich,
J. Phys. Chem. Solids, 2, 131, 1957.

(3) H. Ehrenreich,
J. Phys. Chem. Solids, 9, 129, 1959.

(4) J.T. Edmond,
Proc. Phys. Soc. (London), 73, 622, 1959.

(5) J.C. Eidson and G.S. Kino,
Appl. Phys. Letts., 8, 7, 183, 1966.

F

(1) K. Fuchs,
Proc. Camb. Phil. Soc., 34, 100, 1938.

(2) S.J. Fray, F.A. Johnson and R.H. Jones,
Proc. Phys. Soc. (London), 76, 939, 1960.

(3) H.P.R. Frederikse and W.R. Hosler,
Bull. Amer. Phys. Soc., 6, 298, 1955.

(4) H.Y. Fan and G.W. Gobeli,
Phys. Rev. Letts., 4, 546, 1960.

(5) A.S. Filipchenko and D.N. Nasledov,
Phys. Stat. Sol., 19, 435, 1967.

(6) J.H. Fisher,
Private communication (Imperial College).

(7) D.R. Frankl,
'Electrical Properties of Semiconductor Surfaces',
Pergamon Press, 1967.

(8) H. Fujisada, S. Kataoka and A.C. Beer,
Phys. Rev., B, 3, 10, 3249, 1971.

(9) H. Frohlich and B.V. Paranjape,
Proc. Phys. Soc., B69, 21, 1956.

(10) H. Flietner,
Ann. Physik Leipzig, 3, 396, 1959.

G

(1) R.F. Greene, D.R. Frankl and J. Zemel,
Phys. Rev., 118, 4, 967, 1960.

(2) V.V. Galavanov, D.N. Nasledov and A.S. Filipchenko,
Phys. Stat. Sol., 8, 671, 1965.

(3) von K.G. Gunther and H. Freller,
Z. Naturforsch., 16a, 279, 1961.

(4) A.M. Gulyaev,
Private communication (Moscow University).

(5) M. Glicksman and W.A. Hicinbothem,
Phys. Rev., 129, 4, 1572, 1963.

(6) J.B. Gunn,
J. Electronics, 2, 87, 1956.
(7) M. Glicksman and M.C. Steele,
Phys. Rev., 110, 5, 1204, 1958.
(8) S.L. Golub,
PhD Dissertation, Syracuse University, 1968.
(9) C.G.B. Garrett and W.H. Brattain,
Phys. Rev., 99, 376, 1955.

H

(1) C. Hilsum,
Proc. Int. Conf. Phys. of Semicond., Paris, 1964, p1127.
(2) C. Hilsum and A.C. Rose-Innes,
'Semiconducting III-V Compounds',
Pergamon Press, 1961.
(3) D.J. Howarth and E.H. Sondheimer,
Proc. Roy. Soc. (London), A219, 53, 1953.
(4) E. Haga and H. Kimura,
J. Phys. Soc. Jap., 18, 777, 1963.
(5) H.J. Hrostowski, F.J. Morin, T.H. Gaballe and
G.H. Wheatley,
Phys. Rev., 100, 1672, 1955.
(6) H.K. Henisch,
'Rectifying Semiconductor Contacts',
Clarendon Press, 1957.
(7) D.B. Holt,
J. Phys. Chem. Solids, 23, 1353, 1962.
(8) D.B. Holt,
J. Phys. Chem. Solids, 25, 1385, 1964.
(9) I. Hlasnik,
Solid-State Electronics, 8, 461, 1965.
(10) H.F. van Heek,
Solid-State Electronics, 11, 459, 1968.

(11) C. Hammer and P. Weissglas,
Phys. Stat. Sol., 24, 531, 1967.
(12) J.J. Harris,
PhD Thesis, Sussex University, 1971.
(13) F.S. Ham and D.C. Mattis,
IBM Journal, 4, 143, 1960.

I
(1) V. Ilkovic,
Phys. Stat. Sol (b), 46, 483, 1971.
(2) H. Ikoma,
Jap. J. Appl. Phys., 6, 10, 1226, 1967.

J
(1) C. Juhasz,
PhD Thesis, London University, 1968.

K
(1) E.O. Kane,
J. Phys. Chem. Solids, 1, 249, 1956.
(2) M. Kohlner,
Z. Physik, 125, 679, 1949.
(3) S.H. Koenig,
J. Phys. Chem. Solids, 8, 227, 1959.
(4) Y. Kanai,
J. Phys. Soc. Jap., 13, 967, 1958.
(5) Y. Kanai,
J. Phys. Soc. Jap., 13, 1065, 1958.
(6) Y. Kanai,
J. Phys. Soc. Jap., 14, 10, 1302, 1959.
(7) N. Katera, K.F. Komatsubara and E. Yamada,
Proc. Int. Conf. Phys. of Semicond., Kyoto, 1966, p411.
(J. Phys. Soc. Jap., 21, Suppl., 1966.)

(8) J. Kołodziejczak,
Acta Physica Polonica, 20, 379, 1960.

(9) J. Kołodziejczak,
Acta Physica Polonica, 20, 289, 1960.

(10) J. Kołodziejczak,
Phys. Stat. Sol., 19, 231, 1967.

(11) R.H. Kingston and N.F. Neustadter,
J. Appl. Phys., 26, 718, 1955.

(12) H. Koelmans and H.C. de Graaff,
Solid-State Electronics, 10, 997, 1967.

L

(1) D.L. Lile,
J. Appl. Phys., 14, 8, 348, 1970.

(2) D.L. Lile,
Solid-State Electronics, 14, 855, 1971.

(3) M.S.P. Lucas,
J. Appl. Phys., 36, 5, 1632, 1965.

(4) R.H. Lyddane, R.G. Sachs and E. Teller,
Phys. Rev., 59, 673, 1941.

(5) I. Licea,
Phys. Stat. Sol., 25, 461, 1968.

(6) D.L. Lile,
PhD Thesis, London University, 1968.

(7) I. Licea,
Phys. Stat. Sol., 26, 115, 1968.

(8) I. Licea,
Phys. Stat. Sol., 37, 795, 1970.

(9) A.C.B. Lovell,
Proc. Roy. Soc., A, 157, 311, 1936.

M

(1) O. Madelung,
'Physics of III-V Compounds'
John Wiley and Sons, 1964.

(2) D. Matz,
Solid State Communications, 4, 491, 1966.
(3) D. Matz,
J. Phys. Chem. Solids, 28, 373, 1967.
(4) A. Many, Y. Goldstein and N.B. Grover,
'Semiconductor Surfaces',
North-Holland Publishing Company, Amsterdam, 1965.
(5) I.M. Mackintosh,
J. Electronics, 554, 1956.
(6) R.K. Mueller and R.L. Jacobson,
J. Appl. Phys., 33, 2341, 1962.
(7) H.F. Matare,
'Defect Electronics in Semiconductors',
John Wiley and Sons, 1971.
(8) K.B. McAfee, E.J. Ryder, W. Shockley and M. Sparks,
Phys. Rev., 83, 650, 1951.
(9) K.G. McKay,
Phys. Rev., 94, 4, 877, 1954.
(10) K.G. McKay and K.B. McAfee,
Phys. Rev., 91, 5, 1079, 1953.
(11) S.L. Miller,
Phys. Rev., 99, 4, 1234, 1955.
(12) J.C. McGroddy and M.I. Nathan,
Proc. Int. Conf. Phys. of Semicond., Kyoto, 1966, p437.
(J. Phys. Soc. Jap., 21, Suppl., 1966.)
(13) D. Matz,
Phys. Rev., 168, 3, 843, 1968.
(14) O. Madelung and H. Weiss,
Z. Naturforsch, 9a, 527, 1954.
(15) D.K.C. MacDonald and K. Sarginson,
Proc. Roy. Soc., A, 203, 223, 1950.

O

(1) M. Ohshita,
Jap. J. Appl. Phys., 10, 10, 1365, 1971.

(2) M. von Ortenberg and G. Landwehr,
Solid-State Communication, 8, 1955, 1970.

P

(1) H. Pfister,
Z. Naturforsch., 10a, 79, 1955.
(2) R.F. Potter,
Phys. Rev., 108, 653, 1957.
(3) G. Persky and D.J. Bartelink,
IBM, J. Research and Development, 13, 5, 607, 1969.
(4) E.H. Putley,
Proc. Phys. Soc., 73, 280, 1958.
(5) E.H. Putley,
'The Hall Effect and Semiconductor Physics',
Butterworth and Co., 1960.
(6) E.H. Putley,
Proc. Phys. Soc., 73, 128, 1959.
(7) H. von Pagnia,
Z. fur angewandte Physik, 16, 209, 1963.
(8) Roy F. Potter and H.H. Wieder,
Solid-State Electronics, 7, 253, 1963.
(9) R.L. Petritz,
Phys. Rev., 104, 6, 1508, 1956.
(10) A.C. Prior,
J. Electronics and Control, 4, 165, 1957.
(11) T.N. Pinsker and V.B. Sandomirskii,
Soviet Physics - Solid Physics, 7, 4, 984, 1965.
(12) M.H. Pilkuhn,
J. Appl. Phys., 34, 3302, 1963.

R

(1) D.L. Rode,
Phys. Rev., B, 2, 4, 1012, 1970.

(2) U. Roberts and J.E. Quarrington,
J. Electronics, 1, 152, 1953.

(3) D.L. Rode,
Phys. Rev., B, 3, 10, 3287, 1970.

(4) R. Koike and Ryuzo,
Jap. J. Appl. Phys., 3, 191, 1964.

(5) W.T. Read,
Phil. Mag., 45, 775, 1954; 45, 1119, 1954;
46, 111, 1955.

(6) F.J.U. Ritson and J. Wood,
Electronic Engineering, 36, 483, 1964.

(7) L. Reimer,
Z. Naturforsch., 13a, 148, 1958.

S

(1) E.H. Sondheimer,
Phil. Mag., 1, 1, 1952.

(2) J.R. Schrieffer,
Phys. Rev., 97, 3, 641, 1955.

(3) B. Szigeti,
Trans Faraday Soc., 45, 155, 1949.

(4) W.G. Spitzer and H.Y. Fan,
Phys. Rev., 99, 1893, 1955.

(5) R.A. Smith,
'Semiconductors',
Cambridge Press, 1959.

(6) J.E. Smith, M.I. Nathan, J.C. McGroddy, S.A. Porowski and W. Paul,
Appl. Phys. Letts., 15, 8, 242, 1969.

(7) R.A. Stradling and R.A. Wood,
J. Phys., C, 3, 5, L94, 1970.

(8) S.A. Semiletov and P.S. Agalarzade,
Soviet Physics - Crystallography, 9, 4, 409, 1965.

(9) R.J. Sladek,
Phys. Rev., 120, 5, 1589, 1960.

(10) J. Sinkkonen,
'4th Nordic Solid State Conference',
TURKU, Finland, Augus 11, 1970.

(11) H. Sewell,
PhD Thesis, London University, 1972 (to be submitted).

(12) W. Shockley,
Bell System Tech. J., 30, 990, 1951.

(13) R. Stratton,
Proc. Roy. Soc., A246, 406, 1958.

(14) M.C. Steele and M. Glicksman,
Phys. Rev., 118, 2, 474, 1960.

(15) M.C. Steele and S. Tosima,
Jap. J. Appl. Phys., 2, 7, 381, 1963.

(16) M.S. Sodha, J. Kamal and P.K. Pubey,
J. Phys. Soc., Jap., 28, 6, 1461, 1970.

(17) W. Shockley,
Phys. Rev., 56, 317, 1939.

(18) R. Seitwatz and M. Green,
J. Appl. Phys., 29, 1034, 1958.

(19) R. Stratton,
J. Phys. Soc. Jap., 17, 590, 1962.

<u>T</u>

(1) B. Tavger,
Phys. Stat. Sol., 22, 31, 1967.

(2) M. Tannenbaum, G.L. Pearson and W.L. Feldman,
Phys. Rev., 93, 912, 1954.

(3) H.C. Torrey and C.A. Whitmer,
'Crystal Rectifiers',
McGraw-Hill, 1948.

(4) J. Tauc,
J. Phys. Chem. Solids, 8, 219, 1959.

(5) S. Tosima,
J. Phys. Soc. Jap., 22, 4, 1025, 1967.
(6) I.E. Tamm,
Z. Physik, 76, 849, 1932.

V

(1) J. Volger,
Phys. Rev., 79, 1023, 1950.

W

(1) H. Weiss,
Z. Naturforsch., 8a, 463, 1953.
(2) J.D. Wiley and M. DiDomenico,
Phys. Rev., B, 2, 2, 427, 1970.
(3) H.H. Wieder,
'Intermetallic Semiconducting Films',
Pergamon Press, 1970.
(4) H.H. Wieder,
Solid-State Electronics, 9, 373, 1966.
(5) H.H. Wieder and D.A. Collins,
Solid-State Electronics, 11, 1093, 1968.
(6) W.J. Williamson,
Solid-State Electronics, 9, 213, 1966.
(7) H.H. Wieder,
J. Appl. Phys., 40, 8, 3320, 1969.
(8) A.F.W. Willoughby,
PhD Thesis, London University, 1965.
(9) A. Waxman, V.E. Henrich, F.V. Shallcross, H. Borkan
and P.K. Weimer,
J. Appl. Phys., 36, 1, 168, 1965.
(10) Welker et al - For a review see
O. Madelung, Handbuch der Physik, 10, 137, 1957
(Springer, Berlin).

(11) S. Whitehead,
'Dielectric Breakdown of Solids',
Clarendon Press, Oxford, 1951.
(12) P.A. Wolff,
Phys. Rev., 95, 6, 1415, 1954.
(13) P. Weissglas and K. Blotekjaer,
Phys. Stat. Sol., 28, 711, 1968.
(14) A.H. Wilson,
'The Theory of Metals',
Cambrideg University Press, 1965.

Y

(1) J. Yamashita and M. Watanabe,
Prog. Theor. Physics, 12, 443, 1954.

Z

(1) J.N. Zemel,
Phys. Rev., 112, 3, 762, 1958.
(2) C. Zener,
Proc. Roy. Soc. (London), 145, 523, 1934.
(3) J.M. Ziman,
'Electrons and Phonons'
Oxford University Press, 1960.